Magnetophotonic Sensor Systems for Fibre-Optic Magnetic Diagnostics in Tokamak Fusion Reactors

Philip J. G. Orr

A thesis submitted for the degree of Doctor of Philosophy to

Institute for Energy and Environment

University of Strathclyde

May 2011

This thesis is the result of the author's original research. It has been composed by the author and has not been previously submitted for examination which has led to the award of a degree.

Signed:

Date:

Abstract

Electrical power generation through controlled nuclear fusion has the potential to make a substantial contribution to the global generation pool within the next century. However, continuous operation of fusion reactors is not yet achieved. As such, a key objective of the next-generation machines is to increase the duration of operational pulses. As fusion reactors progress towards steady-state operation, the use of present inductive transducers as part of critical magnetic diagnostic systems becomes increasingly unfeasible.

In this thesis, it is proposed that due to their record of high performance in adverse conditions, optical fibre sensors may be the most appropriate alternative measurement technology. However, in order to reap the benefits associated with fibre sensors—such as minimised wiring, serial multiplexing, and electrical and chemical passivity—a new class of intrinsic point sensors is required that can operate within the extremely harsh nuclear fusion environment. To achieve this, two spectrally-encoding reflection-mode sensors that function on a purely magnetophotonic basis are developed, since it is shown that only this mechanism will succeed in the fusion environment.

By exploiting the nonreciprocality of the Faraday effect, it is shown how fibre Bragg gratings incorporating structural defects can yield enhanced, localised measurements. An alternative scheme enables direct measurement of the magnetic circular birefringence using polarisation mode switching. Both techniques provide a true all-fibre point measurement of magnetic field and retain serial multiplexing capabilities. Additionally, a supporting interrogation system is demonstrated that combines high-resolution measurement with high-speed multiplexing.

The transducers and associated systems described in this thesis are shown to meet the criteria both for performance and for environmental robustness. As such, their further development as part of a tokamak magnetic diagnostic scheme is recommended.

Acknowledgements

Firstly, my thanks to Paweł Niewczas for inviting me to undertake such an interesting project, for allowing me a great deal of freedom in my approach, and for humouring my biannual *it's the end of the world* e-mails.

Thanks to John Canning and the rest of the team at IPL for giving me the opportunity to spend a happy 3 months at their Sydney laboratory. The trip and their input were crucial to the project (and the food was great).

Thanks to Cyril Lescure, Sergei Gerasimov, Glynn Nash, and Mike Walsh for their advice and assistance during my visits to Culham and JET.

Thanks to my colleagues at Strathclyde for keeping my spirits up and providing welcome distractions. In particular, thanks to Marcus Perry for his help with radiation physics.

Most importantly, thanks to my partner Helen Hastie and my parents Clare and Ian Orr for their constant interest and encouragement!

Contents

List of Figures

List of Tables

Glossary of Abbreviations

AC	Alternating Current
ADC	Analogue-to-Digital Conversion
BBS	Broadband Source
CCFE	Culham Centre for Fusion Energy
CP	Circularly Polarised
CW	Continuous Wave
CWDM	Course Wavelength Division Multiplexer
DAC	Digital-to-Analogue Conversion
DAQ	Data Acquisition
DC	Direct Current
DFB	Distributed Feedback
DL	Delay Line
DSP	Digital Signal Processing
DWDM	Dense Wavelength Division Multiplexing
EMF	Electromotive Force
FBG	Fibre Bragg Grating
FPI	Fabry-Perót Interferometer
FFPI	Fibre Fabry-Perót Interferometer
FSR	Free Spectral Range
FWHM	Full-Width Half-Maximum
Hi-bi	High-Birefringence
ITER	International Thermonuclear Experimental Reactor
JET	Joint European Torus

LIA	Lock-In Amplifier
Lo-bi	Low-Birefringence
LP	Linearly Polarised *or* Linear Polariser
MAST	Mega-Ampere Spherical Tokamak
MEMS	Micro Electro-Mechanical System
MO	Magneto-optical
MZI	Mach-Zehnder Interferometer
NEP	Noise Effective Power
OPD	Optical Path Difference, nd
PBS	Pulsed Broadband Source
PCF	Photonic Crystal Fibre
PF	Poloidal Field
PM	Polarisation-Maintaining
PSC	Pure Silica Core
RIA	Radiation-Induced Attenuation
rms	Root-Mean-Square
SFP	Scanning Fabry-Perót Filter
SM	Singlemode
SNR	Signal-to-Noise Ratio
SoP	State of Polarisation
TE	Transverse Electric
TF	Toroidal Field
TDM	Time Division Multiplexing
TM	Transverse Magnetic
UV	Ultraviolet
WDM	Wavelength Division Multiplexing

Chapter 1

Introduction

1.1 Introduction to the Research

Rising energy demands of the global population will produce a shortfall in worldwide energy production and hence availability over the next few decades, according to the World Energy Council[Cou07]. This mismatch between energy supply and demand is likely to worsen over the proceeding century through a combination of population expansion, the fast economic growth of developing nations, the decline in availability of existing fuel sources, and the increasing pervasiveness of technology in everyday life[Div08]. It is estimated that by 2050 the global generation capacity must be doubled in order to avoid a potential energy crisis. To achieve this, a mixture of power sources and supporting technologies and infrastructure must be developed that together will meet this demand in an environmentally safe and sustainable manner.

As part of the proposed mix, electrical power through nuclear fusion is one of the most promising technologies for large scale power generation. Although nuclear fission will continue to make a large contribution to the generation pool, nuclear fusion has a number of key advantages that justify its development. These include a practically unlimited fuel supply, zero production of greenhouse gasses, a 100-year recycle time for all radioactive waste, and an inherently safe mode of operation. The production of electrical power by controlled nuclear fusion is currently under joint multinational development by the EU, the US, Russia,

Japan, China, India and South Korea in a research collaboration of unprecedented scale, following decades of preliminary research by separate, smaller international groups.

Among the many significant engineering challenges posed by nuclear fusion power generation is the development of systems for the confinement, heating, and monitoring of a superheated plasma. Crucially, it is the monitoring of the strength and shape of the magnetic field generated by the plasma current which allows operators to derive information on the plasma characteristics (such as geometry and current density) while they evolve. Indeed, the plasma itself is ignited and sustained by the machine's central solenoid, and thereafter contained within a toroidal magnetic bottle. Thus seen, it is clear that real-time knowledge of the magnetic field, as used in various locations and for various purposes within the machine, is vital to the success of the fusion reaction and hence to the machine's ability to deliver a constant power output for long periods of time.

The demands on the sensor system that must deliver these measurements are considerable. The reactor environment, within and around which the transducers and addressing components must operate, is extremely harsh. Components of the sensor system must remain functional under conditions of high electric field, high voltage potentials, strong vibration, high temperatures, and, in certain locations, a high level of cumulative irradiation. In addition, these effects should interfere minimally with the measurement, making the design and fabrication of the sensor systems themselves a substantial engineering problem.

Optical sensors, particularly those based on fibre optics, are fast becoming an important benchmark in sensing. Optical fibre measurement technology is often the only solution to measurement in harsh environmental conditions, commonly achieving high performance, remote operation and large-scale monitoring. In this thesis it will be argued that the high performance and robustness of optical fibre sensors may be harnessed, through appropriate designs, to address the shortcomings and improve upon the functionality of the inductive techniques presently used for measurement of magnetic field in the fusion environment.

1.2 Justification for Research

To increase the performance and efficiency of fusion reactors to a level where net output power is produced, and thus continuous operation is possible, is a primary goal of fusion research. Since this has not yet been achieved, both the largest experimental fusion reactor in operation (JET, Joint European Torus) and the next-generation experimental reactor (ITER, International Thermonuclear Experimental Reactor) operate according to pulsed regimes. The massive electrical power (around 700 MW in JET) required for plasma ignition, sustainment (heating), and control (magnetic confinement) is delivered to the machine over a relatively short period of time by external sources; in JETs case by simultaneously drawing directly from the United Kindgom 400 kV grid (from which they are permitted to draw up to 1% of the national supply for a limited duration) and discharging two flywheel generators, positioned locally, each with a maximum output power of 400 MW. An increase in this operational duration is planned; from around 10 seconds in JET to up to 10 minutes in ITER[Com03].

All magnetic sensors presently integrated into the JET machine are based on electromagnetic induction. As such, error in the measurement of quasistatic magnetic fields accumulates over the duration of the operational pulse as a direct result of deriving field information from integration of voltages induced on pickup coils. While the pulse durations are short enough in JET's case for signal post-processing to provide sufficient compensation, it is considered that in ITER's case the larger errors may not be acceptable[PP99]. As reactor engineering progresses, and pulse durations are further increased, this effect is likely to worsen to a point where the performance of inductive techniques for magnetic field measurement becomes unacceptable more generally. This has led to a small number of proposals for alternative steady-state magnetic field sensor designs based on magnetic force[Woo95][HKN$^+$99].

Given the extensive research to date on magnetostrictive fibre-optic sensors, it may seem that optical sensors could straightforwardly provide an accurate, absolute measurement of the field strength, thus circumventing the source of this

accumulating error. The ability of common fibre sensor interrogation techniques to multiplex such sensors along a single fibre undoubtedly lends itself to applications such as plasma confinement where quasi-distributed measurement of the confining magnetic fields would improve operator's knowledge of the plasma stability. This, in turn, means more effective control of the plasma geometry and better protection against harmful extinction and disruption events. However, as discussed in Chapter 3, the highly nonlinear behaviour of these materials at the levels of magnetic field strength used by machines such as JET and ITER (as strong as 10 T in certain locations) makes them unsuitable for this application. Additionally, the manufacturing of extrinsic transducers would lead both to greater costs and to rising complexity in terms of chemical vulnerability and the effects of irradiation on component materials. As such, if optical fibre sensors are to be seriously proposed for this application then transducers must be developed that do not make use of magnetostrictive materials.

Magneto-optical (MO) sensors—those that function purely on the basis of direct interactions between a quasistatic magnetic field and the electromagnetic wave without making use of an intermediate material—have been developed primarily for measurement of electrical current. Existing MO sensors function by measuring the degree by which the incident magnetic field alters the polarisation characteristics of the traveling electromagnetic wave. In most low-loss media, including silica glass fibres, this effect is very weak. The weakness of this effect is compensated for in existing MO sensor designs by using large interaction lengths (commonly fibre coils) or by guiding the interrogating light into a bulk glass sensor element that has been heavily doped specifically to enhance MO interactions. The development of a practical in-fibre MO sensor with a sharp spatial resolution poses a number of engineering challenges that have not previously been addressed.

The research presented in this thesis details ways by which intrinsic magneto-optical point sensors can be realised in optical fibre, as it will be argued that this underdeveloped subset of optical fibre sensors can provide an appropriate solution to high field measurement in this extreme environment. Two types of MO point sensors and associated addressing, interrogating, and processing elements are

described, as well as a fast, multiplexing sensor interrogation system suitable for, but not limited to, these sensors. In the case of each design, the commonly-cited benefits of optical fibre sensing are upheld—the proposed sensors and systems incorporate multiplexability, excellent spatial resolution, and high interrogation rates.

1.3 Principal Contributions

The principal contributions to knowledge by this research work can be summarised as follows:

- A critical discussion of optical techniques for magnetic field measurement and their suitability to fusion diagnostics,
- A review and analysis of the effects on optical fibres and sensors of combined gamma-neutron irradiation, leading to recommendations for sensor lifetimes and installation locations,
- A technique for fast linear or circular optical polarisation-mode switching in optical fibre sensors, facilitating an optoelectronic system design for polarisation mode switched interrogation of serially-multiplexed fibre Bragg grating (FBG) sensors,
- The demonstration of common-polarisation noise removal using polarisation-mode switched FBG interrogation,
- The laboratory demonstration of circular polarisation mode switched FBG interrogation for simultaneous measurement of dynamic magnetic field strength and temperature, and of linear polarisation mode switched FBG interrogation for simultaneous measurement of bend and longitudinal strain,
- A proposed technique for polarisation-mode switched FBG sensing of static magnetic fields,

- A demonstration of the enhancement of magneto-optical Faraday rotation in FBGs by incorporation of multiple defects (phase-shifts) in the index modulation profile,
- A general, scalable, optimum design of superstructured "slow-light" FBGs for obtaining giant reflective group delays of incident light at the Bragg wavelength,
- An automatable technique for fabrication of superstructured "slow-light" FBGs incorporating low linear birefringence and multiple phase-shifts,
- The design and simulation of superstructured "slow-light" FBGs as magnetic field sensors incorporating enhanced polarimetric sensitivity,
- An optoelectronic system design for interrogation of serially-multiplexed superstructured FBGs used as polarimetric point sensors for magnetic field strength,
- A proposed application of superstructured FBGs as narrowband wavelength-tunable optical delays for use in novel optical fibre communications applications,
- The design and laboratory demonstration of an ultrafast (potentially >100 kHz), wavelength-switching FBG sensor interrogation system having interferometric measurement resolution,
- The design of a flexible large-scale time-multiplexing FBG sensor interrogation system having interferometric measurement resolution,
- The design of hybrid time-and-wavelength division multiplexing interrogation systems based on the above fundamental interrogation schemes,
- The design of a full sensor system for quasi-distributed poloidal field measurement incorporating the above demonstrated elements.

1.4 Thesis Overview

The thesis begins with two chapters that provide background information on the fusion reactor environment and the state of the art in relevant optical fibre sensing technology.

Chapter 2 introduces the reader to the concept of the *tokamak*; its architecture and how it functions. The JET machine—an example of the dominant tokamak design—is then used to describe present magnetic diagnostic systems and their specifications, performance, and limitations. The reader is introduced to ITER and the relevant differences between this tokamak and JET. The environmental conditions expected for ITER are analysed, including the fusion reaction's radioactive products and the need for robust transducers. By the end of the chapter, the reader will have acquired an understanding of the diagnostic problems that the thesis aims to address.

Chapter 3 begins with a broad review of existing mechanisms for optical magnetic field measurement, tending by a process of elimination towards the mechanisms most appropriate for this environment. Relevant optical fibre sensors are reviewed, with particular attention paid to those concepts fundamental to the proposed systems. Limitations in the present state of the art are discussed, revealing key research opportunities in the area of intrinsic magnetic point sensors and their interrogation. Following identification of the most appropriate measurement basis, the effects of the fusion reaction's radioactive products on in-fibre sensors are analysed.

The first of two purely magnetophotonic sensor systems is presented in Chapter 4. The reader is introduced to previous research on bulk glass (non-fibre) multilayers and magnetophotonic crystals that forms the conceptual basis for an in-fibre polarimetric sensor. It is demonstrated how superstructured FBGs can be designed to yield a strong localised enhancement of the Faraday effect, and how this can be harnessed for high-resolution point sensing of magnetic field. The effects on sensor response of tuning the grating parameters are discussed, culminating in the description of an optimum, scalable sensor design. A fabrica-

tion technique for this type of device is described, and the preliminary laboratory characterisation of sample gratings is reported. A detailed description of the full system design, including the proposed technique for high-resolution interrogation, is provided. This chapter also discusses an alternative use of the superstructured gratings as highly-tunable optical delay lines for modern communications architectures.

Chapter 5 presents the second magnetophotonic sensor system, based on direct detection of the magnetic-field-induced circular birefringence. A technique for polarisation mode switching within a fibre transducer is described that allows polarisation-sensitive measurands, such as magnetic field, to be detected after the removal of polarisation-independent noise. The design and fabrication of the polarisation-switching sensor interrogation system is detailed. Laboratory demonstrations of simultaneous measurement of magnetic field and temperature using low-birefringence FBGs are described. Additionally, a demonstration of simultaneous measurement of bend and strain using the system is reported. Chapter 4 is not a prerequisite of this chapter, and may be skipped by readers with a specific interest in the polarisation-switching method.

The resolution, accuracy, and measurement rate of the system described in Chapter 5 is strongly related to the performance of the FBG wavelength monitoring scheme that it incorporates. In present interrogation systems an excellent resolution is achieved only at the expense of either multiplexing capability or measurement rate. To make the proposed system suitable for high-performance distributed monitoring of magnetic field, Chapter 6 describes a powerful FBG interrogation system that combines high resolution, high measurement rates, and large-scale multiplexing capability. This chapter may be read in isolation by those with an interest in optical sensor interrogation systems, however the discussions in Chapter 3 relating to interferometry and multiplexing will assist the reader.

The work in preceding chapters is consolidated in Chapter 7 which illustrates a potential distributed fibre sensor installation that integrates joint magnetic field and temperature diagnostics into a generalised tokamak architecture. Improvements in the performance and functionality of the hypothetical magnetic

diagnostics system are discussed. Chapters 3, 5 and 6 are prerequisites of this chapter.

Chapter 8 summarises the research presented in this thesis, and identifies key areas of further work for the improvement of the systems and techniques described here.

1.5 Publications

The following publications have resulted directly from the work described in Chapters 4 and 5 of this thesis. Work described in Chapter 6 is not published at the time of writing due to an ongoing patent application.

1.5.1 Journal Articles

1. P. Orr and P. Niewczas. Polarization-Switching FBG Interrogator for Distributed Point Measurement of Magnetic Field Strength and Temperature. *IEEE Sensors Journal*, 11(5):1220–1226, May 2011.
   DOI: 10.1109/JSEN.2010.2091124.

2. P. Orr, P. Niewczas, M. Stevenson, and J. Canning. Compound Phase-Shifted Fiber Bragg Structures as Intrinsic Magnetic Field Sensors. *IEEE/OSA Journal of Lightwave Technology*, 28(18):2667–2673, September 2010.
   DOI: 10.1109/JLT.2010.2060314.

3. P. Orr and P. Niewczas. An Optical Fibre System Design Enabling Simultaneous Point Measurement of Magnetic Field Strength and Temperature Using Low-Birefringence FBGs. *Sensors and Actuators A: Physical*, 163:68–74, September 2010.
   DOI: 10.1016/J.SNA.2010.07.009.

4. P. Orr and P. Niewczas. A Robust, Multiplexable Fiber Sensor for Simulataneous Measurement of Bend and Strain. *IEEE Sensors Journal*, 11(2):341–342, September 2010.
   DOI: 10.1109/JSEN.2010.2072497.

5. P. Orr, J. Canning, M. Stevenson, and P. Niewczas. Automatable Fabrication of Dispersion-Tailored Bragg Gratings for Tunable Narrowband Delays. *Electronics Letters*, 46(18):1283–1284, September 2010.
   DOI: 10.1049/EL.2010.2011.

1.5.2 Conference Papers

1. P. Orr and P. Niewczas. Polarization-Switching FBG Interrogator for Wavelength-Encoded Polarization-Sensitive Measurements. In *21st International Conference on Optical Fiber Sensors*, Ottawa, Canada, May 2011.

2. P. Orr, J. Canning, M. Stevenson, and P. Niewczas. Controlled Fabrication of Tunable Delay Using Compound Phase Shifted Resonators. In *19th Australian Institute of Physics Congress incorporating the 35th Australian Conference on Optical Fibre Technology*, Melbourne, Australia, December 2010.

3. P. Orr, M. Stevenson, J. Canning, and P. Niewczas. Magnetic Field Strength Measurement Using Tailored Dispersion Characteristics of Phase-Shifted Fibre Bragg Gratings. In *Fourth European Workshop on Optical Fibre Sensors*, Porto, Portugal, September 2010.
   DOI: 10.1117/12.865456.

4. P. Orr and P. Niewczas. Point Measurement of Magnetic Field Strength Using Compound Phase-Shifted FBGs. In *Joint Workshop on Frontier Photonics and Electronics 2010*, Sydney, Australia, March 2010.

5. P. Orr and P. Niewczas. Passive, Multiplexable Measurement of Magnetic Field Strength and Temperature Using PM Fibre Bragg Gratings and Chiral Fibre Devices. In *20th International Conference on Optical Fiber Sensors*, Edinburgh, UK, October 2009.
   DOI: 10.1117/12.834173.

6. P. Orr, P. Niewczas, J. R. McDonald, M. Walsh, and W. Morris. In-Fibre Point Sensing of Magnetic Field Strength Using Novel Photonic Sensor Con-

figuration. In *Fifth International Conference on Condition Monitoring and Machinery Failure Prevention Technologies*, pages 1119-1124, Edinburgh, UK, July 2008. Paper 181.

1.5.3 Related Publications

The following publications are in the related area of power systems monitoring using optical fibre sensors.

1. P. Orr, G. Fusiek, P. Niewczas, A. Dysko, C. Booth, F. Kawano, and G. Baber. Distributed Optical Distance Protection Using FBG-Based Voltage and Current Transducers. In *IEEE Power Engineering Society General Meeting 2011*, Detroit, United States, July 2011.

2. P. Orr, P. Niewczas, A. Dysko, and C. Booth. FBG-Based Fibre-Optic Current Sensors for Power Systems Protection: Laboratory Evaluation. In *44th International Universities' Power Engineering Conference*, Glasgow, UK, September 2009.

3. P. Orr, A. J Reid, and M. D. Judd. Sensor Response Characteristics for UHF Location of PD Sources. In *International Conference on Condition Monitoring and Diagnosis 2008*, Beijing, China, April 2008.
   DOI: 10.1109/CMD.2008.4580480.

Chapter 2

Tokamak Magnetic Diagnostics

2.1 Introduction to the Tokamak

Electrical power generation through nuclear fusion will rely on capturing and putting to work the energy released by the fusion of two gasses. As occurs within stars on a continuous basis, energy is released by a fusion reaction when two light atomic nuclei are fused together to form one heavier atom. For fusion to be useful as a terrestrial energy source, the fuel (deuterium and tritium; two isotopes of hydrogen) must be heated to temperatures over 100 million °C. At such high temperatures, the gaseous fuels ionize and become a plasma—a fourth state of matter distinct from the gas phase—comprised of positive ions and negative electrons that are free to flow and conduct.

In order to avoid contamination or cooling of the plasma, it cannot be allowed to come into contact with any materials. To do so would both quench the plasma and most likely destroy the contacting material. The plasma must therefore be forcefully confined to a specific volume and density. Due to its abundance of charge carriers, the plasma is highly electrically conductive and responsive to electromagnetic fields. Utilising this characteristic, the most common technique to shape and contain a plasma is to assemble a set of powerful magnetic fields which exert Lorentz force on the moving charges that comprise the plasma.

Following the 1955 United Nations International Conference on the Peaceful Uses of Atomic Energy, previously-secret research on nuclear power was declas-

sified and international collaboration on the topic of fusion power and plasma confinement began. Research on the tokamak—a device for magnetic confinement of a plasma within a toroidal vacuum vessel—was pioneered in the late 1950s by the Kurchatov Institute in Moscow[Kur56]. In reference to the Soviet origins of the device, the word *tokamak* is a transliteration of a Russian acronym for *toroidal chamber with magnetic coils*.

The tokamak remains to this day the most successful concept for magnetic confinement of plasma. It is the core item of plant in today's experimental fusion reactors, and the basis for prototype commercial fusion reactor designs.

2.1.1 Magnetic Confinement

The tokamak is a toroidal vacuum vessel incorporating a combination of surrounding electromagnets that are configured to produce strong field lines both in the torus plane (toroidal field, TF) and in the vertical plane (poloidal field, PF) in order to confine the circulating plasma current. The primary function of the TF electromagnets—those coiled around the torus walls—is to confine the plasma particles, while the field generated by the PF magnets above and below the toroid—contributed to by the plasma current's own circulating magnetic field—acts to pinch the plasma away from the walls of the vessel and help maintain the overall shape and stability of the plasma. Figure 2.1 illustrates how the TF and PF coils are positioned in relation to the plasma current in a standard tokamak.

The plasma current is induced by a changing current in the third torus electromagnet, known as the Central Solenoid, which produces a large back-EMF to ignite the plasma at the start of each pulse. The device, positioned in the centre of the torus, is essentially the primary of a large transformer. By providing a path for current flow, the plasma loop itself becomes the secondary of this transformer. In this way, after plasma ignition, the Central Solenoid is able to contribute to the inductive flux that drives the plasma.

The effect of the combination of the TF and PF fields is a resultant helical field that winds around the plasma current. This helical field acts as a magnetic

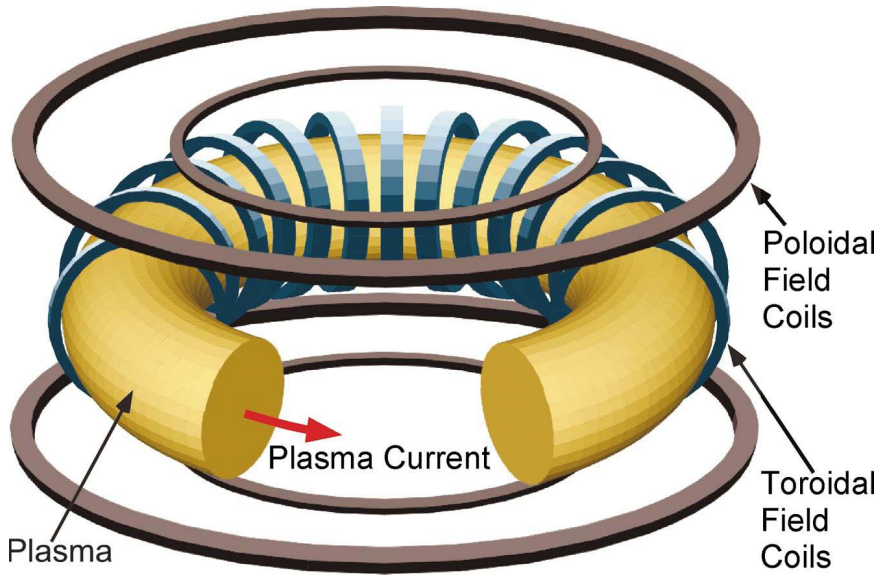

Figure 2.1: A simplified view of the toroidal and poloidal magnetic field coils of a tokamak[Boo04]

bottle, continually redirecting the plasma particles inward away from the vessel walls[Kra95]. As an illustration of the strength of the magnetic fields used, the ITER magnetic confinement system will employ 18 equispaced superconducting TF coils, each with a maximum field of 11.8 T. This is in addition to a number of PF coils positioned above and below the torus that will generate similar maximum fields.

Tokamaks are therefore permeated by a number of extremely strong magnetic fields generated by the magnetic confinement and plasma driving systems. The size and location of the magnetic coils planned for installation in the ITER tokamak are illustrated by Figure 2.2, which also indicates the size of the modern tokamak as designs scale upwards towards true commercial machines. Correct operation of the magnet systems is vital to the stability of the plasma, and as such the generated fields require continuous monitoring and adjustment during the operational period. This monitoring may be achieved by measurement of the current through the magnets (by Rogowski coils or Faraday loops), which can be related to the field strength in a range of locations, but also more directly by the use of magnetic field point sensors which are installed within and around the vacuum vessel.

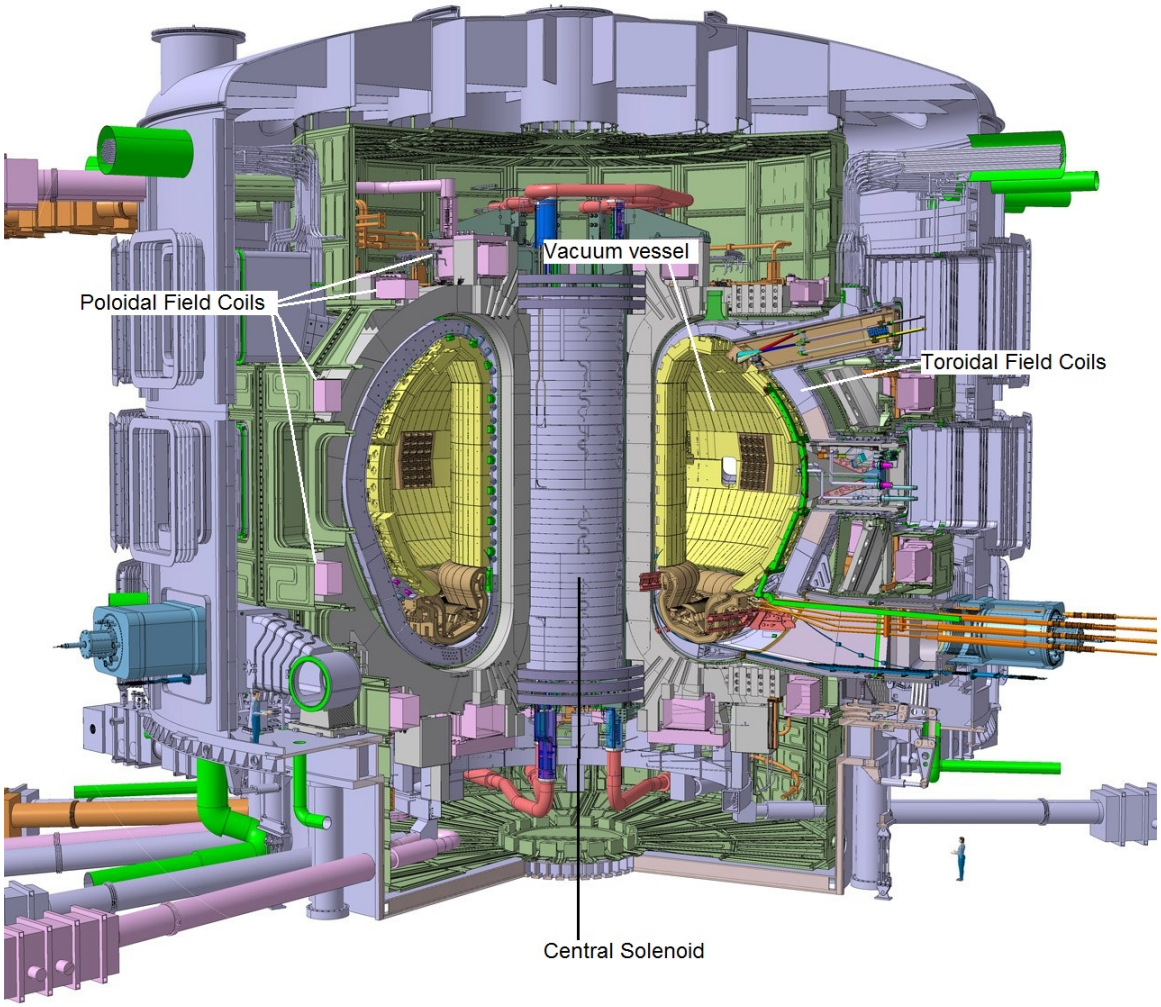

Figure 2.2: A cut-away computer illustration of the ITER tokamak

2.2 Magnetic Diagnostics

Both the JET and ITER machines incorporate an extensive suite of diagnostics systems that are used to provide the operating physicists and engineers with information on structural integrity, fusion reaction products, and plasma shape, stability and temperature. When categorising these diagnostic sets the ITER Technical Basis makes a simple distinction between what are deemed to be *basic* and *advanced* diagnostics[PP99]:

- *Basic* diagnostics are those that are required for machine protection and basic plasma control. They are fundamental to operation and will be re-

quired to function during every pulse. Consequently, they have the highest priority for resources such as manpower, budget, and space.

- *Advanced* diagnostics are those that may provide measurements for advanced plasma control and analysis. These diagnostics will not be crucial to the success of every pulse, and may not require real-time control or monitoring.

Magnetic diagnostics systems are the means by which several of the key *basic* diagnostic demands are met, including the monitoring of generated fields and the resultant plasma geometry, and it is these diagnostics that are most relevant to this thesis. Several parameters that are absolutely fundamental to the operation of the tokamak, such as plasma current, loop voltage, plasma position and shape, and the plasma stored energy, are measured by magnetic diagnostics alone and in real-time throughout every pulse. This section will look at how tokamak magnetic diagnostic systems presently deliver these fundamental measurements, the performance requirements for the installed sensors, and the known difficulties with current techniques.

2.2.1 Principal Uses of Magnetic Diagnostics

The principal uses of the magnetic diagnostics systems installed in tokamaks can be summarised as follows[TTC+10][PP99]:

- *Measurement of the magnetic fluxes and fields surrounding the plasma for reconstruction of the magnetic and plasma equilibria*,

  Flux and field measurements are made inside and outside the vacuum vessel for computer reconstruction of the magnetic field geometry—in real-time for protection and control, and post-pulse for data analysis. Particularly detailed measurements are required of the complex field in the divertor region beneath the plasma where impurities and helium ash are redirected to a target chamber. In addition to the measurement of fields and flux in the

poloidal plane, the variation in the toroidal flux provides information on the energy stored in the plasma and also provides a direct estimate of the toroidal field strength.

- *Measurement of total plasma current*,

  Historically, measurement of the plasma current was provided by Rogowski coils measuring the contour integral of the magnetic field in order to yield the current passing through the enclosed surface. This was problematic in that when the coil was placed outside the vacuum vessel the resulting measurement would include all currents flowing in the vessel walls. To avoid this, a *virtual* Rogowski coil is now commonly constructed by a weighted sum of individual poloidal field measurements. However, for ITER, true Rogowski coils are being developed that will employ liquid helium cooling to allow them to be installed inside the vacuum vessel. Importantly, a fibre-optic Faraday rotation measurement device is also under development which, similar to the Rogowski coil, must be placed inside the vessel and enclose the plasma current entirely[MBB+09].

- *Measurement of currents flowing between the plasma and the vacuum vessel walls (halo currents)*,

  Halo currents are currents which flow outside the confined plasma region. During a Vertical Displacement Event, the plasma makes contact with a limiter and starts to be "scraped off", causing a fraction of the plasma current to flow along the field lines. The current path can intercept a material surface, where the current will take the path of least resistance, causing intense heating and deformation of the material. Halo currents can therefore cause great damage and are a concern for future devices such as ITER. To achieve a satisfactory level of halo current monitoring, a large number of sensors will be required, using a variety of different technologies including Rogowski coils and current shunts, so as to maximise the quality of the

data gathered. The main issue for achieving this level of monitoring is a practical one—the number of required sensors will generate a large amount of additional wiring.

- *Production of feedback error control signals that identify plasma position and tilting instabilities that may be corrected by fast TF or PF adjustment.*

  There are two main plasma instabilities that may be stabilised by magnetic feedback control: positional and tilting instabilities. Correcting these instabilities requires fast action by power supply operators who control the currents applied to the TF and PF magnets, and their response relies on information derived in real-time from the magnetic diagnostic set. Distortions or time-delays in the measurements can reduce the quality of this fast-acting control. Separately, magnetic diagnostics are also used to provide feedback for plasma shaping. This is less demanding in terms of speed of operation, but requires excellent measurement precision.

The above diagnostics are critical to the operation of the tokamak in terms of real-time control, real-time and post-pulse reconstruction of the plasma and magnetic field geometries, vessel protection, and safety. Although some ex-vessel magnetic sensors are employed to provide additional field information, the critical diagnostics above are delivered by suitable radiation-hardened in-vessel sensors based on well-established inductive measurement techniques. It is the measurement demands of these diagnostics that determine the performance requirements of both the presently-installed sensors and any alternative or assistive measurement technologies that are proposed. From the relevant diagnostics, it is clear that sensor characteristics such as wiring demands and the spatial, temporal, and measurement resolutions are of high importance, and in terms of functional performance it is these characteristics that new proposals should seek to improve.

2.2.2 Inductive Magnetic Point Sensors

The measurements acquired by present tokamak magnetic diagnostic systems are performed using simple conducting loops and coils installed at appropriate positions on the tokamak to enable the induction of voltage by the appropriately aligned magnetic flux. The reason for using inductive techniques is, to a large extent, a historical one—the well-established physics of the method require no new development for use in, for example, the ITER installation and sufficient materials research has been performed to ensure an acceptable level of radiation hardness. However, there are crucial drawbacks to the inductive technique that ultimately will render this method useless in future reactors that are capable of continuous operation. Here, the measurement technique and architecture of present sensors is described.

2.2.2.1 Method of Operation

A photograph of a typical JET measurement coil prior to installation in the machine is shown in Figure 2.3. These coil and loop based sensors function by electromagnetic induction, whereby the changing flux of a magnetic field through the loop's enclosed surface generates a voltage over the loop terminals. The generation of loop voltage V can be expressed mathematically as

$$V = -N\frac{\Delta(BA)}{\Delta t} \tag{2.1}$$

where N is the number of loops that comprise the measurement coil, B is the axially-aligned component of magnetic field strength ($\mu_0 H$) in Tesla, and A is the area enclosed by each loop. Since the induced coil or loop voltage is proportional to the rate of change of the magnetic flux, rather than the absolute value of magnetic field strength, the voltage signal on the coil can be related only to a *change* in the magnitude of the aligned magnetic field.

In order to use inductive techniques to measure magnetic fields with prolonged static magnitudes, an electronic integrator is used to effectively convert the differential analogue measurement of the rate of change of magnetic flux to a

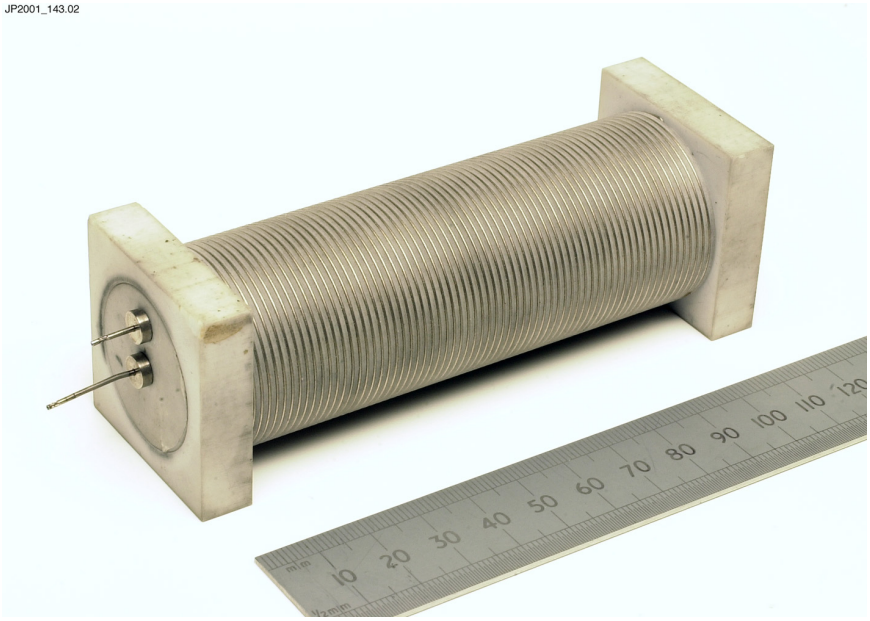

Figure 2.3: A JET measurement coil wound from titanium wire on an alumina ceramic former (Image courtesy of CCFE)

continuous measurement of the magnetic field magnitude. To do so, an electronic scheme refers to the sampled analogue voltage V and increments or decrements, as appropriate, the current stored value of magnetic field strength. Thus, a "running tally" of the present field strength is maintained over the duration of the tokamak pulse. Figure 2.4 illustrates the timescales of a typical JET pulse in terms of the plasma and magnet currents. As discussed in the next section, the problems associated with unwanted drift in the currently-stored value, especially over prolonged steady-state conditions, are well known.

2.2.2.2 Environmental Shielding

The most significant environmental effects in both the JET and ITER reactors are the high-levels of neutron and gamma radiation and the high surface temperatures. ITER's in-vessel magnetic sensors should ideally be capable of withstanding this bombardment for the operational lifetime of the machine—approximately 30,000 pulses over 20 years, or 200 days of total integrated operation. Compared with those in JET, the conditions in ITER will be far harsher, with neutron flux (the rate at which neutrons flow through a unit area) and fluence (the ac-

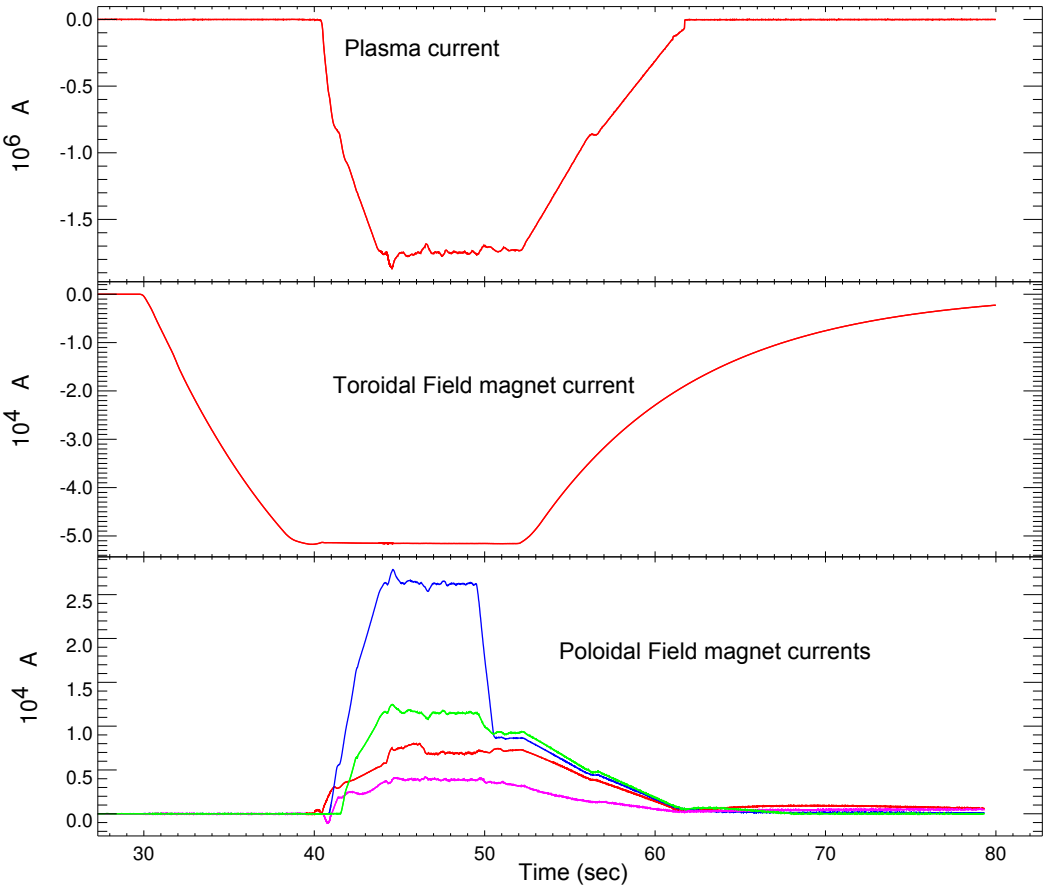

Figure 2.4: Plasma and magnet current magnitudes and timescales during a typical JET pulse. Steady-state conditions are achieved for approximately 15 s. (Data courtesy of CCFE)

cumulated number of neutrons that intersect a unit area) increased by factors of 5 and 10,000 respectively[CCK+01]. Emitted neutrons will interact with other particles to produce highly-ionizing gamma radiation which, combined with the high-energy neutrons (E > 0.1 MeV), will affect the integrity and performance of exposed materials in the vicinity, including electrical devices and conductors. Table 2.1 summarises the relevant radiation levels that in-vessel magnetic sensors will be subject to[CCK+01]. Levels at the First Wall—the immediate plasma-facing surface—are included for comparison.

The *blanket* is a modular, tiled shield that covers almost all of the vacuum vessel's internal walls. In a commercial reactor, it is the heat generated in the blanket by the neutrons that will be put to work to generate electricity. By slowing the neutrons and absorbing heat, the blanket also acts to attenuate the

Location	**Fast Neutron Flux** (> 0.1 **MeV**) n/m^2s	**Ionizing Dose Rate** Gy/s
First wall	3×10^{18}	2×10^3
Near blanket gap	$0.2–1 \times 10^{17}$	20–100
Behind blanket	2×10^{16}	≤ 20
Inboard TF coil side	1×10^{14}	0.1

Table 2.1: Predicted neutron flux and ionizing radiation levels at key in-vessel magnetic sensor locations

neutron flux and high temperatures experienced by components situated behind it. With reference to Table 2.1, the in-vessel magnetic sensors will be located both in the gaps of the blanket (the harshest proposed location), and also behind the blanket. The final entry of Table 2.1 refers to sensors that will be installed on the inner side of the torus, near the Central Solenoid.

The locations of the in-vessel pick-up coils and voltage loops that will be installed in ITER are shown in Figure 2.5, which illustrates a slice of the toroidal vacuum vessel. Presently, in the JET machine, over 400 measurement coils or loops are installed in similar locations. This collection comprises coils and loops mounted on the back plate of the blanket structure, coils mounted in the divertor cassette region, and various coils in toroidal Rogowski configurations that enable the detection and measurement of the transient halo currents.

The effects of Radiation-Induced Conductivity (RIC), Electrical Degradation (RIED), and Induced EMF (RIEMF) act to undermine the suitability of electrical devices, including inductive measurement coils, for use in radioactive environments. Careful material selection, analysis and testing are performed before devices and materials are deemed suitable for installation. In the case of JET, to protect the electrical sensors as much as possible from radiation damage and radiation's influence on measurements, exposed sensors installed in the torus vacuum are housed in individual stainless steel cases with a longitudinal slot. The plasma facing surface of the stainless steel case is protected by a carbon tile that further slows the bombarding neutrons and lessens the inflicted damage. An alumina

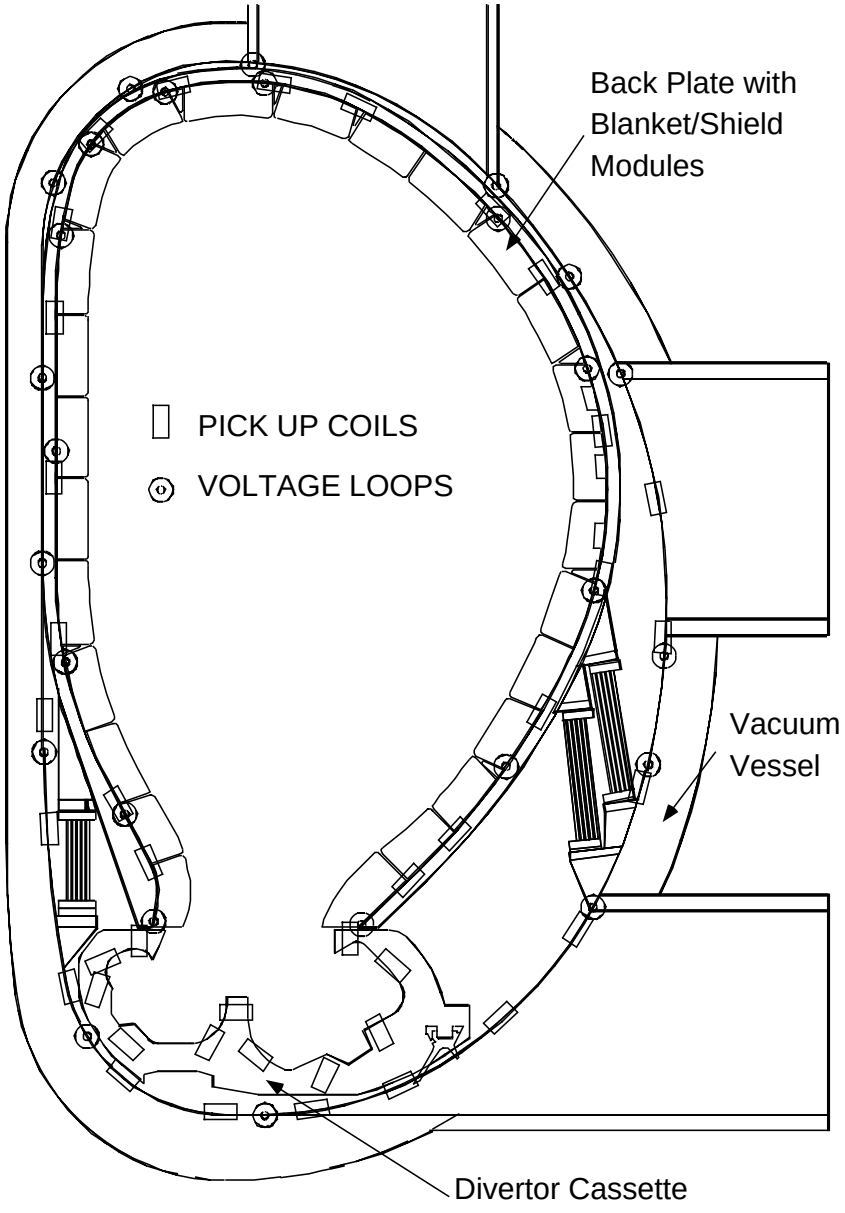

Figure 2.5: Cross-section of ITER showing the pick-up coils and voltage loops on the inner wall of the vessel, on the plasma side of the back plate, and embedded in the divertor cassette[PP99]

core and titanium wire are chosen to match the thermal expansion coefficients, and all of the materials used in the coil design and housing are high vacuum compatible up to at least 350 °C.

Addressing electrical cables must also be shielded as much as possible from the particle fluxes. The wires used to address sensors are mineral insulated with an alumina outer coat. Where possible, sensors and addressing cables are also placed in naturally shielded locations. Fixed connections between wires are welded, and connectors use spring-loaded contacts with guiding rods to assist the remote (robotic) handling of components that have recently been irradiated—sensor lifetimes, installation procedures, and the ease of their inevitable maintenance are key concerns of reactor designers.

Although temperatures of the plasma-facing surfaces rarely exceed 400 °C (with certain surfaces in the divertor region experiencing 800 °C)[PP99], the design of in-vessel sensors must take into consideration the effects of combined heating and exposure to the high neutron flux and gamma radiation dose. Similarly, any proposed alternative and supplementary sensors must undergo exhaustive materials testing before they may be viewed as sufficiently robust for the fusion environment. To this end, the influences of neutron and gamma irradiation on fibre performance—both as a waveguide and as a sensor—will be analysed in Chapter 3.

2.3 Performance of Present Techniques

The design of sensors to reliably enable the diagnostics listed in Section 2.2.1 must take into account a number of key performance characteristics. These are: measurement resolution, measurement drift, spatial resolution, measurement rate and dynamic response, linearity, and feasibility of installation including the wiring requirements and resistance to environmental effects. Here, the functional demands on present sensors are analysed in order to indicate the required performance, in terms of these key characteristics, of alternative non-inductive fibre-optic sensors that will be proposed in later chapters.

2.3.1 Measurement Resolution

To achieve the level of performance required for the fundamental magnetic diagnostics, the sensors must be capable of providing sufficient measurement resolution under conditions of large magnetic fields and fast fluxes produced by the plasma confinement systems, but also when and where the field strength is low. Sensors proposed for point measurement of the field in this application must be able to demonstrate the potential for measurement resolutions similar to that achieved by the presently-deployed inductive sensors. The performance demand on inductive magnetic sensors in present tokamak magnetic diagnostics is relatively high: a common target for sensors installed in JET is a measurement error of between 1–3% for all sensors, and an absolute error of less than 0.2 mT when the field is low[Ger11]. Similar error magnitudes will be required in ITER[Dia10].

2.3.2 Error Sources

There are a number of error sources that contribute to the total error exhibited by the inductive magnetic sensors installed at JET[Dia05]:

- Integrator drift
- Imperfect coil calibration
- Uncompensated and unwanted toroidal field pickup
- Uncertainty of the coil location and orientation
- Noise from Analogue-to-Digital Conversion (ADC noise)
- Local eddy currents

The eddy current influence is difficult to compensate for without placing the sensor in a less vulnerable position which, given the nature of the required measurements, is not practical. The two main sources of error are then processing noise (due primarily to integrator drift) and physical errors in the geometry of the coil, its location, or its correct alignment with the field or flux of interest. In

practice, the inductive sensors installed at JET and planned for installation at ITER generally exhibit an error due to ADC noise of less than 1 mT, which in the case of many sensors is doubled in magnitude if errors due to drift are also taken into account. The errors due to mis-location and mis-alignment are larger, often by an order of magnitude, but it may be assumed that such sources of error will be universal to all conceivable sensor technologies.

2.3.3 Principal Disadvantage of Inductive Sensors

The most relevant source of measurement error in JET's magnetic sensors is therefore, as is mentioned extensively in the literature[TTC+10][PP99][CCK+01], the error due to drift incurred during integration of induced voltages—an error source that is unique to the presently-deployed inductive sensors. It must be noted that the recorded error on JET sensors due to integrator drift is incurred over the duration of standard JET pulse lengths which, as mentioned previously, are brief by the standards that will be adopted in ITER and beyond.

It is also important to note that drift error is stated after the implementation of a complex drift compensation procedure. In JET, the drift compensation procedure for the integrators is initiated 2 minutes prior to the onset of the pulse, and the entire measurement procedure including drift measurement, integrator resetting, signal measurement, and ADC takes a full 4 minutes per pulse—including a measurement period of only a fraction of this time (20 s). In future tokamaks, the longer pulse lengths will reduce the effectiveness of such procedures, and the pre-pulse preparatory measurements will become increasingly cumbersome. It is notable that these issues are of clear and justified concern to ITER designers:

> The principal new aspect of ITER will be the extremely long pulse length, which may require the development of measurement methods additional to the traditional inductive magnetic measurements.
>
> ...
>
> For very long ITER pulses (longer than a few thousand seconds), alternative approaches are required because of the possibility of un-

> acceptable errors arising from drifts in the inductive methods. Direct measurements of the magnetic field using non-inductive methods are being considered.
>
> — **ITER Physics Expert Group** [PP99]

In fact, beyond ITER the measurement of truly steady-state magnetic fields will be necessitated, which will undermine the inductive techniques entirely. In intervening stages of development, drift compensation procedures will require drastic improvements to reduce error over extended pulse durations and to reduce the time required for the compensation procedures. In order to deal with this issue, efforts are being made to develop long-time electronic integrators for ITER that will reduce the drift to acceptable levels by improved signal processing, but such techniques cannot remove drift entirely over ITER-like pulse durations and will not, in the long term, enable an inductive steady-state magnetic field sensor[KK97]. Alternative non-inductive electronic sensors are in development that may be suitable for measurement of a steady-state magnetic field directly, but at the expense of simplicity of construction[Woo95][HKN$^+$99]. In general it is considered that the non-inductive electronic alternatives (Hall effect and magnetic force) are either not suitable for use in a nuclear environment or are too elaborate for in-vessel use. As such, alternative non-inductive and non-electronic proposals are sought.

2.3.4 Spatial Resolution

The spatial resolution of sensors is of particular importance for plasma equilibrium reconstruction, plasma reshaping, and for identification of halo current locations. Present inductive sensors for JET and ITER can achieve a spatial resolution of $100 \times 25 \times 25$ mm which is determined by the size of the measurement coil and by the minimum induced voltage magnitudes. If optical fibre sensors can be developed for this application, the achievable spatial resolution of the magnetic diagnostics may be improved to the dimensions of common in-fibre sensors: $10 \times 0.01 \times 0.01$ mm. Further, if the installation density of such sensors can

be made high enough, an unprecedented improvement in the reconstruction of plasma and magnetic field geometries would be possible.

2.3.5 Wiring and Multiplexing

Increasing the installation density in the manner proposed above introduces the problem, mentioned earlier with regards to halo current monitoring, of wiring each individual sensor. Present inductive sensors are addressed individually by radiation-shielded twisted pair wire. Each additional sensor therefore introduces one additional addressing cable, and the practical difficulty of expanding the sensor installation increases accordingly. This is an important limitation of electronically-wired sensors, where serial multiplexing of transducers is not possible due to the inability to discriminate between responses of individual sensors.

In contrast, as will be discussed in Chapter 3, the measurement information from optical fibre sensors is commonly encoded in the wavelength of returning light, allowing many sensors to be installed at discrete locations along a single optical fibre to provide a quasi-distributed measurement. As such, in the case of optical fibre sensors there is not a linear proportionality between sensor density and practical installation difficulty, since it is as practical to install a single sensor as it is to install twenty such sensors. In a tokamak with over 400 similar transducers, optical fibre sensing has the unique potential to greatly reduce wiring demands and hence the required designated access space.

2.3.6 Measurement Rate

Measurements from the magnetic sensors installed in JET are acquired at different rates depending on what fraction of the tokamak pulse is underway. The detection of certain disruption events can trigger a window of fast acquisition and high sample density for post-event analysis. In general however, acquisition of measurements is performed slowly (at approximately 80 Hz) with interspersed periods of fast sampling at either 2.5 kHz or 5 kHz that are both fixed and event-triggered.

2.4 Summary

Due to the inability of present magnetic field sensors to operate within tokamak pulse regimes incorporating prolonged steady-state periods, alternative non-inductive (preferably also non-electronic) sensors that can match the performance of the present technique are sought. The functional and environmental demands on in-vessel sensors for this purpose are summarised in Table 2.2.

Measurement error:	$< 3\%$ (large fields)
Acquisition rate:	5 kHz maximum
Spatial resolution:	$\leq 100 \times 25 \times 25$ mm
Maximum field strength:	1–10 T (location/regime dependent)
Temperature (behind first wall):	< 400 °C
Integrated operational lifetime:	4,600 hours

Radiation levels:

	Fast Neutron Flux (> 0.1 **MeV**) n/m^2s	**Ionizing Dose Rate** Gy/s
Blanket gap	$0.2\text{–}1 \times 10^{17}$	20–100
Behind blanket	2×10^{16}	≤ 20
Inboard TF coil side	1×10^{14}	0.1

Table 2.2: Summary of the operational and environmental requirements for ITER in-vessel magnetic sensors.

Since the demands on measurement rate and spatial resolution are surpassed by most common optical fibre sensor types (see Chapter 3), point measurement of magnetic field strength by optical means could form an attractive alternative or complimentary technology if suitable transducers and systems are developed. A suitable optical fibre sensor should—while retaining excellent spatial and temporal resolution—be capable of measuring large magnetic fields (>1 T) with a sufficiently low measurement error (ideally <3%). A fibre-optic solution may also allow for simpler, more flexible wiring of sensors if the capability for multiplexing

is retained. As will be discussed in Chapter 3, present fibre-optic point sensors for magnetic field do not yet achieve this level of performance and functionality. However, it will be demonstrated in this thesis that the required operational performance can be achieved by all-glass fibre sensors that make use of tailored optical resonant structures (Chapter 4) or novel optical polarisation processing schemes (Chapter 5).

In parallel with the functional requirements of a proposed alternative sensor technology, alternative sensors must be capable of withstanding the neutron and gamma radiation bombardment and the high surface temperatures. In ITER there will be a number of in-vessel sensor locations that experience a range of irradiation levels. Chapter 3 will include an analysis of the effects of relevant radiation levels on optical fibre sensors in order to recommend which in-vessel locations may be suitable for long-term fibre sensor deployment.

Chapter 3

Optical Fibre Sensors: Review of Key Science and Technologies

3.1 Introduction

Since their inception almost 40 years ago, optical fibre sensors have evolved—driven principally by research in the academic and military sectors—to become an important reference in high-performance instrumentation. Fibre sensors excel in three areas in particular that together justify the development of this technology for use in highly demanding applications and environments[Lee03][Rao97]:

1. *Robustness.* An incorrect preconception of optical fibre sensors is that they are fragile. In fact, for their size and weight they are extremely robust. Fused silica (SiO_2) fibres can withstand large longitudinal and transverse strains and small bend radii. Their simple and pure all-glass composition imbues them with chemical and electrical passivity, lending them to applications where the possibilities of corrosion, mutual chemical contamination, or electrical conductivity are often insurmountable problems for conventional sensors. Additionally, they have been shown to operate at temperatures of over 1200 °C[BCB+11].

   Fibre sensors are, in general, immune to electromagnetic interference—however, in this thesis methods to deliberately sensitise fibre transducers

to quasi-static magnetic fields will be introduced. At appropriate operating wavelengths they exhibit substantial resistance to deterioration under neutron bombardment and ionizing radiation[Gus10][FBB+02], as will be discussed later in this chapter. Due to their robustness and reliability, fibre sensors have been applied in the oil and gas, nuclear, aerospace, and biomedical industries, where they are frequently the *only* viable sensor technology.

2. *Geometry and flexibility.* The outer diameter of a standard optical fibre is 125 μm—similar to that of a human hair. Fibres have long been used by the telecommunications industry to transmit information over hundreds of kilometres with a minimum of attenuation and distortion, and remain the gold standard of media for this purpose. The use of such a small, low-loss, information carrier to both host *and* interrogate sensors allows a great deal of flexibility in wiring, multiplexing, and sensor placement, and enables distributed measurements over the entirety of a single fibre.

   As passive devices, requiring no power source, fibre sensors can be deployed at very large distances ($>$ 100 km) from the interrogator[FNM05]. Their small size and light weight lends them to environments with limited access space or strict weight requirements, such as in down-hole applications or on board marine or aero craft[NM07]. They can also be integrated into structures such as bridges or items of plant to provide monitoring of, for example, structural integrity[LHRCQIC11].

3. *Performance.* Fibre sensors have been developed for measurement of a wide variety of parameters including longitudinal and transverse strain, bend, temperature, pressure, ultrasound, electromagnetic fields, voltage, current, refractive index (liquid level, gas concentration), and humidity[KDP+97]. Due to the range of optical properties that can be modulated by these external parameters, it is often possible for optical fibre sensors to measure multiple parameters simultaneously for increased functionality, or to incorporate compensation for drifts in, for example, ambient temperature.

The bandwidth and dynamic response of optical sensors is potentially extremely high, owing to their passive, light-based nature. In terms of noise levels, it has recently been shown that in-fibre point sensors can exhibit a measurement resolution as low as the thermodynamic noise floor[CFK08]—a resolution that is unparalleled by other sensor types. In practice, the speed and accuracy of optical fibre sensors is determined by the abilities of the interrogation system that retrieves the information, and this is particularly so in applications requiring high numbers of sensors[GFVM09]. As such, a technique for better harnessing their intrinsically-high temporal and measurement resolutions is described in Chapter 6.

The previous chapter considered the operational and environmental demands on generic magnetic point sensors for use in tokamak diagnostics. It was shown that due to the combined demands of high performance and environmental robustness, very few sensor technologies will be suitable candidates to support or replace existing inductive sensors for dynamic magnetic field. With their excellent record of high performance in adverse conditions, optical fibre sensors are a strong candidate for delivering the required functionality. However, before this technology can be considered suitable for fusion diagnostics, it must be demonstrated that both the performance and robustness requirements summarised in Table 2.2 can be met by an optical fibre sensor.

In this chapter, the most appropriate basis for an optical fibre approach to tokamak magnetic diagnostics will be determined. The ways by which light, guided by a fibre, can be modulated in some respect by a quasi-static magnetic field—and therefore the ways by which a fibre-optic magnetic sensor may be implemented—are reviewed, and the most appropriate method of modulation selected. Following this, the architectures and functionality of relevant optical fibre transducers are analysed in order to determine the most appropriate techniques for this application. A focussed discussion on the interrogation, wiring, and multiplexing of the chosen sensor type is then conducted, providing the foundation for the sensor-specific interrogators supporting Chapters 4 and 5 and the efficient, general-application interrogator detailed in Chapter 6. Lastly, the vulnerability

of the selected measurement technique and transducer to the expected radiation levels is analysed in order to estimate both the survivability of these sensors and the most suitable areas for installation inside the tokamak.

3.2 Candidate Sensing Mechanisms

The measurement of magnetic field strength by optical fibre sensors has, to date, been accomplished by three fundamental approaches, each of which conveys the magnetic field information by a different process. These are: magnetostriction, magnetic force, and magneto-optics. In the development of these approaches the objective has traditionally been to improve measurement resolution with little concern for structural complexity, robustness to environmental fluctuations, or performance at high flux densities. In this section, each of these approaches will be briefly reviewed in terms of their candidacy for further development as part of a tokamak magnetic diagnostic.

3.2.1 Magnetostriction

Magnetostrictive optical fibre sensors are the most well-developed of all fibre-based magnetic field sensors[PDD06]. This is due in part to the simplicity of the implementation—the sensor must only be capable of measuring longitudinal strain, arguably the simplest of all fibre-optic measurements. The performance of magnetostrictive fibre sensors is dominated therefore not by the limitations of optical fibre sensors, but by the characteristics of the magnetostrictive host material. It is the properties of these ferromagnetic materials that must be analysed to determine the suitability or otherwise of this type of actuation to the tokamak environment.

Magnetostriction is the change of a material's physical dimensions in response to a change in its level of magnetisation. It is a property of all ferromagnetic materials, and is the reason for the well-known "transformer hum" heard around electrical substations. Although most ferromagnetic materials exhibit a measurable magnetostriction, in most cases the effect is too small to be useful for

actuators or sensors. However, by alloying elements it is possible to produce materials that exhibit large magnetostrictions—usually expressed as the fractional change in length—under small magnetic fields. The sensitivity achievable by sensors incorporating such materials is very high, with minimum measurable fields of the order of 100 pT[SMP00]. Unfortunately, though the achievable resolution is excellent, the magnetostrictive response of such materials becomes unstable and nonlinear outside of a narrow range of temperatures and magnetisations.

The dimension change, illustrated by Figure 3.1, can be considered as being due to the reshaping and realignment of magnetic domains within the structure of the material. Magnetic domains are small volumes of the material within which all magnetic moments are aligned in parallel with each other. Initially orientated at random, magnetic domains will align parallel to the direction of an applied magnetic field causing the material to lengthen along that direction. During the parallel elongation, the material's total volume remains constant and there is an opposite dimensional change in the orthogonal direction.

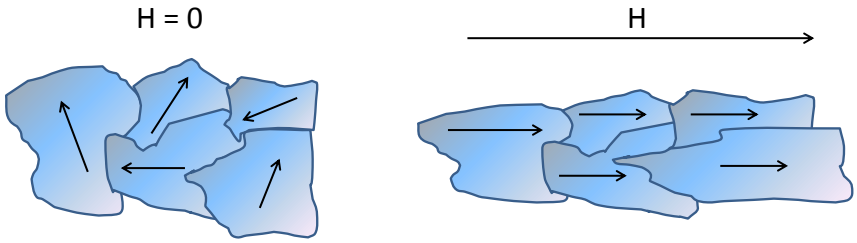

Figure 3.1: Effect of applied magnetic field H on magnetic domains and magnetic moments (arrows) within a ferromagnetic material

In order to measure magnetic field strength by magnetostriction, sensors may be coated with or bonded to a magnetostrictive material[SMP00][RWF+04]. The strain of the material under magnetisation is then imparted to the fibre strain sensor. In order to measure bidirectional magnetic field, it is required to construct a biasing magnetic field around the structure using a permanent magnet in order to offset the initial domain alignment. Thereafter, the sensor may be used to determine both the magnitude and direction of an applied parallel magnetic field at the expense of increased structural complexity.

The magnitude of the magnetostrictive response as a function of magnetic

field strength varies greatly between materials. Of the pure elements, cobalt exhibits the largest magnetostriction, reaching 60 $\mu\epsilon$ at saturation. Terfenol-D, an alloy created specifically to enable giant magnetostrictions, exhibits the strongest room-temperature response of any material—a relative elongation of 2000 $\mu\epsilon$ at a saturating magnetic field of 160 kA/m (a vacuum magnetic flux density of 200 mT)—and is the most commonly used magnetostrictive material for engineering purposes[Cla80].

As it is related to the level of magnetisation of the ferromagnetic material, the magnetostrictive response is highly nonlinear. Ferromagnetic materials will, after the external magnetising field has been removed, tend to retain their magnetisation to some extent. This tendency to "remember" the magnetisation history (hysteresis) results in a relationship between magnetisation (hence strain) and applied field that depends on the recent magnetisation. The effects of hysteresis in the biasing magnet and the magnetostrictive material give rise to a strong frequency dependency. Eddy currents induced in the material will also contribute to the dynamic behaviour and to the heat generated within the structure. These dynamic effects are of high importance when considering the performance of this measurement technique within the tokamak environment, where fast magnetic fluxes will produce large errors if sensors are unable to respond quickly and in a repeatable manner. Figure 3.2 illustrates the magnitude (strain) and phase response of Terfenol-D, where it can be seen that beyond approximately 1 kHz the magnetostrictive response diminishes rapidly.

The nonlinear response of these materials is most clear at high magnetic field strengths. Useful magnetostrictive materials experience magnetic saturation at field strengths below 500 mT, with a linear response over only a fraction of this range[SMP00]. Moreover, the saturation magnetisation diminishes as the material is heated, culminating in a total loss of ferromagnetic properties including magnetostriction at the Curie Temperature. In the case of Terfenol-D, the maximum operating temperature is 200 °C, which is considered to be high by the standards of other ferromagnetic materials[SFC$^+$94]. Figure 3.3 illustrates the saturation at room temperature of the magnetostrictive response in three embodiments of

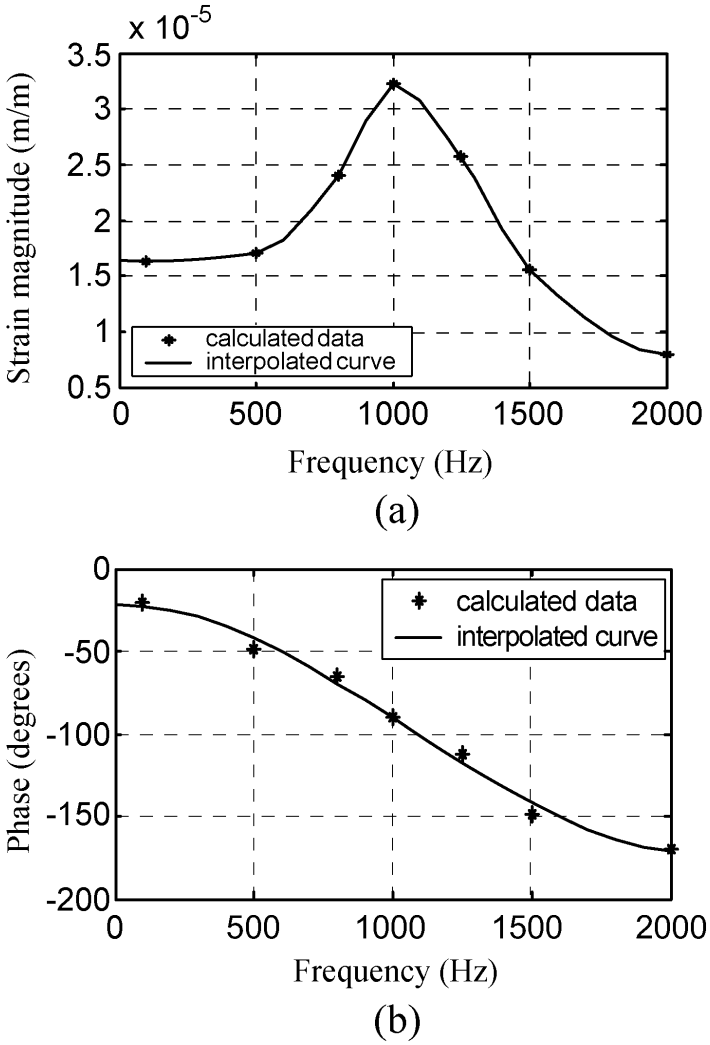

Figure 3.2: Magnitude (a) and phase (b) responses of the magnetostrictive alloy Terfenol-D illustrating the dynamic response of the material[HWC+07]

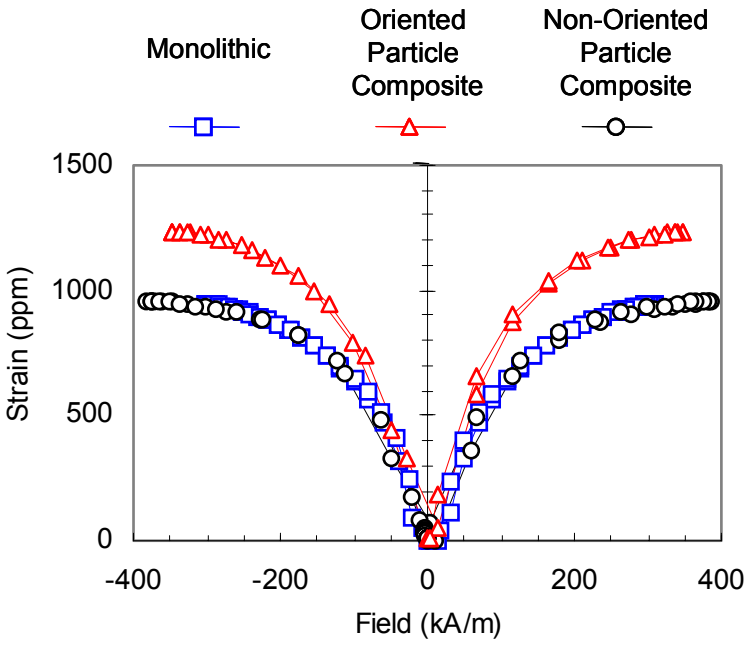

Figure 3.3: Magnetostrictive saturation of pure (monolithic) and particulate composite Terfenol-D[MC01]

the Terfenol-D alloy.

Due to the excellent sensitivity achievable, the magnetostrictive mechanism is highly suited to sensing and actuating applications in benign room-temperature environments, under conditions of low field strength, and up to frequencies of approximately 1 kHz. However, its use as part of in-vessel tokamak diagnostic systems, which must be robust to the large temperature fluxes and be capable of measuring the large magnetic fields and fluxes with a minimum of distortion and error, is inappropriate. Since the magnetostrictive response changes dramatically in response to temperature fluctuations, sensors based on this mechanism would be unable to inherently discriminate between magnetic field and temperature. Compared to a pure intrinsic fibre sensor, the chemical and structural complexity of a biased magnetostrictive sensor increases the possibility of undesirable radioactive interactions, chemical contamination, and damage due to the powerful magnetic forces that will be exerted upon the ferromagnetic component. Additionally, the processing and coating of fibres in magnetostrictive materials is a complex process that would substantially raise transducer fabrication costs.

3.2.2 Magnetic Force

Lorentz force is the force exerted upon a point charge by an electromagnetic field, and may be expressed as

$$F = q(E + (v \times B)) \tag{3.1}$$

where F is force, E is the electric field, B is the magnetic flux density, q is the electric charge of the particle, and v is the instantaneous velocity of the charged particle. In this expression, $\times$ denotes the cross product.

As discussed in Section 3.2.1, ferromagnetic materials are comprised, at the microscopic level, of volumes of aligned magnetic moments known as domains. These magnetic moments are contributed by electron spins, the plane and direction of which are mutually parallel within a magnetic domain. Ferromagnetic materials can be processed to produce permanent magnets, within which the magnetic domains are permanently aligned in the same direction resulting in a strong net magnetic field. Fundamentally, it is the Lorentz force of Equation 3.1 that gives rise to both the forces exerted by an electromagnetic field on charged particles in motion—including electrons in a current-carrying wire—and the forces exerted on permanent magnets by an external magnetic field including those generated by a second permanent magnet. Based on these forces, three mechanisms for measurement of the magnetic field have been proposed:

- *Conductor-Coated Fibre.* Either by fabricating a fibre with a conducting jacket, or by attaching a fibre to a conducting wire or strip, the Lorentz forces exerted upon the electrons moving in the wire by the external magnetic field will produce a deflection of the fibre which can be measured by a variety of optical fibre sensors[Oka90][CFK09]. The requirement for current flow and electrical conductivity, the elaborate physical design of the transducer, and the cross-sensitivity to vibration and electric field do not permit this approach to be used outside of the most benign environments.

- *Permanent Magnet on Fibre.* A transverse strain can be exerted upon a fibre via an attached permanent magnet that experiences force from the

external field. This approach has been used primarily for current measurement around an electrical conductor[GW09]. Due to the hazards involved in placing ferromagnetic materials near the tokamak magnetic confinement system, this is not a suitable measurement basis for this application. It also suffers from structural complexity and would contribute to a distortion of the tokamak confinement fields, which would not be permitted.

- *Fibre Infiltration by Liquid Crystals or Ferrofluids.* Recently, the effects of filling microstructured fibres with liquid crystal materials have been investigated with a view to enabling new types of fibres and sensors that are highly tunable in terms of spectral and polarising characteristics[WSE+06][WEL+06]. The potential for measurements of parameters that affect liquid crystal orientation has been demonstrated for use in measurement of electric field and hydrostatic pressure, both of which will strongly affect the structure of the infiltrated liquid crystal. Magnetic dipoles can be inherent in liquid crystals, or they can be induced by application of a magnetic field which will tend to align them as discussed previously. Through application of either an electric or magnetic field, the structure of the liquid crystal can be changed within the fibre in order to affect either the opacity or the birefringence of the medium—the difference between the refractive indices and propagation constants as experienced by orthogonal optical polarisations. Unfortunately for this diagnostic application, the strong cross-sensitivity to electric field will make ambiguous any magnetic measurements due to the large voltages developed within the tokamak.

  Ferrofluids are suspensions of magnetic (sub-domain) nanoparticles dispersed inside a liquid carrier. The particles possess an inherent magnetic moment and will be aligned by an external magnetic field. This magnetisation results in changes in the volume and viscosity of the ferrofluid, which in turn affects the propagation of light through the infiltrated region of fibre[CKMP10]. The magnetic field can be used to move the ferrofluid along the fibre into regions where sensors are hosted, adjusting the response of

the sensor regions. As with the ferromagnetic magnetostrictive materials discussed in Section 3.2.1, the low maximum operating temperatures and magnetisations of these particles makes ferrofluids unsuitable for tokamak use.

3.2.3 Magneto-optics

The disadvantages of the modulation mechanisms described above preclude their application to tokamak diagnostics. With reference to the principal benefits of optical fibre sensors discussed at the start of this chapter, it is clear that even after further development these approaches will not allow fibre-optic sensors to be utilised to their full extent. Sensors based on these mechanisms are limited by bandwidth, measurement range, operating temperature range, cross-sensitivities, and chemical and structural complexity as a result of the characteristics of the actuation methods. The extent of these problems is such that the deployment of these mechanisms within a tokamak environment would be both fruitless and potentially damaging.

Of the three principal methods, only the third—magneto-optics—has the potential to function to the desired standard under the extreme conditions of the tokamak environment. An inherently simple and intrinsic measurement principle that requires no intermediate transducer, magneto-optics relies only on the direct interactions between the electromagnetic wave and its magnetised propagation medium. This allows the sensor element to remain all-glass, with no external components or internal infiltrations, such that chemical and electrical passivity are retained and there is no distortion of the external magnetic field.

3.2.3.1 Magnetic Circular Birefringence

In the mid-1800s Michael Faraday discovered that when a transparent medium such as glass is subject to a magnetic field, it becomes optically active. Specifically, he noticed that when linearly-polarised light passes through a block of glass along the direction of the applied magnetic field, it undergoes a rotation of its polarisation azimuth. This was the first indication of the connection between

light and magnetic fields, which were previously thought to be entirely unrelated, and the beginning of the field of magneto-optics.

Magneto-optics can be defined as the study or theory of phenomena arising as the result of interaction between light and matter when the latter is subject to a magnetic field. At a fundamental level, the presence of a magnetic field changes the dispersion curves of the optical absorption coefficient of a material and leads to the appearance or variation of optical anisotropy. This splitting of system energy levels by an external magnetic field is known as the Zeeman effect, after Pieter Zeeman who noted that the bright yellow light emitted by a sodium lamp was affected, in terms of emitted wavelengths, by the presence of a magnetic field. Essentially, all magneto-optical (or *magnetophotonic*) effects are a result of this splitting of the emission and absorption spectra.

In this thesis, we will be concerned with magneto-optical interactions in the Faraday geometry (optical propagation along the magnetic field direction)[1]. In this geometry, the Zeeman effect manifests itself as circular dichroism—a difference between absorption coefficients for the two orthogonal circular polarisations[ZK97]. From the Kramers-Kronig relations, it follows that this magnetic circular dichroism is connected with the splitting of the refractive index of the medium for these two orthogonal circular polarisations[oLPT11]. Thus, the effect of guiding light in a fibre aligned parallel to a magnetic field is the induction of a circular birefringence.

Linearly polarised light may be represented by the sum of two orthogonal circular polarisations with a definite relative phase difference. Prior to the induction of circular birefringence by a parallel magnetic field, both the right-handed and left-handed circular polarisations experience the same refractive index n_0 and hence propagate at the same velocity c/n_0. Thus, the phase difference between the circular polarisations remains constant as they propagate, as does the polarisation azimuth of the resultant plane-polarised wave. Upon magnetisation of the medium, the refractive index splits into n_+ and n_- resulting in the two circular

[1]In liquids and gasses, a magnetic field applied perpendicular to the direction of optical propagation will give rise to a linear birefringence. This is known as Voigt geometry and is not relevant to in-fibre propagation.

polarisations propagating at difference velocities (c/n_+ and c/n_-). In this case, a phase difference accumulates between the circular polarisations as they propagate, and the resultant linear polarisation undergoes a rotation of its plane of polarisation that may be expressed as

$$\theta = \frac{\omega}{2c}(n_+ - n_-)L \tag{3.2}$$

where ω is the angular frequency, c is the speed of light, and L is the path length traversed by the optical beam. Often, this relationship is expressed more concisely as

$$\theta = VBL \tag{3.3}$$

where

$$VB = \frac{\omega}{2c}(n_+ - n_-) = \frac{\pi}{\lambda}(n_+ - n_-) \tag{3.4}$$

is the rotation per unit length, or *specific rotary power*, with units rad/m. In this case, V is the *Verdet constant*, a convenient measure of the strength of the magneto-optical interaction in a medium, with units rad/Tm, B is the magnetic field strength ($\mu_0 H$) in Tesla, and λ is the optical wavelength in metres. Figure 3.4 illustrates the azimuthal rotation of plane polarised light propagating in a magnetised medium.

It is worth noting at this stage that the sign of the Faraday rotation angle θ is dependent on the direction of the applied parallel magnetic field. This gives rise to a property of this mechanism that is key to the technique proposed in Chapter 4: nonreciprocality. If, after traversing a distance L and undergoing a corresponding azimuthal rotation θ, the plane-polarised wave undergoes a normal reflection and travels back to the source, the rotation angle is doubled to 2θ. This is in contrast to the behaviour of natural optical activity, for example in a fibre where material circular birefringence has been induced by twisting, in which case the azimuthal rotation is reversed upon reflection and the net rotation is zero. It follows that if multiple reflections within the magnetised region can be arranged,

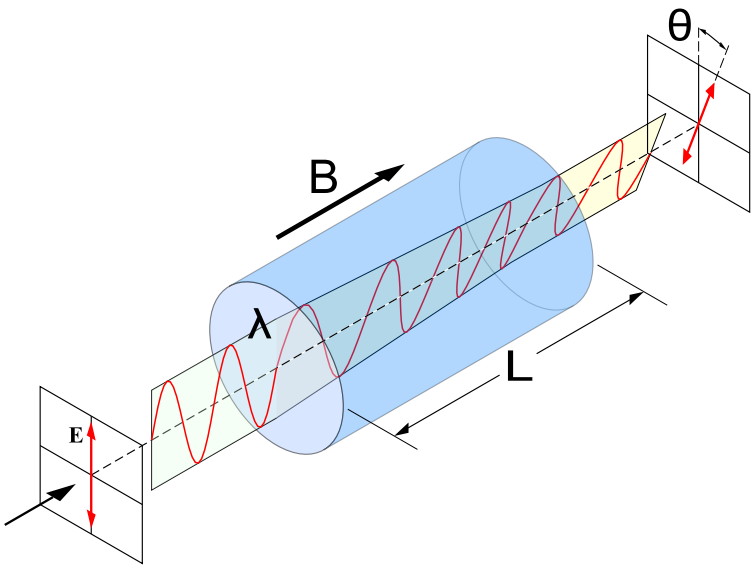

Figure 3.4: Faraday effect: Azimuthal rotation of linearly-polarised light propagating through a magnetised (blue) medium. The plane of the electric field is rotated through an angle θ as a result of the phase difference accumulated between the orthogonal circularly-polarised components.

the specific rotary power will be increased proportionally.

Re-arranging Equation 3.4, we may derive an expression for the circular birefringence Δn in terms of V:

$$\Delta n = \frac{VB\lambda}{\pi} \tag{3.5}$$

From Equation 3.5 it is seen that the specific rotary power and the associated level of circular birefringence are dependent not only upon the magnetic field strength but also upon the optical wavelength. In fact, the constant V is also proportional to the optical wavelength, which becomes clear if one considers the split eigenfrequencies of electrons in the magnetised propagation medium. These may be expressed as

$$\omega_{\pm} = \omega_0 \pm \frac{eH}{2mc} \tag{3.6}$$

where H is the magnetic field strength in A/m, and e and m are the electron charge and mass. It is the appearance of these two resonance frequencies that gives rise to the relative displacement of the curves $n_+(\omega)$ and $n_-(\omega)$

$$n_{\pm}(\omega) = n_0(\omega) \pm \frac{dn}{d\omega}\frac{eH}{2mc} \tag{3.7}$$

that, when substituted alongside Equation 3.2 into Equation 3.3 results in a thorough expression of V in terms of the optical wavelength λ:

$$V = \frac{e}{2mc^2}\lambda\frac{dn}{d\lambda} \tag{3.8}$$

The strength of the magneto-optical Faraday effect, expressed as V, is therefore both wavelength and temperature dependent (due to the $\frac{dn}{d\lambda}$ term), although as discussed later both dependencies are relatively weak and exhibit a proportionality that is, in general, beneficial to the proposed application.

3.2.3.2 Use in Measurement Applications

From the above analysis two separate but related techniques emerge that may be used to derive the magnetic field strength information using magneto-optical interactions:

- *State of Polarisation (SoP) measurement*: The azimuthal rotation θ of a linearly-polarised wave over a known path length L may be measured, and this may then be related to the average magnetic field strength B over the path (by Equation 3.3 if the path length is known). An immediate problem with this polarimetric approach is the large path length required to produce substantial rotations—an issue when the application requires excellent spatial resolution.

- *Refractive index measurement*: The change in refractive indices n_+ or n_- from their initial value n_0 may be detected and related to the field strength by a suitable refractive index sensitive technique. Notably, if the differential index Δn can be found, the absolute value of the field strength at that point can immediately be determined from Equation 3.5.

Of these two approaches, the former (polarimetry) is by far the most progressed. In general, the focus of this development has not been for point measure-

ment of magnetic field, but rather for measurement of the contour integral of the circulating magnetic field around an electrical conductor in order to measure the enclosed current for power system diagnostics[DPBRH82][BGNB02][BTd96][BGKB04]. An alternative technique relies on coupling light out of the addressing fibre into a bulk glass transducer that may be heavily doped in order to increase the Verdet constant. In this case, the azimuthal rotation takes place over the length of the glass block, which is placed near the electrical conductor[CMM$^+$99][NMM$^+$00]. In both arrangements, the polarisation state may be analysed by either interferometric or amplitude-based means—the former measuring directly the phase difference accumulated between the propagating circularly polarised modes, and the latter by re-polarising the exiting light in order to determine the fraction of the amplitude that has been transferred from the incident axis to the orthogonal one (referred to as a *crossed-polariser* arrangement if the second polariser is aligned orthogonally to the initial plane of polarisation). A far better resolution is achievable with the interferometric approach due to the sensitivity of optical interferometry and the robustness of this approach to amplitude-based noise.

Prior to the work in Chapter 4, application of the polarimetric approach to intrinsic fibre point sensors for magnetic field remained undeveloped—the principal difficulty being the large path lengths required to induce measurable azimuth rotations in SiO_2 fibre, within which the Verdet constant is only 0.57 rad/Tm at 1550 nm (0.8 rad/Tm at 1310 nm)[REW97]. With reference to Equation 3.3, the rotary power of a magneto-optical arrangement can be increased in two ways: by increasing the Verdet constant of the medium, or by increasing the path length. An increase of the Verdet constant in fibre is achievable by doping with strongly paramagnetic elements such as the rare earth metals (in particular the terbium ion Tb^{3+}), however the factor of 3–4 improvement in sensitivity is minimal and cannot justify the costly doping process[BS95]. Additionally, the doped fibre (now paramagnetic) will possess a rotary power that is inversely proportional to temperature, reducing its suitability to high temperature applications. Conversely, if the fibre is left undoped its magnetic response is limited to that of intrinsic diamagnetism. Though providing weak magneto-optical interactions,

the diamagnetic fibre will exhibit a rotary power that is directly, and weakly, proportional to temperature, minimising temperature fluctuations of the Verdet constant ($\frac{dV}{dT} \approx 4 \times 10^{-5}\ ^{\circ}\mathrm{C}^{-1}$ at 1550 nm [WRD+91]) and allowing the transducer to take advantage of high operating temperatures[2].

Simply increasing the path length to improve rotary power is undesirable since the objective is to enable point measurement of the field. However, it is possible to increase effective path length using resonant or distributed feedback (DFB) structures, within which light at the resonant frequencies is trapped for extended periods while it undergoes multiple reflections due to simple mirrors or coherent backscattering (from Bragg structures). Since the Faraday effect is nonreciprocal, the rotary strength will be increased by a factor approximately equal to the finesse of the resonator. Therefore, if suitable in-fibre resonant structures can be created and interrogated they may be used as in-fibre point sensors for magnetic field. This approach, and the associated engineering problems such as interrogation, sensor bandwidth, multiplexing capabilities, and temperature compensation form the basis of the work in Chapter 4.

The refractive index measurement approach was first proposed in a fibre point sensor context by Kersey and Marrone in 1994, who also suggested the suitability of the technique to plasma diagnostics[KM94]. The approach did not, however, experience further development. This is likely due to the practical difficulties arising from the requirements for very high-resolution interrogation and for certainty of the SoP within the sensor element. Additionally, any inherent material linear birefringence (a differential refractive index between linearly polarised modes) within the sensor elements will act to reduce the achievable Faraday rotation. The reduction of this birefringence within the sensor is not a trivial problem, particularly since the fabrication process for in-fibre sensors will often introduce birefringence. These issues make the interrogation of such sensors highly problematic, especially where serial multiplexing is desired. As such, prior to the work in Chapter 5 this approach had not been developed beyond Kersey's preliminary

[2]It is often stated that the magnetic response of diamagnetic materials is—in contrast to those that are paramagnetic or ferromagnetic—not dependent on temperature. This is usually a deliberate oversimplification.

laboratory demonstration of the concept.

3.2.4 Summary

Of the available mechanisms for in-fibre point measurement of magnetic field strength, magneto-optics will be the only suitable basis for purely intrinsic sensors with the potential to function under the extremely harsh conditions of the tokamak. Two sensing mechanisms may be proposed on this basis: polarimetric point sensing using magneto-optical resonant structures, and point measurement of the induced circular birefringence.

In both cases, the use of standard (diamagnetic) fibre will enable a linear measurement of magnetic field that does not saturate or diminish as magnetisation, temperature, or rate of flux are increased. Hence, a very broad operating range will be achievable without any inherent bandwidth limitations resulting from material properties. The magneto-optical response possesses a weak positive temperature dependence that may be used to improve sensitivity at higher temperatures. Additionally, both mechanisms are electrically isolated and passive, chemically inert, and retain the flexibility and geometry of standard optical fibre.

It is clear that sensors based on this mechanism have the potential to meet the requirements for tokamak diagnostics, however it remains to engineer the sensor systems and transducers that will solve the fundamental problems associated with exploiting the magneto-optical mechanism for point measurement in fibre. A number of design problems arise primarily as a result of the low sensitivity due to the small Verdet constant in diamagnetic fibre, and the probability of polarisation corruption due to intrinsic linear birefringence in sensors and addressing fibres. These lead to engineering challenges in transducer design, sensor network topologies, and interrogation procedures (particularly the issue of meeting the combined requirements of high speed multiplexing and high resolution for large numbers of sensors).

Prior to addressing these challenges, the operation and interrogation of existing fibre sensor architectures that are particularly applicable to implementation

of the magneto-optical mechanism will be reviewed, leading to a foundation for the proposed solutions.

3.3 Intrinsic Fibre Point Sensors

A number of properties of the electromagnetic wave may be modulated by an external influence in order to form the basis of an optical fibre sensor. These are principally the intensity, phase, polarisation state, and wavelength of the guided wave. For this diagnostic application it is desirable to consider only sensor architectures that are:

1. Small, with an excellent spatial resolution,
2. Structurally simple, using a minimum of different materials,
3. Robust to fluctuations in attenuation and signal intensity,
4. Capable of reflection-mode interrogation,
5. Amenable to serial multiplexing.

By the elimination, in Section 3.2, of those transduction mechanisms that are extrinsic or elaborate, Criteria 1 and 2 above are satisfied thus far. Since they do not meet the multiplexing and robustness criteria above, intensity-based sensors will not be considered in this thesis. For multiplexing purposes it is highly desirable to have the transducer encode the measurement within the optical spectrum, which also provides immunity to power fluctuations (Criterion 3). As such, wavelength-encoding measurement techniques should form the basis of the proposed sensors. Known also as *spectrally-encoded* sensors, this type of sensor is interrogated by monitoring the transmitted or reflected spectra which will be altered in some way by the measurand. By encoding all measurement information in the reflected optical spectrum, Criterion 4—a typical demand in industrial applications where the chance of failure must be minimised—is satisfied.

Sensors based on phase or polarisation modulation are incapable, as used in isolation, of meeting above criteria since they are often extrinsic, transmission-mode interrogated, structurally complex, and difficult to multiplex. However, the principals of *interferometric* (phase-based) and *polarimetric* (polarisation-based) optical sensors may be used in conjunction with a wavelength-encoding foundation in order to expand a spectral sensor's overall measurement capability. In this section, two high-performance in-fibre spectrally-encoded point sensors will be reviewed: the fibre Fabry-Pérot interferometer, and the fibre Bragg grating (FBG). In the following chapters, the principles of both these sensors will be utilised in hybrid arrangements that blend their complimentary characteristics in order to meet the required criteria.

3.3.1 Fibre Fabry-Pérot Interferometers

The Fabry-Pérot interferometer (or resonator) (FPI) is essentially a cavity between two partially reflecting mirrors, the response of which to a given optical frequency can be derived from its physical and material attributes. The basic Fabry-Pérot takes the form of two parallel reflective surfaces, one of which the optical beam enters at some angle to the normal. Inside the cavity, the beam experiences multiple partial reflections (and transmissions) at both cavity boundaries. In the case of fibre Fabry-Pérot interferometers (FFPIs), the angle of incidence and propagation of all beams within the cavity can be assumed to be zero—i.e. the rays are considered to propagate parallel to the fibre core.

3.3.1.1 Theory

Figure 3.5 illustrates a simple FFPI comprised of a short section of fibre with core index n_2, surrounded by fibre with core index n_1. Due to the step change in the longitudinal refractive index, two partially-reflecting boundaries are created with reflectivity r given simply by $(n_1 - n_2)/(n_1 + n_2)$. Importantly, the mirrors may alternatively be created by coherent backscattering via minor periodic variations in the core refractive index (the foundation for fibre Bragg gratings, discussed in the next section), however for this discussion we will assume simple cavity

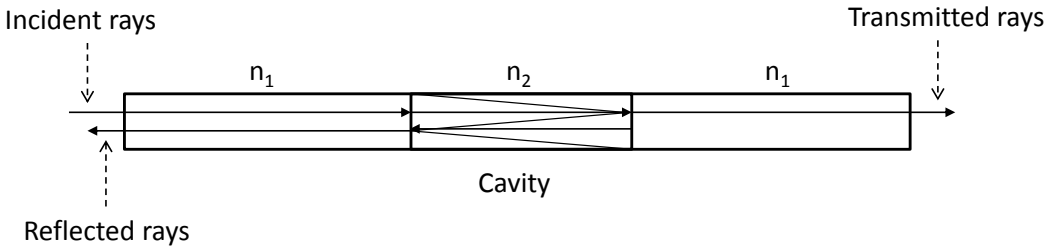

Figure 3.5: The structure of a simple in-fibre Fabry-Pérot interferometer. In practice the beam paths are parallel to the fibre core—here they are spread out to illustrate the multiple reflections.

boundaries.

A comb-like transmission spectrum of the FFPI results from the interference between the multiple reflections of light between the two reflecting surfaces. Constructive interference occurs if the transmitted beams are in phase, corresponding to a spectral peak in transmission. If the transmitted beams are out of phase, the resulting destructive interference produces a transmission minimum. Due to the large number of interfering rays, the contrast of the interference fringes may be very high compared to the case of two-path interferometers.

In the case of the simple FFPI of Figure 3.5, the optical path difference (OPD) between successive transmitted rays may be described by

$$\mathrm{OPD} = 2n_c d \tag{3.9}$$

where d is the cavity length and n_c is the cavity refractive index—in this case the fibre core index (n_2 from Figure 3.5). Hence the optical phase shift δ is given by

$$\delta = \frac{2\pi}{\lambda}\mathrm{OPD} = \frac{4\pi}{\lambda}n_c d \tag{3.10}$$

where λ is the incident optical wavelength. The wavelengths of successive peaks in transmission are those that satisfy the condition

$$\lambda = \frac{2nd}{m} \tag{3.11}$$

where m is an integer, at which point the beams experience maximum constructive interference at the exit boundary.

An expression for the intensity of transmitted rays as a function of wavelength λ, reflectivity r, and optical phase shift δ can now be readily developed. From the sum to infinity of partially reflected waves, the total transmitted electric field E_t at some point P, in terms of the optical phase shift, is

$$E_t = E_0 e^{i\phi} t^2 [1 + r^2 e^{-i\delta} + (r^2 e^{-i\delta})^2 + (r^2 e^{-i\delta})^4 + \ldots] \tag{3.12}$$

where in this case ϕ is an arbitrary phase term giving the distance travelled to reach P and the time dependence of the electric field. This sum can be expressed succinctly by geometric series as

$$E_t = E_0 e^{i\phi} \left(\frac{t^2}{(1 - r^2) e^{-i\delta}} \right). \tag{3.13}$$

Then, the intensity I_t of the field at point P is given by the time average of the expression $E_t E_t^*$. Performing this operation on Equation 3.13 yields

$$I_t = \frac{I_i}{(1 + r^4) - 2r^2 \cos\delta}. \tag{3.14}$$

Using the trigonometric identity $\cos\delta = 1 - 2\sin^2 \delta/2$ this equation can be expressed as

$$\frac{I_t}{I_i} = \frac{1}{1 + F \sin^2 \frac{\delta}{2}} \tag{3.15}$$

where F is known as the *Coefficient of Finesse*, defined as

$$F = \left(\frac{2r}{1 - r^2} \right)^2. \tag{3.16}$$

The reflected intensity I_r is then simply the reciprocal of this transmission expression, i.e. $I_r/I_i = 1 - I_t/I_i$.

Finesse f is a function of F and is a measure of the sharpness of the interference fringes, or the contrast. By defining the Full-Width Half-Maximum (FWHM, $\delta\lambda$) and the Free Spectral Range (FSR, $\Delta\lambda$) of the interference pattern as the width of a fringe at half its maximum intensity, and the distance between adjacent fringes respectively, the finesse f can be stated as

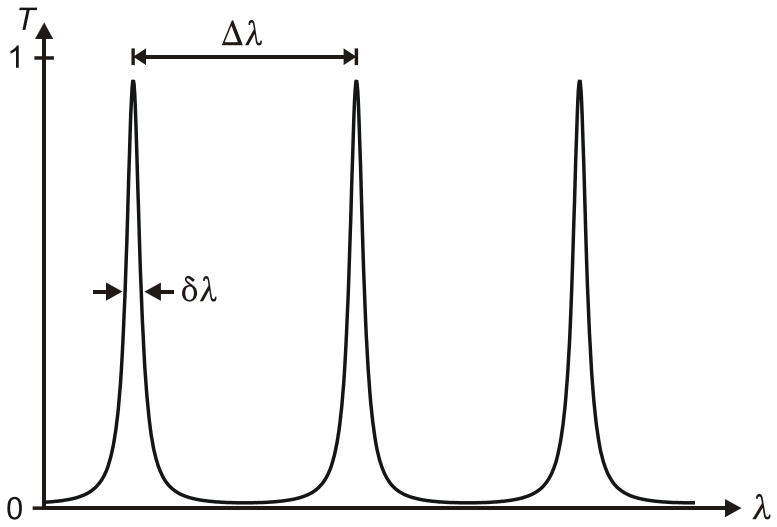

Figure 3.6: The transmission spectrum of a simple Fabry-Pérot interferometer with the FSR ($\Delta\lambda$) and FWHM ($\delta\lambda$) labeled (The reflection spectrum is the reciprocal, i.e. $R = 1 - T$)

$$f = \frac{\pi\sqrt{F}}{2} = \frac{\Delta\lambda}{\delta\lambda}. \tag{3.17}$$

The FSR is related to the fringe wavelength λ, the refractive index of the cavity n_c, and the cavity length d in the following manner:

$$\delta\lambda = \frac{\lambda_1\lambda_2}{2nd}. \tag{3.18}$$

The transmission spectrum of a simple FPI is shown in Figure 3.6, where the FWHM and FSR are indicated. If the spectrum is interrogated in reflection, the resonances appear as sharp notches in the reflected spectrum, which in off-resonance regions is close to unity. By monitoring the reflected spectrum, either the FSR (Equation 3.18) or the wavelength of a single resonance (Equation 3.11) may be tracked and related to a change in the core index n_c or the cavity length d. In this way, the FFPI may be used as a sensor for longitudinal strain or temperature (which will alter n_c via the thermo-optic coefficient)[YKIO82].

3.3.1.2 Use as Faraday Effect Amplifier

Resonant wavelengths—those that satisfy the condition of Equation 3.11—undergo multiple reflections within the cavity before they are transmitted. The number

of round trips that this light undergoes is of the order of the finesse of the resonator, which is proportional to the reflectivity of the mirrors. If we recall that in Section 3.2.3.1 it was noted that magnetic circular birefringence is nonreciprocal upon reflection, it is seen that resonant structures such as FPIs may be used to amplify the Faraday effect when the cavity is magnetised. This concept was proposed by Rosenberg *et al* in [RRH64].

By placing a magnetised FPI between crossed polarisers, one creates a so-called *Malus FPI* (after the pioneer of polarimetry Étienne-Louis Malus) that is able to produce large Faraday rotations over a short distance by addressing the structure with a resonant wavelength[VBL$^+$99]. At this wavelength, the Faraday rotation is increased to approximately $\theta = fdVB$ where f and d are the finesse and length of the resonator and V and B are the Verdet constant and magnetic field strength as defined previously. It is important to note that an increase in the finesse of the resonator will not only increase the effective path length of light at the resonant wavelength, but by Equation 3.17 will also decrease the FWHM of the resonant spectral feature.

Key problems with this interesting approach include linear birefringence in the cavity, which quenches the achievable Faraday rotation[WLZ07], and the transmission of all strongly resonated light. In bulk glass cavities, as used by Vallet *et al* in [VBL$^+$99], the rotary power of the medium can be giant, and the birefringence small. However, in the fibre analogue of this structure the rotary power is very small, and intrinsic or strain-induced linear birefringence is common. In practical terms, the proportionality between finesse and rotary power enhancement means that as the finesse of the magnetised cavity is increased to further improve the rotary power, the bandwidth of the resonant region becomes vanishingly small such that interrogation of the device becomes unfeasible. The low Verdet constant of fibres may therefore only be compensated for to a small extent by a simple resonant structure. Finally, in order to use this rotary enhancement as part of a serially-multiplexed sensor array, it must be possible for the interrogating system to differentiate between cavities spectrally, which in the case of simple FFPIs is not possible since the resonances are periodic over a continuous

spectrum.

3.3.2 Fibre Bragg Gratings

A fibre Bragg grating (FBG) is a periodic perturbation of the refractive index along a fibre core. By a process of coherent backscattering, the FBG has peak optical reflection at a specific wavelength known as the Bragg wavelength. In sensor applications, their wavelength-encoding nature coupled with their simple reflected spectrum mean that FBGs are relatively easy to interrogate and multiplex, and are effectively immune to the problems of intensity fluctuations and attenuation. For these reasons the FBG is now ubiquitous in the field of optical instrumentation, and may be credited with making a large contribution to the increasing market presence of optical fibre sensors.

3.3.2.1 Fabrication

The fabrication of in-fibre Bragg gratings was first reported by Hill *et al* in 1978[HFJK78]. By guiding two counter-propagating visible wavelength beams within the fibre, they noted a periodic modulation of the refractive index along the fibre corresponding to the interference pattern of the two beams. It was, however, not until 1989 that Meltz *et al*, working at the United Technology Research Centre, demonstrated that such in-fibre structures could be more conveniently written in the fibre core by an intense sidelong interference pattern from a coherent ultraviolet (UV) source[MMG89]. An implementation of the interferometric writing method that uses a phase mask to create the two coherent beams is predominant today due to the flexibility of selecting the Bragg wavelength independently of the wavelength of the UV source.

In the phase mask configuration (Figure 3.8), light from the UV source is incident on a slab of silica glass, transparent to UV radiation, with a periodic corrugation on one surface. The corrugation has a square-wave depth profile that, when illuminated through the polished side of the silica slab, diffracts the UV light that is incident normal to the mask. The zeroth order mode is suppressed in grating-writing phase masks, with the majority of intensity being distributed be-

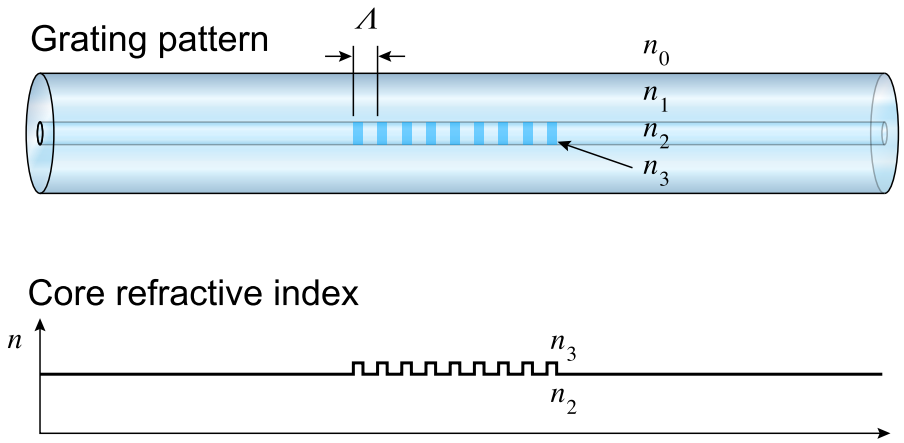

Figure 3.7: Illustration of the modulation profile of the fibre core refractive index in an FBG. Often, the modulation will approximate a raised-sine profile.

tween the two first order modes. Though the fibre may be *direct written* through the phase mask, as in Figure 3.8, a Sagnac mirror configuration is often deployed to loop these beams under the fibre and back into the fibre core from the other side where they interfere, requiring the operator to adjust only the mirror positions in order to alter the interference pattern and hence the periodicity of interference maxima at the fibre. Fibres that are photosensitised through doping with certain materials, usually germanium, will respond to the UV illumination with a proportional change in the refractive index. As the UV laser is scanned along the phase mask, this interference pattern is inscribed into the photosensitive fibre core leaving its refractive index modulated with the same periodicity, as illustrated in Figure 3.7.

3.3.2.2 High Temperature Gratings

A number of photosensitivity mechanisms have been proposed and demonstrated through which refractive index modulation may be induced in the fibre[Can08][DXT+97]. The temperature response and maximum operating temperature of each FBG depends greatly on its photosensitivity mechanism, and research is ongoing in this area in order to identify and explain the chemical processes underlying the change in refractive index. Presently, there is a great deal of interest in regenerated gratings which are formed at high temperatures after the initial erasure of a more

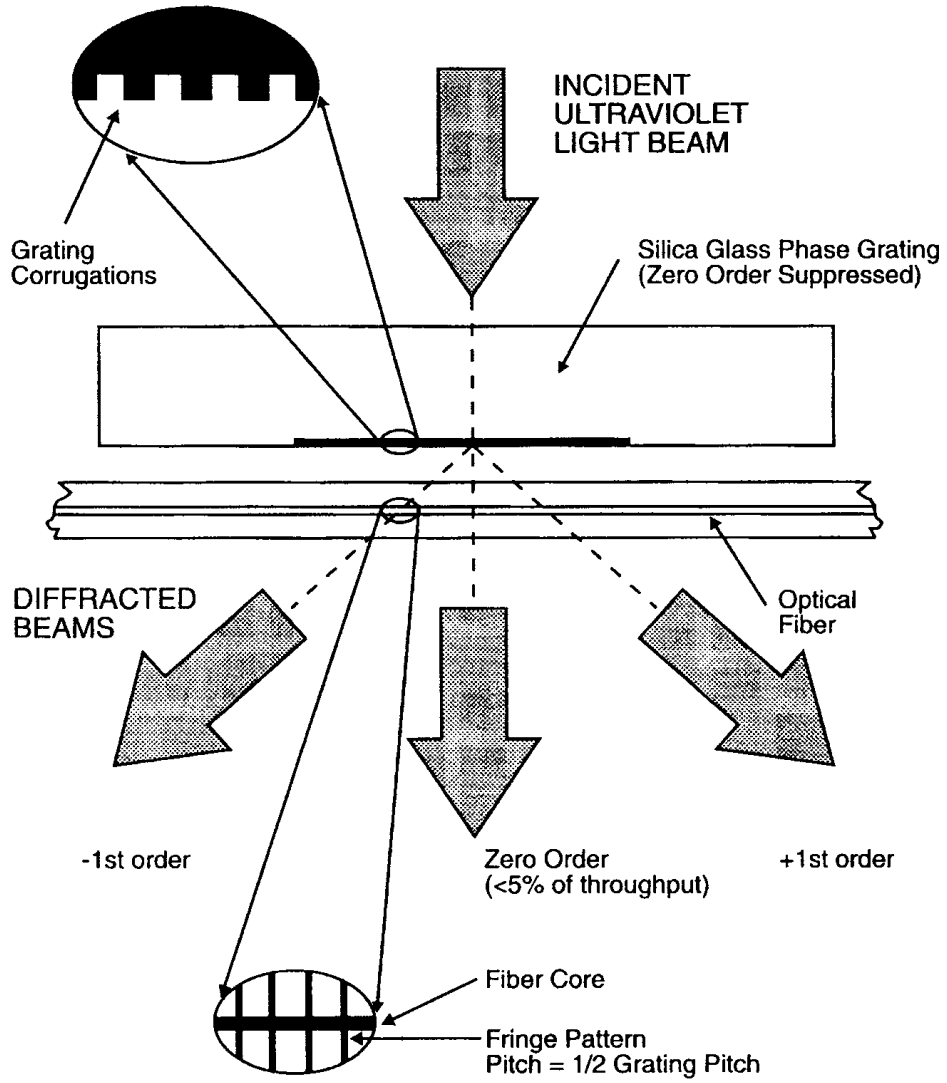

Figure 3.8: Fibre Bragg grating fabrication apparatus based direct writing through a diffraction phase mask. The amplitude of the phase mask grooves is chosen such that more than 80% of the throughput is in the ± 1 diffracted beams.[HM97]

conventional grating.

A number of groups have demonstrated the stability of regenerated gratings at temperatures of over 1000 °C[BCSC08][Fok02]. Of particular note is the 2008 work by Canning *et al* which demonstrated the robustness of a hydrogen-loaded boron-germanium co-doped silica fibre grating at temperatures of up to 1295 °C with little change in the reflection spectrum after repeated thermal cycling[CSBC08]. Such gratings outperformed the host fibre, which by 1200 °C had become brittle and fragile. In terms of high-temperature operation then, FBGs are presently capable of operating at temperatures far above the maximum surface temperatures expected in ITER.

3.3.2.3 Linear Birefringence

Standard optical fibres possess an intrinsic linear birefringence of the order of 10^{-6} as a result of asymmetries in the cross-sectional geometry or non-uniform stress distributions formed during fibre drawing. These may be reduced by thermal annealing of the fibre and by improving the quality of drawing procedures. However, the process of grating inscription will superimpose a linear birefringence in fibres of the order of 10^{-4} which will dominate the intrinsic birefringence. The mechanisms responsible for this are still under debate, however a recent comprehensive review of UV-induced birefringence in fibres was produced by Canning *et al*[CDSK05].

The processes involved in the birefringence production are numerous and complex; however, it has been established that UV-induced linear birefringence may be compensated for by adjustments in the optical writing scheme and may be removed post-inscription by low-temperature (120 °C) annealing[CDSK05]. In particular, longer UV wavelengths have been shown to contribute less birefringence, while the polarisation and alignment of the UV source relative to the fibre has a significant influence on both the axis of linear birefringence and its magnitude.

The gratings utilised in the work described in this thesis were fabricated in such a way as to keep UV-induced birefringence to a minimum. The overall

birefringence levels, measured using the technique proposed in [EM94], were confirmed to be under 10^{-6}. Minimisation of the linear birefringence in this manner is crucial to maintaining the mechanism of Faraday rotation via the magnetic circular birefringence, ensuring it is not dampened by phase shifts produced between the linearly polarised modes. This is of particular concern in arrangements where light is resonant within the grating (Chapter 4), in which case the detrimental effects of intrinsic linear birefringence on polarisation-sensitive measurements will be amplified resulting in a reduction of the rotary power[Rog88]. Additionally, no polarisation mode conversion is experienced by polarised light within low-birefringent (lo-bi) gratings prior to magnetisation.

Retardance represents the integrated effect of birefringence acting along the path of a light beam that traverses a length of optical fibre. Given that some level of intrinsic linear birefringence Δn_i will remain in the grating region even if preferred fabrication procedures are followed, the linear retardance $\Delta\beta_i$ of the fibre may be defined as

$$\Delta\beta_i = \left(\frac{2\pi}{\lambda}\right)\Delta n_i l \tag{3.19}$$

where λ is the optical wavelength and l is the length of interaction along the fibre. Where the length of fibre is longer than π/β_i, it has been established that the circular retardance β_c due principally to the magnetic circular birefringence[3], will be quenched[Smi80][PH76]. Given that the fibres and gratings utilised in this thesis will be shown to retain a linear birefringence of $<10^{-6}$, the worst-case intrinsic linear retardance may be calculated to be 4 rad/m. This implies a maximum usable length of 0.775 m to avoid quenching of the Faraday rotation. From Equation 3.3 ($\theta = VBL$) it is then clear that at a wavelength of 1550 nm and a corresponding Verdet constant of 0.57 rad/m, the maximum rotary power before quenching due to linear birefringence will be approximately 0.442 rad/T or 25 °/T (ignoring the reduction in rotary power as β_i increases). It will be shown in Chapter 4 that this interaction length will yield sufficient localised rotation

[3]The circular retardance β_c in a fibre with zero intrinsic circular birefringence is exactly equal to the Faraday rotation θ_F.

within the sensor region.

In [RU79], Rashleigh and Ulrich demonstrated that the quenching of magnetically-induced circular retardance by intrinsic fibre linear birefringence may be greatly reduced by a simple twisting of the fibre. By twisting the fibre, a material circular birefringence is formed by a process of converting the existing linear birefringence into one whose axes of birefringence experience a rotation evolution as light propagates along the fibre. The resultant elasto-optic circular birefringence may be described as

$$\alpha_\tau = g\tau \tag{3.20}$$

where τ is the induced twist and g is a material constant that is given approximately as 0.15 for silica fibres. For strong twists such that $|\alpha_\tau| > \beta_i$, the circular retardation dominates the linear retardation and the resulting elliptical birefringence of the fibre (resulting from the superposition of both birefringences) is predominantly circular. The more the fibre is twisted, the more negligible the linear birefringence becomes. With sufficient twist, the rapidly-varying linear component is quenched and the twist-induced birefringence acts as a constant bias superimposed on the magnetic circular birefringence. This suppression technique has been successfully demonstrated in a fibre scheme with an interaction length of 10 m with strong intrinsic and bend-induced linear birefringence.

Importantly for the resonator implementation in Chapter 4, the twist-induced birefringence is reciprocal, unlike the magnetically-induced components. Therefore, the suppression of the remaining intrinsic linear birefringence through twisting will be an ideal solution for this application, and will allow the scheme to avoid the reduction of effective magnetic sensitivity as interaction lengths are increased.

3.3.2.4 Spectral Characteristics

The peak reflected wavelength (the Bragg wavelength, λ_B) is a function of the average or effective refractive index n_{eff} over the region of periodic modulation and the grating pitch $\wedge$. It is defined as

$$\lambda_B = 2n_{eff} \wedge . \tag{3.21}$$

Note the similarity between this expression and Equation 3.11 which defined the condition for peak transmission in an FFPI ($\lambda = 2nd/m$). The spectral dependence on refractive index and longitudinal structure is identical in both cases. The implication is that FFPIs and FBGs that experience the same changes in refractive index and longitudinal geometry will undergo an identical shift of spectral features.

The Bragg wavelength is inherently sensitive to strain and temperature and may be sensitised to other measurands through various arrangements, some of which have been discussed in previous sections[Rao97]. In general, the FBG is a far more convenient sensor than the FFPI. It is mechanically stronger due to the lack of fibre splices, more easily multiplexed due to the small bandwidth, and enables a linear response and absolute measurement without complex signal processing.

An excellent review of fibre grating spectra and the coupled mode equations describing their relationship to the grating's physical parameters is provided by Erdogan in [Erd97]. As an initial approximation, the FBG reflection spectrum takes a form similar to the function

$$\left(\frac{\sin x}{x}\right)^2 . \tag{3.22}$$

The FWHM of this reflection peak is proportional both to the length of the grating (the number of refractive index perturbations, N) and the strength of the perturbations (the modulation depth δn, which is proportional to the total UV fluence). Using the 4×4 state matrix method for stratified periodic media[BW99], the reflection spectra R of FBGs with arbitrary structures may be simulated numerically as in Figure 3.9.

For many applications, it is desirable to reduce the strength of the modulation depth towards the edges of the grating. This process is known as *apodisation* and can be applied according to a number of distributions such as a raised sine or

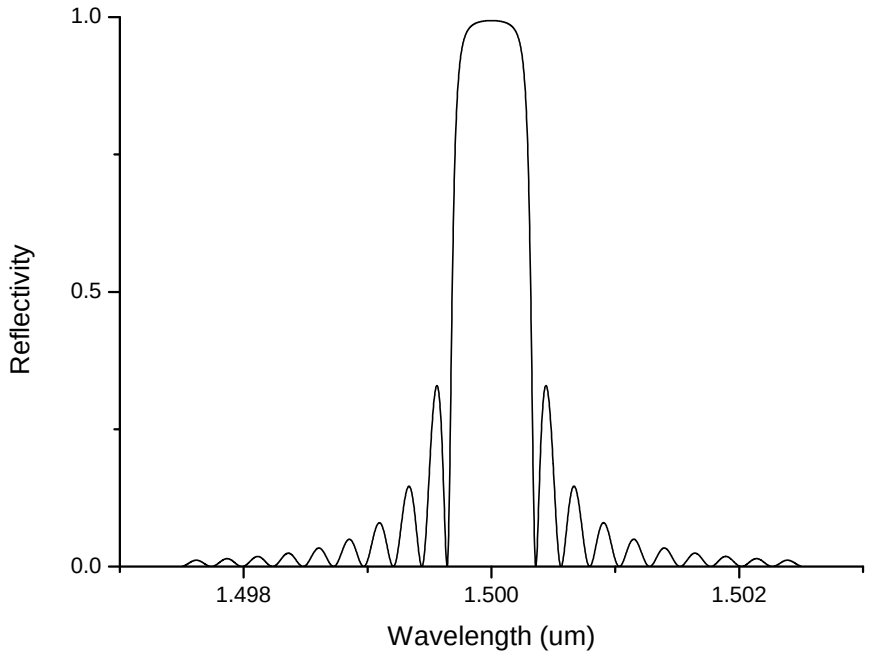

Figure 3.9: Simulated uniform (unapodised) FBG reflection spectrum [$\lambda_B = 1550$ nm, $\delta n = 10^{-3}$, $N = 6000$ (total length = 5 mm)]

Gaussian. In uniform (unapodised) gratings, *sidebands* (smaller reflection peaks that flank the principal peak in Figure 3.9) arise due to the resonance created by the step change in refractive index at the grating edges (between n_{eff} and the unexposed regions), which is sufficient to create an effective cavity reminiscent of the Fabry-Pérot resonator. Applying apodisation to the grating profile dampens these side-bands by removing the source of this resonance, making the grating profile simpler and the reflection purer in terms of spectral content (Figure 3.10).

A resonance may be deliberately introduced into a fibre Bragg grating by incorporating a defect into the periodic index modulation. Figure 3.11 illustrates the incorporation of a single $\pi/2$ phase-step in the index modulation profile at the centre of the grating. The resulting spectrum possesses a sharp notch in the reflected spectrum (and peak in the transmitted spectrum) that corresponds to a highly precise value of the Bragg wavelength. In such a grating, light at the resonant frequency does not sum coherently upon crossing the phase shift, and is instead reflected back, forming a resonant cavity between the two distributed reflectors.

The temporal characteristics of the resonator may be illustrated by the group

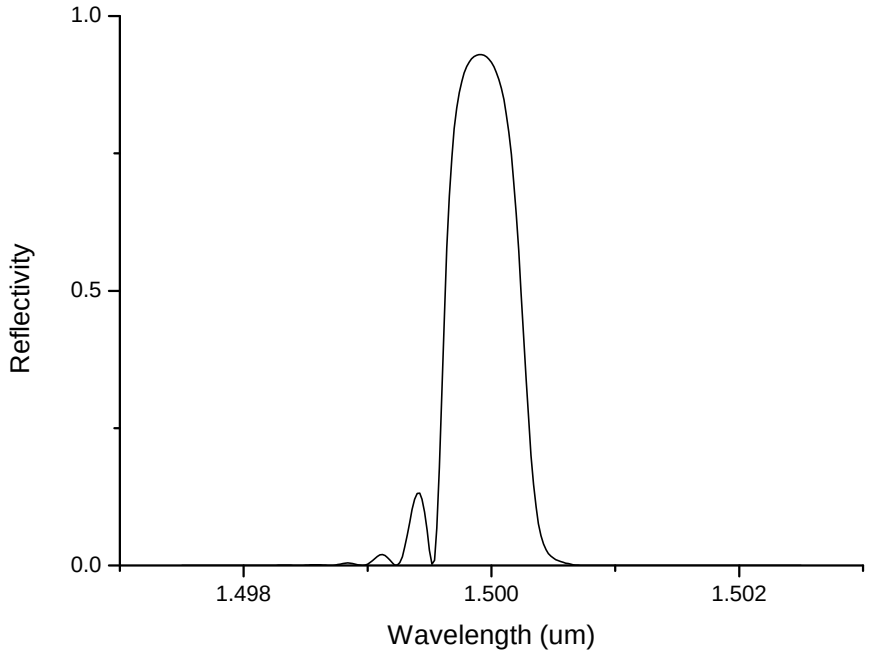

Figure 3.10: Simulated Gaussian-apodised FBG reflection. Grating parameters as in Figure 3.9 [$\lambda_B = 1550$ nm, $\delta n = 10^{-3}$, $N = 6000$ (total length = 5 mm)]

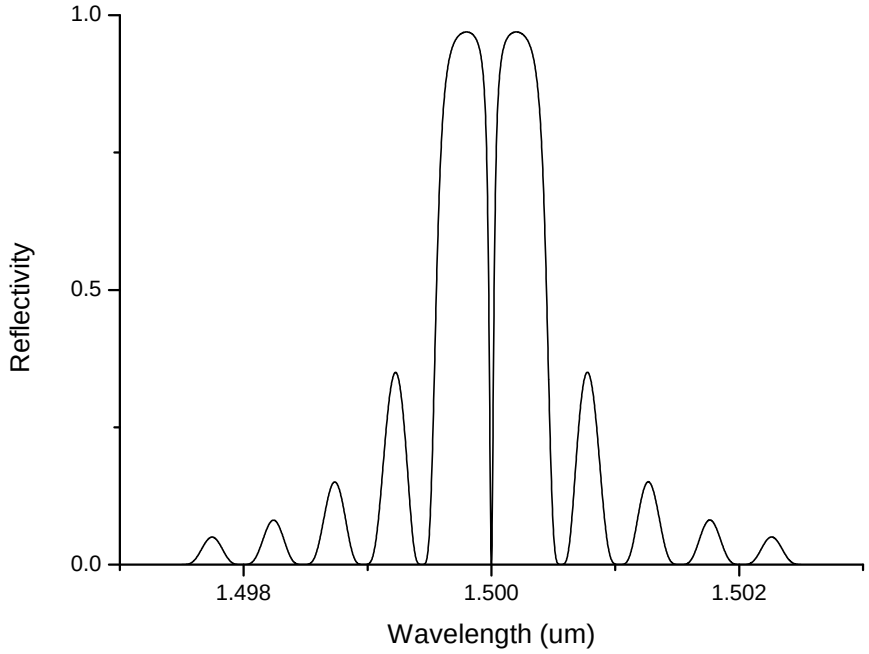

Figure 3.11: Simulated single (central) phase-shifted FBG reflection. Grating parameters as in Figure 3.9 [$\lambda_B = 1550$ nm, $\delta n = 10^{-3}$, $N = 6000$ (total length = 5 mm)]

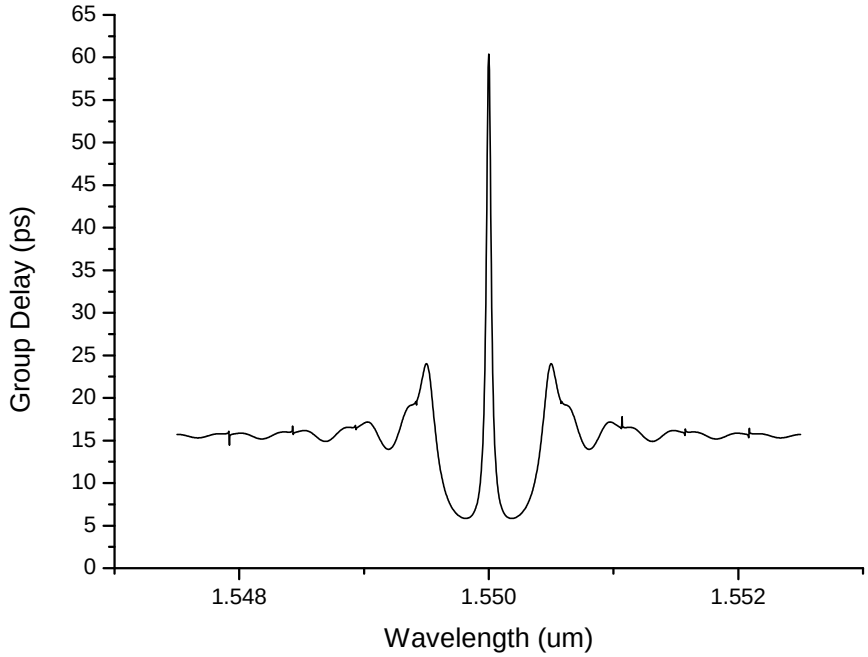

Figure 3.12: Reflected group delay spectrum for a single phase-shifted FBG. Grating is identical to that in Figure 3.11 [$\lambda_B = 1550$ nm, $\delta n = 10^{-3}$, $N = 6000$ (total length = 5 mm)]

delay of reflected light. Figure 3.12 illustrates the group delay spectrum corresponding to the phase-shifted grating shown in Figure 3.11. It can be seen that light at the resonant wavelength is delayed within the grating structure for extended periods of time. In contrast, the group delay spectrum of a uniform grating exhibits no such peak. It is clear from Figure 3.12 that phase-shifted gratings will allow for amplification of any time or location dependent effects, such as magneto-optical Faraday rotation, due to the increase in interaction time within the FBG.

Such in-grating resonators formed by phase-shifted fibre Bragg gratings may form a basis for realising spectrally-windowed Fabry-Pérot resonators, and hence the polarimetric point sensors suggested conceptually in Section 3.3.1.2. There are, however, crucial problems to overcome before this approach will be useful. In particular, by comparing Figures 3.11 and 3.12 it is notable that the wavelengths experiencing the greatest delay are ultimately transmitted rather than reflected. This makes such structures useless as reflection-mode sensors without further development. This, and other fundamental problems with this approach, will be

tackled in Chapter 4.

3.3.2.5 Sensitivity to Strain and Temperature

The sensitivity of the Bragg wavelength λ_B to longitudinal strain on the fibre may be expressed as

$$\Delta\lambda_B = \lambda_B(1 - \rho_\alpha)\Delta\epsilon \tag{3.23}$$

where $\Delta\epsilon$ is the relative elongation, and ρ_α is the photoelastic coefficient of the fibre. For silica fibre, the strain sensitivity is $\sim$1.15 pm/$\mu\epsilon$ for an initial Bragg wavelength of 1550 nm, and $\sim$1 pm/$\mu\epsilon$ at 1300 nm[Rao97].

For a temperature change of ΔT, the Bragg wavelength will shift by

$$\Delta\lambda_B = \lambda_B(1 + \xi)\Delta T \tag{3.24}$$

where ξ is the thermo-optic coefficient of the fibre. For silica fibre, the temperature sensitivity is $\sim$13 pm/°C at 1550 nm, and $\sim$10 pm/°C at 1300 nm[Rao97].

When using FBG sensors in any but the most benign of environments, the drifts in λ_B due to temperature and strain fluctuations must either be minimised or compensated for. This is most commonly achieved by introducing redundancy, for example by installing a second, dummy FBG to measure temperature drifts. The temperature drift in a co-located FBG measuring strain may then be removed. Alternatively, two FBGs may be configured to measure both strain and temperature in an arrangement where their sensitivities differ. This may be achieved by co-locating FBGs with sufficiently different operating wavelengths, or simply by the orthogonal alignment of installed sensors. In both cases, the response of each FBG differs to the extent that both parameters may be extracted simultaneously by monitoring the movement of both Bragg wavelengths.

Since the sensitivity to temperature and strain cannot be removed from FBGs, the sensitisation of the device to a third measurand, such as magnetic field, further complicates the problem of cross-sensitivity. Where fibre strain cannot be sufficiently minimised, techniques must be developed to extract a reliable mea-

surement from a system of three variables. This is particularly important in situations where the sensitivity to the third measurand is very weak, and the response may therefore be dominated by drifts in temperature or strain.

3.3.2.6 Sensitivity to Magnetic Circular Birefringence

With reference to Equations 3.5 and 3.21, the sensitivity of the Bragg peak position to an induced magnetic circular birefringence may now be derived by considering the change in the mean grating refractive index n_{eff} as experienced by a single incident circular polarisation. The sensitivity of the Bragg wavelength to a change in mean refractive index is given by

$$\Delta\lambda_B = 2\wedge\Delta n_{eff}. \tag{3.25}$$

From Equation 3.5, which described the splitting of the refractive index for circularly polarised modes, we can define the refractive index change experienced by a single circular polarisation (of either handedness) as

$$\Delta n = \frac{VB\lambda}{2\pi} \tag{3.26}$$

which is a more useful definition when considering the simplest effect on the FBG peak wavelength—a shift rather than a spectral separation. Combining these expressions yields the sensitivity of the FBG—illuminated with appropriately-polarised light—to a parallel magnetic field:

$$\Delta\lambda_B = \frac{\wedge V\lambda}{\pi}\Delta B. \tag{3.27}$$

It should be stressed that this shift will not occur for unpolarised or linearly polarised light. In those cases, the reflected spectrum will separate rather than shift, which in the case of a standard grating (where the FWHM bandwidth is typically between 0.1–0.4 nm) will be undetectable before a field strength of approximately 3.5 T. From Equation 3.27, the sensitivity $d\lambda/dB$ of a standard 1550 nm FBG may therefore be estimated to be 148 fm/T.

With reference to the temperature and strain sensitivities at 1550 nm (13

pm/°C and 1.15 pm/$\mu\epsilon$ respectively) it is clear that over tokamak-relevant operating ranges (temperatures between 20–500 °C and magnetic fields between 0–10 T) the peak shift due to temperature or strain will be vastly greater than the shift due to magnetic field. During a full-scale magnetisation, the FBG peak will move by a mere 1.48 pm, while a full-scale temperature flux will shift the peak by 6.5 nm—a full three orders of magnitude more. Unless the shift due to magnetic field can be cleanly extracted from the compound response, measurement of the field strength using FBG shifts will not be feasible.

Chapter 5 focusses on the development of a measurement system to exploit the Bragg wavelength's sensitivity to magnetic circular birefringence while reducing the impact of the comparatively giant temperature drifts. Prior to this however, the most appropriate basis for high-resolution interrogation must be determined.

3.4 Interrogation of In-Fibre Bragg Grating Sensors

The generic architecture of an FBG sensor scheme is illustrated in Figure 3.13. In this generalised example, light from an optical source is guided by fibre to the array of serially-multiplexed FBGs. The reflections from the FBGs are returned via a coupler to the interrogating device, at which the peak reflected wavelength from each FBG is demodulated. Typically, the wavelength shifts of each grating are then digitised and passed to monitoring software.

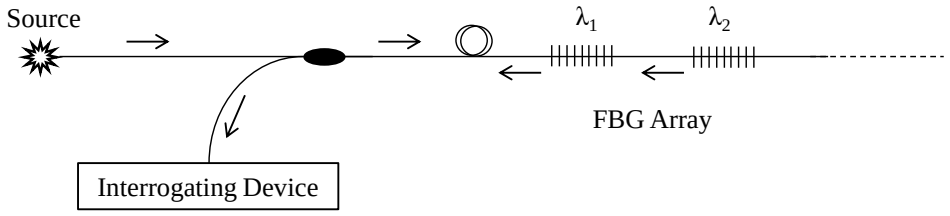

Figure 3.13: A generic FBG measurement scheme. λ_1 and λ_2 are FBG peak reflected wavelengths.

At the electronic and photonic system level, there are essentially two parts to the interrogation of an FBG sensor array. These are: the method of multiplex-

ing, and the method for wavelength measurement. In some cases—such as with tunable filters—one leads straightforwardly to the other. In other cases, a high performance wavelength measurement technique may have few suitable multiplexing counterparts, thus limiting its use in multi-sensor applications. This section will provide a brief overview of relevant FBG sensor interrogation techniques in order to recommend a suitable basis for the interrogation of low-sensitivity magneto-optical FBG sensors.

3.4.1 Interferometric Wavelength Detection

As discussed, the detection of the Bragg shift in magnetised gratings due to magnetic circular birefringence will require very high resolution wavelength-shift detection to overcome the extremely low sensitivity. A high measurement resolution and low noise floor is thus the primary requirement of interrogation techniques for this application.

Of all the techniques proposed for interrogation of FBG sensors thus far, it is the oldest technique—Mach-Zehnder interferometry—that offers the highest performance for a single sensor in terms of both the achievable noise floor and sensitivity. In terms of strain measurements (a common cross-system benchmark for fibre sensor systems), dynamic resolutions of the order of 5–10 nϵ are readily achievable with interferometric interrogators[KBM92]. While other proposed techniques, such as tunable filters and CCD arrays, may possess better multiplexing capabilities, they generally exhibit resolutions that are worse by at least one order of magnitude or are not applicable to C-band wavelengths[KBM93][Lee03]. The wavelength-decoding basis for magneto-optical FBG sensors should therefore be interferometric.

Figure 3.14 illustrates the fundamental Mach-Zehnder interferometer (MZI) interrogation scheme. In this arrangement, light from a broadband source illuminates an FBG, and its reflection is guided via a coupler to the MZI. The MZI is typically constructed between two 2×2 fibre couplers, where one arm of the interferometer is bonded to a piezoelectric actuator to allow for voltage-controlled adjustment of the optical path difference. At the final coupler before the detec-

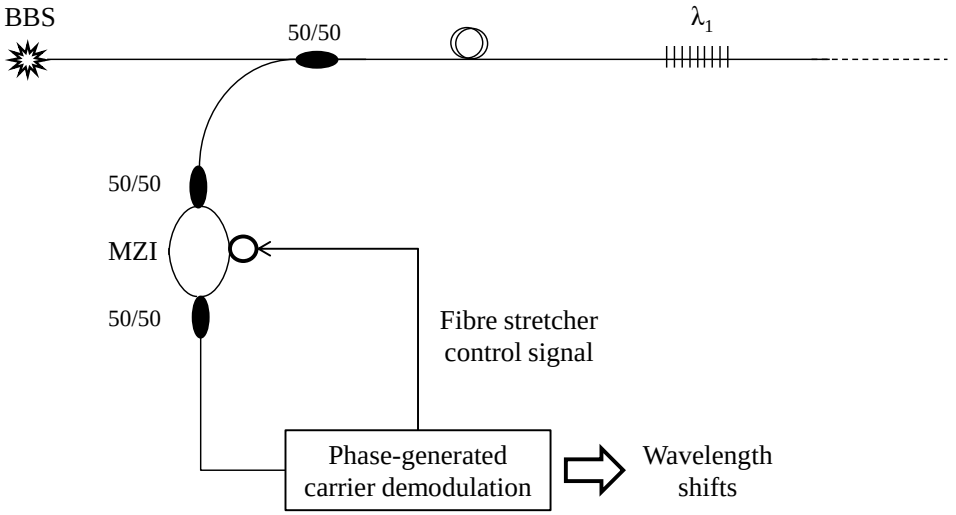

Figure 3.14: Mach-Zehnder interferometric FBG interrogation scheme. Using feedback control the interferometer may be either locked in quadrature or phase-swept. BBS is Broadband Source, MZI is Mach-Zehnder Interferometer.

tion system—the point of interference—the phase difference accumulated between the coherent beams is converted to an intensity modulation through interference. The intensity I at this point is related to the accumulated phase difference ϕ by the general expression

$$I = A + B\cos\phi \tag{3.28}$$

where A and B represent the nominal Bragg reflection intensity and the modulation depth respectively. Modulation depth will reduce as the optical path difference between the interferometer arms tends towards the coherence length of the input light, which is set by the bandwidth of the FBG reflection according to the common definition

$$L_c = \frac{\lambda_B^2}{n\delta\lambda} \tag{3.29}$$

where λ_B is the Bragg wavelength, n is the refractive index of the medium ($n \approx 1.4682$ for silica fibre), and $\delta\lambda$ is the FWHM bandwidth of the FBG reflection peak. Given a standard FBG with 0.2 nm bandwidth situated near the telecommunications band ($\sim$1550 nm), the coherence length of the FBG reflection may be approximated to be 8 mm. The OPD (given by nd where d is the physical

path difference) may therefore be no longer than this without compromising the depth by which the intensity may be modulated by interference, and therefore the sensitivity of any derived measurement.

The power and sensitivity of optical interferometry may be illustrated clearly by considering the change in path difference required to alter the intensity at the point of interference from a maximum to zero. The phase difference between these conditions is π rads, which for a 1550 nm beam in silica fibre requires a change in the physical length of either interferometer path of just 527 μm to produce a full-scale attenuation of the beam.

The phase difference ϕ at the output of the interferometer is described by the relationship

$$\phi = \frac{2\pi nd}{\lambda} + \phi_d \tag{3.30}$$

where the term ϕ_d represents gradual drifts in the phase difference, primarily due to environmental temperature fluctuations which will affect both the path lengths and the refractive index. Compensation for this drift in nd is one of the main problems associated with practical utilisation of interferometric FBG interrogation, and techniques must be developed to deliver this compensation if quasi-static measurements are required. For the measurement of purely dynamic (ac) signals, the drift in nd is not as problematic. However, changes in the path lengths will also affect the sensitivity of the interferometer (by Equation 3.30), and if the basic 2×2 MZI is not locked in quadrature ($\phi = \pi/2 \pm n\pi$) it may lose its sensitivity to phase changes altogether (by Equation 3.28).

If the MZI is terminated by a 2×2 coupler, the interference pattern is replicated on both outputs with a relative phase offset of π rads. To reduce error in phase demodulation due to fluctuations in the input intensity, these outputs are often processed ratiometrically after photodetection. Thereafter, a feedback loop may be used to lock the interferometer in quadrature where the sensitivity is a maximum and the drift is minimised. Such a scheme may be used to detect rapidly-changing ac signals, and also slowly-varying phase changes. However, the action of the feedback loop renders detection of static (dc) signals infeasible

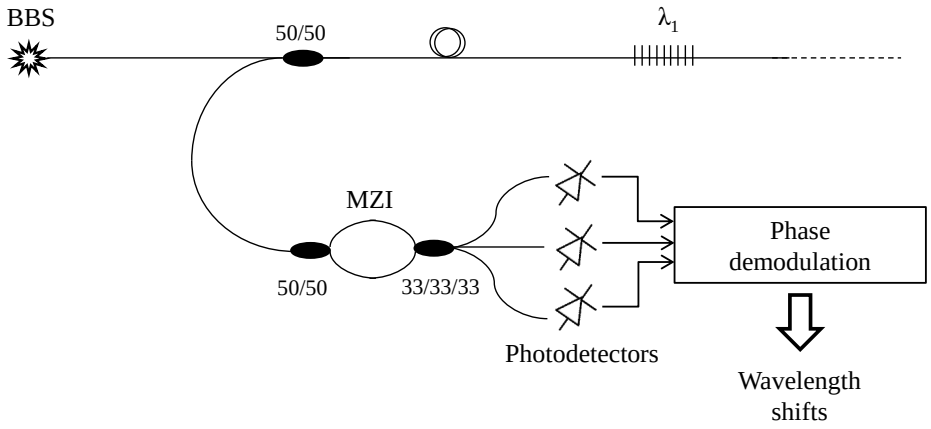

Figure 3.15: FBG interrogation using a 3×3 coupler based MZI. BBS is Broadband Source, MZI is Mach-Zehnder Interferometer.

since the output is continually being nulled[KM94]. This may be compensated to some extent by tailoring the gain and response time of the feedback loop to accommodate measurands of different rates. Alternatively, a sawtooth voltage may be applied to the fibre stretcher of Figure 3.14 in order to ramp the phase difference between 0–2π rads, which removes ambiguity due to the drift term ϕ_d by phase-modulating the wavelength shift. Phase-sensitive detection at the modulation frequency between a reference signal and the sensor signal may then be used to accurately extract the phase shift—and hence wavelength shift—of the sensing FBG[KB92].

The key problem with interferometric wavelength-shift detection as discussed thus far is that multiplexing is cumbersome where modulation of path lengths is required in order to overcome ambiguity in the response. Kersey has proposed a technique for the simultaneous phase-sensitive detection of a number of FBG reflections that makes use of a passive wavelength-division multiplexer to discriminate between reflections prior to their separate photodetection[KB96]. This is a promising basis for high-resolution multiplexing interrogation—however, it suffers from error at low frequencies due to numerous drifts inherent in the interferometer phase that cannot be fully compensated for by the ratiometric detection of only two outputs.

In 2000, Todd *et al* proposed a solution to this problem which allows for

both dc *and* ac measurements to be made with interferometric accuracy[TJC99]. Using a 3×3 coupler as the point of interference instead of the conventional 2×2, the interference pattern is again replicated at the coupler outputs, but now with a mutual phase difference of $\frac{2\pi}{3}$ rads[She81]. This scheme is illustrated in Figure 3.15.

With this approach, after photodetection of the coupler outputs the voltages may be expressed as

$$V_n = A_n + B_n \cos(\phi + \theta_n) \tag{3.31}$$

where $n = 1, 2, 3$ for the three photodetectors, the (A_n, B_n, θ_n) terms contain mean intensity level, fringe visibility, photodetector responsivity, and the coupling properties of the 2×2 and 3×3 couplers that form the interferometer, and the term ϕ is the phase signal of interest. The phase differences θ_1, θ_2 and θ_3 are ideally given by 0, $+2\pi/3$ and $-2\pi/3$ respectively.

If the parameters A_n and B_n are normalised arbitrarily to those of the first channel then an algorithm can be constructed based on the three scaled outputs that is robust to fluctuations in input power level and provides a method for calculation of the interferometer phase. The parameters that must be determined for such an algorithm are therefore the fringe maxima, minima, and mean on each channel, and the phase differences between coupler outputs. Importantly, the mutual phase difference is unlikely to be exactly $+2\pi/3$ in practice, which can be compensated for by inclusion in the demodulation algorithm once true phase differences are measured (using, for example, the technique in [SHS93]).

Given that the parameters (A_n, B_n, θ_n) have been determined, it is then convenient to define the dimensionless parameters $\alpha_n = A_n/A_1$ and $\beta_n = B_n/B_1$ and scale the photodetector voltages by their corresponding parameter to produce the normalised channel voltages $\bar{V}_n = V_n/\alpha_n$. Standard trigonometric relations can then be used to rearrange Equation 3.31 to produce an exact expression for the tangent of the phase as a function of the voltages and interference pattern characteristics[TSB02]:

$$\tan\phi = \frac{(\mu_2 - \mu_3)\bar{V}_1 + (\mu_3 - \mu_1)\bar{V}_2 + (\mu_1 - \mu_2)\bar{V}_3}{(\gamma_2 - \gamma_3)\bar{V}_1 + (\gamma_3 - \gamma_1)\bar{V}_2 + (\gamma_1 - \gamma_2)\bar{V}_3}. \tag{3.32}$$

In this expression, $\mu_n = \frac{\beta_n}{\alpha_n}\sin\theta_n$ and $\gamma_n = \frac{\beta_n}{\alpha_n}\cos\theta_n$ have been introduced to allow for the inclusion of arbitrary phase angles between coupler outputs which are measurable and constant. After voltage normalisation the expected fluctuations in fringe visibility and mean interferogram levels affect each channel simultaneously and in proportion, thus rendering Equation 3.32 immune to fluctuations in input optical power.

Thus seen, the 3×3 MZI technique provides a method for determining passively and immediately the phase in an interferometer. An FBG interrogation system based on this approach would not be constrained by the path length modulation or stabilisation procedures that other interferometric regimes require for phase demodulation since here the determination of phase is immediate for both ac and dc measurands. This approach may therefore form the basis of an interferometric interrogation scheme suitable for use with sensor arrays and quasi-static measurands, while retaining the excellent resolution and noise levels associated with conventional interferometric techniques.

3.4.2 Wavelength Division Multiplexing

In the context of FBG sensors, Wavelength Division Multiplexing (WDM) refers to the differentiation between sensor reflections based on their spectral location. This is achieved by writing each grating with a different modulation period, resulting in an array of serially-multiplexed FBGs that are spaced periodically over the bandwidth of the broadband source. In the basic scheme, all grating reflections return to the detector simultaneously and constantly, which then discriminates between them and deploys the chosen wavelength-demodulation technique.

Although prism/CCD array techniques can allow for sub-10 nϵ resolutions while providing multiplexing and simultaneous detection[Lee03], the processing is complex and the responsivity of the silicon detectors (i.e. their quantum efficiency) begins to drop off as wavelengths approach the near-infrared—beyond

which FBGs are conventionally fabricated. Most common FBG WDM is therefore achieved by more rugged means: a scanning filter with a narrow passband (less than or similar to the FBG FWHM), in combination with a broadband source and broadband detectors. In scanning WDM regimes, the filter is tuned periodically over the bandwidth of the source such that a single grating is illuminated at any given time. Generally, the tunable filter is either a voltage-controlled Fabry-Pérot resonator (see Section 3.3.1) or a frequency-controlled acousto-optic filter[KBM93][BWDN01]. The control signal applied to the filter is used to map the reflection peaks to the source spectrum, and in this way the wavelength-shift of FBG reflections may be determined.

In scanning filter systems, the technique for wavelength-shift detection is immediately amenable to multiplexing since the filter provides both measurement and discrimination between FBGs. However, as stated, the wavelength detection resolution is relatively poor compared with interferometric methods. In addition, the bandwidth of the scanning filter approach is often relatively low (< 1 kHz) due to the limitations of the required electronic processing schemes. Despite these limitations in bandwidth and sensitivity, the scanning filter remains popular due to the flexibility in selecting the amount of FBGs and their wavelengths and its ability to deliver both static and dynamic measurements with relative ease.

In order to overcome the limitations of both the interferometric and scanning filter approaches, Todd *et al* proposed in 2001 a hybrid technique incorporating both the 3×3 MZI method and a scanning filter[JTAC00][TJA01]. In this scheme, illustrated in Figure 3.16, the scanning filter is configured to cover the bandwidth of the source, and the FBG centre wavelengths may be placed anywhere within this region of the spectrum. As the scanning filter moves over an FBG peak, the MZI is illuminated by the reflected wavelength. At the moment of precise correspondence between the filter and FBG peak wavelengths, the phase at the output of the interferometer may be related directly to the FBG peak wavelength.

A supporting electronic processing scheme, shown in Figure 3.17, was proposed in order to extract the relevant MZI output levels at the time of total overlap. The peak voltages encountered at the photodetectors as the scanning filter

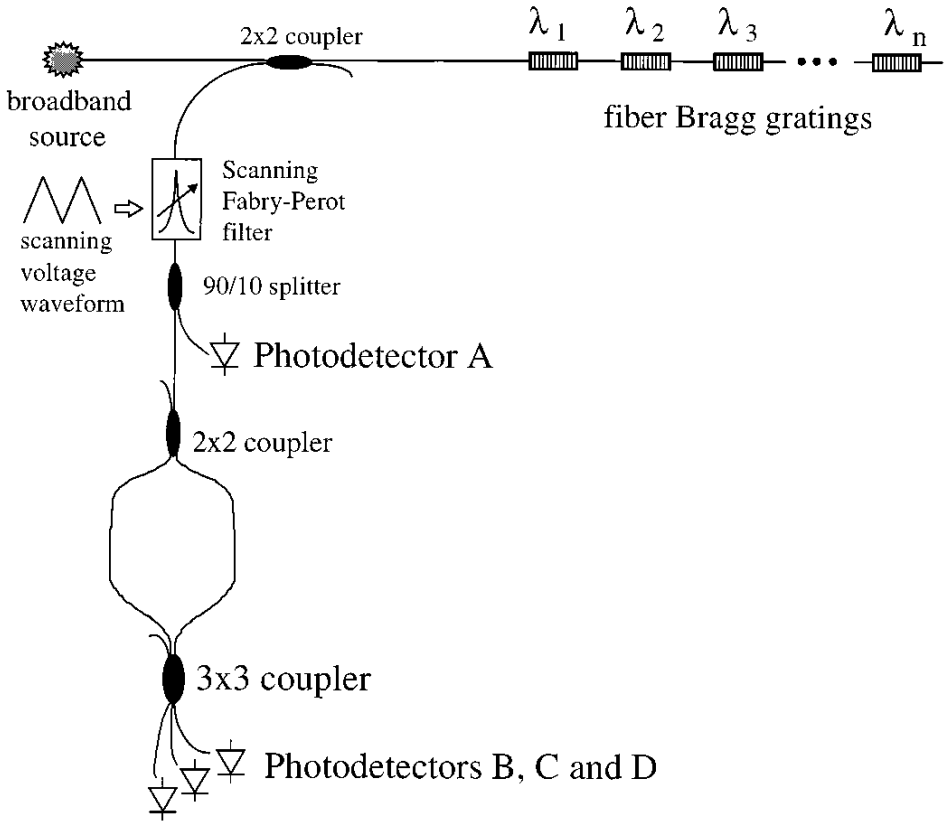

Figure 3.16: Optical scheme proposed by Todd *et al* for combining interferometric wavelength-shift detection with scanning filter-based multiplexing[JTAC00]

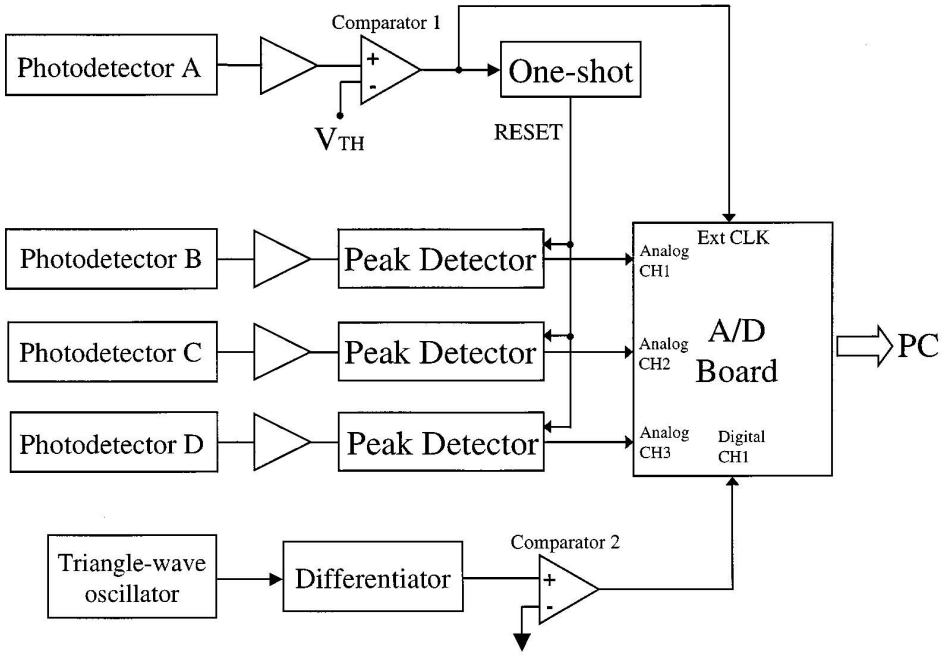

Figure 3.17: Electronic processing scheme proposed by Todd *et al* for capturing relevant photodetector outputs during filter scan[JTAC00]

moves over the FBG reflection peak are retained by peak-hold circuitry. Once the voltage at the output of Photodetector A (from Figure 3.16) rises above a threshold to indicate the occurrence of an FBG and then returns to the nominal low level, the voltages at the peak holds may be sampled. Thereafter, the phase demodulation technique described in the previous section is deployed and the peak hold circuitry is reset.

The system proposed by Todd to exploit the passive and immediate phase demodulation allowed by the 3×3 MZI method has outstanding potential in terms of combining high-resolution interrogation and flexible multiplexing. An excellent noise floor of 5 $n\epsilon/\sqrt{\text{Hz}}$ was demonstrated with this system at a measurement rate of up to 10 kHz. Additionally, its multiplexing capability is similar to that of the flexible scanning filter methods, i.e. 16–20 sensors. The overall performance of the hybrid technique makes it highly applicable to interrogation of an array of magneto-optical sensors. However, there are limitations with the approach which derive primarily from the requirement for the electronic processing stages of Figure 3.17.

The electronic stages are required in order to capture the voltages that occur momentarily at the photodetector outputs when the scanning filter overlaps the FBG reflection. Between these moments, the scanning filter is moving over empty spectrum, and the processing stages are simply waiting to be triggered—rendering approximately 99% of operating time unutilised. This wasted time is always present in scanning filter regimes—however, it is more obvious in a scheme where the spectrum is no longer continuously sampled, as with Todd's hybrid technique.

Additionally, noise is introduced between the photodetection and phase demodulation stages by the addition of the electronic subsystems. Therefore, in order not to compromise the excellent resolution achievable with interferometry, a great deal of effort is required to reduce noise contributions within the electronic circuitry and keep these modules isolated from interference, temperature fluctuations, and vibration.

Based on this discussion, techniques derived from multiplexing interferometry (using the 3×3 MZI method) should form the basis of the interrogation components for the magneto-optical systems proposed in this research. It is clear, however, that further improvements to the state of the art in multiplexing interferometric interrogators will be possible. To this end, an alternative to Todd's scanning/electronic implementation will be demonstrated (Chapter 6) that may solve both the noise and efficiency issues discussed above, while allowing the interrogation rate to move far beyond what is achievable by systems reliant on scanning filters.

3.4.3 Time Division Multiplexing

The Time Division Multiplexing (TDM) of FBG sensors is an alternative to WDM where sensors are discriminated by their time of arrival at the detector, rather than their wavelength. In fact, for simplicity and cost-saving purposes, all FBGs within the array may be written at precisely the same wavelength within TDM-based measurement schemes.

Due to the limitations imposed by FBG and source bandwidths, it is common for WDM-based interrogation systems—including the hybrid technique discussed

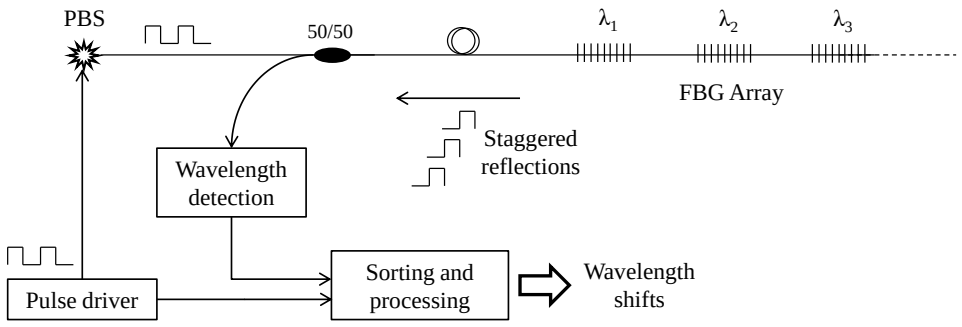

Figure 3.18: Basic TDM interrogation scheme for serially-multiplexed FBGs using a pulsed broadband source (PBS)

above—to acquire measurements from less than 20 sensors, which is sufficient for many applications. In stark contrast, applications such as sub-sea hydrophonics or wind farm condition monitoring require the acquisition of hundreds, or even thousands of sensors[GFVM09]. In these cases, conventional WDM interrogation is insufficient.

TDM interrogation of FBG sensors allows for potentially unlimited numbers of serially-multiplexed sensors to be interrogated by a single system. In general, the source in such systems is configured to be pulsed periodically rather than continuous, facilitating the staggered illumination of FBGs and hence the arrival of their reflections at the interrogation system (illustrated by Figure 3.18)[ZCW+02][Rao97]. Optical delay lines may be placed between FBGs in order to space the arrival of their reflections at the interrogator, since sufficient illumination time must be allowed for the processing of one reflection before the arrival of the next in line. For these reasons, the rate at which sensors may be interrogated is relatively low in TDM schemes and is inversely proportional to the number of sensors. In order to overcome this and allow interferometric interrogation of large sensor arrays (> 100 sensors), Chapter 6 includes a proposal for a hybrid WDM/TDM/interferometric scheme.

3.5 Fibre Irradiation Effects and Resistance

Irradiation is known to affect the characteristics of optical fibres, and specifically those of in-fibre Bragg grating sensors. The cautious nature of the nuclear indus-

Location	**n flux** (> 0.1 **MeV**) n/m^2s	**γ dose rate** Gy/s	**n fluence** n/m^2	**γ dose** MGy
Near blanket gap	$0.2–1 \times 10^{17}$	20–100	$0.4–2 \times 10^{24}$	200–1000
Behind blanket	2×10^{16}	≤ 20	2×10^{23}	≤ 200
Inboard TF coil side	1×10^{14}	0.1	10^{21}	1

Table 3.1: Predicted total gamma (γ) dose and neutron (n) fluence at key magnetic sensor locations over the ITER operational lifetime (see Section 2.2.2.2)

try requires that the radiation-induced effects must be investigated thoroughly before fibres may be deployed in a nuclear environment for either communications or sensing purposes. Although research is ongoing in this area, with many of the observed effects yet lacking satisfactory explanations, a great deal of irradiation testing of fibres and FBGs has been performed—often by institutions associated with the ITER project. From these studies, we may draw conclusions as to the suitability, and survivability, of FBG sensors as part of the ITER diagnostics.

Under conditions of combined gamma and neutron irradiation, optical fibres will exhibit a proportional increase in both attenuation and luminescence that is wavelength-dependent. Additionally, both gamma and neutron radiation will contribute to a densification of the glass structure. Prior to discussing these effects, the cumulative radioactive dose experienced by the hypothetical sensor installation is required. From the operational lifetime and gamma and neutron fluxes expected in the relevant ITER locations (see Table 2.1), we may estimate the total gamma dose and neutron fluence over the sensor lifetimes, shown in Table 3.1. To facilitate this calculation the total exposure time to the predicted radiation levels—taking into consideration the temporal distribution of the irradiation over a pulse—may be estimated to be 10^7 s ($\sim$2800 hours)[CCK$^+$01].

3.5.1 Radiation-Induced Defects

Attenuation of the guided light in commercial grade optical fibre is due primarily to Rayleigh backscattering and, where applicable, macrobend losses. For the industry standard Corning SMF-28e fibre, the attenuation in pristine fibre

is just 0.2 dB/km at 1550 nm (the standard telecommunications wavelength), and 0.35 dB/km at 1383 nm—the location of the previously problematic "water peak" in attenuation due to residual hydrogen-based impurities in early optical fibres[Cor11]. For the most part, absorption defects in pristine commercial grade fibre have been engineered out by substantial improvements in the drawing process and in the purity of the fibre preform's chemical composition. The remaining intrinsic sources of loss are broadband, contributing uniformly to attenuation over the spectrum.

In contrast, the introduction of point defects in the glass structure will tend to produce narrowband absorption regions in the spectrum. It is these strongly wavelength-dependent contributions to the absorption spectra that are of primary concern to those proposing the use of optical fibres in nuclear environments. In a 2005 review, Skuja *et al* summarise the defects that may be produced in optical fibres[SHHK05]. Relevant defects include:

- *Neutral Oxygen Vacancy.* An oxygen vacancy may be produced either by the collision of neutrons with bridging oxygen atoms in the SiO_2 glass network, or following intense (MGy) doses of gamma radiation. The oxygen deficiency defect will absorb UV photons at a wavelength of 163 nm. However, where the silicon atoms involved possess a divalent bond, the defect will instead absorb at 240 nm and photoluminesce at 280 nm and 460 nm.

- *Interstitial O_2 or O_3.* The compliment of the defect above. An oxygen molecule that has broken free of the glass network may becoming trapped, forming an interstitial defect. The O_2 molecules will absorb at < 190 nm, 770 nm, 1280 nm, and 6.5 μm. Alternatively, irradiation of oxygen-rich silica may produce O_3 molecules that may become similarly trapped, absorbing at 250 nm and photoluminescing at 1300 nm.

- *Peroxy Linkage.* An oxygen-oxygen single bond may form that will absorb photons at 190 nm, and thereafter may shift to absorption at 175 nm by a process of photolysis.

- *Silicon Dangling Bond.* Also known as an *E' centre*, these are the result of an unconnected silicon atom bond. These defects absorb strongly in the 200–250 nm range, dominating the absorption spectrum at shorter wavelengths, and may be created more rapidly under conditions of the combined neutron and gamma fields expected in ITER.

- *Hydroxyl Ions.* If hydrogen or water is present in the fibre, interstitial hydroxyl (OH^-) ions may be introduced to the glass network resulting in Si-OH and Si-O-OH groups. The OH ions possess a vibrational resonance at 2.3 μm, with relevant harmonics at 950 nm, 1240 nm and 1390 nm.

- *Silicon Hydride.* If both are present, interstitial hydrogen may react with the oxygen vacancy to produce a silicon-hydride defect, absorbing photons at 1530 nm and 4.4 μm.

Based on the possible radiation-induced defects, it is clear that where hydrogen is not present in the fibre the infrared range from 1400–1600 nm (including the telecommunications band at 1550 nm) is the most robust region of the spectrum. The entirety of the defect-based absorption and emission events in non-hydrogenated fibre occur at shorter wavelengths (100–1300 nm), requiring treatment and preparation of the fibre pre-irradiation to make light guidance in this range feasible.

A substantial amount of work has been done to reduce the radiation-induced absorption (RIA) at these shorter wavelengths. One of the most successful techniques for dampening the most prominent absorption lines—due primarily to the dangling bond defects—is to soak the fibre in hydrogen at high-pressure in order to diffuse molecular hydrogen into the glass structure[HHK$^+$08]. This has the effect of saturating the dangling O or Si bonds. As can be seen from the descriptions above however, hydrogen-loading the fibre in this way introduces strong absorptions at the longer infrared wavelengths—including a reintroduction of the "water peak" at 1383 nm which thereafter dominates the absorption spectrum over the range 1300-1500 nm. As an alternative to hydrogen loading, fibres may be fluorine-loaded to achieve a similar saturation of dangling

bonds, without reintroducing the "water peak". However, it is beneficial that the telecommunications band—for use in which the majority of photonic components are manufactured—experiences a minimal increase in absorption due to radiation-induced defects. Thus seen, for ITER applications it will be most convenient to propose only sensors and systems that function in the 1550 nm region.

3.5.2 Dependence on Fibre Coating

In environments such as fusion reactors, where the fast neutron ($E > 0.1$ MeV) flux will be substantial, appropriate selection of the fibre coating material becomes critical to the minimisation of defect absorption. Commonly, fibres are shielded by an acrylate outer coating that may possess a hydrogen content as high as 14%. It has been shown that the nuclei of these hydrogen atoms (protons) may be ejected from the coating upon collision with incident neutrons, allowing them to become embedded in the glass network of the fibre. In [SH97] it was demonstrated that, compared with hydrogen-free coatings, acrylate coatings will contribute a 21% increase in attenuation to the host fibre (by the hydrogen-based defects outlined above).

In general, coatings comprised of heavier atoms such as metals will be less mobile under neutron collision conditions. In [BBF+01], pure silica core fibres with fluorine-doped claddings were coated in either polymers or aluminium to allow for a direct comparison between the radiation-induced attenuation. After 6 months of irradiation, the polymer-coated fibres exhibited strong absorption around 1390 nm (shown in Figure 3.19), which corresponds with the "water peak" formed by the hydroxyl defect discussed earlier. The proposed explanation was that the hydrogen atoms are ejected from the coating by incident neutrons, forming OH groups in the glass. Indeed, it was shown that after irradiation the attenuation continued to grow, implying that once the hydrogen had been loosened it was able to diffuse into the core from the coating without further irradiation. Fibres for use at infrared wavelengths in nuclear environments should therefore strive to use coatings with only minimal hydrogen content.

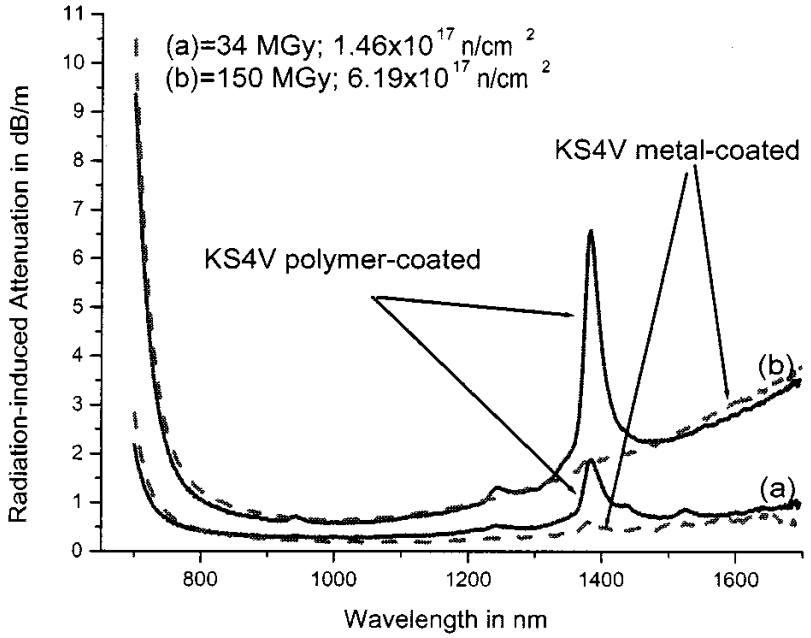

Figure 3.19: Comparison of the near-infrared radiation-induced absorption of pure silica core fibres coated in a polymer or metal. Radiation field is combined neutron-gamma.[BBF+01]

3.5.3 Dependence on Dopants

Fibres are not comprised purely of SiO_2. In order to meet the total internal reflection requirements for waveguiding, a sufficient difference in the core and cladding refractive indices must exist (of the order of 10^{-3}). This difference is conventionally created by doping the glass, for example with Ge (germanium) or P (phosphorus) to raise the refractive index, or F (fluorine) or B (boron) to lower it.

The fibre chemical composition will to a large extent determine its susceptibility to gamma radiation. This is due not only to direct interactions between the dopant bonds and photons, but also due to the adjustment of the glass' fictive temperature (melting point). A higher fictive temperature implies increased bond strain at lower temperatures, which in turn increases the probability that gamma radiation will cause damage to the glass network by breaking these bonds. In general, a more relaxed glass network is less susceptible to damage by gamma radiation.

The effect of the common Ge dopant on irradiation sensitivity was studied

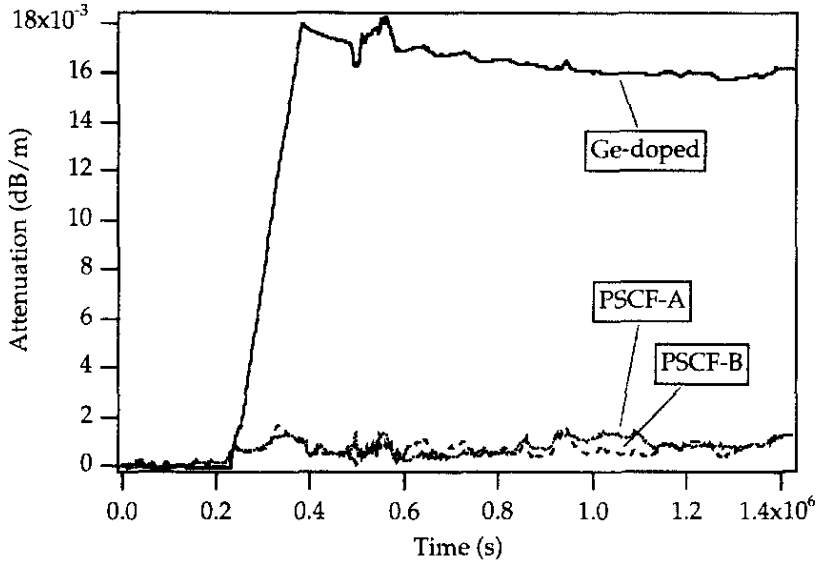

Figure 3.20: Radiation-induced attenuation in Ge-doped and Pure Silica Core (PSC) fibres during 6 MeV neutron test[GGP$^+$94]

experimentally in [GGP$^+$94]. During irradiation with 6 MeV neutrons (a total fluence of 8×10^{13} n/cm^2), a factor of 20 increase in radiation-induced attenuation was noted between pure silica core fibres and those that were Ge-doped as shown in Figure 3.20. For a 10 kGy dose of 0.5 MeV gamma rays, the attenuation was similarly larger in the Ge-doped fibre by a factor of 5. From these studies, it may be concluded that fibres with pure silica cores are the least susceptible to radiation in the 0.8–1.5 μm range. Crucially, this implies that standard telecommunications fibre such as SMF-28e, which uses Ge as a primary dopant, will not be suitable for use in the ITER environment.

As an alternative to Ge-doped fibres, PSC fibres may achieve waveguiding by doping the cladding with fluorine. This type of PSC fibre has attracted much interest, due both to the reduction in the detrimental Ge content, but also due to the bond-saturating pre-treatment discussed in Section 3.5.1 that acts to reduce the occurrence of dangling bond defects. Aside from reducing the absorption at short wavelengths, fluorine doping also has the effect of relaxing the glass structure, making it less susceptible to breakage under gamma radiation[SHHK05]. The beneficial effects of fluorine-doped PSC fibres in comparison to standard Ge-doped telecommunications fibres at 1550 nm under gamma irradiation are clearly

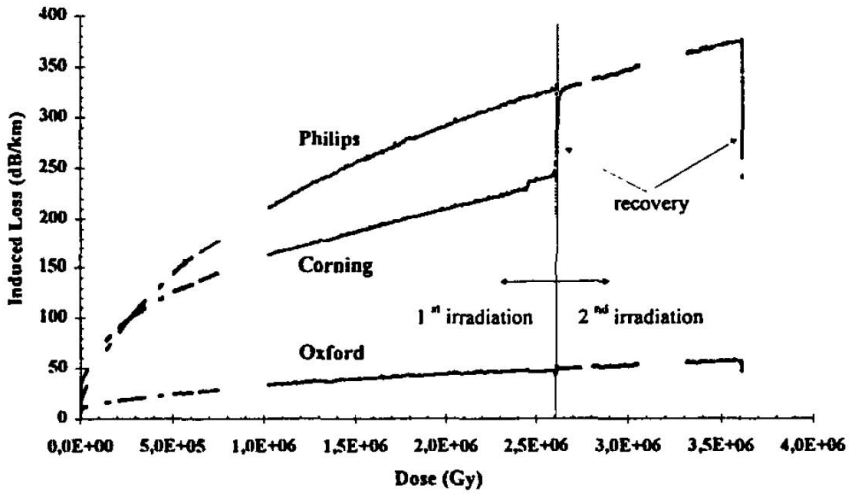

Figure 3.21: Induced loss at 1550 nm for three irradiated fibres: Corning and Philips fibres are Ge-doped; Oxford fibre is pure SiO_2 core and F-doped cladding[VUBN$^+$99]

demonstrated in Figure 3.21.

3.5.4 Glass Densification

Densification is the compaction of the glass network that may occur under neutron and, to a lesser extent, gamma irradiation. In [POH00], Piao *et al* explain by thermodynamic principles how a localised region of high-pressure high-temperature may change silica glass from its A-phase to its B-phase. In the B-phase, also known as the metamict phase, the angle between bonds in the glass network is smaller by 10°, leading to an increase in the density of the network in that area.

During neutron bombardment, highly localised thermal spikes may be created in the glass network[Pri58]. Temperatures of 5000–10000 °C may be experienced in the region around the bombardment ($\sim 10^4$ atoms), combined with a pressure of between 0.3–0.7 GPa. Under these conditions, the glass phase maybe changed permanently, even after the glass is returned to low temperatures. By this process, under neutron bombardment the glass will gradually become denser, leading to a compaction of 2–3%. Interestingly, this is far lower than the densification achieved by heating through non-radioactive means. The implication is that neutron bombardment also creates many voids in the glass structure that contribute to a reduction in density.

Under gamma radiation, densification can occur by a different mechanism. At room temperature, bonds in the glass network are under strain. The breaking of one bond by ionizing radiation leads to a relaxation of the entire network, which may be considered to be an array of strained springs. Upon relaxation, the density of the network is increased. Since the neutron compaction mechanism depends on thermal spikes, it varies minimally between fibres of different chemical composition. In contrast, the gamma contribution—which depends on the relaxation of strain in the glass network—must be dependant on the atomic composition of the glass.

By the Lorentz-Lorenz equation, the change in glass density as a result of irradiation may be related directly to a change in refractive index[Pri58]. Additionally, by the Kramers-Kronig relationship—utilised previously in Section 3.2.3.1—the change in refractive index will then correspond to a change in the intrinsic absorption of silica glass, and hence the attenuation of the guided wave[oLPT11]. In this way, densification may contribute directly to radiation-induced attenuation in optical fibres. In non-hydrogenated fibres that do not have polymer-based coatings, it has therefore been suggested that densification may be the *primary* contributor to the RIA at 1550 nm (seen at the longer wavelengths in PSC fibres in Figure 3.19), where the defects outlined in Section 3.5.1 are not applicable[BBF$^+$01].

3.5.5 Temperature Dependance

As mentioned, a relaxed glass network will incur less damage from incident gamma radiation. It is notable that as the environmental temperature is raised, studies show that the RIA in exposed fibres is reduced. This may be explained by considering that as the glass is brought closer to the fictive temperature, the bonds are less strained and are therefore less likely to be broken by ionizing radiation[Per11].

As an illustration of this temperature dependence, it was demonstrated in [VUBN$^+$99] that by increasing ambient temperature from 45 to 80 °C the RIA in both SMF-28e and fluorine-doped pure silica core fibre was decreased by factors

of 2 and 0.5 dB/km/°C respectively. In a gamma field therefore, it is beneficial to operate at raised temperatures. Given that the operating temperatures of in-vessel magnetic sensors are likely to be up to 300 °C during irradiation, a substantial improvement in RIA levels can be expected compared with sensors irradiated at room temperature. However, it was shown that when temperatures are lowered, the expected loss levels return, indicating that the damage is not being recovered; rather, it is being masked. For this application however, it may be possible to take advantage of the raised temperatures since measurements will only be acquired during pulsing while temperatures will be raised.

3.5.6 Birefringence and Polarisation Control

Since the systems proposed in Chapters 4 and 5 rely on polarisation control, it is of interest how PM fibres react to gamma and neutron irradiation. Of primary concern is the possible change in the beat length of the fibre, given as

$$L_b = \frac{\lambda}{B} \tag{3.33}$$

where B is the birefringence in the PM fibre ($B = n_{fast} - n_{slow}$). In such fibres, a high birefringence is deliberately introduced in order to make the propagation constants of the two polarisation modes very different. In this way, the relative phase of the copropagating modes rapidly drifts away, and any disturbance along the fiber will produce a coupling between the modes only if it has a significant frequency component with a wavenumber similar to the difference of the propagation constants of the two polarisation modes. If this difference is large enough, the usual disturbances in the fiber—such as bend, heat, strain, or even stray magnetic fields—are too slowly varying to couple the modes effectively.

Thus, when linearly-polarised light is launched into one axis of PM fibre, it will continue to propagate along this axis with its azimuth being generally unaffected by external disturbances, including the Faraday effect. This property will be utilised later in the thesis to ensure measurements are confined to grating regions. However, if the beat length were substantially altered by irradiation,

this could undermine the ability of the PM fibre to maintain and isolate linear polarisations.

There are a number of ways to create highly-birefringent PM fibre. Often, birefringence is introduced by including two stress rods of a modified glass composition in the fibre preform on opposite sides of the core in order to cause mechanical stress with a well-defined orientation. This will then create two orthogonal modes with a sufficiently large birefringence. Alternatively, elliptical core fibre may be used. In a photonic crystal fiber (PCF), strong birefringence can be obtained with an asymmetric arrangement of air holes, or simply by the insertion of stressing elements. As will be discussed, PCF is extremely resistant to radiation-induced attenuation, and would therefore be an excellent choice in this PM application.

The effects of gamma radiation on a stress-induced PM fibre were studied independently by Marrone *et al* and by Voloshin *et al*[MRFL84][VVI+09]. Although it was found that radiation-induced attenuation increased proportionally with gamma dose (as would be expected), it was found that the polarisation-holding quality of the fibre was unaffected. No significant changes in the fibre birefringence or the beat length were observed up to a gamma dose of 10^4 Gy. Indeed, "radiation-resistant" PM fibres are commercially available[Nuf11]. These are promising results for the work in this thesis, since they demonstrate that even in basic PM fibre there exists a robustness of the beat length to irradiation. Since many PM fibres, such as PM PCF, rely on form birefringence to enable polarisation-holding, the beat length's robustness to radiation-induced changes should be excellent. It is reasonable to conclude that the polarisation-maintaining qualities of these fibres will be sufficient for this application even in strong radiation fields.

3.5.7 Radiation-Induced Attenuation (RIA)

It follows from the above sections—which identified the factors contributing to radiation-induced attenuation in fibres—that pure silica core fibres, with a metal coating (not acrylate or polymer) and minimal hydrogen content (no hydrogen-

preloading), will be the most appropriate waveguiding medium for the ITER environment. It has also been established that the wavelength range from 1300-1600 nm will be the least affected by radiation. Pure silica core waveguiding is often enabled by fluorine-doping of the cladding to lower the refractive index, which as shown will be beneficial to the radiation resistance.

Unfortunately there have been a limited number of ITER-relevant studies performed with this type of fibre. This is due primarily to the high interest in visible-spectrum or UV fusion diagnostics, for which the fibres must overcome the large absorption peaks that are developed in this region (see Section 3.5.1). As discussed, fibres for this purpose are hydrogen-loaded to minimise the effects of defects in the UV and visible regions, introducing large losses in the infrared. Thus, the majority of fibre irradiation studies are irrelevant for 1550 nm operation in non-hydrogenated fibres.

Due to the number of factors involved in the RIA process—such as dopants, pre-treatment, OH content, and coating—it will not be appropriate to extrapolate based on "similar" fibres. In order to estimate the losses induced in the preferred type of fibre over the ITER lifetime, the analysis must rely on studies performed with the *specific* type of fibre recommended for this application. Of the research carried out with this type of fibre, the 2001 study by Brichard *et al* stands out as the most relevant[BBF$^+$01]. This is due to the gamma dose rates and neutron fluxes involved, and the total dose and fluence, which are comparable to those expected for sensors over the ITER lifetime (see Table 3.1). Other relevant studies exist, such as [VUBN$^+$99] and [BTO$^+$07], however in these cases both the data at 1550 nm and the total dose levels are limited. At this point, there is no published study that is focussed primarily on high-level irradiation of pure silica core, hydrogen-free, metal-coated, fluorine-doped fibres for 1550 nm operation—however this type of fiber has been used as a non-hydrogenated reference in studies of "radiation-hardened" fibres for use in the UV regions.

The data from [BBF$^+$01] is presented graphically in Figure 3.22. Although the neutron (gamma) flux (dose rate) and fluence (total dose) are similar to those of ITER lifetime conditions, the ratio between neutron flux and gamma dose rate

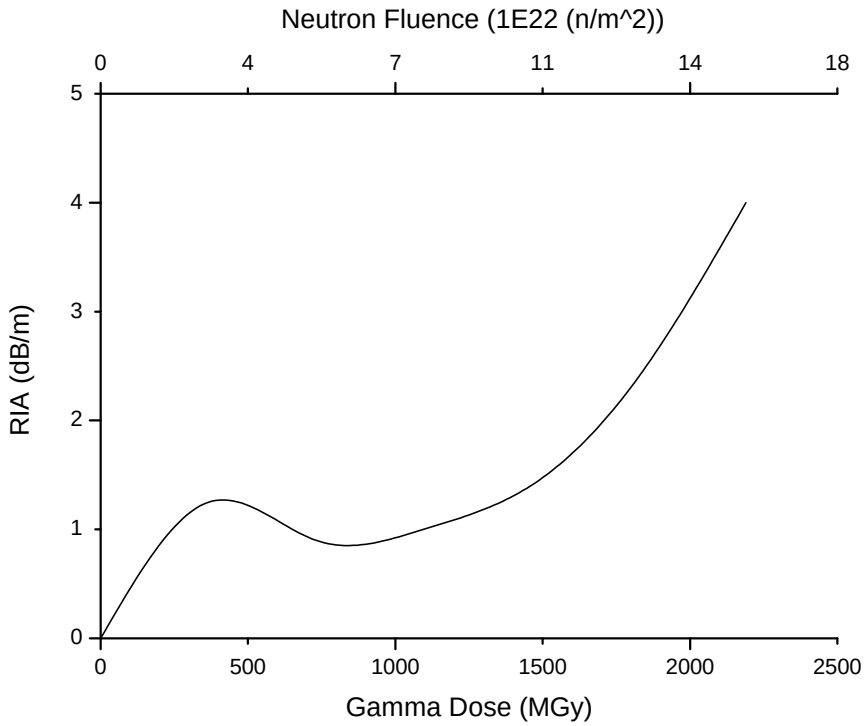

Figure 3.22: Radiation-induced attenuation at 1550 nm in pure SiO_2 core fibre (F-doped cladding, Al-coated, non-hydrogenated). Temperature is 50–55 °C. Data is extracted from [VUBN$^+$99].

(or fluence to total dose) is not similar. In Brichard's study, this ratio is generally of the order of 10^{13} n/m^2/Gy, while from Table 3.1 the ratio in ITER will be of the order of 10^{21} n/m^2/Gy, i.e. under realistic ITER conditions there will be a higher neutron flux for a given gamma dose rate. However, the data may be used to estimate bounds for the attenuation in dB/m at the relevant dose rates, which will be sufficient for approximating the RIA in an ITER fibre sensor installation.

From Figure 3.22, it is possible to estimate the attenuation that will be experienced at each of the three in-vessel sensor locations by the end of the ITER operational lifetime. The *inboard TF coil side* location is the simplest to predict, since it undergoes the least intense irradiation (1 MGy, 10^{21} n/m^2) and is easily compared with the measured attenuation at these levels. This region will accumulate an RIA of approximately 0.1 dB/m, corresponding to an averaged attenuation growth rate of 0.005 dB/m/year over ITER's 20 year lifespan.

For the *behind blanket* location we can determine bounds for the RIA of 0.8–5 dB/m by conservatively assuming the curve will continue to increase linearly up to

the required neutron fluence (2×10^{23} n/m^2, while the gamma dose remains < 200 MGy). Since the gamma contribution to the attenuation curve in Figure 3.22 is likely to be far less than the neutron contribution[VUBN$^+$99], it is reasonable to propose that the attenuation will be closer to the upper bound than the lower bound. Thus, an RIA of 4–5 dB/m may be estimated for this region over the ITER lifetime, corresponding to an averaged growth rate of 0.225 dB/m/year.

RIA in the final region, near the *blanket gaps*, is the most difficult to predict based on present studies that do not irradiate relevant fibres at the levels expected in this region (up to 2×10^{24} n/m^2 and 1000 MGy). Based on the available data in Figure 3.22—again conservatively assuming a constant gradient and no saturation beyond this data set—we may propose an RIA of 7 dB/m over the ITER lifetime, corresponding to an averaged growth rate of 0.35 dB/m/year.

Since the RIA will, in combination with the source power spectral density, determine the signal level at the photoreceiver, the voltage signal-to-noise ratio (SNR) at the photoreceiver output may now be estimated. Additive noise due to photoluminescence may be assumed to be negligible at 1550 nm[BUF$^+$01]. Present commercially-available low-noise photoreceivers achieve a Noise Effective Power (NEP) of approximately 10 fW/$\sqrt{Hz}$, while broadband sources suitable for illumination of a series of FBGs will distribute 30 mW of optical power over a bandwidth of 30 nm (an average power density of 1 mW/nm). Ignoring coupler losses, the power incident on the detectors in Todd's 3×3 system (see Section 3.4.1) from a single FBG (FWHM = 0.2 nm) may then be estimated to be 0.2 mW, or 67 μW per photodetector, prior to RIA losses. For correct representation of input optical signals that may be rapidly optically-switched to enable sensor multiplexing (discussed in depth in later chapters), a photodetector bandwidth of around 1 MHz may be estimated, yielding an NEP of 10 pW at each photodetector.

Thus, the pre-RIA photodetector SNR may be estimated to be 68.26 dB. To illustrate the losses induced by RIA, we will presume that 10 metres of the addressing fibre will be subject to the RIA levels predicted above. For the mid-band *behind blanket* location, the induced losses in the irradiated fibre after 20 years of

installation will be 10×4.5 dB = 45 dB. Thus, the signal at each photodetector is now only 2.11 nW, yielding a post-RIA SNR of 23.26 dB. From Todd's voltage error analysis of the preferred wavelength-detection technique—which assumes that voltage drift errors are the dominant source of phase-demodulation error—the absolute strain error for the pre-RIA and post-RIA conditions are then 0.05 $\mu\epsilon$ and 10 $\mu\epsilon$ respectively[TaFBNT06]. A factor of $\sim$200 deterioration in the wavelength-detection resolution for the *behind blanket* location over the ITER lifetime can thus be expected.

By a similar process of analysis, we can expect an RIA-induced lifetime resolution deterioration factor of $\sim$10 for the *inboard* sensor location, based on a lifetime voltage SNR of 57.26 dB. For the *blanket gap* region, the end-of-life SNR will be extremely poor ($<$ 1 dB), indicating that, based on present fibre technology, this location will not be suitable for an optical sensor installation. In both cases, the exposure of a full 10 metres of fibre to the peak radiation levels has again been assumed. We may conclude however that both the *inboard* and *behind blanket* sensor locations will be suitable for the installation of spectrally-encoded optical fibre sensors.

It should be noted that initial research indicates photonic crystal fibre (PCF) may be a more radiation-resistant alternative to silica-core fibre. In PCF, the wave is guided by photonic bandgap effects rather than total internal reflection, which allows the refractive index of the core to be less than that of the cladding. This enables a new class of air-core fibres that are not as susceptible to RIA since only a fraction of the wave is guided in silica. Although FBG fabrication in these fibres will be extremely difficult due to the air-guidance, they may be used to guide light from the source to the grating host fibre and back in order to minimise the RIA contributed by these off-sensor regions. In [GBL05], the gamma-induced RIA in air-core PCF at 1550 nm was recently found to completely saturate at 0.1 dB/m after a dose of only 10 Gy. This saturation behaviour has been verified by other studies, up to total dose rates well beyond those in the harshest conditions of ITER[CLVB07]. In this case, the lifetime resolution deterioration factor of $\sim$10 predicted for the *inboard* region would be applicable to all proposed sensor

locations. Thus, it may be possible to vastly reduce overall RIA in the sensor system and enable measurement in the harshest locations (including the *blanket gap*) by deploying air-core PCF between sensor elements.

3.5.8 Effects on FBG Sensors

Given that photosensitivity—the mechanism by which fibre Bragg gratings may be UV-inscribed—is likely related to photoinduced glass densification[GD00], it follows that radiation-induced densification (see Section 3.5.4) may also affect the FBG characteristics directly. This has indeed been found to be the case. Importantly, it has been demonstrated that FBG irradiation can induce both semi-permanent Bragg wavelength shifts and changes in peak reflectivity, and that the magnitude of the changes are dependant not only on the characteristics of the irradiation field, but also on the fibre composition, optional pre or post-treatments, and the chosen fabrication technique[BBF$^+$08].

The influences of grating composition and fabrication procedure on the irradiation response were studied by Gusarov in [Gus10]. In this work, eleven gratings were inscribed in two fibres (high-Ge content photosensitive fibre, and standard telecommunications fibre) in order to test the effects on the irradiation response of hydrogen-loading, pre-ageing (high-temperature annealing), and pre-irradiation. After comparison of pre- and post-irradiation (after 10^{21} n/m^2 and 10 MGy) reflectivities and Bragg peak locations, it was found that the simplest fabrication procedure (no hydrogen-loading, pre-treatment or post-treatment) in photosensitive (Ge-doped) fibre yielded the smallest changes in both peak shift and reflection amplitude—changes of 0.05 nm and -0.09 dB respectively.

Although the reduction in reflectivity of irradiated gratings has not been seen to saturate, the choice of appropriate fabrication techniques can render this effect negligible over ITER lifetime gamma-neutron fluences if the sensor interrogation method is immune to intensity fluctuations. However, the radiation-induced Bragg peak shift—a potentially large source of measurement error—must be quantified and kept to a minimum. To this end, the kinetic response of the Bragg wavelength to irradiation has been studied by Gusarov[GBF$^+$00] and by

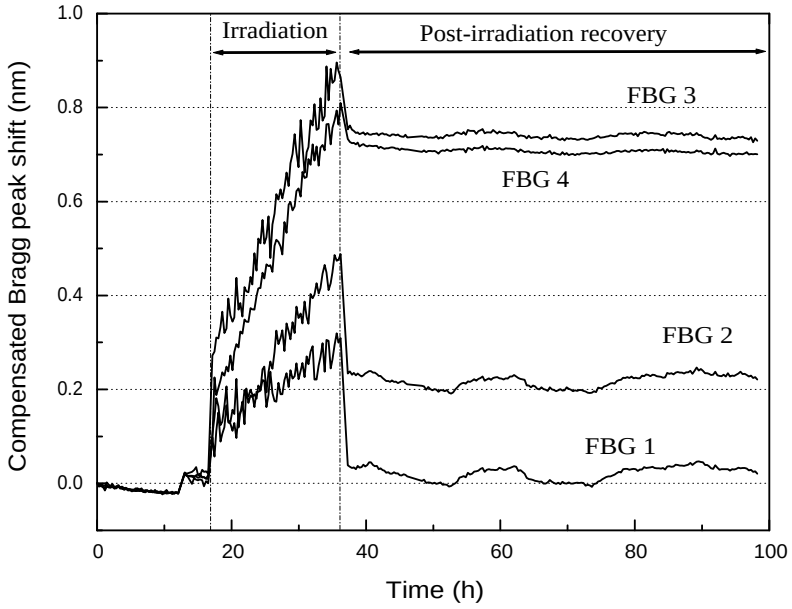

Figure 3.23: Radiation-induced Bragg shift and recovery. Greatest recovery is seen in FBG1, which experiences the lowest neutron irradiation. Fluence and dose are 10^{21} n/m^2 and 10 MGy.[FBB$^+$02]

Fielder[FKSB04]. In both cases (gamma field only and combined gamma-neutron field) the Bragg wavelength shift was found to saturate and remain constant after at most 30 minutes of irradiation. It was shown by Brichard and Fernandez that after removing the radiation field the Bragg peak shift will experience a recovery (Figure 3.23), but only from the gamma contribution—the neutron contribution to peak shift, although saturable, will not experience recovery when the neutron field is removed. Importantly, only FBGs written in photosensitive fibre with both no pre-treatment and no hydrogen-loading were found to have a saturating radiation-induced shift, as confirmed by Fujita[FBB$^+$02][FKNT00].

Therefore, for minimisation of changes in reflectivity and Bragg wavelength in nuclear-application FBG sensors, hydrogen-loading to enable photosensitisation will not be appropriate. This has implications for high-temperature operation since hydrogen-loading is ubiquitous in the fabrication of regenerated gratings[BCB$^+$11][Fok02]. Fortunately, it has recently been demonstrated that regenerated gratings, stable at up to 1000 °C, can be fabricated without hydrogen-loading in highly-photosensitive Ge-doped fibre[LCC$^+$11]. This type of high-

temperature grating is thus a good candidate for in-vessel sensing, since it can be expected to retain the radiation-hardness of non-H_2-loaded non-preprocessed FBGs, while withstanding the high surface temperatures.

Given the previous section's recommendation of pure silica core fibres for waveguiding in radioactive environments, mention should be made of pure silica core gratings which require hydrogenation to impart photosensitivity[AFM02]. A direct irradiation comparison of non-hydrogenated Ge-doped gratings and hydrogenated pure silica core gratings has unfortunately not yet been performed—indeed, no irradiation test of pure silica core gratings has been performed to date. At this stage it is therefore not possible to state conclusively which approach to grating regeneration will yield the most radiation-resistant sensors. Still, it can be expected that a trade-off will exist between the techniques due to the inclusion of hydrogen and the exclusion of the Ge core dopant.

Finally, the effects of both gamma and neutron irradiation on the fibre Verdet constant—which will govern the FBG's sensitivity to an incident magnetic field—have been shown to be negligible over ITER-relevant radiation levels[Bri09b][Bri09a]. Since the Verdet constant is dependant on both temperature and wavelength (see Section 3.2.3.1) the influence of the radiation-induced Bragg shift will be of greater concern. However, since the Verdet constant in diamagnetic fibre will change very little even over the high surface temperature fluxes expected in-vessel, the shifts in λ_B due to the compound effects of temperature and irradiation may be treated as one. Given that the Bragg peak wavelength shift due to radiation will saturate quickly and in a repeatable manner, its characterisation and isolation may be possible during signal post-processing.

3.5.9 Summary of Irradiation Effects

From the above study of irradiation effects, the following practical recommendations can be made:

- The most appropriate wavelength range of operation will be the telecommunications band from 1530-1570 nm,

- Of the solid-core fibres, the most radiation-hard will be pure silica core with fluorine-doped cladding,
- Where possible, hollow-core PCF should be used in off-sensor regions to minimise attenuation,
- Fibre protective coatings should be metallic,
- High-temperature grating fabrication should be performed in Ge-doped photosensitive, non-hydrogenated fibre,
- Hydrogenated pure silica core gratings may offer greater radiation resistance, but this has yet to be demonstrated,
- Appropriately-fabricated FBGs will experience negligible changes in reflectivity and FWHM over the ITER lifetime,
- Radiation-induced Bragg shift will occur, however isolation will be possible due to its saturation and repeatability over numerous irradiations,
- The *inboard* and *behind blanket* sensor regions will be suitable for a lifetime fibre installation,
- Over a 20-year ITER lifetime, measurement resolutions in the *inboard* and *behind blanket* regions will gradually worsen by factors of $\sim$10 and $\sim$200 respectively if no maintenance is performed,
- The *blanket gap* region is expected to be unsuitable due to the high neutron flux and resultant fibre damage,
- The magneto-optical sensitivity (Verdet constant) in silica fibres will be unaffected by irradiation.

3.6 Summary and Recommendations

In this chapter, the most appropriate basis for the technical solution to the measurement problem has been determined. Additionally, the robustness of this

technical basis to the expected environmental conditions of ITER was analysed and found to be sufficient.

It was established in Section 3.2, through a review of potential magnetic transducer mechanisms, that magneto-optics will be the only suitable basis for magnetic field measurement under conditions of high field strength, irradiation, and high temperatures. It was demonstrated that there exists two development paths by which magneto-optical measurement of the magnetic field may be implemented. These are: direct measurement of the magnetic circular birefringence, or polarimetric measurement of the Faraday rotation. As discussed, neither of these approaches has yet been sufficiently developed for in-fibre point measurement.

In Section 3.3, the use of FBG point sensors to implement magneto-optical sensing of magnetic field was shown to be desirable due to their small size and spectrally-encoding nature. As such, the foundations of FBG-based implementations of both magneto-optical sensor mechanisms were described, both of which have the potential to meet the performance requirements stated in the previous chapter. Chapters 4 and 5 will detail the research performed to technically develop both of these approaches.

Additionally, the interrogation of FBG sensors was subject to a focussed discussion on combining multiplexing and high-resolution wavelength-shift detection in Section 3.4. It was established that the detection technique should be interferometric, but that there is room for further development of the state-of-the-art interferometric multiplexing systems. As such, contributions to this area will be made in Chapter 6.

The effects of radiation on fibre waveguides and the selected measurement basis were analysed in Section 3.5. The causes of the most substantial effects were established, leading to recommendations for the choice of fibre and for grating fabrication. It was established that fibre sensors will be suitable for radioactive environments, and that sufficient research has now been performed in this area to support such an installation. Based on the performance of the preferred sensors, fibres, and fabrication techniques at ITER-relevant radiation levels, it was estimated that two of the three preferred sensor locations (*behind blanket*

and *inboard*) will be suitable for the installation of fibre sensors over the ITER lifetime.

Chapter 4

Compound Phase-Shifted Fibre Bragg Structures as Slow-Light Magnetic Field Sensors

4.1 Chapter Overview

In the previous chapter, a distinction was made between the two potential implementations of an intrinsic magneto-optical fibre point sensor for magnetic field strength—that is, the polarimetric or wavelength-encoded approaches. In this chapter, the focus is on the former, where the azimuthal rotation of an incident linear optical polarisation is the measured quantity.

Through simulation it will be shown that the Faraday rotation spectra of phase-shifted gratings can be tailored by tuning the ratio of substructure lengths. This leads to the characterisation of compound phase-shifted fibre Bragg structures for use as novel in-fibre magnetophotonic point sensors. A design process for tailoring the magneto-optical spectrum is illustrated, and it is shown that a general optimum structure exists for producing a region of total reflection that incorporates magneto-optical Faraday rotation that is greatly enhanced, both in strength and spectral width, relative to standard gratings or even those with a single phase-shift.

Following the characterisation of these novel fibre transducers, a practical

optoelectronic system is detailed that exploits the proposed distributed feedback (DFB) structures to enable novel all-fibre sensors for the dual measurement of magnetic field strength and temperature. The response of an optimum grating structure is then simulated, allowing for calculation of the measurement resolution achievable by this system.

The study is supported by laboratory fabrication of the proposed fibre DFB structures, demonstrating the principle of enhancement in terms of tailored group delay spectra. Based on this, a supplementary proposal for a novel optical delay component for tunable wavelength-selective control of path delays is presented. In both cases, the practical issues for sensor packaging—key to the performance and reliability of the devices—are highlighted.

4.2 Introduction and Background

In the previous chapter, the concept of Faraday rotation enhancement in resonant optical cavities was introduced. It was shown that the enhancement factor was proportional to the finesse of the resonator, which is related to the number of round-trips experienced by light within the resonant linewidth. It was also shown that distributed reflectors such as Bragg gratings have the potential to incorporate resonances, and that these may be deliberately induced by introducing defects in the refractive index modulation profile.

In the field of bulk glass optics, magnetophotonic thin-film multilayers have been shown to be capable of providing enhanced azimuthal rotation of a transmitted linear polarisation by the insertion of magnetic defect layers[SLO00][VAB$^+$06]. In such structures, light at the resonant wavelength undergoes magneto-optical Faraday rotation that is strongly enhanced in relation to neighbouring spectral regions by the principle outlined above. These devices are developed primarily to enable small optical isolators, where the resonant Faraday rotation enhancement is used to reduce the physical size required to produce a given azimuthal rotation. In contrast to the present application, these bulk glass structures are inherently magnetic—the inserted defect layers which induce the phase-shift are themselves

ferromagnetic glasses or garnets and thus no external field is required for magnetisation. Additionally, the magneto-optical interactions in these structures can be very large due to the high rare-earth dopant concentrations achievable in bulk glass, the minimal linear birefringence, and the large refractive index step between layers.

Phase-shifts in the UV-inscribed index modulation profile of the fibre analogue of these structures—fibre Bragg gratings—are commonly used to produce distributed feedback structures for use as spectral filters for wavelength division multiplexers and as elements in DFB fibre lasers[CS94][ASK+95]. Standard photosensitive fibres do not contain rare-earth ion dopants and are therefore diamagnetic, possessing weak magneto-optical interaction. In the previous chapter the level of intrinsic linear birefringence present in conventional FBGs was discussed and found to be far greater than that in bulk glass[CDSK05]. For in-fibre devices this may compromise both the ability to write precise phase-shifts into the grating profile (since the resonances will separate) and the ability of the structure to process strongly polarised light without substantially altering the state of polarisation. Finally, the achievable index modulation depth in fibre Bragg gratings is relatively weak ($< 10^{-3}$), and thus a greater physical length and number of layers (or modulation periods) will be required compared to bulk glass distributed Bragg reflectors to produce a similar resonator finesse.

There has previously been interest in utilising the resonances induced by inserting phase shifts into the index modulation profile of FBGs for tailoring of the reflection and transmission spectra. By inserting multiple phase shifts at different locations within the grating, it was shown by Zengerle and Leminger that the lengths between phase-shifts could be tuned at the design phase to produce rectangular filter characteristics in reflection and transmission[ZL95]. The optimum substructure length ratio for such filters was confirmed by Wei and Lit to be symmetric, taking forms such as $A : B : A$ for two phase-shifts, or $A : B : B : A$ for three phase-shifts, where A and B are substructure lengths or number of perturbations between phase-shifts ($B > A$ such that substructure lengths reduce towards grating ends)[WL97]. This symmetrical approach to

producing quasi-flat-top filters was also employed by Levy *et al* and separately by Vasiliev *et al* to improve the transmission characteristics of bulk glass multilayer filters, including for magnetophotonic crystal applications where the defect layers are ferromagnetic[LYSF01][VKA^{+}08]. However, as shown in Figure 4.1, the symmetrical approach does not yield optimal enhancement in the group delay spectrum, which has implications for the dependent magneto-optical rotation spectra. Additionally, the Kerr rotation of symmetrical magnetic multilayers is very poor, even in bulk glass structures.

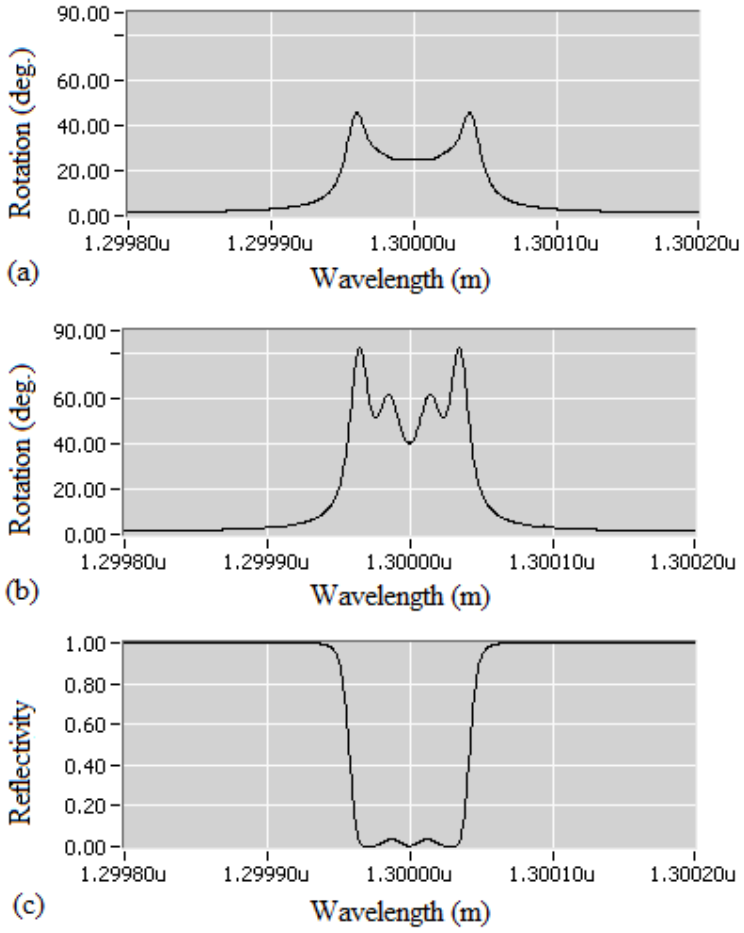

Figure 4.1: (a) Kerr rotation via symmetrical 8.8 mm FBG with substructure ratio 2/4/4.5/4.5/4/2 and (b) with addendum (relative length of 8) to force reflection of rotated wavelengths. (c) illustrates the quasi-flat reflection spectrum of the symmetrical structure. These graphs were generated using the modelling procedure described in Section 4.3.

Building upon the research into symmetrical multi-defect Bragg structures and photonic crystals, this chapter reports on investigations into magnetised fibre

DFB structures possessing low linear birefringence in the interests of developing a new type of magnetic field strength sensor based on in-grating containment and enhancement of Faraday rotation. Section 4.3 summarises the details of the simulation procedure. The characteristics of magnetised asymmetrical π-shifted grating structures are investigated in Section 4.4 where a design process for optimal compound phase-shifted sensor structures is described alongside guidelines for structural dimensions. Section 4.5 documents the laboratory characterisation of fabricated structures of the proposed type. In Section 4.6 a practical interrogation system design for the deployment of the tailored structures as novel sensor elements is detailed, including simulation of the sensor response and a discussion of achievable performance. Additionally, the use of such structures as highly tunable optical delay elements for future optical communications architectures is discussed in Section 4.7.

4.3 Modelling Procedure

Phase-shifts in fibre DFB structures may be numerous and can be tailored in position and magnitude. It is therefore of interest whether such structures can, through such tailoring, yield magneto-optical rotations of useful magnitude and bandwidth in reflection (Kerr rotation[1]). In this thesis we will consider only π shifts in the index modulation, and tune the response through adjustment of substructure lengths. This is due to the requirement for reflection-mode sensor operation, which as will be shown is more straightforwardly enabled by this tuning method.

To study the magnetic effects on compound phase-shifted fibre gratings, a software simulator was written in C++/*LabVIEW* based on the 4×4 state matrix analysis method for multilayer magnetophotonic media described by Inoue[IF97]. The software application, shown in Figure 4.2, is capable of simulating assemblies of magnetised silica-based FBGs with arbitrary phase-shifts (magnitude and location along the grating). This numerical multilayer approach was chosen since

[1]The use of the term *Kerr rotation* is appropriate in this instance as only light that is ultimately reflected by the structure is subject to azimuthal rotation.

it allows for rigorous calculation of transmission, reflection, and Faraday/Kerr rotations via any structure that can be appropriately described in terms of a series of thin-films. Details on the theory and implementation of the simulation software can be found in Appendix A.

The finesse of resonators created in optical fibre by writing phase-shifted Bragg gratings is proportional to number N of high-low evolutions of the grating refractive index n, and the grating's strength, or *modulation depth*, dn. In this work, an assembly of thin-films is first calculated to represent a single raised-sine index perturbation on fibre. This *perturbation matrix* is then treated as one film that is used to construct grating regions. Although phase-shifts may be induced in fabricated FBGs by a number of methods, a step-change in the index modulation phase is usually enabled by a rapid shift in the phase-mask position, resulting in a gap or blurring of the modulation at the phase-shift location rather than a true point phase-reversal. As such, the π-shifting region is realistically modelled as an unperturbed region of fibre of length half the grating period $\wedge$, which can be placed at any points along the grating and whose locations define the lengths N_1–N_k of k substructures. The general compound phase-shifted grating structure that forms the basis of these simulations is illustrated in Figure 4.3.

Since the FBG's UV-inscribed grating profile is comprised of a continuous, sinusoidal modulation—as opposed to the discrete step changes that comprise photonic crystals or bulk glass multilayer stacks—the fraction of light reflected at each perturbation will be much less in an FBG than in multilayer structures. A realistic model of the magnetised FBG will therefore need to incorporate this continuous change in refractive index. Since the model used here utilises the state matrix approach (see Appendix A), the larger continuous change may be approximated by a perturbation matrix comprised of a number of smaller discrete layers with stepping refractive indices. During simulation, it was found that as the number of such minor step-changes used to approximate the continuous change increases from 1 to 50, the reflectivity of the grating as a whole decreases in proportion, as would be expected. Beyond 50 step-changes, the reflection and transmission characteristics of the structure do not change any further, and

Figure 4.2: Simulator for magnetised fibre Bragg gratings. Allows determination of transmission, reflection, Kerr rotation, Faraday rotation, and reflective group delay spectra for a given magnetic induction. Customisable parameters: Substructure lengths, phase-shift magnitudes and locations, off-sensor stray magnetisation, optical power levels, scanning filter characteristics, magneto-optical sensitivity.

thus using any more than 50 minor step-changes will needlessly introduce further processing demands. As such, 50 minor step-changes are utilised in this model to construct the state matrix for the approximation of a single "continuous" (raised-sine) FBG index change of width $\wedge$.

For further efficiency, grating structures are built from blocks comprising 250 such raised-sine perturbations (each corresponding to approximately 0.25 mm in a 1550 nm FBG), which is therefore the spatial resolution of these simulations and of the structural optimisation process. The model assumes zero linear birefringence in the FBGs (discussed later) and simulates only the effects resulting from the introduction of circular birefringence Δn_c that is due to a magnetic field parallel to the fibre core—namely, the differential phase between circularly-polarised modes that gives rise to azimuthal rotation.

A structural optimisation algorithm was written to identify the optimal grating structures for reflection-mode polarimetric sensing. As described in Appendix A, the algorithm functions by evaluating the peak azimuthal rotation of reflected light at a constant magnetic field strength (nominally 1 Tesla) for different asymmetrical substructure length ratios. It also aims to maximise the reflected intensity at the resonant wavelength, and to take into consideration the linewidth of the resonant region by convolving the intensity spectra with a scanning filter passband to represent the practical difficulty in utilising narrowband rotary regions. This trade-off between the resonant spectral width and peak optical rotation will be discussed in the next section. The algorithm enabled the establishment of governing rules for optimal sensor structures for up to five defects

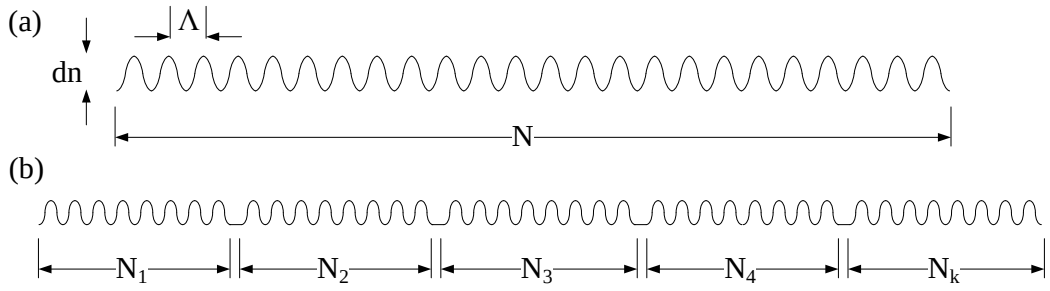

Figure 4.3: Structural layout of uniform (a) and compound phase-shifted (b) fibre Bragg gratings

(six substructures).

4.4 Sensor Structure Design

The objectives of the sensor design may be summarised as follows:

1. Maximise reflectivity over the resonant region, such that light undergoing a resonant enhancement of azimuthal rotation is ultimately reflected: This will enable reflection-mode sensing,

2. Maximise the FWHM bandwidth of the resonant spectral region, in order to reduce the difficulty of interrogating the structure with resonant wavelengths,

3. Maximise the peak Kerr rotation of the structure, in order to improve the sensitivity (specific rotary power in rad/T) of sensors based on these structures.

To enable reflection-mode sensor operation, light undergoing large reflection within these structures must return to the interrogation system. As discussed in the previous chapter, resonant frequencies in conventional Fabry-Pérot resonators will be transmitted and not reflected. Intuitively, this can be reversed by increasing the reflectivity at one cavity boundary. As such, during this design process the requirement for reflective operation is ensured by making the length N_k of the final substructure sufficient to guarantee complete reflection over the FBG bandwidth. This region would otherwise contain sharp resonant passbands corresponding to the unwanted transmission of rotated wavelengths. The reflection-mode criteria may therefore be met by use of asymmetrical structures.

The potential of phase-shifted FBGs to implement high localised rotations may be illustrated by increasing the length N_1 of the entrance substructure in a single phase-shifted asymmetrical magnetised FBG. From Figure 4.4, it is clear that by increasing the reflectivity around the phase-shift, the rotary power at the resonant wavelength is increased. Therefore, measurable rotations can be

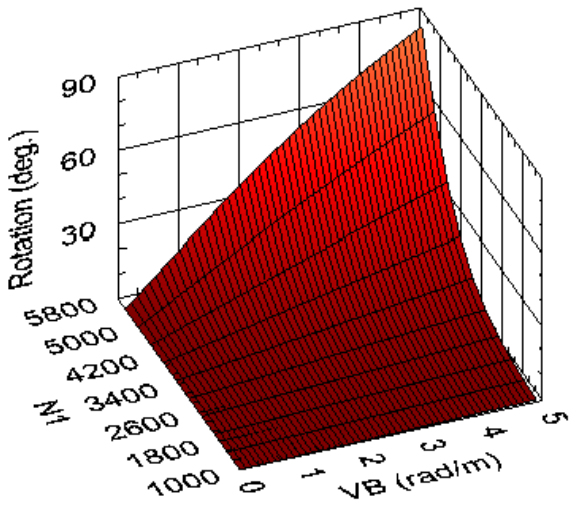

Figure 4.4: Peak Kerr rotation in single phase-shifted asymmetrical Bragg structure with increasing entrance substructure N_1 ($N_k = 12 \times 10^3$, $dn = 10^{-3}$)

produced by such structures. However, in the discussion of Fabry-Pérot cavity theory, it was stated that cavity finesse is inversely proportional to the linewidth of resonant regions. Therefore, when designing the structure to maximise the resonance FWHM, the peak rotation will be decreased, and vice versa. Figure 4.5 illustrates this trade-off between the number of round-trips and the full-width half-maximum (FWHM) bandwidth of a grating resonance in terms of Kerr rotation via the structure.

From Figure 4.5 it can be seen that as the rotary power (considered as *degrees per Tesla*) increases, the FWHM of the resonance rapidly scales towards the sub-picometer. Due to the impracticality of interrogating light spectrum within such a narrowband region, while temperature or strain may be causing the entire spectral region to shift, the potential of this structure to act as the rotator element in a polarimetric sensor is strongly limited. This key problem with the in-grating resonator must be overcome by broadening the region to useful widths.

The solution proposed here relies on the introduction of further defects into the asymmetrical structure. By introducing multiple phase-shifts into the grating profile, a corresponding number of such resonances will appear in the grating reflection spectrum. Then, by tuning either the substructure lengths or the phase-shift magnitudes, it is possible to tune the spectral position of each resonance

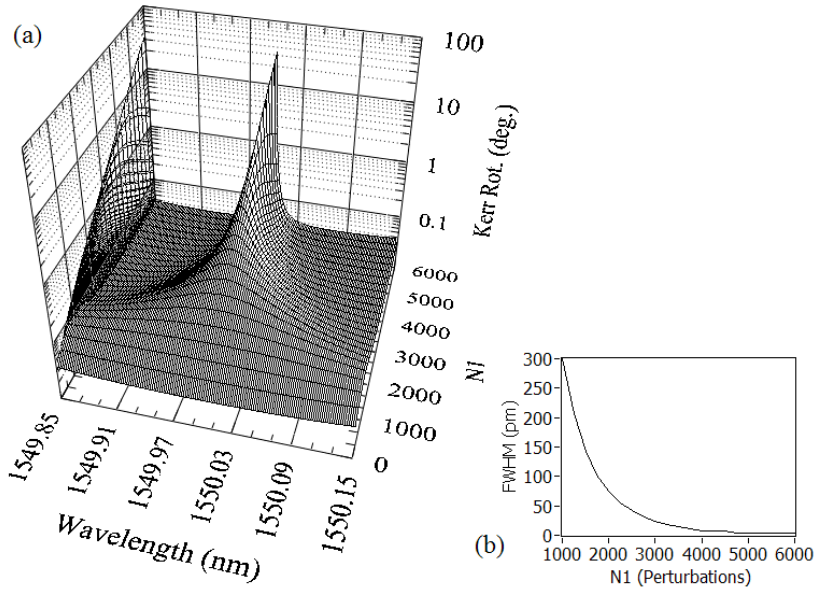

Figure 4.5: (a) Kerr rotation spectrum with lengthening entrance substructure for a single phase-shifted FBG at a field strength of 1 Tesla. Y-Z plane projection illustrates the increase in peak rotation. (b) Clarification of the reduction in resonance FWHM over the range. ($N_k = 2 \times 10^4$, $dn = 10^{-3}$)

within the FBG bandwidth. Although it has been established that symmetrical substructure ratios will enable quasi-flat top transmission spectra, these structures do not translate well to magneto-optical rotation spectra. A different type of phase-shift layout over the grating will be required in this instance, and it is of interest whether there are general rules that can be applied during grating design and fabrication that will allow for the FWHM/peak trade-off to be overcome.

For this application, since we are concerned with reflection-mode operation, by increasing the length of the final substructure N_k we can enable >90% reflectivity over the entire grating bandwidth, such that the insertion and adjustment of further phase-shifts will have no effect on the reflection spectrum. Under such conditions, the resonant effects will only become apparent when the magneto-optical rotation spectra (or group delay spectra) are measured or simulated. Therefore, the reflection spectrum can be neglected for the remainder of this analysis, since it is assumed to be close to unity over the resonant regions.

To illustrate the technique for overcoming the tradeoff between resonance spectral width and rotary power, a second rotary region may be introduced by

the addition of a third substructure positioned between N_1 and N_k. By increasing the length N_2 of this section, while keeping the entrance substructure length N_1 constant, the rotary regions contributed by both defects can be combined spectrally in order to effectively superimpose their contributions to the delay of light at the merging wavelength. This effect of combination through tuning the substructure length N_2 is key to the design procedure that follows, and is illustrated in Figure 4.6.

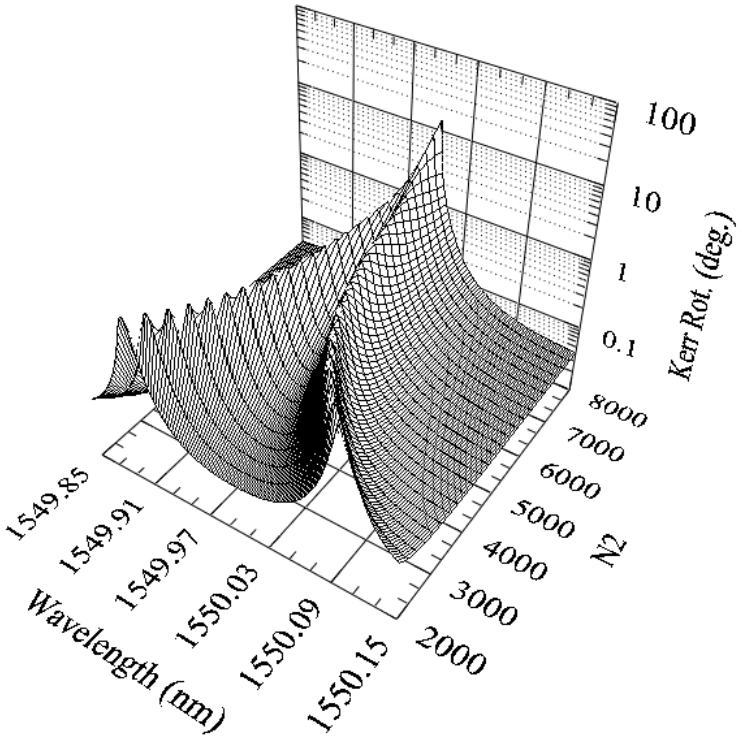

Figure 4.6: The combining of Kerr rotation peaks within a 2-shift asymmetrical grating (structure: 3000 / N2 / 20000)

By the addition of further substructures prior to N_k, peaks in the Kerr rotation spectrum may be successively combined in the manner of Figure 4.6, in order to produce a single enhanced peak that possesses both increased bandwidth and increased peak rotation. By combining peaks in this manner, the resonant region may be broadened by expanding the wavelength coverage of the resonant region. Also, the peak group delay or peak Kerr rotation may be increased by co-locating resonances such that the group delays at the common wavelength are summed. In this way, such multi-shift structures are able to overcome the problems associated

with the single-shift structure.

This combination of peaks in magneto-optical rotation over the grating bandwidth will therefore allow reflection-mode sensors to be designed which produce large compound group delays to enable true slow-light sensors within traditional FBG structures. Secondary applications for these structures may also be proposed, such as that of Section 4.7, that will benefit from the production of large group delays in grating structures. Indeed, it has very recently been suggested that such structures (often referred to as slow-light structures when the group delay is large) will enable novel sensing applications[ZZZ$^+$09]. However, due to the non-reciprocality of the Faraday effect, the measurement of magnetic field in the manner proposed here may be one of the clearest applications of slow-light structures for sensing.

Building upon this resonance superposition process, the numerical optimisation algorithm discussed in Appendix A was used to identify common structural characteristics between grating designs that yielded large, broad Kerr rotations, while maintaining high reflectivity. From this analysis, the following general guidelines were verified empirically over the complete range of substructure length ratios:

1. Successive substructures should be greater in length than the preceding substructure, i.e. $N_n > N_{n-1}$. This is always the case for structures that yield superimposed Kerr rotation peaks.

2. The difference in length between consecutive substructures should reduce with each additional substructure, i.e. $(N_n - N_{n-1}) < (N_{n-1} - N_{n-2})$.

The final substructure N_k is an exception to the second criterion, and should simply be made long enough to provide total reflection as described previously. Importantly, if the first guideline is adhered to, then further increases in N_k will not affect Kerr rotation. The general optimum structure that results from adhering to the above rules is one in which the series of substructures preceding N_k follow an approximately logarithmic growth profile as illustrated by Figure 4.7. Where this is the case, the resonances contributed by each phase-shift will be

tuned to superimpose on the spectrum, resulting in a giant Kerr rotation enhancement at a common wavelength. Where the phase-shift magnitudes are π, this common wavelength is simply a highly-precise value of the Bragg wavelength.

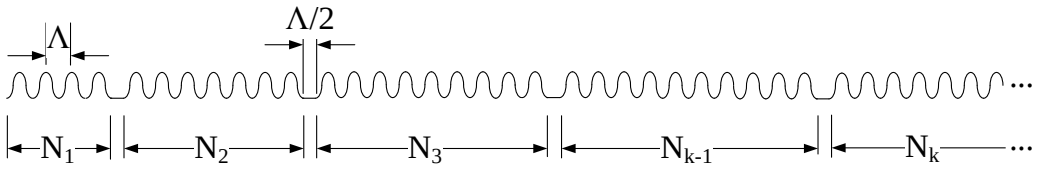

Figure 4.7: Structural layout of the general optimal sensor grating, which adheres to $N_n > N_{n-1}$ and $(N_n - N_{n-1}) < (N_{n-1} - N_{n-2})$

In order to clearly illustrate the multiple phase-shift design process for successive superposition of Kerr rotation peaks, Figure 4.8 demonstrates the enhancement of Kerr rotation at each stage during a tailoring process of 1–6 substructures (5 resonances). During this design process, the two design criteria above have been adhered to in order to ensure superposition of resonances and hence provide large peak rotation. The properties of each curve in Figure 4.8 are summarised in Table 4.1. It can be seen from the data that as the structure develops, the peak rotation and FWHM are altered in such a way that the area under the curve is increased. By increasing this area, both the ease of interrogation and the sensitivity to magnetic field for measurement applications are improved. The area under the curve can be understood to be a useful metric in this application, since it incorporates both the increase in rotary power and the trade-off in terms of resonance spectral width. It is clear from Table 4.1 that this trade-off is completely overcome by utilising multiple phase-shifts that are logarithmically-spaced. For comparison, the 6-section structure developed in Figure 4.8 possesses a curve area that is a factor of 5 greater than the 2-section structure of Figure 4.5 (for similar peak rotation).

Although the above design process allows for maximisation of peak Kerr rotation and a substantial broadening of the enhancement region, it may be preferable to compromise peak rotation in order to further broaden, and flatten, the Kerr rotation region. With reference to the proposed interrogation technique for such structures (Section 4.6), a broader, more uniform region of azimuthal rotation

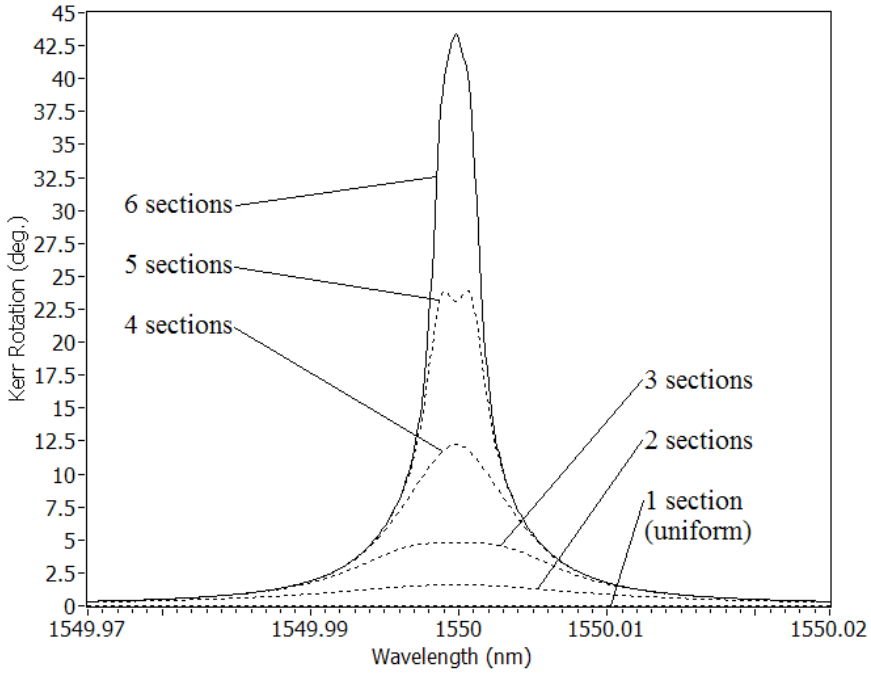

Figure 4.8: Enhancement of peak Kerr rotation within developing structure from uniform grating to final 5-shift logarithmic grating. Final structure is 3000 / 7000 / 8750 / 10000 / 11000 / 20000 (total length 31.72 mm). ($B = 1$ Tesla, $V = 0.57$ $rad/(Tm)$, $dn = 10^{-3}$)

Structure ($N_1/N_2/N_3/N_4/N_k$) (1000s)	Peak Rotation (deg.)	FWHM (pm)	Area under curve (deg·$m \times 10^{-3}$)
3/20	1.591	22.739	49.3
3/7/20	4.788	16.310	102.9
3/7/8.75/20	12.242	9.500	156.6
3/7/8.75/10/20	23.919	5.893	210.4
3/7/8.75/10/11/20	43.385	3.996	264.1

Table 4.1: Properties of enhanced rotary regions featured in Figure 4.8

would relax demands on the linewidth of scanning sources. This may be achieved by allowing only partial superposition of the resonances introduced by each defect.

A broad magneto-optical Kerr rotation spectrum, with a quasi-flat-top response reminiscent of the flat-top transmission filters designed by Zengerle and Leminger, is illustrated in Figure 4.9. Here, an alternative design that yields a widened quasi-flat-top Kerr region at the expense of peak rotation is shown. It should be noted that the increase in Kerr rotation towards the edges of Figure 4.9 are simply due to the minor peaks in group delay that exist for all FBGs—these minor peaks can be seen in greater detail in Figure 3.12 where they surround

the central resonance. Thus, in general, the slow-light structures proposed here based on compound phase-shifted FBGs can be designed either for a small rotary enhancement with good uniformity over a wide bandwidth, or purely for maximisation of the rotary strength over a narrower bandwidth. This tailoring is achieved by adjusting the degree to which the resonances are superimposed, which is determined by the location along the grating of each defect.

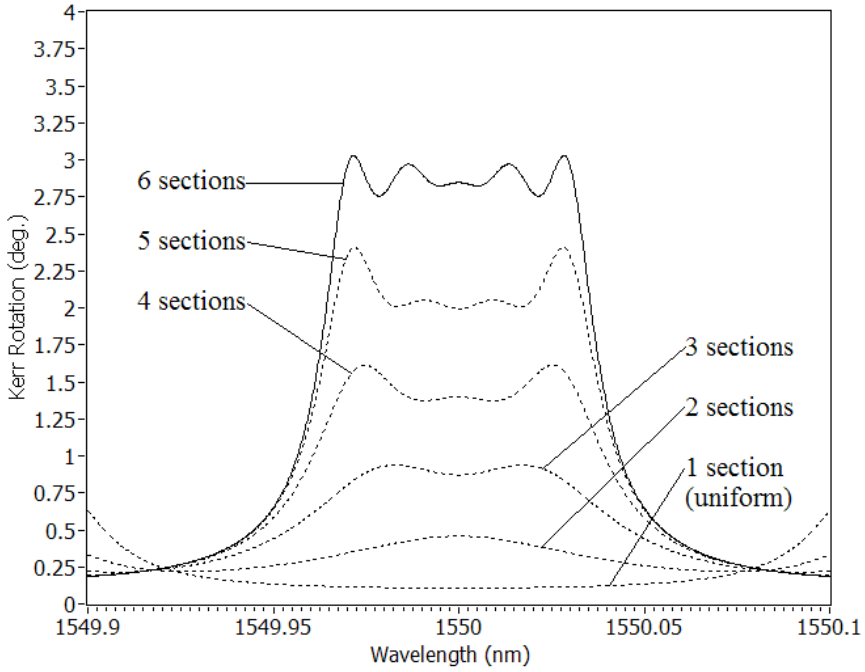

Figure 4.9: Production of a "flat top" Kerr rotation region by 5-shift logarithmic grating. Final structure is 3000 / 7250 / 9000 / 10000 / 11250 / 20000 (total length 32.11 mm). ($B = 1$ Tesla, $V = 0.57\ rad/(Tm)$, $dn = 0.3 \times 10^{-3}$)

It is an important feature of such structures that by keeping the ratio between substructure lengths constant, both the bandwidth and peak of the Kerr rotation regions can be tuned without affecting the general spectral shape—governed by the degree of resonance superposition. This tuning can be achieved by adjusting either the grating strength dn or total grating length. In this way, a reduction in grating strength can be compensated for by a corresponding increase in length, and vice versa. The fabrication of these structures can therefore be achieved using a pre-determined substructure ratio for any suitable grating length by post-tuning of the modulation depth. Additionally, it is important to note that since the enhancement of group delay or magneto-optical rotation is dependant primarily

on the substructure length ratio, the designs suggested here will be transferrable to bulk glass multilayers and integrated optics devices (where physical dimensions and refractive indices will differ) which may also benefit from dispersion tailoring in this manner.

4.5 Fabrication and Characterisation

As Kerr rotation enhancement within the magnetised structures depends on the increased containment and delay of light falling within the resonant region, the effect is directly proportional to the group delay of reflected light. The magnitude of this delay will therefore undergo an identical enhancement over the spectrum. Thus, by monitoring the reflective group delay during fabrication of such gratings, the enhancement factor can be verified at the time of inscription without the use of test magnetic fields or polarimetric interrogation techniques. Using this procedure, fibre Bragg gratings based on single-shift and 2-shift structures were inscribed in order to demonstrate the enhancement simulated in the previous section.

The multi-shift gratings were fabricated in standard boron co-doped germanosilicate (B/GeO_2) fibre by a frequency-doubled 244 nm Argon-ion laser using direct writing through a phase mask, as described in Section 3.3.2.1. CW 244 nm was chosen since it does not contribute significantly to linear birefringence[CDSK05].

All gratings were written with a laser output power of 35 mW at a speed of 1 mm/min. The gratings were then over-written in order to tune the index modulation strength dn of the structures, since as discussed this enables the simulated responses to be approached even where total UV fluence is not accurately known. The peak wavelength of all FBGs was approximately 1570 nm, placing them within the telecommunications band recommended for use in Chapter 3. No apodisation was applied since, as established previously, this would reduce the finesse of the resonators produced by phase-shifting.

Precise π phase-shifts in the index modulation were introduced during the writing process at accurate locations by controlling the voltage applied to a piezo-

electric stage supporting the phase mask. The driving voltage for this phase-mask was determined by a central LabVIEW-based control programme, which generated the synchronous control signals for the optical shutters, and two piezoelectric stages; for enabling slow scanning of the laser through the phase mask, and for introducing step changes in the phase-mask location.

The transmission, reflection, and reflective group delay of each grating were recorded at regular intervals during the writing process. Using a tunable laser source controlled by the central LabVIEW control programme, the input wavelength was scanned over the grating bandwidth to allow the acquisition of transmitted and reflected photodetected signals at each wavelength step.

Measurement of the reflective group delay was performed by the phase difference method using an Agilent/HP 8753D network analyzer[SD79]. Group delay measurement is based on a subcarrier technique, and relies on the detection of the phase difference between the optical signal transmitted to the grating and the optical signal detected after reflection from the grating. To implement the technique, a fast intensity modulator based on a tunable Mach-Zehnder interferometer was used to modulate the optical source. The output of this modulator was then coupled via a photodetector to the electrical network analyser to provide a reference phase signal.

Upon reflection from the grating, the optical signal is photodetected and passed to the signal input of the network analyser, which performs phase-sensitive detection of the signal and reference inputs to determine their relative phase and hence the time delay accumulated between them. This time delay is then taken to be the group delay. It will, however, contain an offset corresponding to the time taken to travelling to and from the grating region. This offset is compensated for in the figures shown here by shifting the group delay spectra down in order to zero the delay of off-grating wavelengths. The group delay measurement is performed for each wavelength step as the tunable laser source is scanned over the bandwidth of the grating. Within LabVIEW, a group delay spectrum is then developed based on measurement information passed by the network analyser.

Using feedback from peak reflective group delay, incremental adjustments were

made to grating modulation depths by repeated fast overwriting. In this way, the structure can be tuned to approach the simulated optimum design, as indicated by a peak in the growth curve of the reflective group delay, at which point there is optimal superposition of contributing resonances. Importantly, this process may be automated in future to be performed by the central control software so that human monitoring during fabrication is minimal.

The measured and simulated reflective group delays are compared in Figures 4.10 and 4.11 for the fabricated single-shift and 2-shift structures respectively. In both cases, the total exposure and hence grating strength dn is identical (0.4×10^{-3}) to within $\pm 2.5\%$, as are the total structure lengths (apertured to 10 mm during grating fabrication using steel razer blades). These strengths and total lengths are replicated in the simulations to allow for comparison between theory and practice.

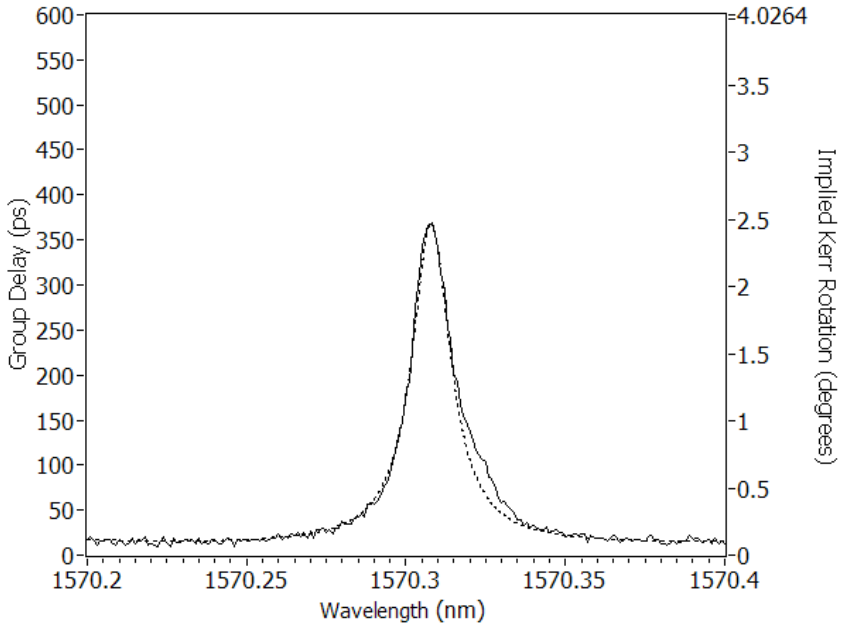

Figure 4.10: Simulated (dashed) and measured (solid) group delay for single-shift grating of length 10 mm ($dn = 0.4 \times 10^{-3}$, structure 6000 / 13000). Peak delay is approximately 350 ps. Implied Kerr rotation is calculated for a parallel field strength of 1 Tesla.

It can be seen that restructuring the 10 mm gratings from 1-shift to 2-shift results in the expected enhancement of the group delay, and by implication the possible Kerr rotation. There is also excellent agreement between the simulation

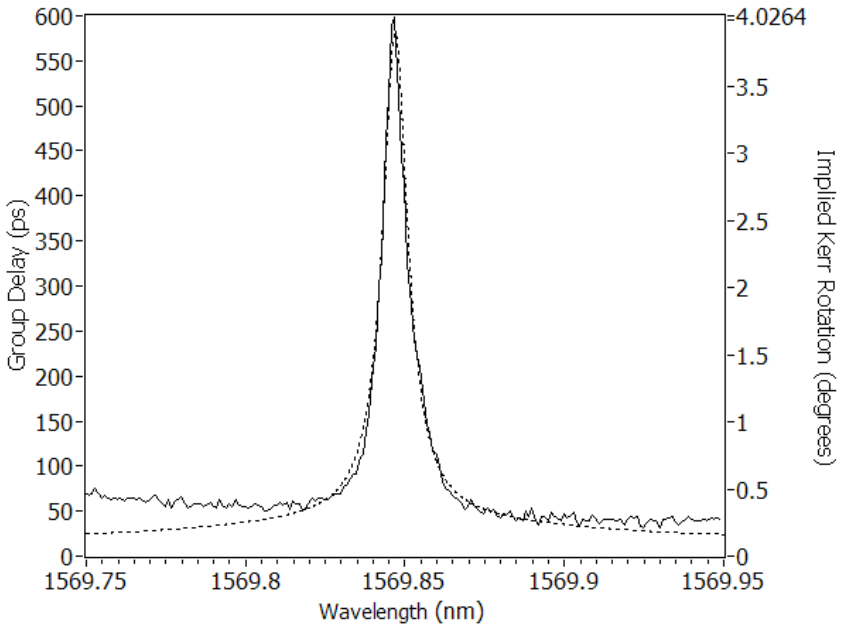

Figure 4.11: Simulated (dashed) and measured (solid) group delay for 2-shift grating of length 10 mm ($dn = 0.4 \times 10^{-3}$, structure 1750 / 9000 / 11000). Peak delay is approximately 600 ps. Implied Kerr rotation is calculated for a parallel field strength of 1 Tesla.

and measurement in both cases. Comparing Figures 4.10 and 4.11 with the corresponding 2-section and 3-section curves in Figure 4.8, it is clear that there is a general agreement between simulation and fabrication in terms of the relative improvement, indicating that the desired tailoring of dispersive and magneto-optical characteristics is achievable in practice by the proposed techniques.

To illustrate the high reflectivity retained with such structures, Figure 4.12 shows the recorded reflection spectra for both the single-shift and 2-shift structures after fabrication. It can be seen that a reflectivity of >70% was achieved, however it should be noted that this can be improved in future by extending the final substructure length during the design phase, which will act to improve reflectivity over the resonant regions.

The importance of birefringence-reduction within these structures was investigated by measuring the effect on the group delay spectrum of introducing circular and linear birefringence through applying twist and transverse strain. By mounting the fabricated 2-shift grating between rotatable clamps, it was confirmed that by increasing birefringence over the grating in either form it is possible to

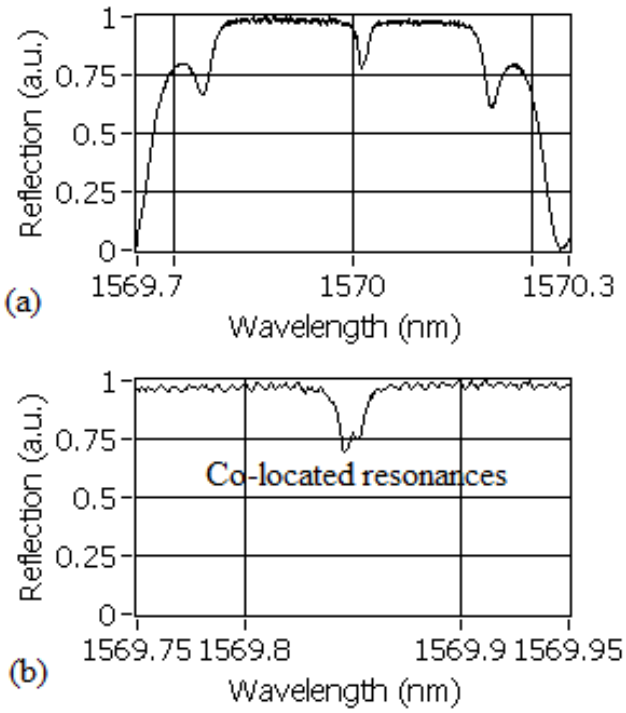

Figure 4.12: Reflection spectra of fabricated (a) 1-shift and (b) 2-shift slow-light gratings (Figures 4.10 and 4.11). Reflectivities at resonance wavelengths may be further improved by extending the final substructure length.

alter or remove the enhancement region by causing individual contributing peaks to separate. This separation will undermine the mechanism of Kerr rotation enhancement. An example of this effect is shown in Figure 4.13 where fibre twisting has been used to adjust the resonance superposition such that the single peak degenerates into multiple sharper peaks.

It is clear that the superposition of resonances in group delay or Kerr rotation may be undermined even by minor twists over the grating region. In practice therefore, the sensor must be packaged appropriately to reduce environmentally-induced twist or transverse strain. This can be achieved using commercial packaging techniques developed for DFB fibre lasers which are identically vulnerable to these effects. However, in contrast to existing fibre laser packaging techniques, the materials used for packaging these structures should be both diamagnetic and dielectric in order to avoid distortion or diversion of the incident magnetic field as a result of magnetisation or eddy current generation.

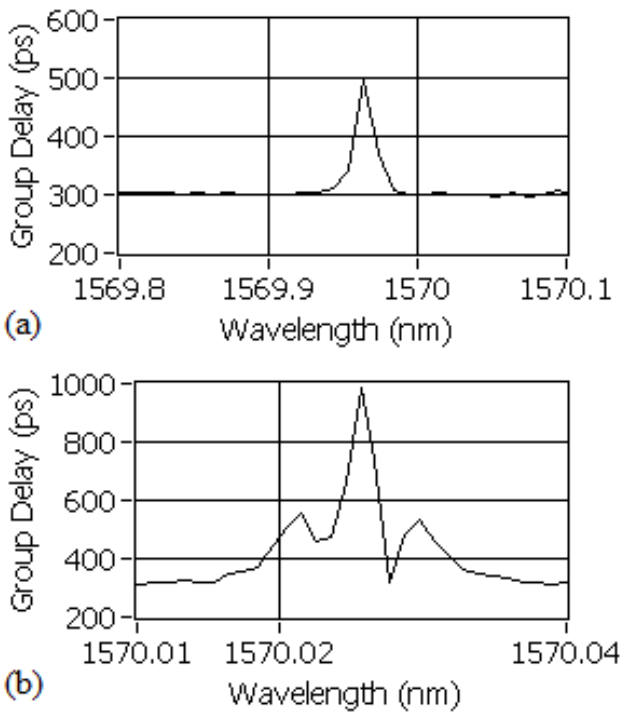

Figure 4.13: Demonstration of the effect of twist and transverse strained induced birefringence on the superposition of resonances. Nominal (pre-twist) (a) and twisted ($\sim 360°$) (b) are shown. The group delay peak can be either increased or removed entirely by fibre adjustment in this way, highlighting issues for sensor packaging.

4.6 Interrogation of Sensor Structures

In order to utilise the proposed compound phase-shifted Bragg structures as magnetic field strength sensors, a technique for measuring the Faraday rotation at the resonance superposition wavelength is required. This will nominally be a precise value of the Bragg wavelength if the design and fabrication procedures described above have been followed.

By utilising polarisation-maintaining (PM) addressing fibre prior to the sensor structures, the strong rotation at the resonance superposition may be harnessed by illuminating sensors with a single linear polarisation. In this case, the spectrum will, upon reflection from the Bragg structure, contain a strong peak in group delay and Kerr rotation. This will lead to a proportional re-distribution of optical intensity onto the orthogonal PM axis in the returning signal. Figure 4.14 illustrates this redistribution effect.

By then either re-polarising the reflection from the structure on the original polarisation axis or by interrogating only the orthogonally-polarised amplitude component, which is nominally zero at all wavelengths, a traditional polarimetric measurement of the magnetic field strength may be made. In this way, the peak reflected wavelength may be used to measure either temperature or strain in the standard fashion, while extra measurement capability is added in the form of spectral features (notch or peak) that appear during—and are proportional to—the level of magnetisation.

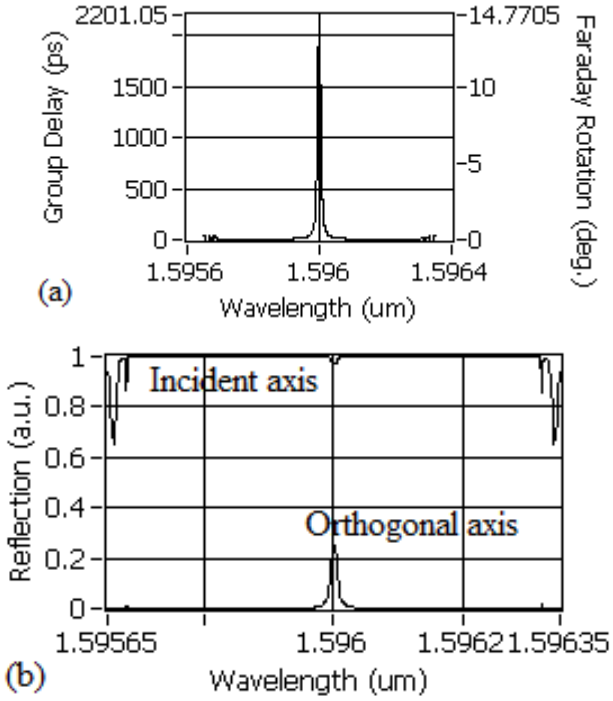

Figure 4.14: (a) Simulated group delay and Faraday rotation of light reflected from optimum sensor structure (substructure ratio 3/6.75/8/9/16, total length 23 mm) at a field strength of 1 Tesla. (b) Corresponding simulated reflection spectrum after re-polarising either on the input polarisation axis or on the orthogonal axis, demonstrating measurable spectral features relatable to field strength.

Due to its simplicity, the repolarisation/redistribution technique for utilising the sensor structures is an attractive interrogation approach. However, in this case the measurement of field strength has ultimately been reduced to an intensity-based measurement at the local interrogator. As discussed in the previous chapter, this yields a poor measurement resolution when compared with that achievable by interferometric techniques, such as the 3×3 interferometric

wavelength-detection scheme (see Section 3.4.1). If the sensor structures are to be fully exploited, it will thus be preferable to directly measure the phase difference between the circularly polarised modes rather than the resultant azimuthal rotation.

An optical fibre measurement system is illustrated in Figure 4.15 that uses the proposed compound phase-shifted structures as multiplexable transducers for bidirectional magnetic field strength based on direct detection of the phase difference accumulated between the orthogonal circularly polarised modes. By a method similar to that proposed for fibre coil-based current sensors[BGKB04], a reciprocal path may be constructed for two waves guided to the sensors, such that only the non-reciprocal differential phase introduced by the magnetic field is detected. Thus, the technique is immune to changes in linear birefringence or vibration along the addressing fibre, and also to any magnetisation in off-sensor regions.

For this application, the wavelength-detection technique described by Todd has been adapted to measure a phase difference directly, rather than the incident wavelength. Light from a broadband source, passed through a scanning Fabry-Pérot filter to control and limit the interrogating bandwidth, is guided via the 3×3 coupler to linear polarisers aligned to the PM slow axis. Alternatively, a tunable laser source may be used as the narrowband scanning source. A 90° splice between one polariser and the 1×2 coupler ensures that the linear polarisations are orthogonal during guidance to the sensor array. At the quarter-wave retarders, the waves are converted to orthogonal circular polarisations within the multi-shift grating. These orthogonal modes will experience a differential delay, which upon reflection will manifest as a differential phase at the point of interference.

For wavelengths outwith the bandwidth of the immediate sensor, the waves are converted back to orthogonal linear polarisations and guided to the next sensor region, thus allowing the serial WDM multiplexing of such transducers. These off-sensor wavelengths undergo only non-resonant levels of rotation over the grating length, which are negligible in comparison to resonant rotations—for example, a rotary power of $< 1^\circ$ per Tesla over a 30 mm grating region.

Within the appropriate sensor, a phase difference of twice the Kerr rotation angle is accumulated between the circularly polarised modes in the tailored fashion detailed in previous sections.

Upon reflection from the gratings, the handedness of the circular polarisations is interchanged, and they are converted by the quarter-wave retarders back to orthogonal linear polarisations. Compared to the forward-travelling linear waves, the polarisation alignment of these waves has been interchanged. Then, at the linear polarisers, waves which have travelled non-reciprocal paths are blocked, while waves that have travelled along reciprocal paths are transmitted and brought to interference within the fused 3×3 coupler. To allow continuous phase demodulation, all outputs of the 3×3 coupler should be continuously monitored by photodetectors while the scanning source is tuned over the bandwidth of the source.

The non-reciprocal phase difference (nominally zero) can then be demodulated using Todd's robust method that is immune to variations in signal amplitude[TSB02]. Simultaneous detection of the Bragg wavelength shift will be required due to the Verdet constant's variation with temperature and wavelength (see Section 3.2.3.1). This may be achieved by a number of well-documented methods, such as calibration of the SFP driving signal[FNM05].

As discussed, depending on the measurement application, a transducer structural design can be selected to maximise either the peak value (Figure 4.8) or uniformity (Figure 4.9) of the phase difference. An example sensor response expressed in terms of the measurable non-reciprocal differential phase, using the final structure from Figure 4.8, is simulated in Figure 4.16 for an SFP bandwidth of 10 pm. To facilitate this simulation, the Kerr rotation curve associated with the final structure in Figure 4.8 is converted into a phase differential between the two circularly polarised modes by scaling the azimuthal rotation by a factor of two. A linear relationship between the peak differential phase and magnetic field strength is observable, which is expected given the linear relationship between magnetic field strength, magnetic circular birefringence, and accumulated phase differences.

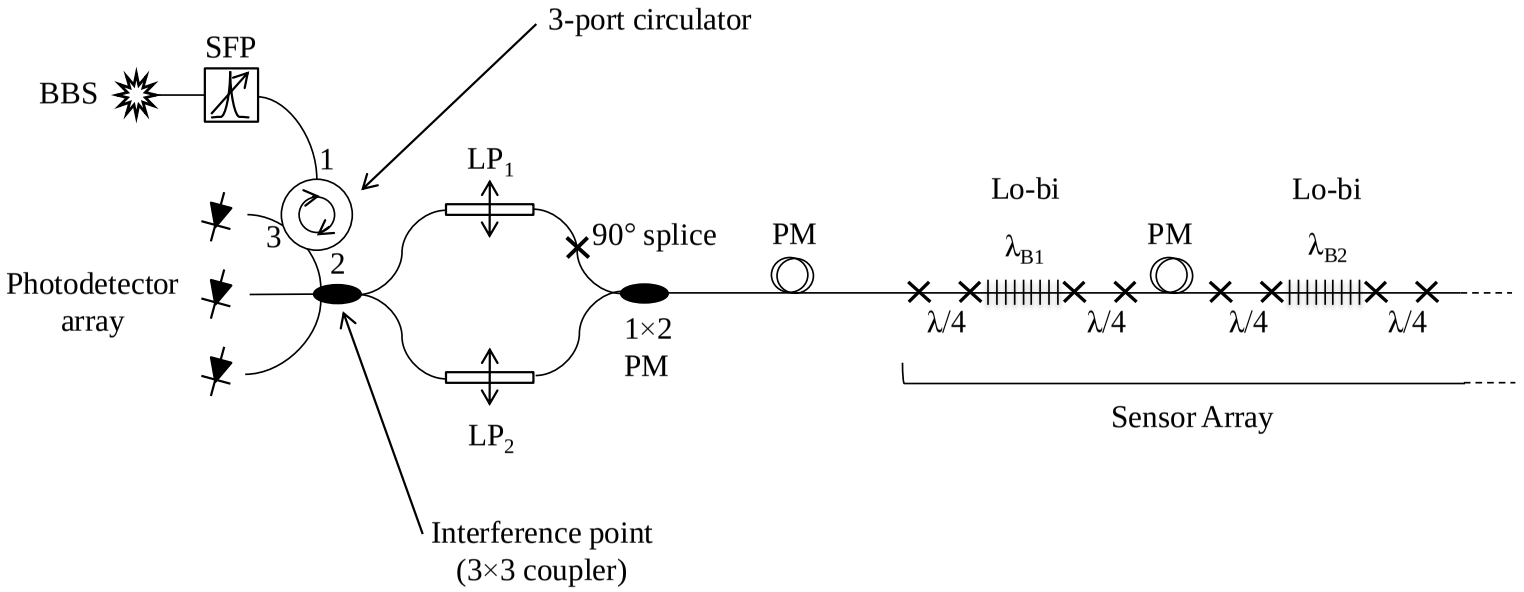

Figure 4.15: Fibre-optic magnetic field strength measurement system based on compound phase-shifted gratings as polarimetric point sensors. At the point of interference, the magnetic-field-induced phase difference between circularly-polarised modes is demodulated. BBS is Broadband Source, SFP is Scanning Fabry-Pérot Filter, LP is Linear Polariser, PM is Polarisation-Maintaining.

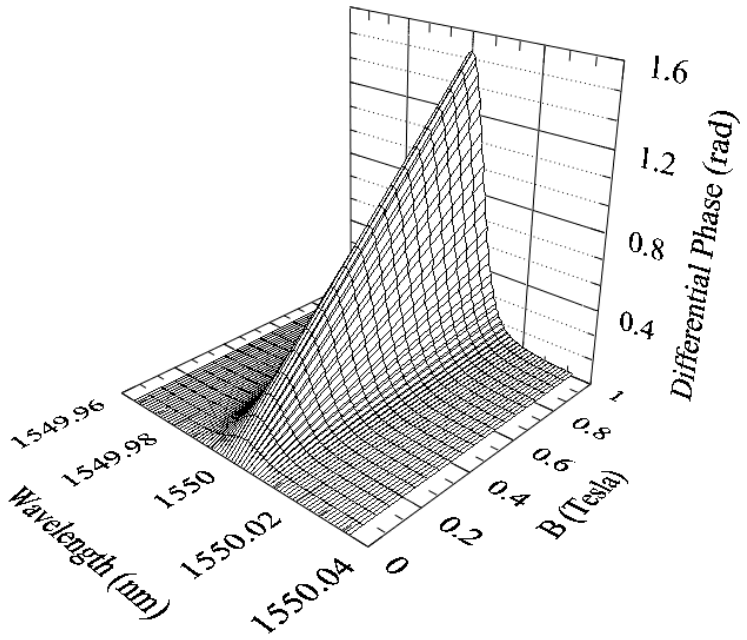

Figure 4.16: Sensor response illustrated by the scanned non-reciprocal differential phase increasing with applied magnetic field strength. Grating structure is 3000 / 7000 / 8750 / 10000 / 11000 / 20000 (total length 31.72 mm). Scanning filter bandwidth is 10 pm. ($dn = 10^{-3}$, $V = 0.57\ rad/(Tm)$)

The maximum measurable field strength for this system may be defined based on the coherence length of the incident light, which in this interrogation system is set by the bandwidth of the scanning filter. For an SFP bandwidth of 10 pm, the coherence length is approximately 72 mm, which allows for maximum measurable phase differences greater than could be produced by any practical magnetic field. It should be noted that in place of the broadband source and tunable filter, a tunable laser could be used for an increase in optical power and coherence length. In this case, the substantial losses induced by such a narrowband filter are removed and, excluding the impact of FBG reflectance, only coupler losses (totalling 12.5 dB for a single reciprocal path in Figure 4.15) will impact on the power reaching photodetectors. The minimum resolvable magnetic field is set by the resolution of the chosen phase demodulation technique, which is taken to be under 50 μrad/$\sqrt{Hz}$ based on the laboratory system constructed in Chapter 5. From the response simulated in Figure 4.16, a linear sensitivity ($\delta\phi/\delta B$) of 1.4 rad/T is apparent. The minimum detectable magnetic field strength may then

be estimated to be

$$B_{min} = \frac{\phi_{min}}{\delta\phi/\delta B} = \frac{50 \times 10^{-6}}{1.4} \approx 0.05 \quad \text{mT} \tag{4.1}$$

A magnetic field strength resolution of better than 0.05 mT/$\sqrt{Hz}$ can thus be estimated for this system, leading to a static resolution of 2.5 mT at a measurement rate of 2.5 kHz without further noise reduction in the interferometer.

4.7 Dispersion-Tailored FBGs as Tunable, Narrowband Delays

In addition to the immediate measurement application, the research presented in this chapter is also directly applicable to modern optical communications networks. Optical tunable and static delay lines—often referred to as "slow-light" devices when the group delay is large—are utilised in a number of communications applications, where a known delay is introduced to provide, for example, phase modulation, dispersion compensation, or improved physical interaction times[TBF97][OBS+05].

A tightly-narrowband miniaturised delay line based on resonant cavities, such as the type presented in the above sections, would be of benefit to potentially any communications application requiring wavelength-selective delay. In particular, the emphasis on wavelength division multiplexing (WDM) and dense WDM (DWDM) as a key element of future optical systems will pose new challenges in applications where dispersion management is critical[DE05]. As such, it is likely that variable delay and variable dispersion devices that are both spectrally and temporally selective will become necessary.

In the preceding sections, a simple general optimum structure for production of large, narrowband group delay over highly reflective spectral regions was illustrated, in addition to an associated automatable fabrication technique for the practical realization of these structures in standard photosensitive optical fibres. Such devices, while being eminently suitable to many sensors applications, may

also form the basis of compact all-fibre delay components possessing a large and narrowband delay, low insertion loss, and tunability in both peak delay and operating wavelength. Such compact devices could offer a highly-desirable solution to the problems of these future networks by offering a method for flexible control of the optical delay on a channel-by-channel basis.

It is clear from Figures 4.10 and 4.11 that the tailoring of dispersive characteristics required for this application is achievable in practice using the proposed technique, even where it is not possible to accurately predict the grating strength *dn* produced by a single inscription—a common difficulty with most grating fabrication techniques. After inscription, the resulting FBG-based delay line is truly narrowband since non-resonant light is immediately reflected back. The customised dispersion characteristics of the device are therefore suitable for use as a component of a DWDM wavelength-selective delay line.

To enable the tuning of the device, the wavelength of the resonant, delayed light may be adjusted by strain or heat applied over the full grating, which will act to wavelength-shift both the reflection and delay spectra over the entire Bragg region. More specific adjustments to the spectral shape and peak magnitude of the delay region can then be actuated through spot-heating or localised compression of the phase-shift regions which will reduce or strengthen the contribution of each resonance, allowing distortion, enhancement, and reshaping of the delay spectrum. Therefore, based on this laboratory demonstration of compound phase-shifted slow-light grating structures, a compact delay line that is continually tunable both in terms of operating wavelength and magnitude of delay may be developed using appropriate packaging that incorporates suitable thermal or strain actuation techniques.

4.8 Chapter Summary

In this chapter it has been shown that compound phase-shifted DFB structures can be tailored in order to enhance their dispersive and magneto-optical properties, which has implications over a wide range of optical measurement and

communications applications. It was demonstrated that the structures could, while retaining high reflectivities, overcome the trade-off between the Kerr rotation peak and bandwidth. This was achieved by inserting multiple phase shifts into the grating profile in order to tune the spectral location of group delay peaks.

Rules governing the structural dimensions of tailored fibre DFB structures were investigated and it was shown that a structure incorporating logarithmically-spaced π phase steps is optimal for combining peaks in the Kerr rotation and reflective group delay spectra. The magneto-optical reflection spectra from these structures can be widely tailored in peak rotation and bandwidth, and is robust to elongation as long as the ratio of substructure lengths is held constant.

A method for laboratory fabrication of these structures was described that uses group delay measurement to monitor the enhancement during writing. Using this method, exemplary fibre gratings were successfully written and characterised, and an excellent agreement with simulated group delay data was achieved for the single-shift and 2-shift structures. The expected vulnerability of the gratings to induced birefringence was confirmed experimentally, indicating the requirement for appropriate packaging after fabrication.

A novel system and procedure for the interferometric interrogation of these gratings as multiplexable point sensors for magnetic field strength was detailed. A resolution of better than 0.05 mT/$\sqrt{Hz}$ is expected for this system over a large and linear measurement range, matching the static resolution achieved by present inductive techniques deployed within the JET diagnostic system. The proposed system and transducers are completely diamagnetic, dielectric, passive, and magnetophotonic, and will be directly applicable to fusion diagnostics. Further work should be focussed on implementing the interrogation technique, and on fabricating structures with greater than three substructures. Additionally, research on packaging methods will be required to enable deployment of the sensors in adverse conditions, which will be further discussed in Chapter 7.

Finally, a novel device for enabling wavelength-selective tunable delay lines for use in DWDM communication networks was proposed based on the compound phase-shifted FBGs fabricated in this study. Such compact devices may, through

appropriate packaging, allow operators to adjust and even switch the optical delay applied to DWDM channels on an individual basis, which may become an invaluable ability in future communication networks or in TDM sensor interrogation schemes.

4.9 Associated Publications

1. P. Orr, P. Niewczas, M. Stevenson, and J. Canning. Compound Phase-Shifted Fiber Bragg Structures as Intrinsic Magnetic Field Sensors. *IEEE/OSA Journal of Lightwave Technology*, 28(18):2667–2673, September 2010. DOI: 10.1109/JLT.2010.2060314.

2. P. Orr, J. Canning, M. Stevenson, and P. Niewczas. Automatable Fabrication of Dispersion-Tailored Bragg Gratings for Tunable Narrowband Delays. *Electronics Letters*, 46(18):1283–1284, September 2010. DOI: 10.1049/EL.2010.2011.

3. P. Orr, J. Canning, M. Stevenson, and P. Niewczas. Controlled Fabrication of Tunable Delay Using Compound Phase Shifted Resonators. In *35th Australian Conference on Optical Fibre Technology*, Melbourne, Australia, December 2010.

4. P. Orr, M. Stevenson, J. Canning, and P. Niewczas. Magnetic Field Strength Measurement Using Tailored Dispersion Characteristics of Phase-Shifted Fibre Bragg Gratings. In *Fourth European Workshop on Optical Fibre Sensors*, Porto, Portugal, September 2010. DOI: 10.1117/12.865456.

5. P. Orr and P. Niewczas. Point Measurement of Magnetic Field Strength Using Compound Phase-Shifted FBGs. In *Joint Workshop on Frontier Photonics and Electronics 2010*, Sydney, Australia, March 2010.

6. P. Orr, P. Niewczas, J. R. McDonald, M. Walsh, and W. Morris. In-Fibre Point Sensing of Magnetic Field Strength Using Novel Photonic Sensor Con-

figuration. In *Fifth International Conference on Condition Monitoring and Machinery Failure Prevention Technologies*, pages 1119-1124, Edinburgh, UK, July 2008. Paper 181.

Chapter 5

Polarisation-Switched Interrogation of Magnetised Fibre Bragg Gratings

5.1 Chapter Overview

In this chapter, the design and implementation of an optical fibre system for the direct measurement of magnetic circular birefringence is described. In contrast to the previous chapter, which detailed a technique for making polarimetric measurements of magnetic field that are localised to the fibre grating, the system proposed in this chapter enables the absolute point measurement of the field strength through active control of the optical polarisation within a fibre Bragg grating.

The proposed technique utilises a polarisation switching subsystem which allows control software to continually switch the polarisation at the FBG between the two orthogonal circular states. This, in turn, allows for ratiometric processing of the equal and opposite sensitivities inherent to each circular polarisation. Common-mode signals such as temperature or strain may then be isolated and measured independently of magnetic field, minimising the impact of the large cross-sensitivity to temperature described in Section 3.3.2.6. In this way, a magnetophotonic measurement of the static or dynamic magnetic field is achieved

simultaneously with a temperature measurement.

A technique for adapting the polarisation switching interrogation system for measurement of bend and longitudinal strain by a related measurement principle is also demonstrated, which may have applications in monitoring of flexural changes in tokamak structural components during displacement events.

5.2 Introduction

In Chapter 3, it was established that if the differential refractive index that is induced between circularly-polarised modes in a magnetised medium can be determined, then the strength of the magnetic field may be derived straightforwardly. Three requirements for successful deployment of this measurement concept may be identified:

1. A technique for measuring fibre birefringence that has sufficient spatial resolution to better the measurement criteria in Chapter 2,

2. A method for either determining or controlling the state of polarisation within the sensor element,

3. A measurement procedure that is able to reduce the impact of the strong cross-sensitivity to temperature described in Section 3.3.2.6.

In Chapter 3, fibre Bragg gratings were shown to exhibit peak reflection at a wavelength proportional to the average refractive index along the grating. It follows that FBGs may be used to detect changes in the fibre refractive index—in fact, this is the mechanism by which FBGs commonly measure temperature.

In order to make the refractive index within the grating sensitive to magnetic field strength, light within the Bragg structure must be circularly polarised. Either of the orthogonal circular polarisations will sensitise the refractive index, and hence the peak reflected Bragg wavelength, to magnetic field strength; however, they will impart equal but opposite sensitivities to the magnetic field. As such, for one circular polarisation the Bragg wavelength will be shifted to a shorter

wavelength by the magnetic field, and for the orthogonal polarisation the Bragg wavelength will be lengthened.

Thus, the reflections experienced by orthogonal circularly-polarised modes propagating within a magnetised FBG will differ in wavelength, and this differential wavelength will be directly proportional to the parallel magnetisation. If the state of polarisation (SoP) within FBGs can be suitably controlled or determined in order to extract this differential wavelength, it may then be related to the field strength to enable an FBG-based spectrally-encoded magnetic field measurement.

Importantly, Bragg shifts that are due to strain or temperature fluctuations will affect both reflected wavelengths in an identical manner. This introduces the possibility of simultaneous, independent measurement of temperature that will not affect the use of the wavelength differential for magnetic field measurement. In fact, due to the temperature dependence of the Verdet constant, it will be beneficial for the overall system accuracy to simultaneously measure the temperature of the fibre at the grating location.

In this chapter, the measurement concept outlined above is implemented by an optical fibre system utilising high-speed polarisation control within low-birefringence FBGs. The technique enables high-resolution measurement of both magnetic field strength and temperature within an array of serially-multiplexed point sensors, while inherently suppressing drifts and cross-sensitivity to vibration. As with the polarimetric technique described in Chapter 4, the sensing mechanism is purely magneto-optical, allowing the transducers to retain their passive, inert, all-glass characteristics that will be required for operation in the fusion environment.

The principle of the magneto-optical measurement will firstly be described in Section 5.3, and thereafter the the system design and operational procedure will be detailed (Section 5.4). Following this, Section 5.5 discusses the practical construction of the scheme. Its laboratory characterisation is reported in Section 5.6, which includes determination of the current noise floor, resolution, linearity of response, and robustness to drift. The scheme's capability for inde-

pendent, simultaneous measurement of both magnetic field and temperature is also demonstrated. Finally, an alternative implementation of the scheme that enables bend and strain measurement is described in Section 5.7.

5.3 Switching Sensor Principle

A magnetic field incident on an optical fibre will induce a circular birefringence for the optical component travelling in parallel with the field lines. From Chapter 3, the magnitude of this magnetic circular birefringence may be expressed as

$$\Delta n = \frac{VB\lambda}{\pi} \tag{5.1}$$

where Δn is the difference in refractive indices experienced by right and left circular polarisations, B is magnetic field strength (μ_0H) in Tesla, λ is the optical wavelength in metres, and V is the Verdet constant with units rad/(Tm). The value of the Verdet constant in conventional diamagnetic optical fibre is approximately 0.57 rad/(Tm) at 1550 nm, which was established in Chapter 3 to be the most appropriate operational wavelength for this nuclear application. In addition, it was established previously that the transducer embodiment should utilise pristine diamagnetic fibre to enable the system to take advantage of elevated temperatures, and to avoid a strong adverse temperature sensitivity. In this case, the weak temperature proportionality of the Verdet constant in diamagnetic fibre will be approximately 4×10^{-5} °C^{-1}[WRD^{+}91].

Peak optical reflection from FBGs is experienced where the wavelength is equal to twice the grating period, i.e. at $\lambda/n = 2\wedge$ where $\wedge$ is the grating pitch in metres. A change in refractive index caused by magnetically-induced circular birefringence will cause this peak reflected wavelength to shift proportionally with magnetic field if the incident light is circularly polarised. If light within the grating is unpolarised or linearly-polarised, then both right and left circular polarisations are contained and a splitting of the peak Bragg reflection will occur, which can be expressed, using Equation 5.1, as

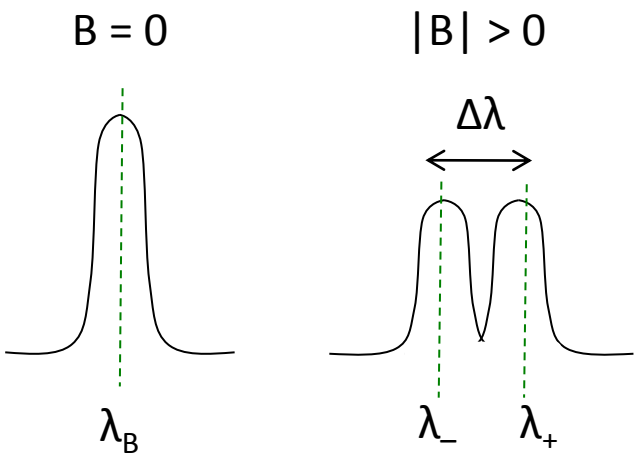

Figure 5.1: An illustration of the degeneration of the FBG reflection spectrum during magnetisation. The effect is greatly exaggerated. Minor peaks under magnetisation correspond to the power distributed in the orthogonal circular polarisations, with peak wavelengths λ_- and λ_+.

$$\Delta\lambda_B = \frac{2 \wedge V\lambda_B}{\pi} B. \tag{5.2}$$

This splitting of the FBG reflection peak has very low sensitivity to magnetic field in diamagnetic fibre gratings—separating by only 0.3 pm/T at a Bragg wavelength of 1550 nm. This degeneration effect is illustrated in Figure 5.1, where the strength of the effect has been greatly exaggerated for clarity. In practice, the separation will only be noticeable (by using state-of-the-art commercial interrogators) above field strengths of approximately 3 Tesla, prior to which the FBG reflection spectrum will broaden but not degenerate into separate peaks. For this reason, interrogation for the differential wavelength by directly comparing the location of separating Bragg peaks will not be feasible. Interrogation for magnetic field strength must therefore rely on changing the state of optical polarisation at the FBG between right and left circular in order to imprint the field strength information onto a wavelength or phase carrier, which can then be demodulated at the interrogator. It is this approach that is developed in this chapter, since it allows for a self-referenced measurement of magnetic field strength with the capability for static field measurement and an improvement in the signal-to-noise, stability, and robustness of dynamic field measurement.

The reflection guided from each magnetised FBG will carry information on the magnetic field strength, temperature, and strain at the grating location. Through modulation of the polarisation state, the measurement will contain a signal at the modulation frequency with amplitude proportional to the magnetic field strength. The quasi-static component of the phase signal at the interferometer is freed up, and can be used to measure either temperature or strain in the well-documented fashion[Rao97]. In the proposed system, the strain response is mechanically dampened such that the quasi-static component of the measurement signal may be related to the temperature in the transducer. This is useful not only to provide additional functionality to the magnetic sensor, but also for making a more accurate estimation of the magneto-optical sensitivity V before the field strength is calculated.

By guiding the reflected wavelengths to an interferometer, the switching wavelength is converted to a switching phase that may be demodulated by the technique described in Section 3.4.1. The method for polarisation switching proposed in the next section produces for each sensor a continually switching phase signal at the interferometer that alternates between equal and opposite sensitivities to magnetic field within the transducer. After photodetection and phase demodulation, the interleaved signals corresponding to the opposing magneto-optical sensitivities may be separated and processed to produce two measurement signals: the mean phase and the differential phase.

This dual measurement principle is illustrated by Figure 5.2. In the differential phase signal, common-mode noise that is primarily due to vibration and temperature drifts in the transducer or the interrogation system components is strongly suppressed. Simultaneously, the mean phase is sensitive only to common-mode signals. Thus, the differential phase may be used to extract magnetic field strength information, while the mean phase of the interleaved signals can be utilised to determine the temperature at the sensor.

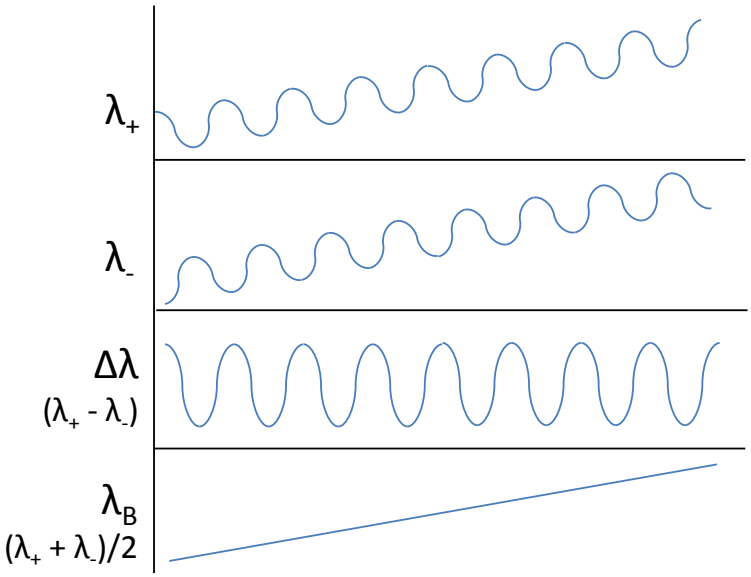

Figure 5.2: The dual measurement principle for magnetic field strength and temperature. In this illustration, the peak Bragg reflections λ_+ and λ_- corresponding to orthogonal circularly-polarised modes are modulated by an ac magnetic field. Their differential $\Delta\lambda$ and mean λ_B are then sensitive only to magnetic field strength and temperature (or strain) respectively, allowing both to be extracted separately.

5.4 System Design

Figure 5.3 illustrates the full system used to implement switched-polarisation measurement of magnetic field. As in standard FBG WDM multiplexing architectures, each grating reflects within the range of the broadband source, which for this application should be centred in the telecommunications band. Alternatively, if hydrogen is not present in the fibres, the system may be designed for operation at lower wavelengths for a corresponding increase in the magneto-optical sensitivity V[REW97]; however, due to the radiation-induced attenuation the operating wavelength should not be reduced below around 1300 nm. Each grating used for the study is fabricated in such a way that the UV-induced linear birefringence is negligible, as will be discussed further in Section 5.5.

An athermal reference grating written in standard single-mode fibre may be installed within the interrogator to allow temperature measurements to be referenced to a stable wavelength. This component does not affect, and is not required for, the drift-insensitive measurement of magnetic field—except for correct esti-

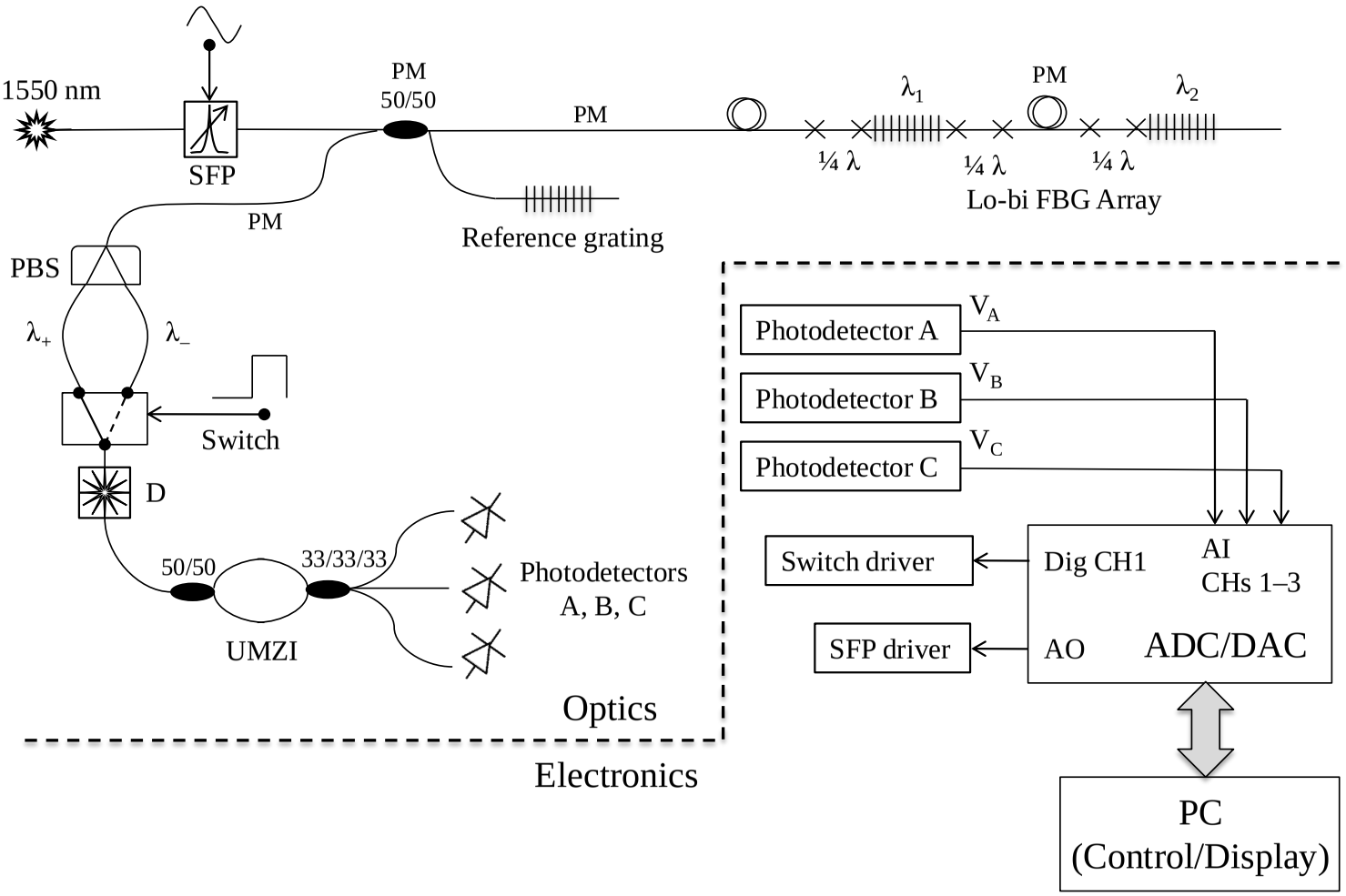

Figure 5.3: All-fibre system for measurement of magnetic field strength and temperature in an array of low-birefringence FBGs. Only two multiplexed gratings are depicted here. PBS is polarisation beam-splitter, SFP is scanning Fabry-Pérot filter, D is fibre depolariser, and UMZI is unbalanced Mach-Zehnder interferometer.

mation of the Verdet constant value.

The core interrogation device is a Mach-Zehnder interferometer (MZI in Figure 5.3), which is an all-fibre construction made from 2×2 and 3×3 couplers as described in Chapter 3. As established, by using this approach it is possible to passively and immediately determine the absolute phase difference at the point of interference, which changes with input wavelength and optical path difference, by photodetecting all three outputs and applying the formula

$$\tan\phi = \frac{(\mu_2 - \mu_3)\bar{V}_1 + (\mu_3 - \mu_1)\bar{V}_2 + (\mu_1 - \mu_2)\bar{V}_3}{(\gamma_2 - \gamma_3)\bar{V}_1 + (\gamma_3 - \gamma_1)\bar{V}_2 + (\gamma_1 - \gamma_2)\bar{V}_3} \tag{5.3}$$

where μ and γ are normalising parameters containing mean intensity level, fringe visibility, photodetector responsivity, and the properties of both couplers used to form the interferometer, and V_1, V_2 and V_3 are the outputs of photodetectors A, B and C from Figure 5.3. Peak hold circuitry may then be used in conjunction with a scanning Fabry-Pérot filter in order to extract the V_{1-3} corresponding to each FBG prior to deployment of Equation 5.3.

5.4.1 Circular Polarisation Switching Technique

Key to the operation of the magnetic field sensor system in Figure 5.3 is the method for switching the optical polarisation at all gratings between left and right circular. Although circular polarisation maintaining fibres have experienced initial development (by incorporation of a high twist-induced circular birefringence), they are costly to fabricate and will require further development before they will be suitable for this application. In particular, it is not yet clear whether circular PM fibres will be capable of maintaining the input polarisation as well as conventional linear PM fibre over long distances. Therefore, in order to reliably maintain circular polarisations within the transducers, the proposed system guides orthogonal linear polarisations using conventional PM fibre (incorporating high linear birefringence), and thereafter converts these to orthogonal circular modes within the transducer package.

To provide a polarisation-switching mechanism, it is possible to utilise the

source-side combination of a fast optical path switch and polarisation beam-splitter (PBS in Figure 5.3). The fibre polarisation splitter acts to passively separate signals on the slow and fast axes of a polarisation-maintaining input fibre onto separate output fibres, and this functionality may be combined with an optical path switch to create a polarisation switch. Then, path selection by the switch determines which input linear polarisation (slow or fast axis) is guided to the output fibre.

By placing the path switch immediately after the polarisation splitter, the switch can be driven at f_{switch} in order to select which axis is being guided to the interferometer platform. By utilising hi-bi PM fibre over the complete path from the first 2×2 coupler to the transducers, and from this coupler to the polarisation splitter, this axial selection can thus be used to determine whether light on the slow or fast axis is addressing the transducers.

It is thereafter required to convert this switching between orthogonal linear modes at the transducers into a switching between orthogonal circular modes, such that the sensitivity to magnetic field may be modulated. Placement of fibre quarter-wave retarders—aligned at 45° to the principle PM axes—immediately before and after the lo-bi gratings will introduce a $\pi/2$ phase-shift between orthogonal linear polarisations. This linear phase shift will act to convert light that is linearly polarised on the PM axes into orthogonal circular polarisations. In this way, the switch is able to choose which circular polarisation is incident on all gratings, and therefore the state of polarisation of light undergoing Bragg reflection. This results in the capability to detect FBG reflections from incident light that is both left and right circularly polarised in turn, allowing both signals to be processed separately at the interrogation system. In this application, this functionality will be used to suppress noise and drift at frequencies lower than the switching rate through cancellation of signals common to both polarisations.

The polarisation states produced within the sensor array and back are illustrated in Figure 5.4 for the case of two serially-multiplexed sensors. The polarisation-conversion procedure illustrated by this figure may be summarised as follows:

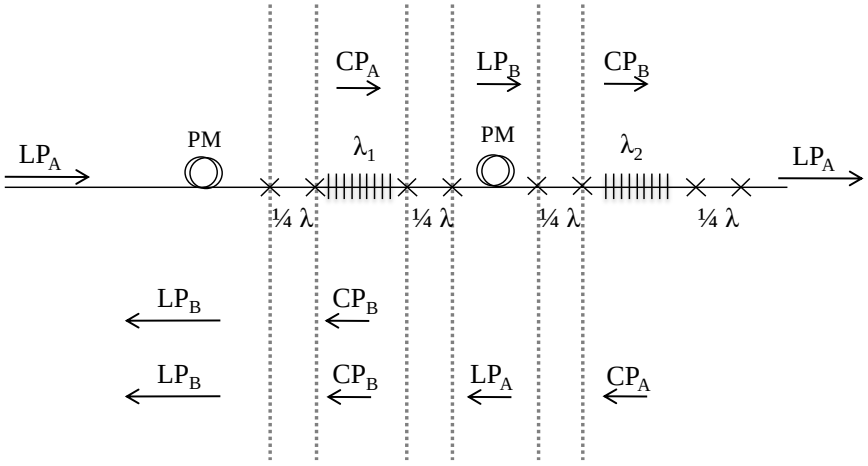

Figure 5.4: Depiction of the state of polarisation at points within the sensor array. Fibre quarter-wave retarders aligned at 45° to the PM fibre principle axes are indicated by $\frac{1}{4}\lambda$. LP_A and LP_B are orthogonal linear polarisations, while CP_A and CP_B are orthogonal circular polarisations.

- Each quarter-wave retarder transforms a linearly polarisation to a circular polarisation;
- The handedness of each circular polarisation is changed only upon reflection from an FBG;
- Where the wavelength is not reflected by an FBG, the individual circular polarisations are re-converted to linear polarisations by the exit quarter-wave retarder and are unable to affect measurements;
- The accumulated phase-shifts for the round trip journey to each sensor always yield a linearly-polarised output signal aligned orthogonally to the input signal.

It may be seen from Figure 5.4 that this procedure can be extended to any number of such sensors in series, enabling the switching interrogator to process all peak wavelengths together even for large arrays of sensors.

5.4.2 Measurement Procedure

In order for the system to incorporate multiplexing, the scanning filter (SFP, Figure 5.3) should be driven by a sinusoidal or triangular voltage waveform with

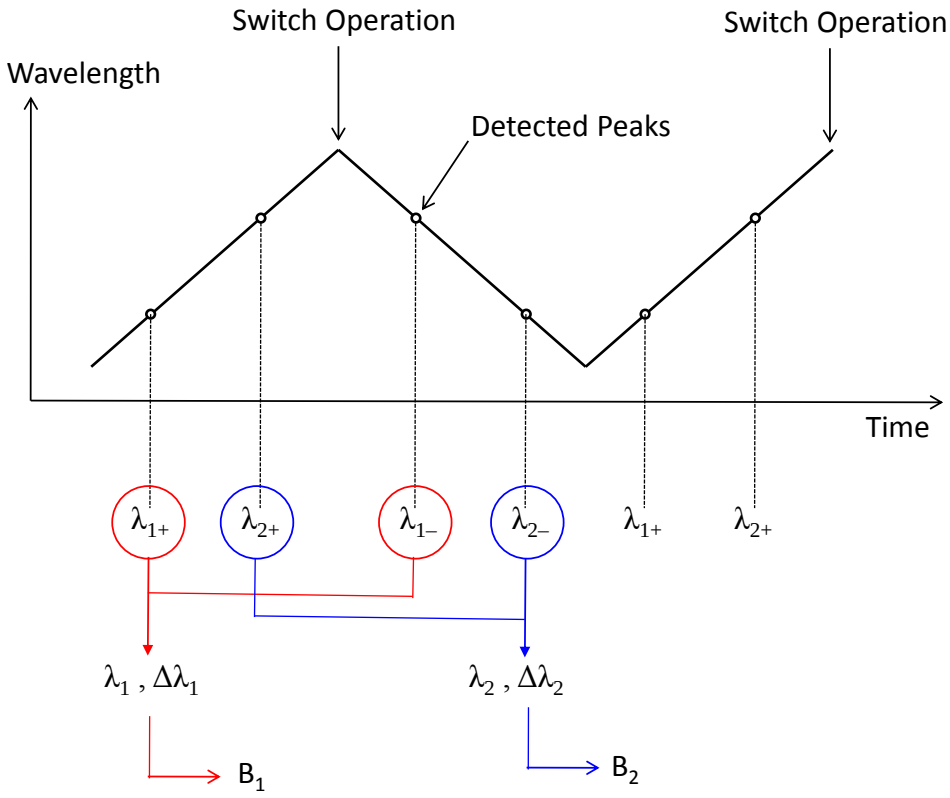

Figure 5.5: Synchronisation of wavelength scanning, polarisation switch operation, and sample acquisition in switched magnetic field measurement system. Two multiplexed sensors are depicted, with Bragg wavelengths λ_1 and λ_2. The subscripts + and - denote right and left handed circular polarisations.

frequency f_{switch}. Synchronously, the optical path switch may be driven using a digital signal of identical frequency. In this way, during the up-scan of the SFP, the switch guides one PM axis to the interrogator, and during the down-scan of the SFP the switch guides the orthogonal axis. This synchronisation of scanning, switching, and sampling, is illustrated in Figure 5.5. Commercially-available optical switches presently have response times in the nanosecond range and repetition rates over 100 kHz, making this synchronization of switch and filter viable for kHz acquisition rates[Agi11][Pho11]. However, for the laboratory demonstration of this system an Agiltron CrystaLatch 5 kHz 1×4 optical path switch was used.

For each grating encountered by the scanning filter passband, the peak voltages V_{1-3} at the photodetector outputs are recorded and used by the demodulation algorithm to determine the phase difference at the interferometer. This may

then be related to the Bragg wavelength. Prior to calculation of the magnetic field strength, one of these phase values (either from the up-scan, the down-scan, or their mean, given as

$$\phi_{avg} = \frac{\phi_+ + \phi_-}{2}, \tag{5.4}$$

may be used to extract the common-mode signal which comprises temperature-induced Bragg shifts. Hence, the Verdet constant at the sensor may be derived on the basis of its known variation with fibre temperature.

Following the derivation of V, the difference in phase between consecutive scans (up and down),

$$\Delta\phi = \phi_+ - \phi_-, \tag{5.5}$$

can be found in order to produce the difference term which is sensitive only to magnetic field strength. With V derived and $\Delta\phi$ known, the field strength can be calculated using the expression

$$\Delta B = \frac{n_{eff}}{2(nd)V}\Delta\phi \tag{5.6}$$

which is obtained by differentiating the phase-wavelength relationship ($\phi = 2\pi nd/\lambda$) in the interferometer with respect to λ, substituting Equation 5.2 for $\Delta\lambda$, and finally by considering that $2\wedge = \lambda_B/n_{eff}$, where n_{eff} is the mean refractive index over the grating profile and nd is the optical path difference (OPD) in the interferometer.

5.4.3 Phase Demodulation Simulation

Since V and n_{eff} cannot be adjusted except through using non-standard or doped fibres, an increase in measurement sensitivity may only be achieved by increasing the optical path difference nd in the interferometer. Clearly, for this application, it would be beneficial to maximise the OPD in order to increase sensitivity, especially since the proposed switching method is immune to error incurred from

drifts in the interferometer paths (since such drifts are common to both polarisation modes). However, the OPD has a practical maximum that is dictated not only by FBG coherence length, but also by demodulation errors introduced by electronic noise and nonlinear distortion that are inherent to the preferred interrogation technique. In this section it will be shown that these errors increase proportionally, but non-linearly, with the OPD, and thus an optimum OPD to maximise the signal-to-noise ratio of the measurement can be identified.

Aside from acoustic noise directly affecting the MZI via vibrational changes of the path lengths, which is the principle source of noise in this system, there will be a contribution from electronic noise in photodetector output voltages. Unlike acoustic noise, the impact of this electronic noise on phase demodulation will scale nonlinearly with the value of OPD.

With reference to Figure 5.6, the origin of this noise source may be described as follows. Peak voltage noise levels in the photodetector outputs V_i are dependent on the optical source power level and the range of optical power variance at the photodetectors between fringe minima to maxima. Minimum V_i levels for this scheme are determined by how deeply the MZI can modulate the FBG reflection, which becomes limited when the fringe spacing is less than the FBG bandwidth. Increasing nd will therefore reduce the output voltage range, increasing the susceptibility to electronic noise. This is a source of error that has not been considered in publications by Todd *et al*, but that has the potential to undermine the system performance entirely in applications such as this one, for which the sensitivity should be maximised.

Since both sensitivity and error will scale proportionally with OPD, but non-linearly in the latter case, an optimum path difference may be determined where the ratio of sensitivity to error (effectively the signal to noise ratio) is maximised. In order to determine the impact of photodetector voltage noise on the phase demodulation algorithm for a range of practical OPD values, the movement of FBG peaks across the MZI fringes was simulated. For each incremental movement, the phase was calculated using Equation 5.3. Then, a small, constant perturbation was added to the voltages V_{1-3} to simulate additive voltage noise,

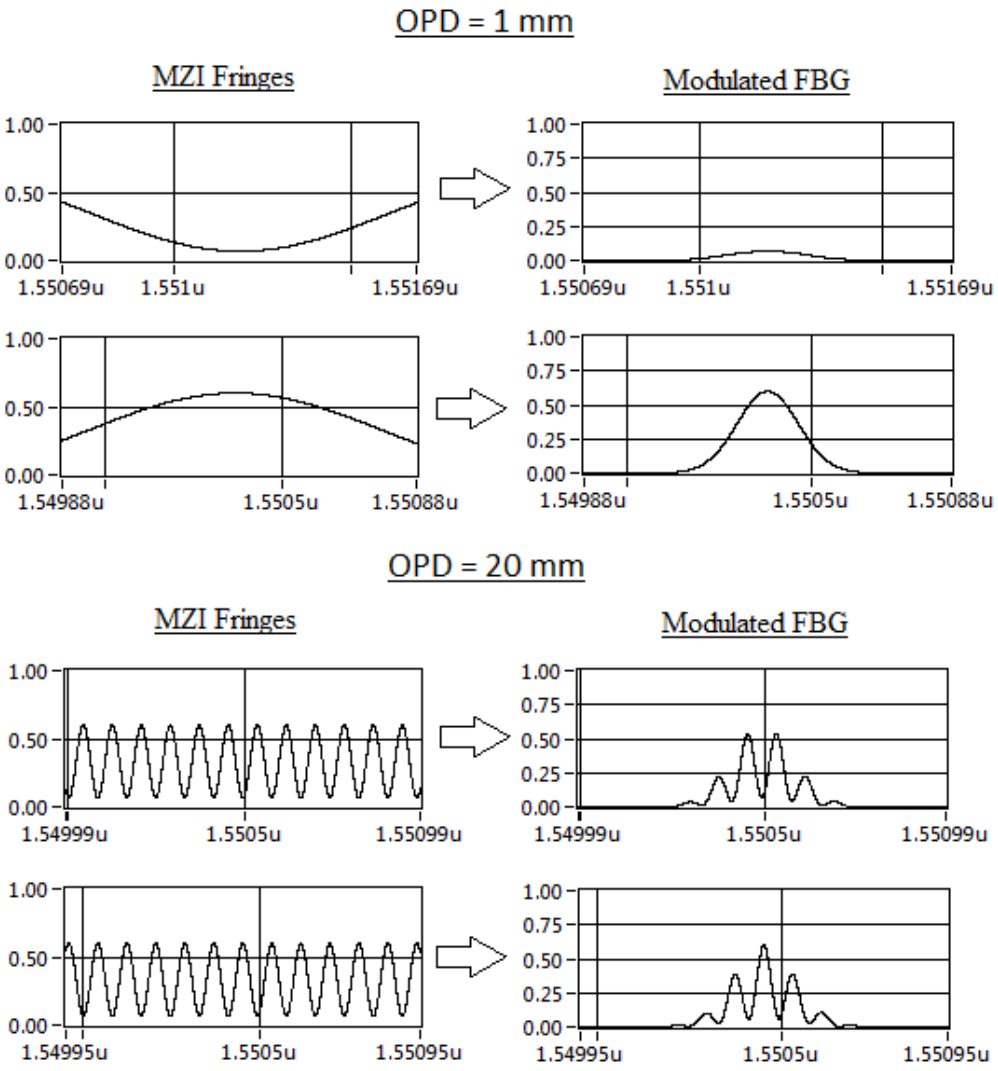

Figure 5.6: Simulation of the reduction in FBG spectrum modulation depth as MZI optical path difference is increased. OPDs of 1 mm and 20 mm are illustrated here. Both the minimum and maximum FBG modulation allowed in both cases is shown. It is clear that as OPD is increased, the ability of the MZI to modulate the FBG *peak* reflection becomes limited.

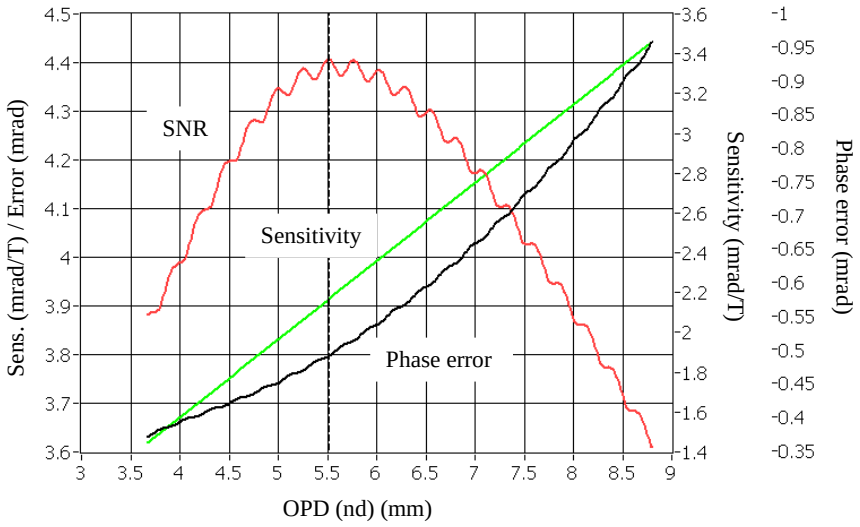

Figure 5.7: Sensitivity, phase error, and their ratio over a practical OPD range for a constant voltage noise level. Optimum performance is found at OPD = 5.5 mm, where the SNR is maximised.

and the phase was recalculated. A comparison of the demodulated phases with and without voltage error allowed for the percentage error in phase demodulation to be determined for a wide range of optical path differences.

In the simulation, a fringe modulation depth of 80%, an FBG FWHM of 0.4 nm, and an SFP bandwidth of 30 pm were assumed. With reference to Figure 5.7, it can be seen that although measurement sensitivity increases linearly in proportion to the increasing path difference (as would be expected), there is also a nonlinear increase in the error in demodulated phase due to the increased susceptibility to voltage noise.

Therefore, in order to optimise the performance of the measurement system, the optimum OPD may be defined as that which yields a maximum measurement signal-to-noise ratio. In this case, with reference to Figure 5.7, the ideal value for nd is 5.5 mm. This is therefore the path difference that should be incorporated into the all-fibre MZI during interferometer fabrication. It should be noted that optimum path difference due to this source of error is independent of the peak voltage noise level in V_{1-3}—i.e. although the optimum SNR will decrease with increasing noise levels, it will remain the optimum while noise is increased. As such the optimal path difference determined here will remain the optimum choice

even with changeable noise levels.

5.5 Construction

5.5.1 Low-Birefringence Grating Fabrication

A key requirement of this system is the elimination of linear birefringence within the gratings, due to the magneto-optical sensitivity's dependence on specific states of polarisation. To fabricate the lo-bi FBGs used in this work, fibre gratings were inscribed in standard H_2-loaded boron co-doped germanosilicate (B/GeO_2) fibre by a frequency-doubled 244 nm Argon-ion laser using direct writing through a phase mask. As before, CW 244 nm was chosen since it does not contribute significantly to linear birefringence[CDSK05].

All gratings fabricated for this system were written with a laser output power of 35 mW at a speed of 1 mm/min, and the peak reflected wavelength of all FBGs was approximately 1560 nm. In order to verify the very low level of birefringence in these structures, gratings incorporating a single central $\pi/2$ phase-shift in the index modulation profile to produce a sharp transmissive resonance were fabricated. After annealing all gratings for 10 minutes at 300 °C to accelerate hydrogen out-diffusion and promote relaxation of internal stresses, spectral analysis of the phase-shifted gratings indicated no observable splitting of the phase-shift's sharply transmissive feature at a measurement resolution of 1 pm. By implication, using the relationship

$$\frac{\Delta n_{LB}}{n_0} \approx \frac{\Delta \lambda}{\lambda_0} \tag{5.7}$$

where $\Delta\lambda$ is the spectral separation of the resonance wavelength, and n_0 and λ_0 are the nominal grating mean index and resonance wavelength respectively, it was established that the linear birefringence Δn_{LB} within the gratings used in this study was less than 10^{-6}—the same order of magnitude as with un-written fibre.

5.5.2 Mach-Zehnder Interferometer Fabrication

The interferometer fabricated for this work was an all-fibre construction, created between the output pigtails of 2×2 and 3×3 couplers by fusion splicing. The overall lengths of the interferometer arms were approximately 20 cm to allow for splicing. An optical path difference of 5.5 mm was introduced between these arm lengths, in order to implement the optimum sensitivity determined in Section 5.4.3.

During fabrication of the interferometer, the exact OPD was measured by viewing the interference fringes on a spectrum analyser in order to determine the spacing between adjacent fringe maxima. The true OPD can then be calculated by noting that to move from one fringe maxima to the adjacent fringe maxima, a change of 2π rad is required in the phase at the point of interference. Then, the OPD can be found from

$$\text{OPD} = nd = \frac{\lambda_{avg}^2}{\Delta\lambda} \tag{5.8}$$

where $\Delta\lambda$ is the separation between a pair of adjacent fringe maxima, λ_{avg} is the mean wavelength between the two fringe maxima, and n is the refractive index of the fibre core. To view the interference fringes for the purpose of verifying the OPD, the source was coupled directly through the MZI to the optical spectrum analyser. For determining the OPD, the input and output ports of the MZI (couplers) were used. To avoid changes in the modulation depth, the source light was depolarised prior to entering the interferometer.

In future implementations, the interferometer may be fabricated on an integrated optical chip in order to facilitate better vibration isolation and temperature control. In the present implementation described in this chapter, this component makes the largest contribution to noise in the phase demodulation scheme since it is particularly sensitive to acoustic noise.

5.5.3 Phase Demodulation Calibration

For this study, a partially-automated calibration procedure was developed in order to extract information regarding the fringe maxima and minima and coupler parameters that are required for effective deployment of the phase demodulation algorithm. The procedure for calibration, from a user's perspective, can be described as follows with reference to Figure 5.8:

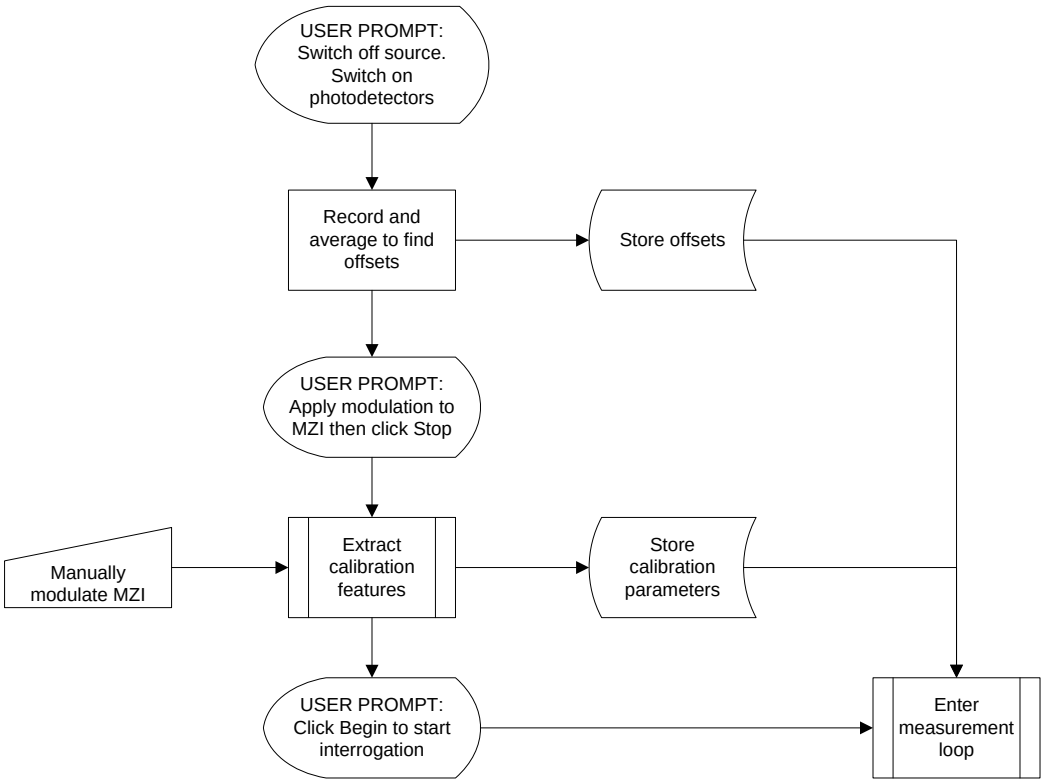

Figure 5.8: User interface procedure for partially-automated calibration of the optoelectronic magnetic sensor interrogation scheme

1. User is prompted to turn photodetectors *on*, while keeping the optical source *off*. System records two seconds worth of samples from the photodetectors and averages these data sets to determine photodetector offsets. These offsets are stored and subtracted from all future measurements.

2. User is prompted to switch the optical source *on* and manually modulate the MZI phase. System continuously samples on all three channels, displaying a 2 second visual history of each. When the user is satisfied that the strain

modulation has produced at least 2π rad modulation in the interferometer, as evidenced by at least one maxima and minima in the channel histories, the user selects the control *Stop* to calibrate.

3. System stops acquiring and uses features extracted from the history data to determine the algorithm parameters (A_n, B_n, θ_n—see Section 3.4.1).

Although the MZI modulation and source delivery are steps that the user must perform manually in the present embodiment of this scheme, the above procedure can be automated using a second optical switch and either a scanning filter or a piezoelectric actuator to provide wavelength scanning. This would remove the requirement for direct path length modulation, since the phase modulation required for calibration would instead be provided by the wavelength shift in the interferometer.

5.5.4 Tuning Method for Fibre Retarder

In this work, a variable waveplate was used to provide the quarter-wave phase shift, however it is considered that in future embodiments a permanent fibre waveplate may be fabricated using techniques established in the field of optical current sensing. As described by Bohnert *et al*, a section of birefringent optical fibre of known beat length may be used to fabricate a temperature-insensitive all-fibre quarter-wave retarder for the conversion of a linear polarisation to a circular one[BGKB04]. The length of this section of fibre may be very short ($\sim$1 mm), as illustrated in Figure 5.9. Elliptical-core fibre retarders are an excellent choice for this particular application since the change in their retardation with temperature is relatively small. The retardation of a phase retarder made from such a fibre was found by Bonhert *et al* to decrease essentially linearly at a rate of -0.35 mrad/°C at a wavelength of 816 nm, while the temperature dependence of fibres with stress-induced birefringence has been shown to be larger by around an order of magnitude[ZL93].

In the laboratory implementation, the fibre waveplate was kept at room temperature. However, the phase error resulting from this mild temperature depen-

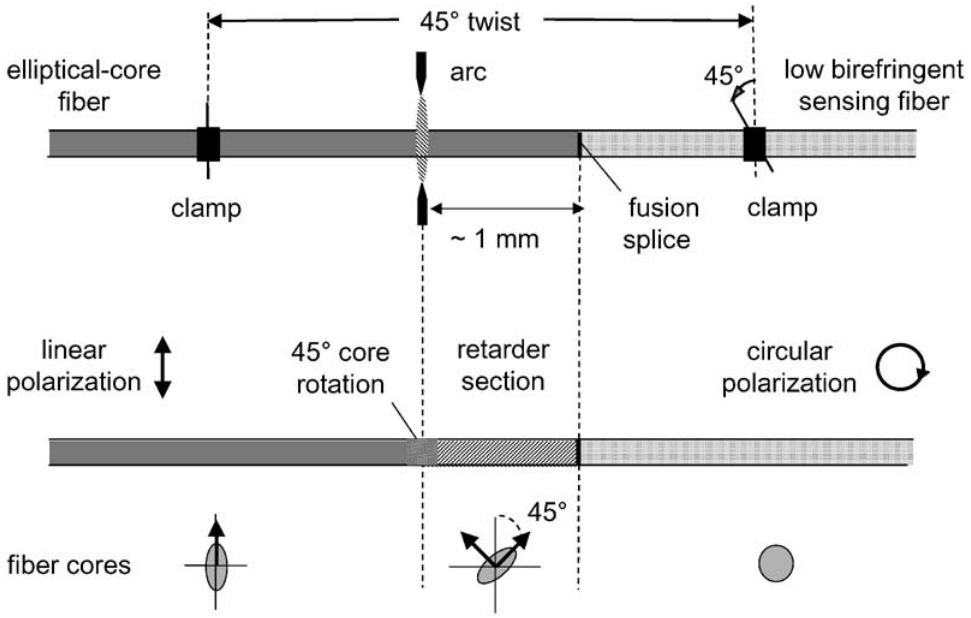

Figure 5.9: Fabrication of a fibre quarter-wave phase retarder using elliptical core birefringent fibre. By applying the required 45° twist between clamps, a fusion splicer may successively heat and relax a location 1 mm from the splice to tune the retardance.[BGKB04]

dence will lead to a maximum error of -0.1 rad in phase over a full-scale tokamak temperature flux of 300 °C, which would cause the orthogonal polarisations in the FBG to diverge slightly from purely circular states. The orthogonal elliptical polarisations that will result from this effect will possess slightly reduced sensitivities to the magnetic field, since a component of the light is now linearly-polarised. In a practical system, this may be compensated for at the design stage in two ways: By fabricating the retarder to provide a precise $\pi/2$ phase retardation at the most likely operating temperature; or by adjusting the initial room temperature retardance such that the change in sensitivity due to SoP error is exactly offset by the mild positive temperature dependence of the Verdet constant.

When fabricating the retarder or making adjustments to a variable waveplate, a circular SoP at the point of reflection (within the grating itself) must be verified. With reference to Section 5.4.1, this was achieved by linearly polarising the broadband source, and then monitoring the reflected power returning using the polarisation switching scheme. In this work, this was achieved by configuring monitoring software to switch between orthogonally-polarised reflections and ex-

tract only the intensity from each. Then, if the source is polarised on the PM slow axis, for example, the retarder should be tuned to maximise power returning on the orthogonal axis. As illustrated by Figure 5.4, a slow axis LP input returning on the fast axis implies that the SoP at the point of reflection must be circular, since it is precisely at the mid-point of this half-wave conversion. In practice, this calibration scheme may be automated in order to periodically measure the SoP within the FBG.

5.6 Characterisation

The measurement system illustrated in Figure 5.3 was constructed using the described components and techniques in order to establish the performance of this technique under laboratory conditions.

To provide both the test magnetic field and the heat source, an air-core solenoid with a known responsivity of 12.5 mT/A was used. The solenoid was suspended from the bench by a layer of vibration dampening materials to suppress acoustic noise in the FBG—primarily at the vibration signal that occurs at twice the frequency of applied current due to magnetic force between the parallel wires. Throughout testing, care was taken to ensure that the measurement was indeed one of magnetic field and not of electrical pickup or vibration. This was achieved using the known frequency characteristics of the magnetic force vibration signal induced in the coil, and by using the technique in Section 5.5.4 to force a circular polarisation at the grating. It should be noted that as the variable waveplate was tuned the magnitude of the measurement signal could be readily adjusted from maximum sensitivity to a state of complete insensitivity to magnetic field, illustrating the dependance of the measurement scheme on the state of polarisation. As illustrated by Figure 5.10, the lo-bi grating, fabricated as described in Section 5.5.1, was attached to a quartz rod to allow the grating to be suspended in the air core of the solenoid such that the magnetic field was parallel to the fibre core.

In order to reduce noise levels, the present system utilises hardware oversam-

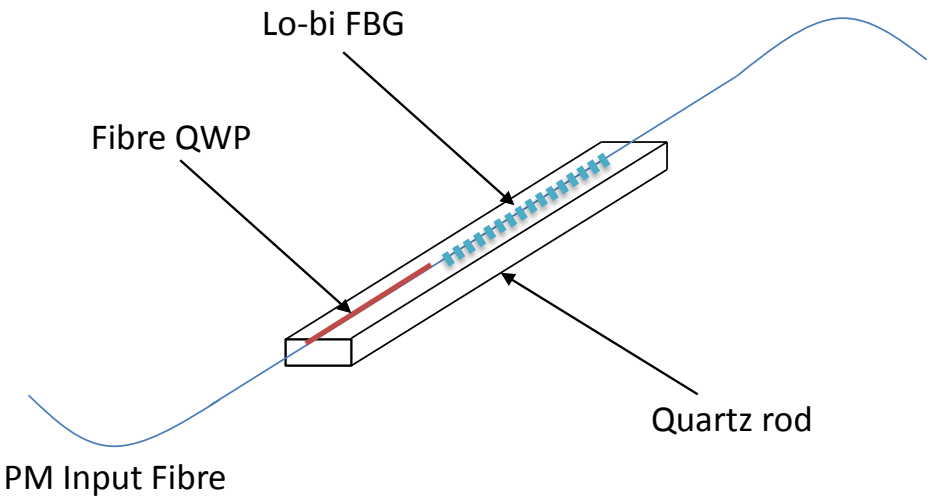

Figure 5.10: Construction of switched-polarisation magnetic field probe. QWP is quarter-wave plate.

pling in order to enable software filtering of the signal after sampling, since—due to the switched interleaved signals—hardware anti-aliasing prior to ADC is not appropriate. This allowed for a substantial reduction in high-frequency noise contributions during testing.

5.6.1 Common-Mode Isolation: Temperature Sensing

In the proposed system, the separation of magnetic field strength from the common-mode signals (strain and temperature) is made feasible by the polarisation switching scheme. As described previously, the system is able to separate the interleaved phase signals constituting the orthogonal circularly-polarised FBG reflections, which possess opposing polarities of magneto-optical sensitivity. Subtracting the de-interleaved signals results in the signals as recorded in Figure 5.11. Here, CP_A and CP_B constitute the de-interleaved orthogonal polarisations, with their differential also shown.

To generate the data in Figure 5.11, both the Mach-Zehnder interferometer plate and the FBG's quartz rod were subject to bending and heating in order to produce strong common-mode signals. It can be seen from the data that both polarisations possess identical sensitivity to strain and temperature, rendering their differential virtually immune to these forms of interference. Within the dif-

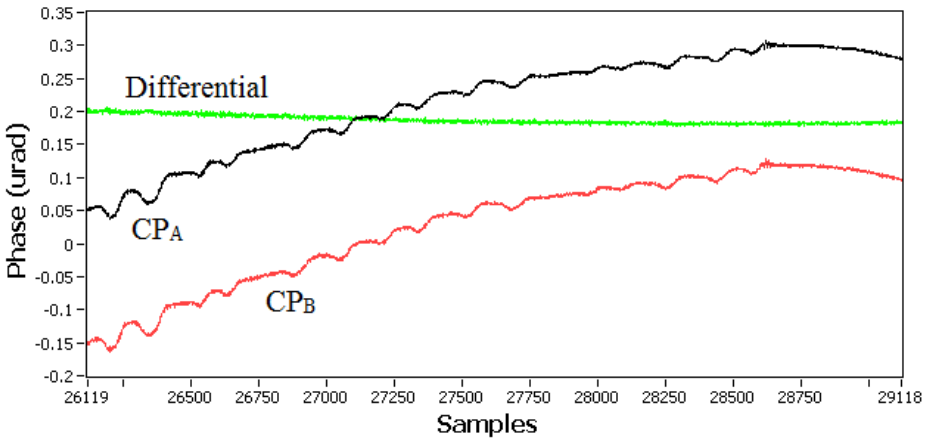

Figure 5.11: Sensor response to bending and heating of both the MZI and the FBG, demonstrating the principle of separation of temperature and magnetic field. CP_A and CP_B are orthogonal circular polarisations. The sample interval is 2 ms for both polarisations.

ferential signal remains the information on magnetic field strength. It should be noted that while the subtraction of signals possessing random noise (contributed by photodetection and quantisation stages) will double the noise power, the magnetic field signal's *amplitude* will double, resulting in a 3 dB increase in the SNR overall, in addition to the clear suppression of interference due to strain or heating.

By isolating either of the orthogonal polarisation signals or their mean, the temperature of the transducer can be monitored (given that the strain response is sufficiently dampened). In this work the test solenoid provided a method for testing this simultaneous detection of temperature by acting as an ohmic heat source for the transducer during application of relatively large solenoid currents. The temperature response shown in Figure 5.12 was recorded during a 1 min heating period by isolation and calibration of the de-interleaved signal CP_A.

5.6.2 Magnetic Field Sensing: Noise Floor and Linearity

After processing the de-interleaved signals to produce the differential signal illustrated in Figure 5.11, the measurement of magnetic field strength can be performed using the procedure in Section 5.3. From Figure 5.13, the noise floor of the present embodiment of the magnetic sensor can be estimated to be approximately

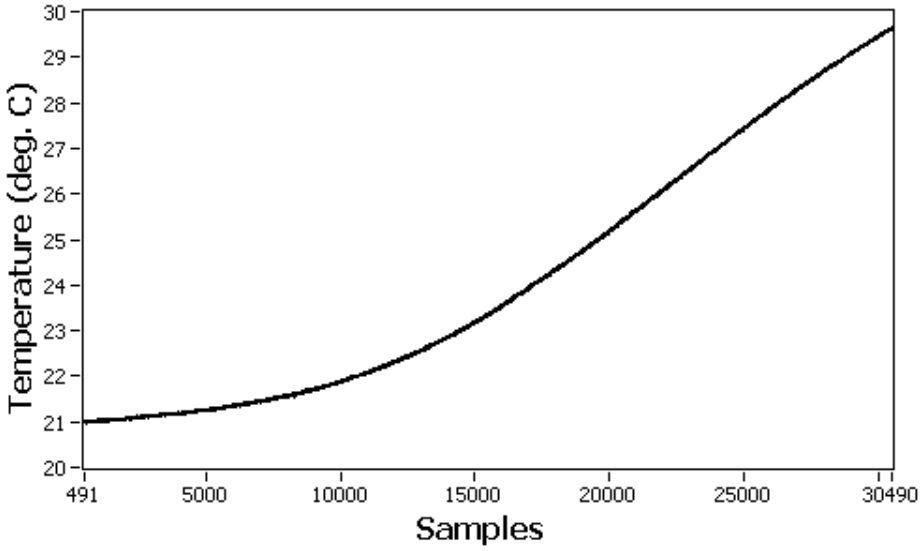

Figure 5.12: Temperature rise in transducer measured during solenoid pulsing. Measurement acquired simultaneously with magnetic field strength information via isolation of CP_A phase signal. A temperature resolution of approximately 0.05 °C was observed. The sample interval is 2 ms.

20 mT rms $/\sqrt{Hz}$ at frequencies above 1 Hz. This noise level constitutes an order of magnitude improvement over embodiments that do not utilise the techniques of oversampling or common-mode noise suppression by orthogonal polarisation switching[ON10]. The strong dc term is due to the existing phase difference between the orthogonally polarised modes in the present embodiment (see Figure 5.11), which can be removed by automatic offset calibration. In Figure 5.13 a small 100 mT rms signal is applied by an ATPS3 current injection unit[Lim]. It should be noted that unlike extrinsic techniques the magnetophotonic point sensor does not require calibration either for sensitivity or offset—given that the Verdet constant of the chosen fibre is known, an absolute measurement of the magnetic field may be made.

Since the response of the magnetophotonic sensor is linear over its entire operational range, its performance at large (> 1 T) fields can be extrapolated from its response to smaller applied fields. In the test solenoid the ac current was ramped from 0–9 A to produce a maximum test field of 112 mT. Figure 5.14 illustrates the raw data response curve to an increase in magnetic field strength, indicating a good agreement between the simulated and experimental responses.

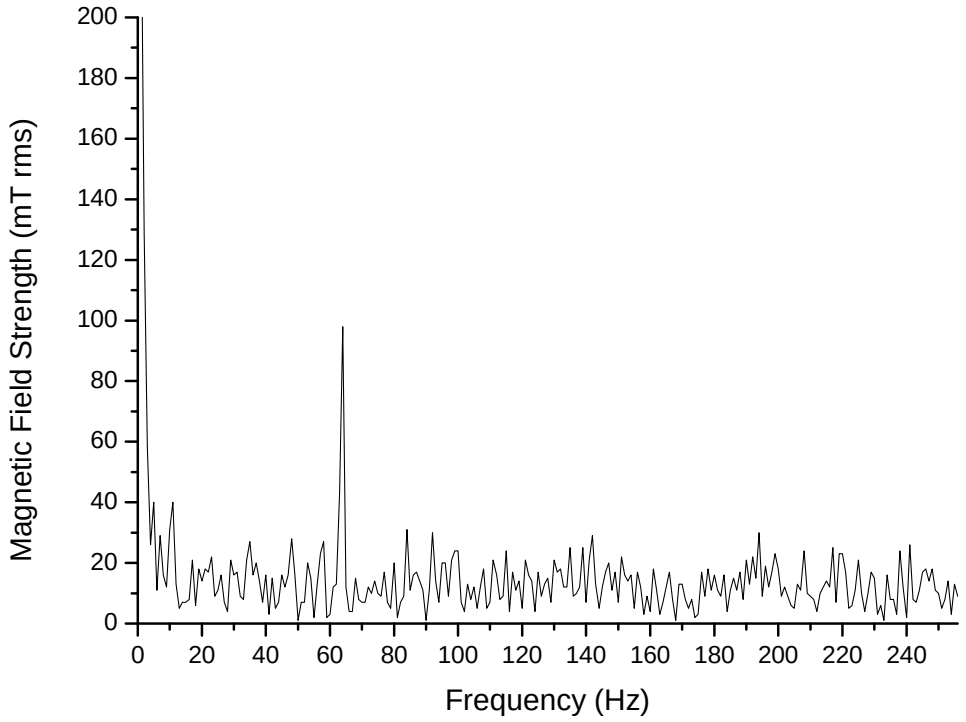

Figure 5.13: Response of magnetic sensor to application of a small (100 mT rms) signal at ∼62 Hz, demonstrating the signal-to-noise ratio. Above 1 Hz the noise floor of the laboratory system is approximately 20 mT rms $/\sqrt{Hz}$.

The present embodiment is therefore capable of measuring a wide range of field strengths at a resolution of 20 mT and with a linear response.

In the present embodiment, measurement noise is contributed for the most part by acoustic noise in the interferometer, by fluctuations in the modulation depth at the interferometer (due to temperature and vibration-induced changes in the SoP), and by the remaining degree of polarisation after the depolariser. As will be discussed in the next chapter, temperature and vibration isolation of the interferometer will be achieved more easily in future embodiments by constructing the MZI in planar waveguide form. Additionally, Section 7.2.2 of Chapter 7 will discuss in detail how the switching interrogator may be constructed to avoid SoP discrepancies within the interferometer. Therefore, it is considered that in future it will be possible to greatly improve the measurement resolution through elimination of these primary sources of noise.

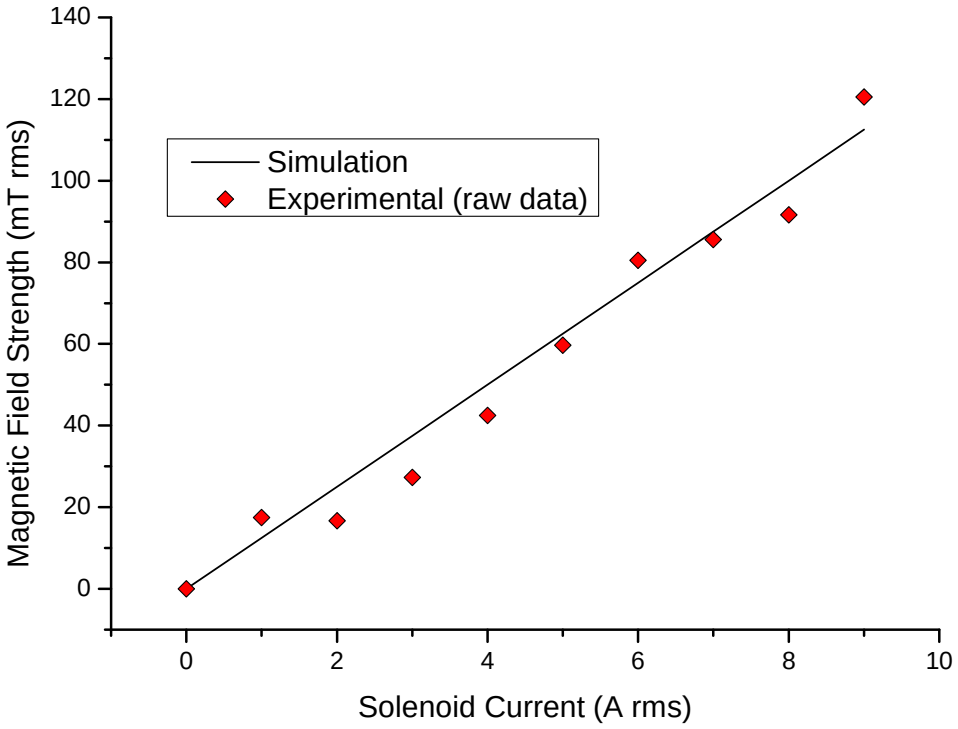

Figure 5.14: Comparison of simulated (square) and raw experimental (circle) data of response to increasing ac current in the test solenoid. No averaging has been applied. Error is due to the inherent noise equivalent to 20 mT.

5.6.3 Quasistatic Magnetic Field Measurement

As will be described in detail in Chapter 7, the system demonstrated here may undergo a straightforward adaptation to enable measurement of quasi-static magnetic fields, since in its present embodiment it readily provides a method for modulating the magneto-optical sensitivity. Although not demonstrated in this thesis, it is envisaged that the system could allow operators to select between detection of ac or dc magnetic fields simply by altering the rate of the polarisation switch and removing the de-interleaving stages of the interrogation scheme.

In this way, the static magnetic field strength becomes amplitude modulated at the switch frequency, allowing for immediate detection of the static field strength with a true measurement resolution of 20 mT. Alternatively, this capability can be exploited by a lock-in amplifier (LIA) technique to provide a phase-locked measurement of the static magnetic field with excellent resolution (<0.5 mT) by driving the polarisation switching scheme at the LIA reference

frequency[BCD+95].

5.7 Measurement of Bend and Longitudinal Strain

5.7.1 Introduction

In this section, a technique is proposed—based on conventional FBGs—that provides a robust independent measurement of longitudinal strain and bend using a polarisation conversion mechanism. The technique utilises the polarisation-switching interrogation scheme detailed earlier in this chapter in order to demodulate strain and bend signals separately at kHz acquisition rates with interferometric resolution. By removing the fibre quarter-wave phase retarder used in the magnetic measurement scheme, the system becomes sensitive to the difference in reflections from orthogonal linearly-polarised modes. It will be shown that this differential may be adjusted by subjecting a section of SM fibre to bending.

A bend sensor may be developed based on this principle that will be applicable to measurement of the large flexural changes in tokamak structural components that are subject to magnetic forces. In particular, the possibility of providing detailed information to operators on structural movement and any potential damage during plasma displacement events (described in Chapter 2) is highly desirable. Since the transducers described here are interrogated by the same fundamental scheme, bend sensors may be incorporated into the sensor array without any further changes in the interrogation hardware.

5.7.2 Existing Fibre Bend Sensors

Optical fibre bend sensors offer a number of advantages over conventional electronic flexural measurement techniques, including high accuracy and repeatability, the freedom to measure bend in every direction, and their capability for deployment in adverse conditions. Bend sensors have been proposed utilising bend loss (commonly with plastic optical fibres)[GR97][KCS02], two-path interferometry[MGM+01], long-period gratings[SCT+07], and etched fibre gratings[YZZ+04].

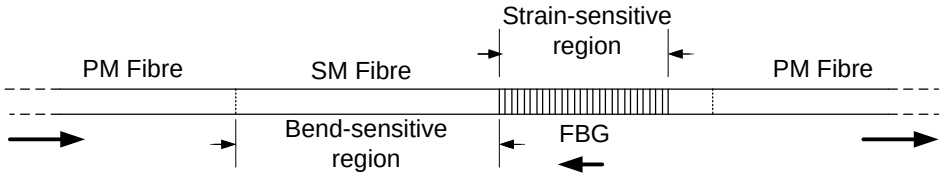

Figure 5.15: Multiplexable fibre transducer for bend and strain. PM is polarisation-maintaining, SM is single-mode, FBG is fibre Bragg grating.

However, the performance of such techniques is limited either in terms of their serial multiplexing capability or their robustness to attenuation and power fluctuations. A narrowband wavelength-encoding optical bend sensor would address these limitations by providing a transducer that is easily multiplexed using existing techniques while being completely insensitive to optical power fluctuations.

5.7.3 Measurement Principle

Figure 5.15 illustrates the multiplexable bend transducer. In this arrangement, a standard FBG sensor is preceded by a short length of conventional single-mode (SM) fibre. This SM region forms the bend-sensitive transducer, and is addressed by the interrogation scheme via high-birefringence polarisation-maintaining (PM) fibre in precisely the same manner as the magnetic sensors.

As discussed, fibre Bragg gratings conventionally exhibit a level of linear birefringence Δn in the core of the order of 10^{-5}–10^{-4} which is dominated by the asymmetry introduced by UV-inscription. Previously in this thesis, we have sought to reduce this level of linear birefringence to minimise interference with an induced circular birefringence. For the bend sensor, however, the existing level of linear birefringence in conventional fibre and FBGs will be utilised.

In accordance with the Bragg equation ($\lambda_B = 2n_{eff}\wedge$) there will be two separate peak reflected wavelengths corresponding to the two orthogonal axes of birefringence. By adjusting the bend-induced linear birefringence within the SM region (effectively a fibre waveplate), the peak reflections experienced by orthogonally-polarised modes exiting the PM fibre can be shifted between two extremes, where orthogonal modes are polarised linearly within the FBG and hence there is the greatest difference between Bragg wavelengths. At the cross-

over point, where the peak reflected wavelengths are equal, the two modes are orthogonally circular within the grating with both experiencing the same mean refractive index.

Applying longitudinal strain to the transducer arrangement produces a shift in Bragg wavelength common to both polarisations. Thus, by interrogating separately for the reflected wavelengths experienced by orthogonally-polarised modes, their strain-insensitive difference can be used to determine flexural changes over the SM region, while their sum can be used to determine either longitudinal strain or temperature.

5.7.4 Measurement Scheme

The single-transducer interrogation scheme implemented for this work is illustrated in Figure 5.16. In terms of optical and electronic components, the interrogation system is identical to that of the magnetic field sensor system. In this case however, the permanent quarter-wave retarders are replaced by conventional fibre and the gratings must not be lo-bi.

As in the magnetic sensor system, the polarisation splitter separates off signals returning from the illuminated sensor on the slow and fast PM axes. The acquisition of photodetector voltages is synchronised with the optical switch such that software phase demodulation for both outputs of the polarisation splitter may be performed after the separation of interleaved signals.

In the interrogation software, processing is performed separately for the two linearly-polarised modes in order to generate their sum and difference signals. These are exclusively sensitive to longitudinal strain and bending, respectively. To enable the serial multiplexing of transducers, PM fibre may be deployed between measurement regions in order to facilitate zero cross-sensitivity by "resetting" the bend-induced polarisation conversion of previous transducers.

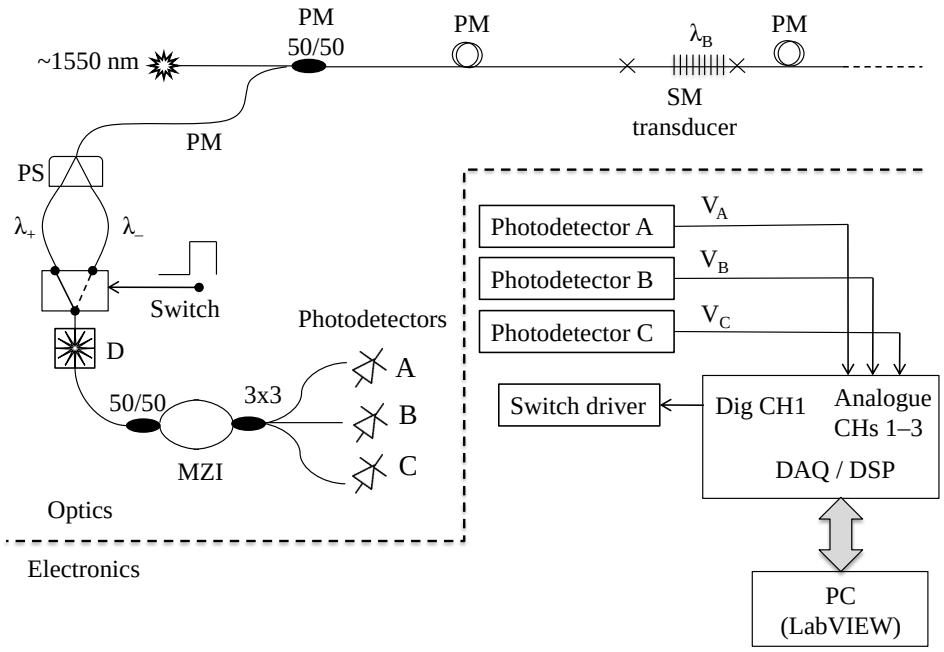

Figure 5.16: Interrogation system for single bend/strain transducer, incorporating a polarisation beam splitter (PS), an optical path switch, a depolariser (D) and an all-fibre unbalanced Mach-Zehnder interferometer (MZI)

5.7.5 Preliminary Tests

A transducer arrangement incorporating a 5 cm bend-sensitive region (SMF-28e fibre) preceding a standard FBG was fabricated in order to demonstrate the bend measurement scheme. The FBG region was bonded by epoxy to an aluminium cantilever beam, while the immediately-preceding bend-sensitive region was allowed to hang freely. By manipulating both the flexural region and the cantilever beam, the independence of the strain and bend measurements using the proposed technique and system could be demonstrated as shown by the waveforms of Figure 5.17.

5.7.6 Discussion

By providing a wavelength-encoded technique for bend measurement, the proposed scheme enables the serial multiplexing of sensors while eliminating errors due to power fluctuations that are common with existing fibre-based techniques. In future embodiments, the bend sensitivity and measurement range can be in-

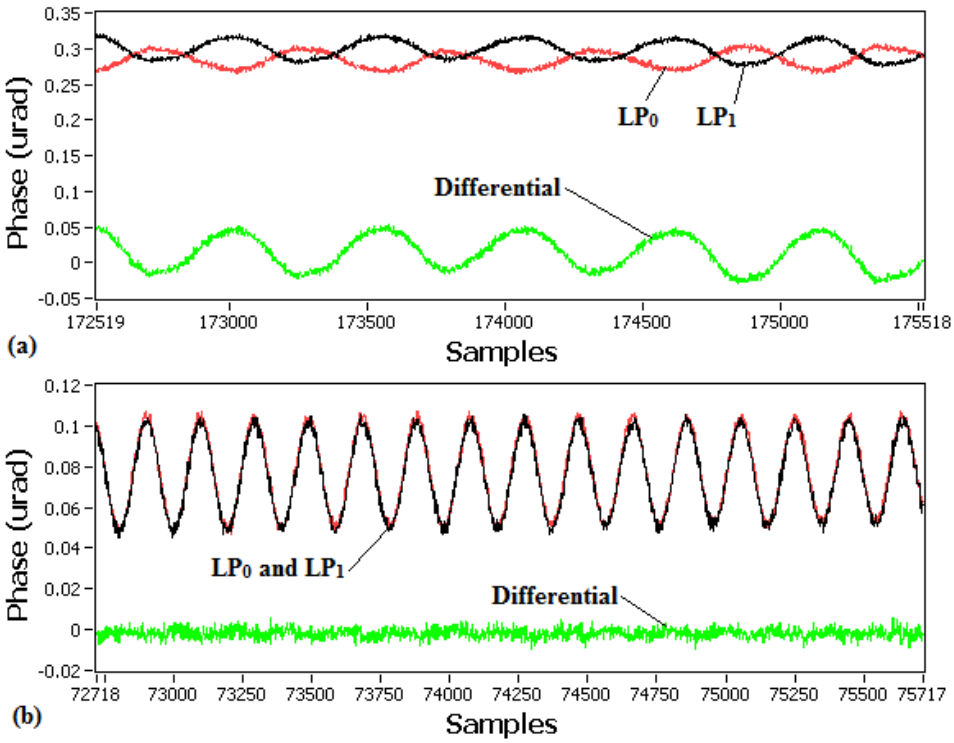

Figure 5.17: Sensor response to (a) manual bending and (b) a small 2.5 $\mu\epsilon$ rms signal applied by cantilever beam, demonstrating the principle of separation of the two measurands. LP_0 and LP_1 are orthogonal linear polarisations. The sample interval is 1 ms for both polarisations.

creased by utilising greater birefringence in the flexing and FBG regions respectively.

It is clear from this demonstration that the polarisation-switching interrogation scheme developed for magnetic field measurement may be adapted to incorporate transducers for fibre bending and longitudinal strain. Thus, the functionality of the system may be expanded to provide additional useful information on structural deformation or transient flexing which may assist operators in predicting or diagnosing damage to tokamak components.

5.8 Chapter Summary

In this chapter, a multiplexable, all-fibre technique for point measurement of magnetic field strength has been proposed and demonstrated. The technique incorporates a polarisation switching scheme that enables the isolation of common-

mode signals such as strain and temperature—improving the performance of the sensor and allowing simultaneous, independent measurement of temperature in the transducer. The scheme utilises conventional PM fibre in combination with fibre quarter-wave plates in order to provide well-determined circular polarisation states at the transducer over long interrogation distances.

In addition, details have been provided of the fabrication technique for low-birefringence FBGs which are required for use in this system, an automatable technique for the tuning of the quarter-wave retarders in order to produce the correct state of polarisation within the sensor elements, and the phase demodulation calibration procedure.

The sensor's response to applied ac magnetic field and heating was demonstrated, indicating resolutions of 20 mT rms $/\sqrt{Hz}$ and 0.05 °C respectively with the present embodiment. In future implementations it will be possible to greatly reduce this noise level by acoustic isolation and improved polarisation stability of the MZI module. Additionally, it will be possible to enable measurement of static magnetic fields using the incorporated polarisation switching technique in order to modulate the magnetic field strength information upon a carrier of known phase and frequency.

A technique for adapting the scheme to measure fibre bend and longitudinal strain was described, based on an alternative transducer package. This capability may be incorporated into the overall scheme to provide additional functionality.

Importantly for use in the fusion environment, the system retains the FBG's capability for serial multiplexing and its all-glass structure. As such, the technique satisfies the criteria for environmental robustness demanded by tokamak applications, while providing monitoring of magnetic field strength over large measurement ranges.

5.9 Associated Publications

1. P. Orr and P. Niewczas. Polarization-Switching FBG Interrogator for Distributed Point Measurement of Magnetic Field Strength and Temperature.

IEEE Sensors Journal, 11(5):1220–1226, May 2011.
DOI: 10.1109/JSEN.2010.2091124.

2. P. Orr and P. Niewczas. An Optical Fibre System Design Enabling Simultaneous Point Measurement of Magnetic Field Strength and Temperature Using Low-Birefringence FBGs. *Sensors and Actuators A: Physical*, 163:68–74, September 2010.
DOI: 10.1016/J.SNA.2010.07.009.

3. P. Orr and P. Niewczas. A Robust, Multiplexable Fiber Sensor for Simulataneous Measurement of Bend and Strain. *IEEE Sensors Journal*, 11(2):341–342, September 2010.
DOI: 10.1109/JSEN.2010.2072497.

4. P. Orr and P. Niewczas. Polarization-Switching FBG Interrogator for Wavelength-Encoded Polarization-Sensitive Measurements. In *21st International Conference on Optical Fiber Sensors*, Ottawa, Canada, May 2011.

5. P. Orr and P. Niewczas. Passive, Multiplexable Measurement of Magnetic Field Strength and Temperature Using PM Fibre Bragg Gratings and Chiral Fibre Devices. In *20th International Conference on Optical Fiber Sensors*, Edinburgh, UK, October 2009.
DOI: 10.1117/12.834173.

Chapter 6

High-Speed, High-Resolution FBG Interrogation and Multiplexing System

6.1 Chapter Overview

In Chapters 4 and 5, two ways by which point measurement of the magnetic field strength may be achieved by purely magnetophotonic means were developed. The requirement for very high resolution interrogation and large-scale multiplexing is apparent in both cases. However, it was shown in Chapter 3 that present schemes for multiplexing and interrogation of FBG-based sensors possess a trade-off between their achievable resolution and multiplexing capability.

In this chapter, a novel interferometric multiplexing scheme is proposed and demonstrated which overcomes this trade-off and enables high-resolution wavelength detection and high-speed, large-scale multiplexing. Two fundamental approaches will be detailed—wavelength-switched WDM and pulsed TDM—and a preliminary laboratory demonstration of the former will be reported. A hybrid design is also divulged that merges the beneficial characteristics of both the WDM and TDM schemes.

6.2 Introduction

As discussed in Chapter 3, existing interrogation schemes for FBG sensors possess a trade-off between their extensibility (number of sensors the scheme can interrogate) and the quality of the measurement (in terms of accuracy, resolution, and rate of measurement). This is due to the high-resolution technique (interferometry, see Section 3.4.1) being unsuitable for combination with existing multiplexing methods. Hence, the high-quality technique is usually limited to a single sensor per system, which is impractical.

The most pertinent prior research was carried out at Naval Research Laboratories (Washington DC, USA) by Todd *et al*, who have developed a technique to break this trade-off[TJA01]. However, as discussed in Section 3.4.2, this technique is limited in speed and resolution by its requirement for a scanning filter and for several electronic processing stages prior to phase demodulation. It would therefore be desirable to develop an alternative implementation of the instantaneous phase demodulation technique in [TSB02] that circumvents these limitations.

The first fundamental solution presented here makes use of a fast optical path switch in combination with a course wavelength division multiplexer (CWDM) in order to select at very high rates (potentially up to 1 MHz) which sensor signal is guided to the interrogation platform. In an second embodiment a pulsed source is used in order to ensure reflections from serially-multiplexed sensors return to the interrogator in a staggered fashion, enabling the sequential demodulation of vast sensor arrays. The core interrogation platform is an interferometric phase demodulation scheme that can produce a measurement of the guided sensor signal instantaneously.

The combination of these elements produces a system that can interrogate many sensors simultaneously at interferometric resolution and a measurement rate limited only by the performance of optical path switches, which may switch between sensors at rates of up to 1 MHz[Pho11]. Presently, all required components can be sourced commercially and possess performances that will allow the proposed techniques to outperform existing interrogation schemes.

Section 6.3 will begin by detailing the designs and operation of the proposed fundamental and hybrid schemes. Following this, Section 6.4 reports on the laboratory implementation and characterisation of the fundamental switched WDM interrogation scheme. Finally, a discussion on the calibration procedure is provided in Section 6.5.

6.3 System Designs

6.3.1 Demodulation Platform

The proposed embodiments of this system utilise the wavelength demodulation technique detailed in Section 3.4.1, where a Mach-Zehnder interferometer is constructed between the arms of 2×2 and 3×3 couplers. This may be realised by fused optical fibre couplers, or as part of an integrated optics planar waveguide. Both the all-fiber and integrated optics versions of the core wavelength demodulation component are illustrated in Figure 6.1, where photodetectors have been included such that the input is optical and the outputs are electronic.

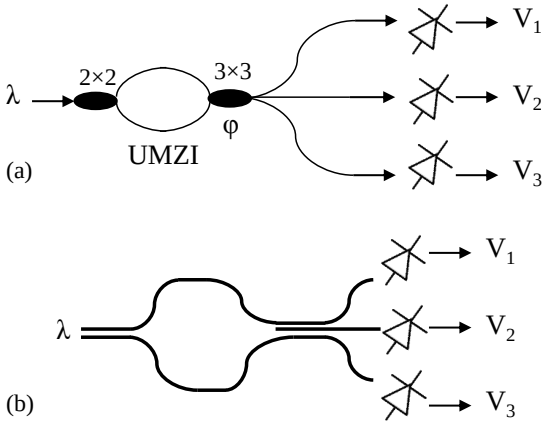

Figure 6.1: The core wavelength demodulation platform in (a) all-fibre and (b) planar forms. The contents of this figure are referred to in future figures by the block labeled 2×3 *UMZI + PDs* where UMZI is unbalanced Mach-Zehnder interferometer and PD is photodetector.

By the physical properties of the 3×3 coupler it is possible to derive the absolute phase at the point of interference of the two beam paths. This may then

be related directly to the wavelength at the input to the interferometer if the optical path difference is known. For further detail on the phase demodulation technique, refer to Section 3.4.1. Based on this demodulation scheme, the input optical wavelength may be determined immediately from a single sample of each photodetector output voltage (V_{1-3}). This capability for immediate calculation of the reflected wavelength from an FBG sensor is key to the operation of all embodiments described in the following section.

6.3.2 Core Scheme 1: Switched Wavelength Division Multiplexing

The first fundamental scheme utilises a wavelength switch, constructed from a CWDM and a fast optical path switch, to fully exploit the immediacy of the phase demodulation technique by selecting, at rates limited only by switching speeds and processing capacity, which sensor reflection is guided to the interferometer for detection.

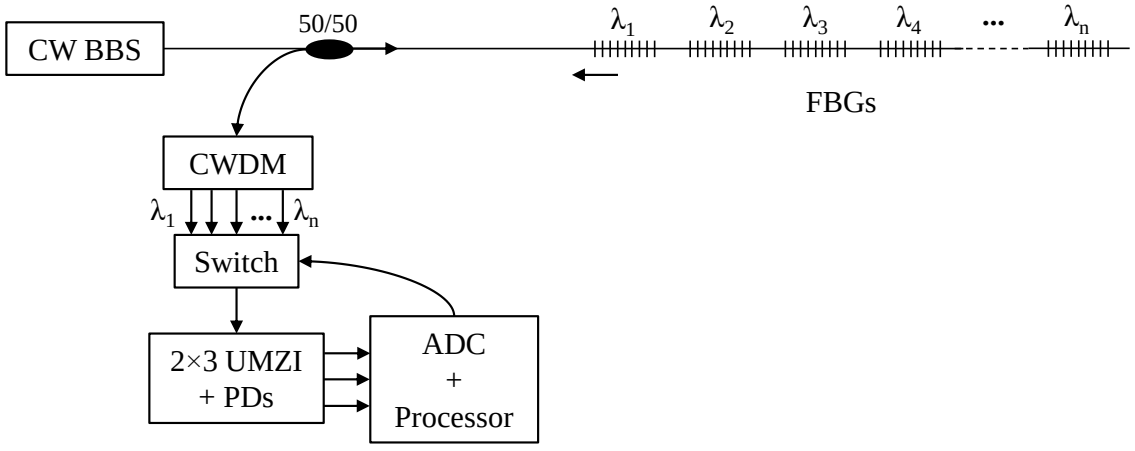

Figure 6.2: Switched wavelength division multiplexing interrogator

As illustrated by Figure 6.2, a continuous wave (CW) broadband source (BBS) illuminates a wavelength range covering the reflection wavelengths of all sensors within the sensor array. Reflected wavelengths from all sensors return simultaneously and continuously to the CWDM unit, which separates off signal from each sensor onto independent output fibres. This is achieved by using FBGs and

CWDM channel passband centre wavelengths which are matched specifically for this purpose. Therefore, every FBG wavelength must be unique and must correspond to a single CWDM channel. In effect, this scheme is a combination of the positive aspects of both [KB96] and [JTAC00], such that the wavelength-shift detection is passive and there are no tuned components.

An optical path switch, driven by the *ADC/Processor* unit, is then used to guide the reflected signal of each sensor in turn to the demodulation platform where the voltages V_{1-3} may immediately be sampled by an ADC unit and thereafter processed to determine the FBG wavelength.

The wavelength switch can select between sensor signals in any order. In addition, the ADC sampling rate may be set to any integer multiple of the switching rate to enable oversampling for the purposes of electronic noise filtering and hence further improved measurement resolution.

6.3.2.1 Parallel-Processed WDM

In a similar vein to the parallel-processed WDM multiplexing proposed by Kersey in [KB96], instead of selecting and guiding to the demodulation platform each sensor reflection in turn, all sensor reflections may be processed in parallel by the processing unit. This concept is illustrated in Figure 6.3.

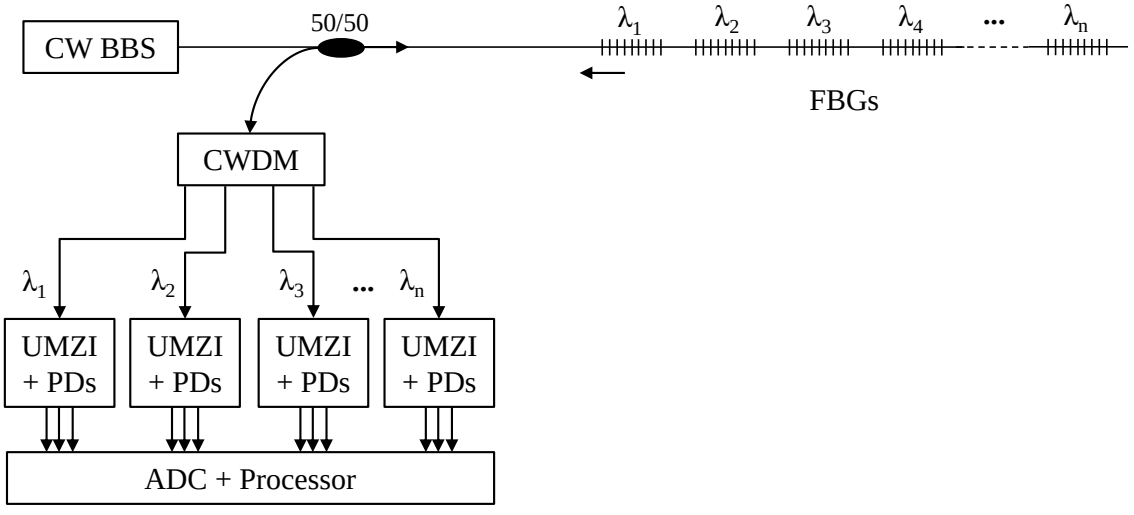

Figure 6.3: Parallel-processed wavelength division multiplexing interrogator

With this embodiment, the switching element has been removed entirely. Instead, the *ADC/Processor* unit processes the set of three voltages V_{1-3} for every sensor in parallel, which may be preferable for future embodiments given the rapid progress in development of planar optical components to construct low-cost, compact multi-UMZI units and multicore processing platforms. In this case, measurement rate is limited only by the capability of the *ADC/Processor* stage.

6.3.3 Core Scheme 2: Time Division Multiplexing

The second fundamental scheme utilises an alternative and complimentary technique for guiding one sensor reflection at a time to the demodulation platform, building upon previous work in TDM interrogation of FBG sensors[ZCW+02][WKB94]. In this embodiment (Figure 6.4), in place of the wavelength switch, a pulsed broadband source (PBS) is used in conjunction with delay lines (DLs) between sensors to ensure that after pulsing the source the sensor reflections return in temporal series to the demodulation platform in the order that they are illuminated.

As the optical pulse triggered by the *ADC/Processor* unit travels out towards sensors, each is illuminated—and will produce a sensor reflection—in turn. The delay lines ensure that the time difference between the arrivals of consecutive sensor signals at the demodulation platform is sufficient for one to be recorded and processed before the next arrives.

In order to capture the crucial voltage levels V_{1-3} as they briefly arrive, ADC units can be employed with a corresponding threshold detector which would command data acquisition on the reception of each returning pulse. Depending on the sampling speed of the ADC unit, several samples can be acquired per single pulse to enable signal averaging for noise reduction.

With the time division multiplexing (TDM) embodiment, the Bragg wavelengths of each sensor are not required to be unique or specified accurately since the system is not multiplexing by way of wavelength division. This allows greater freedom during system design and in applications in two respects:

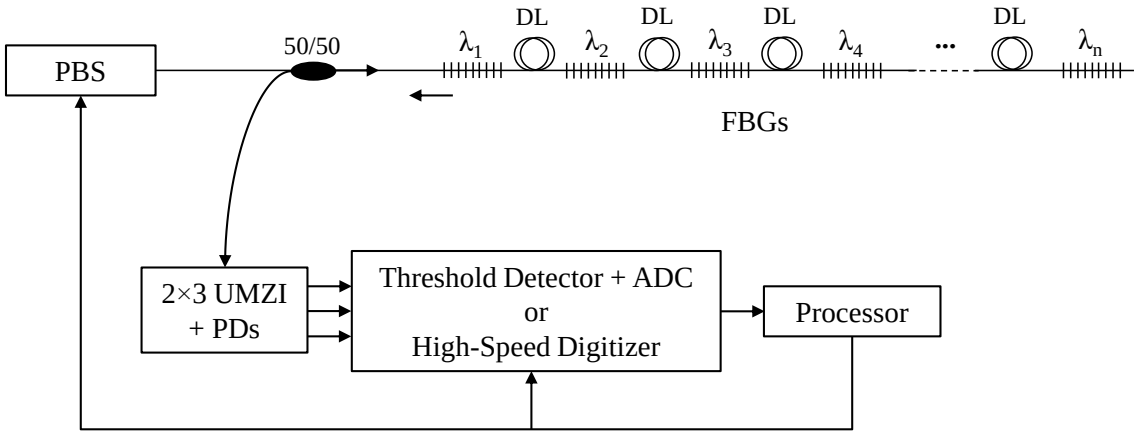

Figure 6.4: Time division multiplexing interrogator

- Sensors can be fabricated to be absolutely identical, simplifying manufacturing, replacements, and the modular nature of installations.

- The number of sensors can be very large (100s), owing to the TDM nature of the system. This is in contrast to the WDM embodiments where sensor numbers are limited to the amount that can fit within the bandwidth of the source (usually 16).

6.3.4 Hybrid Design: Time and Wavelength Division Multiplexing

As with many large-scale monitoring applications, to facilitate the monitoring of vast sensor arrays it is often required to combine a number of different multiplexing techniques to provide further means of differentiation between sensor responses[NH05][GFVM09]. In this case, using the fundamental techniques described in Sections 6.3.2 and 6.3.3 it is possible to combine TDM and WDM elements to produce a system that is capable of interrogation multiple sensor *arrays* (Figure 6.5).

Here, a pulsed broadband source (PBS) is used in a similar fashion to the TDM interrogator of Figure 6.4. At the sensors, arrays of FBGs similar to the array from Figure 6.2 are separated by delay lines such that a set of reflections from arrays return simultaneously, with a time difference between the arrivals of

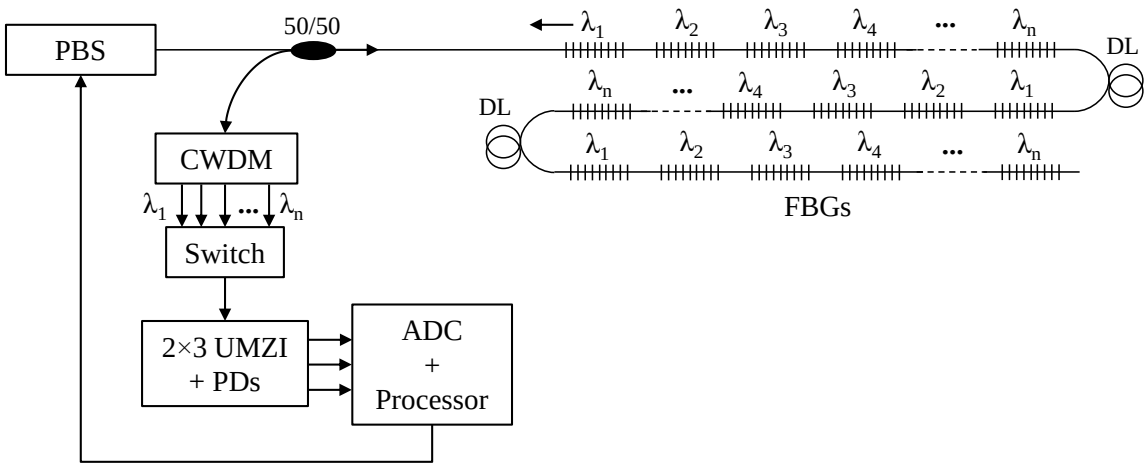

Figure 6.5: Hybrid time and wavelength division multiplexing interrogator

array reflections. Upon arrival of the sensor array reflections, a WDM module is used to split sensor wavelengths λ_1–λ_n onto individual output fibres for selection by the optical path switch. This technique is identical to that deployed in the fundamental WDM scheme (Figure 6.2).

The delay between the arrivals of sensor array reflections should be long enough to allow interrogation of all sensors within the array using Section 6.3.2's switching technique before the arrival of reflections from the next array. In order to synchronize the switching WDM with the arrival of TDM reflections, the processor may wait for illumination at λ_1 before proceeding to interrogate other wavelengths.

With this technique, there is a merging of the benefits of both the TDM and WDM techniques. The fast WDM switching interrogation technique may be implemented over not only one but multiple identical sensor arrays, each of which are illuminated in turn by the travelling broadband pulse. In this way, a very large number of sensors may be interrogated potentially faster than with the pure TDM technique of Section 6.3.3. Additionally, each array of wavelength multiplexed sensors λ_1–λ_n may be used for monitoring of smaller components of a larger system or plant where the mounting of additional delay lines between individual sensors may be restrictive but placing delay lines between the arrays that are spaced farther apart may not pose the same restriction.

6.3.4.1 Parallel-Processed WDM/TDM

The hybrid TDM/WDM approach may alternatively be implemented with the switch removed such that all sensor array reflections must be processed in parallel (Figure 6.6). As sensor array reflections return during illumination from the pulsed source, the WDM unit separates the reflections of individual sensors within the array onto separate output fibres, as in previous embodiments. Then, as in Section 6.3.2.1, before the reflection from the next sensor array arrives, the processor must interrogate all sensor reflections λ_1–λ_n.

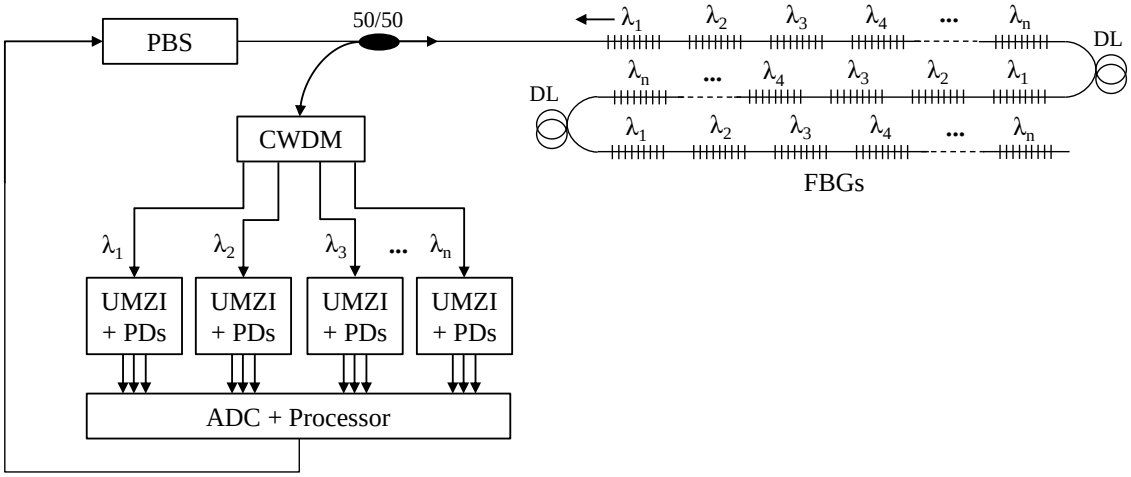

Figure 6.6: Parallel-processed hybrid time and wavelength division multiplexing interrogator

6.4 Laboratory Implementation

In order to demonstrate the fundamental technique described in Section 6.3.2, the system shown in Figure 6.7 was constructed in the laboratory. Optical path switching was provided by an Agiltron CrystaLatch 5 kHz switch, while the CWDM unit was a passive 1×4 configuration with 10 nm channel spacing and 5.5 nm channel passbands.

The three CWDM and FBG centre wavelengths were matched (1535 nm, 1545 nm, 1555 nm). Each FBG was bonded to a piezoelectric stack to allow straining of the FBGs by application of voltage. A three-phase voltage transformer was then

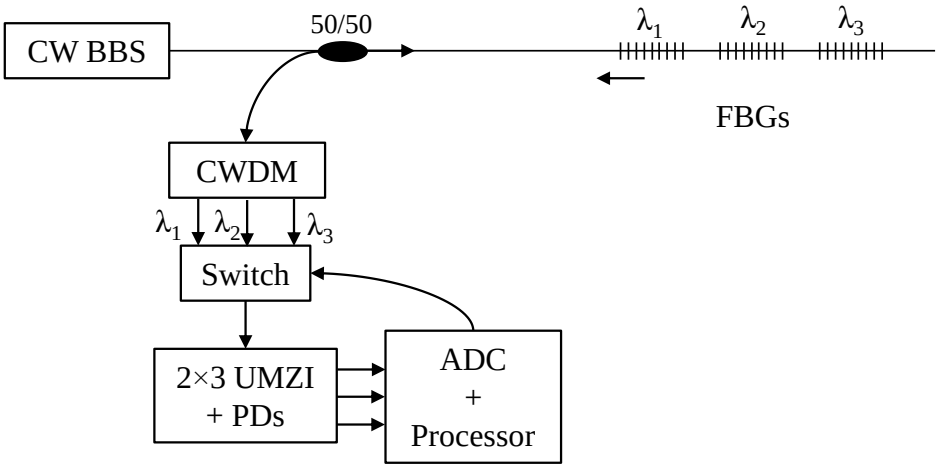

Figure 6.7: Laboratory demonstrator based on the wavelength-switched interrogator described in Section 6.3.2. The demonstration system interrogates three FBG sensors.

used to drive all sensors simultaneously. The *ADC/Processor* unit was configured for 3 kHz switching/sampling rate, allowing for 1 kHz acquisition rate per sensor. Figure 6.8 shows the signals of each sensor during 50 Hz ac voltage application. The expected 120° shift between voltage phasors can be clearly seen.

To illustrate the excellent single-to-noise ratio achievable even without anti-alias filtering or sample averaging, Figure 6.9 shows the frequency domain transform of the signals after phase-to-strain conversion. Similarly, to illustrate the independence of measurements and lack of cross-talk while using this scheme, Figures 6.10 (a)–(c) were recorded during application of a single voltage signal at one sensor (Figure (a)). It can be clearly seen that there is no trace of cross-talk between sensors on the spectra of either other sensor (Figures (b) and (c)).

From Figures 6.9 and 6.10, the excellent resolution of the interferometric technique is demonstrated to be approximately 10 nϵ rms $\sqrt{Hz}$ before application of filtering or sample averaging. This contrasts with the 1 $\mu\epsilon$ resolution of higher end commercially-available interrogation systems, demonstrating an improvement of two orders of magnitude. Though not demonstrated here, with sample averaging or filtering this resolution can be improved by a further order of magnitude by reducing high frequency noise contributions.

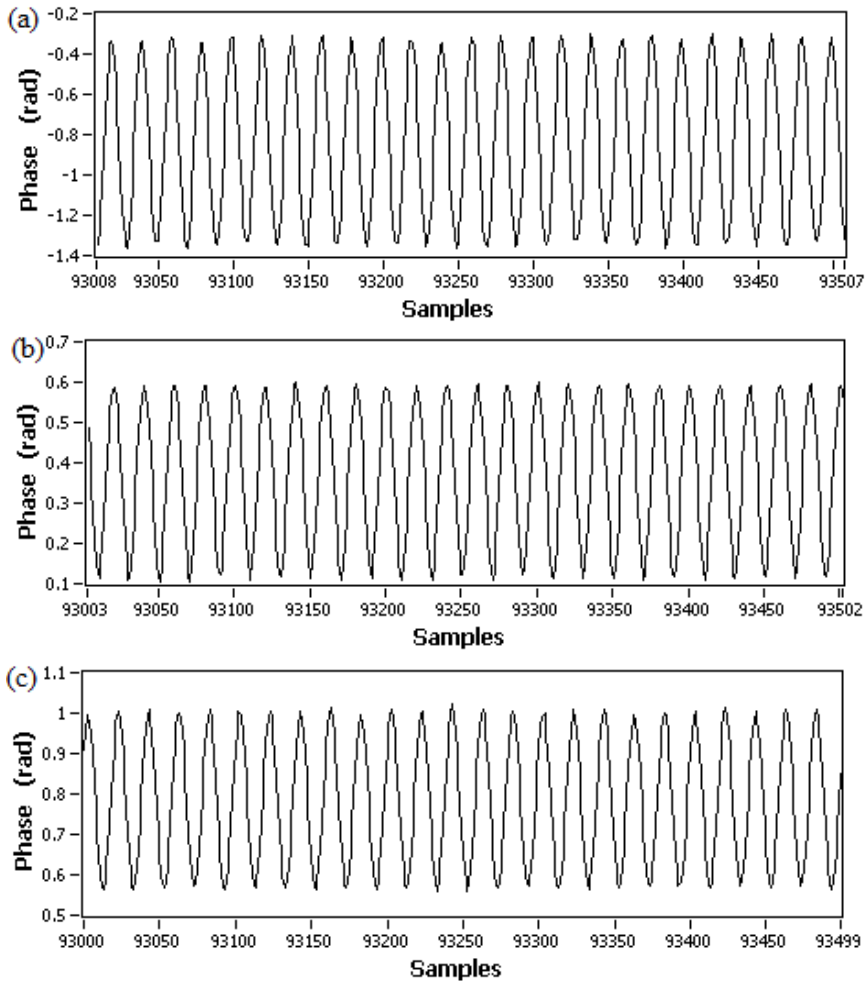

Figure 6.8: Simultaneous interrogation of three FBG sensors ((a) 1535 nm, (b) 1545 nm, (c) 1555 nm) measuring 3-phase ac 50 Hz voltage using the switched CWDM technique

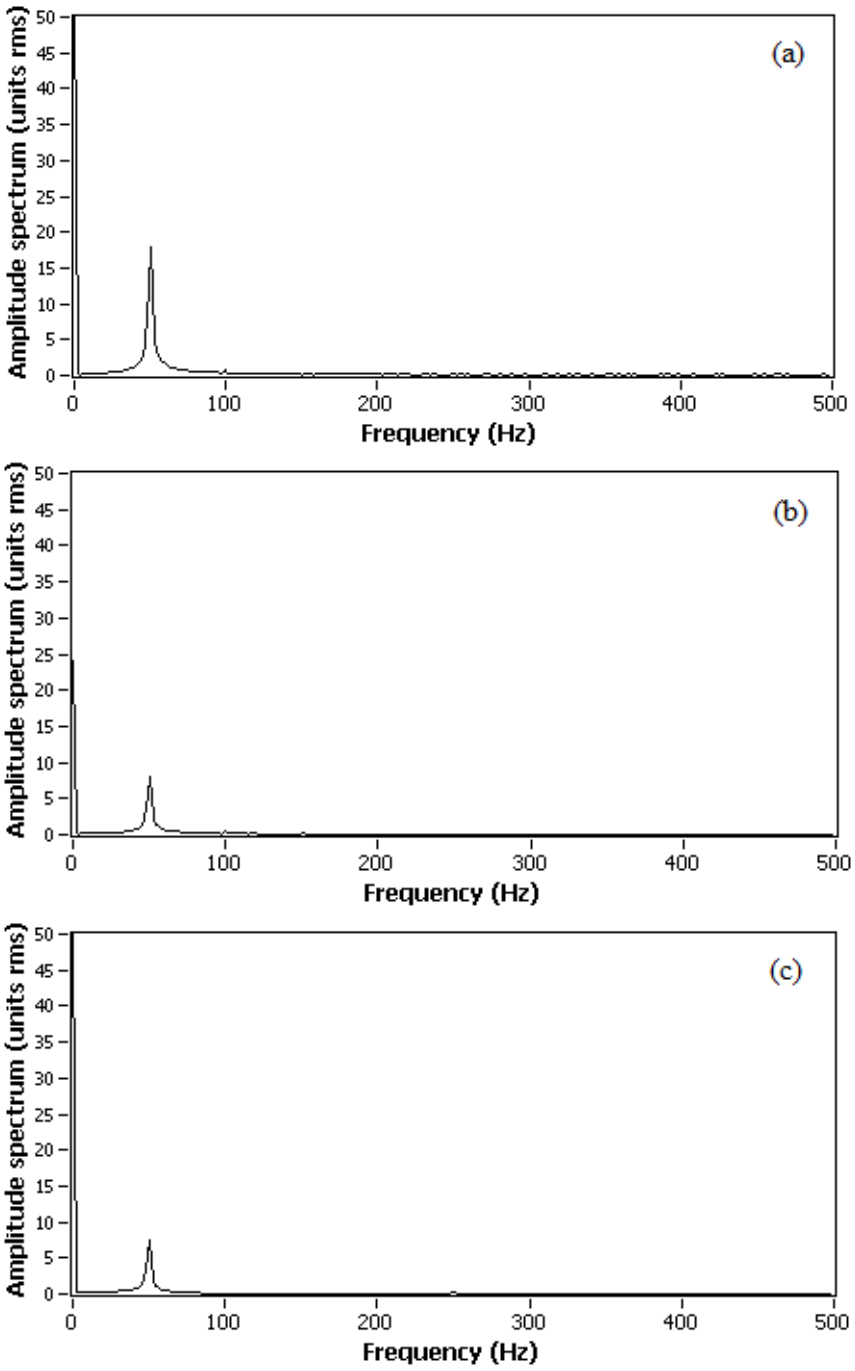

Figure 6.9: Spectra of the three sensor signals ((a) 1535 nm, (b) 1545 nm, (c) 1555 nm) acquired at 1 kHz each. Units are microstrains. Measuring 3-phase ac 50 Hz voltage using the switched CWDM technique. Difference in signal amplitudes is due to difference in piezoelectric stack characteristics.

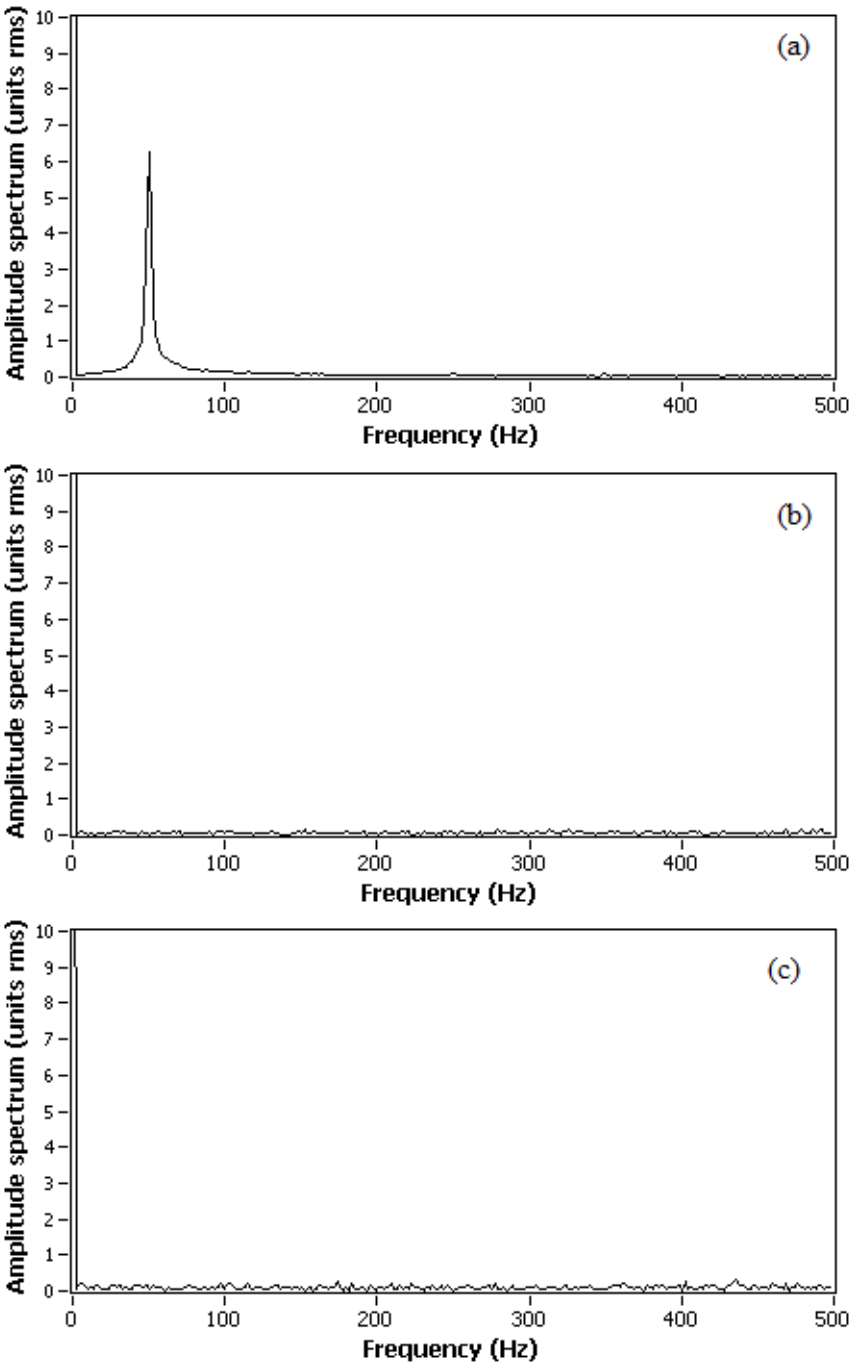

Figure 6.10: Demonstration of robustness to cross-talk between multiplexed sensors during application of strain signal to one sensor (a). From (b) and (c) it can be seen that there is no trace of the applied signal.

6.5 System Calibration

The transfer function (wavelength to phase conversion) of the unbalanced Mach-Zehnder interferometer as described in Section 3.4.1 will drift slowly over time with changes in the environmental temperature. Such drift will alter the sensitivity of the measurement system to changes in measurands. In addition, the device will pick up unwanted acoustic noise and vibrations which will contribute to the noise level of all sensor signals. In practice therefore, the interferometer module must be made robust to the external influence of both temperature and vibration. This can be most easily achieved by miniaturisation of the interferometer, for example by fabrication of the device in a compact, monolithic, planar form rather than using fibre couplers. Fabrication of the device in planar form would allow it to be easily potted in vibration-dampening gel, and thereafter mounted on a thermoelectrically-cooled platform, thus ensuring the robustness of the device to both forms of interference.

After fabrication of the interferometer (either in fibre or planar form) the device must be calibrated to determine the constants required for deployment of the phase demodulation algorithm. To do so, the phase difference ϕ must be modulated by at least 2π rads, thus driving the interference patterns on all three outputs through at least one maximum and minimum. Then, using a straightforward procedure for determining the optical power splitting ratio and the phase angles between 3×3 outputs—such as that described in [SHS93]—the required parameters A_n, B_n and θ_n may be recorded.

The 2π phase modulation required for this calibration procedure can be achieved either by stretching one or both arms of the interferometer, which is feasible for both fibre and planar embodiments of the interferometer. In the fibre embodiment, a piezoelectric stretcher can be employed to stretch the interferometer arms; in the planar construction, a suitable modulation technique can be used, for example by utilising electro- or thermo-optic effects or MEMS (micro-electromechanical systems) actuation. Planar MZI modulators are commercially available and similar techniques could potentially be adopted in this application.

Alternatively, calibration can be achieved through the modulation of the input wavelength. Input wavelength modulation does not require manipulation of the interferometer itself in any way. There are a number of ways by which this may be achieved, the simplest of which may be to guide a strain-modulated FBG reflection through the interferometer temporarily.

In general, system calibration would be required very infrequently, and could be automated to perform during system "start up" or when demanded by the user. To further improve stability, a temperature-controlled athermal FBG can be used as a stable wavelength reference (connected in series or in parallel with the sensor gratings) that can be checked periodically to ensure long-term accuracy of the measurements. Adjustment for changes in measurement offsets (gradual apparent Bragg shifts) over long periods of time as determined by these periodic checks can easily be automated and would form a component of the *ADC/Processor* platform.

6.6 Chapter Summary

In this chapter, a multiplexing, interferometric interrogation scheme for FBG-based sensors has been described. The scheme, based on an instantaneous phase demodulation technique, may be implemented through a number of embodiments that utilise either wavelength or time division multiplexing, or a hybrid combination of both. In this way, the invention will allow the installation of sensor arrays of previously unachievable scope and performance, further improving—in terms of achievable resolution and measurement rate—the magnetophotonic sensor designs of Chapters 4 and 5. As such, the next chapter will illustrate how the schemes described here may be integrated into the magnetophotonic sensor systems described thus far in order to enhance their performance.

A laboratory implementation of the fundamental wavelength-switched multiplexing interrogator was performed, demonstrating the extremely high performance that may be achieved by this approach in the three key areas of speed, resolution, and multiplexing flexibility. With present commercially-available com-

ponents, it will be possible to produce, based on these designs, a multiplexing FBG interrogation system—with nanostrain resolutions and measurement rates over 100 kHz—that is solid-state with minimal electronics.

Chapter 7

Distributed Measurement of Quasistatic Poloidal Field: An Illustrative System

7.1 Introduction

The previous chapters have described and demonstrated techniques for creating viable in-vessel optical fibre sensors for magnetic field and their associated interrogation and multiplexing. In this chapter, these systems and methods are consolidated to produce a single unified design for quasi-distributed measurement of both magnetic field and temperature in a tokamak.

From the two transducer designs described in Chapters 4 and 5, the polarisation-switching technique (Chapter 5) is chosen to enable the magnetic field measurement due to its minimal requirements for bespoke grating design. This sensitisation technique is combined in a synchronised manner with the wavelength-switched embodiment of the high-performance interrogation system described in Chapter 6 to produce a switch-based multiplexing system for intrinsic fibre measurement of magnetic field strength.

To illustrate a potential sensor installation, an in-vessel sensor loop is proposed that enables the quasi-distributed measurement of poloidal magnetic field strength around the inner diameter of the vacuum vessel. Sensor packaging re-

quirements for this installation are analysed, and the expected performance of the proposed installation in terms of quasi-static measurement resolution and rate—based on a proposed lock-in amplifier technique—is discussed.

7.2 System Design

A comparison of fabrication procedures for the switching and resonant transducers (Sections 4.5 and 5.5.1 respectively) illustrates the greater difficulty in manufacturing resonant grating structures compared to standard uniform gratings. Therefore, although the resonant polarimetric approach of Chapter 4 is immediately applicable to measurement of static magnetic fields, in light of the present status of grating fabrication technology it may be preferable to employ the polarisation-switched technique for sensitisation of "simple" (uniform or apodised single-structure) FBGs to magnetic field. In the present chapter the illustrative installation will therefore utilise the technique demonstrated in Chapter 5, which will undergo adaptation to allow for measurement of true dc magnetic fields.

Based on Chapter 6's description of the possible implementations of the proposed multiplexing interferometric interrogator, it will be convenient in this instance to utilise the fundamental wavelength-switched approach—described in Section 6.3.2 and demonstrated in Section 6.4. By synchronisation of the $1 \times n$ wavelength switch with the 1×2 polarisation-selection switch required for the polarisation-switched measurement of magnetic circular birefringence, a single clock (either hardware or software based) may be used within the control system to derive the driving signals for both switches.

7.2.1 Electronic and Photonic System Components

A demonstrative full measurement system for one segment of the poloidal field is illustrated in Figure 7.1. It should be noted that a single interrogator of the type described here would be capable of interrogating a large number of sensors (limited by the bandwidth of the source and the wavelength shift requirements of each sensor), which may be distributed in any manner around one or numerous

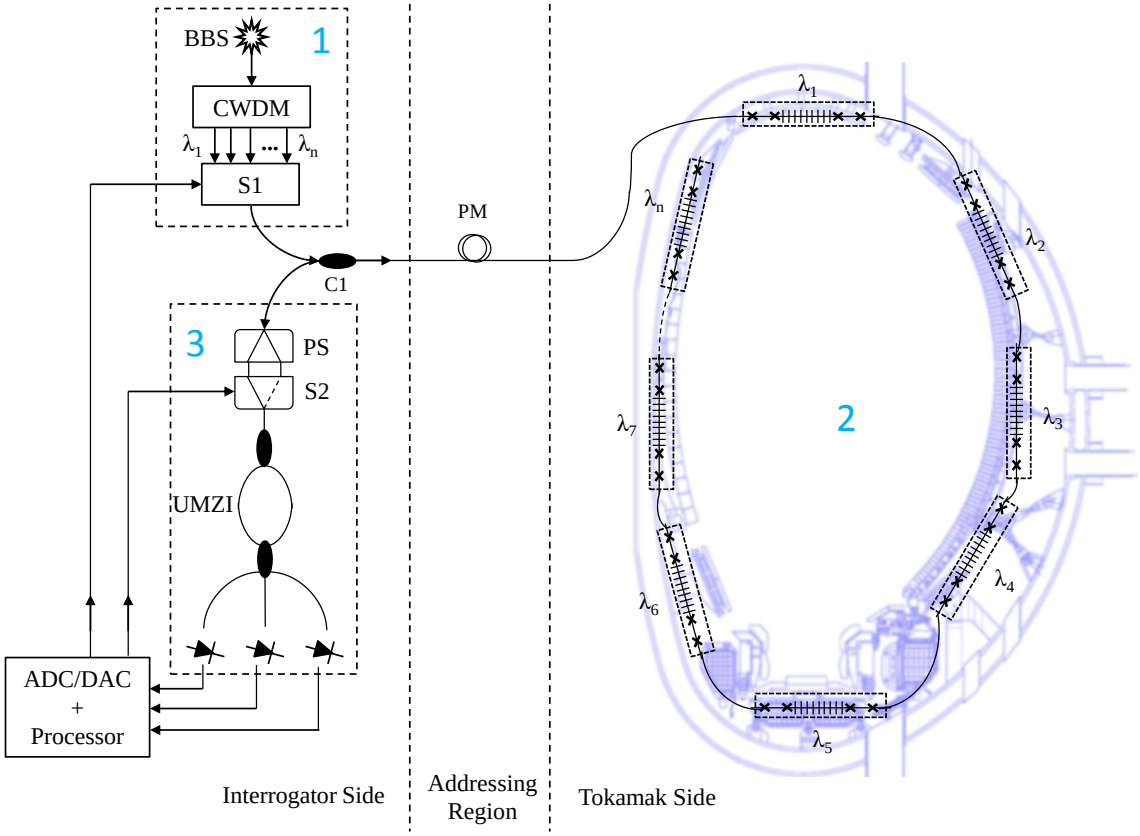

Figure 7.1: Proposed full measurement system for quasi-distributed measurement of poloidal field strength around tokamak inner diameter using low-birefringence intrinsic fibre transducers. Note that the size of transducers is greatly exaggerated. UMZI is unbalanced Mach-Zehnder interferometer, CWDM is course wavelength division multiplexer, PS is polarisation splitter, and S1 and S2 are optical path switches.

in-vessel poloidal loops. In Figure 7.1, the illustrative single-loop poloidal field measurement system is separated into three regions. These are:

- The *interrogator side*, situated in the benign environment outside the torus hall;
- The *addressing region*, comprised of a single radiation-hard polarisation-maintaining fibre that penetrates the torus hall;
- The *tokamak side*, which represents an in-vessel sensor location experiencing intense fluxes of heat, radiation, and magnetic field.

The diagram is also divided into three subsystems:

- *Subsystem 1* is comprised of a telecommunications-band (∼1550 nm) broadband CW optical source, a CWDM module, and an optical path switch ($S1$). This subsystem implements the wavelength-switched FBG multiplexing scheme detailed in Section 6.3.2. For a measurement system with n unique sensors, the CWDM module must have n channels with centre wavelengths corresponding to the nominal Bragg wavelengths of the sensors. The channel passbands must be broad enough to enclose the largest movement of each sensor, which in this application will be dominated by the Bragg temperature shift. The channel passbands should therefore be at least 3.9 nm to correspond to thermal changes of 300 °C (see Section 3.3.2.5).

- *Subsystem 2* is an illustrative poloidal sensor loop, comprised of PM fibre linking serially-multiplexed transducer packages. Each grating is fabricated for low-birefringence—as described in Section 5.5.1—and reflects at a unique wavelength corresponding to CWDM passband centres. Within the transducer package, the grating is flanked on both sides by fibre quarter-wave retarders. Since the transducers are sensitive only to parallel-aligned magnetic fields, this looped architecture is well suited to quasi-distributed measurement of the poloidal or toroidal fields. However, it should be noted that the tokamak may be instrumented with a number of alternative sensor network topologies.

- *Subsystem 3* is comprised of a polarisation beam splitter, a second (1×2) optical path switch ($S2$), and an unbalanced MZI. This subsystem receives the optical reflections from all transducers and converts the optical signals to a ratio of three output voltages representing the phase difference in the interferometer.

In this system, the processing unit must perform two key operations: switch driving and signal processing. For measurement of the magnetic field frequency spectrum with a noise floor of approximately 20 mT/$\sqrt{Hz}$ (see Section 5.6.2), both switches must be driven in a synchronous fashion such that switch $S2$ operates at twice the rate of switch $S1$. This ensures that the processing system,

which must continuously sample at the $S2$ switching rate, receives consecutively the reflections from each transducer polarisation. After both polarisation reflections have been received for a single grating, the wavelength-switch directs the next sensor to the interrogator.

In this way, the synchronous control of two switches allows the system to process both circular polarisations for all sensors in turn, yielding a magnetic field measurement rate of

$$f_{meas} = \frac{f_{S2}}{2N_{FBG}} \tag{7.1}$$

where f_{S2} is the switching rate of the polarisation switch $S2$ and N_{FBG} is the number of sensors. Using a commercially-available 1 MHz optical path switch, the magnetic field measurement rate would therefore be 25 kHz for a scheme of 20 serially-multiplexed sensors. For 20 sensors to match the 2.5 kHz measurement rate that is achieved in presently-installed JET diagnostics systems (see Section 2.3.6), a polarisation-switching rate of 100 kHz would be required, which is achieved straightforwardly by commercial switch modules[Pho11].

7.2.2 Component Birefringence and Polarisation Control

The polarising and polarisation-maintaining properties of system components will be key to the correct operation of this installation. If the broadband source is sufficiently depolarised—which is a natural characteristic of certain sources, or may be introduced by placing a broadband depolariser directly after the source—then the components in *Subsystem 1* from Figure 7.1 are not required to be polarisation-maintaining. This simplifies the selection of the CWDM and $S1$ modules since fluctuations in the waveguide birefringence in this region will have no effect on system operation, sensitivity, or measurements. At the first coupler ($C1$ in Figure 7.1), the optical power of the unpolarised source is distributed evenly over the two principal axes of birefringence, and both are guided orthogonally and independently to the transducers.

At each transducer (*Subsystem 2*), the orthogonal linear polarisations in the

PM fibre are converted by the quarter-wave retarders into orthogonal circular polarisations, as described in Section 5.4.1. Over the grating regions, the linear birefringence is sufficiently low that the polarisation mode conversion of the orthogonal circular modes is negligible. As a result, light at the Bragg wavelength is circularly polarised during reflection. For light with wavelengths outwith the Bragg FWHM, the orthogonal circular polarisations are re-converted into orthogonal linear polarisations during transmission through the exit quarter-wave retarder. In this way, all gratings reflect only circularly-polarised light, sensitising the Bragg wavelengths to parallel magnetic field strength via the magnetic circular birefringence (see Section 3.3.2.6), while in the regions between transducers the orthogonal linearly-polarised modes are immune to any polarisation fluctuations. In this way, only the magnetic field strength at the grating location is detected, and the off-sensor introduction of birefringence—due to, for example, fibre bend, twist, compression, or electromagnetic fields—is unable to influence measurements.

Unlike *Subsystem 1*, the components in *Subsystem 3* that receive the highly-polarised Bragg reflections must be polarisation-maintaining. This subsystem must separate the two orthogonal linear polarisations, and have both in turn generate a phase difference at the point of interference within the UMZI. Thus, the switch module $S2$ should incorporate highly-birefringent waveguides in order to retain aligned input polarisations. For effective utilisation of the interferometer, the two interfering rays must not possess orthogonal polarisations, since in this case no interference can take place. For differential polarisation azimuths between 0–90°, the modulation depth of the interference pattern will be partially compromised, which will translate to a large error in the measurement of phase. To avoid this, for the region following the switch there are two design options that will allow a constant, high-contrast interference pattern to be generated by the MZI:

1. Light may be depolarised prior to entering the MZI. In this case, a fibre depolariser should be placed between the switch output and the interferometer input. This ensures that light within the interferometer is unpolarised,

and that fluctuating birefringence in the MZI paths will not affect the modulation depth. In this case, the MZI is not required to be created from PM components.

2. If the polarisation splitter outputs are aligned such that both output on the same PM axis, then the interferometer may be fabricated using PM components and waveguides. In this case, a depolariser is not required since the polarisation alignment of the interfering beams at the 3×3 coupler is ensured by design. It is this approach that is illustrated in Figure 7.1.

Passive depolarisers function by decoupling the orthogonal polarisation states of an input beam and allowing them to lose coherence over a long distance, usually over a packaged coil of hi-bi PM fibre. Upon recombination at the depolariser output, the polarisation state of the resultant beam from one point in time to another has minimal correlation, such that the polarisation state at any one time is effectively random. Since such commercially-available passive fibre depolarisers will depolarise only 95% of the light, it will be preferable to avoid this approach and instead fabricate *Subsystem 3* entirely from PM components as described by option 2 above. In this case, error resulting from fluctuations in the modulation depth will be kept to a minimum.

7.3 Switch-Based Measurement of Quasistatic Fields

Due to the noise floor achieved by the technique in Chapter 5, the basic switched-polarisation method will not be immediately applicable to the measurement of *static* magnetic fields, which, as discussed in Chapter 2, will ultimately be required in ITER and in future steady-state fusion reactors. However, as mentioned briefly in Section 5.6.3, the polarisation switching method lends itself to the use of lock-in amplifier techniques, which when deployed as part of Figure 7.1's Processor block will enable true measurement of static magnetic fields.

7.3.1 Requirement for Phase-Sensitive Detection

Lock-in amplifiers (LIAs) are able, through a process of frequency-locked phase-sensitive detection, to extract signals that are buried in noise that is thousands of times more powerful than the signal amplitude[Sys11]. In effect, the LIA creates a narrow filter at the signal frequency. To operate, the LIA must be provided with a reference signal of precisely the same frequency as the signal, and which differs in phase from the signal by an arbitrary but constant angle. The LIA module is then able to produce a dc voltage to represent the amplitude of the relevant component extracted from within a signal dominated by noise.

In the proposed system, a method is readily available to switch the transducer's sensitivity to magnetic field between equal and opposite extremes—by controlling the polarisation switch $S2$, which alternates the polarisation within the FBG between left and right circular. By driving the switch $S2$ at f_{ref}, the magnetic field information is wavelength-modulated by the Bragg reflection, and this is then converted to a phase modulation at the interferometer. Thus, after calculation of the interferometer phase, the phase signal will contain a small signal at f_{ref} with an amplitude proportional to the magnetic field strength.

The amplitude of this alternating phase component can be derived based on the expression for $\delta\lambda_B/\delta B$ developed in Section 3.3.2.6:

$$\delta\lambda_B = \frac{\wedge V\lambda}{\pi}\delta B. \tag{7.2}$$

This expression must be increased by a factor of 2 for $\delta\lambda_B$ to represent the *splitting* of the Bragg wavelength, rather than the shift experienced by a single circular polarisation in isolation. It was previously stated that the phase difference at the point of interference in the MZI may be expressed as

$$\delta\phi = \frac{2\pi nd}{\lambda^2}\delta\lambda \tag{7.3}$$

where nd is the optical path difference. Combining the above expressions (and scaling Equation 7.2 by 2) results in an equation for the change in phase difference with respect to the magnetic field strength:

$$\delta\phi = \frac{4ndV\wedge}{\lambda_B}\delta B. \tag{7.4}$$

Since $\lambda_B = 2n_{eff}\wedge$, this may be re-expressed as

$$\frac{\delta\phi}{\delta B} = \frac{2ndV}{n_{eff}} \tag{7.5}$$

where n is the refractive index in the interferometer paths and n_{eff} is the mean refractive index over the FBG. Equation 7.5 is therefore the exact expression for the relationship $\delta\phi/\delta B$—however, if the MZI is fabricated in silica waveguides then $n \approx n_{eff}$ and the exact expression simplifies to

$$\frac{\delta\phi}{\delta B} \approx 2dV \tag{7.6}$$

where d is the physical path difference in the MZI and V is the Verdet constant within the FBG. Equation 7.6 is a particularly interesting result, since it illustrates that only changes in the Verdet constant or the physical path difference of the interferometer will substantially affect the sensitivity to magnetic field. More precisely, from Equation 7.5, a change in the *ratio* of grating and interferometer waveguide refractive indices will also affect the magnetic sensitivity, but this effect will be minor. For a path difference of 5 mm and a Verdet constant (at 1550 nm) of 0.57 rad/(Tm), the sensitivity will thus be 5.7 μrad/mT, which will be stable during Bragg wavelength shifts. The validity of this approximate equation was confirmed experimentally using the laboratory implementation detailed in Chapter 5.

The preliminary implementation of the switched magnetic sensor in Chapter 5 achieved a noise floor of 20 mT/$\sqrt{Hz}$, which equates to a phase noise floor of 115 μrad/$\sqrt{Hz}$. As discussed, this may be improved by better acoustic isolation of the interferometer paths. Based on the present noise floor, a static magnetisation of the FBG of 1 mT will produce a phase modulation amplitude at f_{ref} of only 5.7 μrad—a factor of 20 less than the noise power within the same bandwidth. Using a simple FFT to extract magnetic field information from the relevant frequency band will therefore not be feasible, and thus the use of LIA techniques will

be required. However, based on the noise floor associated with the interferometer's present embodiment, sub-1 mT static magnetic field levels will be readily detectable using the lock-in technique.

7.3.2 Implementation of Multiplexed Lock-In Amplification

To implement the magnetic field LIA technique, the TTL driving signal used to determine the path switch state of the polarisation switch $S2$ may also be used as the LIA reference signal, from which the LIA—which may be implemented in software—extracts the frequency and phase information of the dependent measurement signal. The LIA measurement signal is generated by the processing unit after using all photodetector voltages to determine the phase difference ϕ by Todd's algorithm, detailed in Section 3.4.1. Due to the processing time required for signal de-interleaving and phase demodulation, a phase difference will be introduced between the reference signal and the measurement signal, which must be kept constant by real-time control of the processing loop timings.

For the case of multiple sensors, care must be taken to design a synchronous switching regime that allows the continuous acquisition of interleaved samples of each sensor's phase signal. By Nyquist's theorem, the software-based digital LIA will require samples from each sensor at a rate greater than twice the reference frequency f_{ref} (polarisation switching frequency) in order to perform the phase-sensitive detection. Additionally, to detect a maximum magnetic field frequency of f_{Bmax}, the reference and $S2$ driving frequency f_{ref} must be greater than twice this, i.e.

$$f_{ref} = f_{S2} \geq 2 \times f_{Bmax}. \tag{7.7}$$

The wavelength-selection switch $S1$ must then be driven at

$$f_{S1} = f_{S2} \times N_{FBG} \times m \tag{7.8}$$

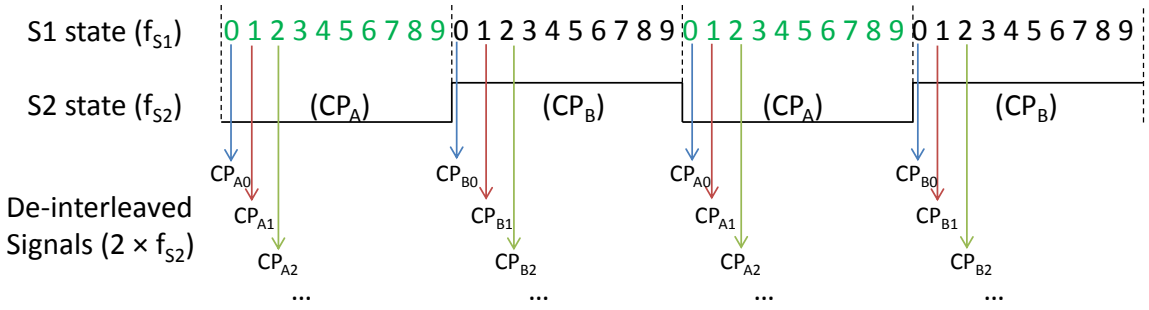

Figure 7.2: Timing diagram of multiplexing magnetic field measurement scheme for quasistatic magnetic fields. The first three de-interleaved signals are shown. f_{S1} and f_{S2} are the switching frequencies for $S1$ and $S2$ in Figure 7.1. De-interleaved sensor signals have a sample rate of $2 \times f_{S2}$.

where N_{FBG} is the number of serially-multiplexed FBG sensors within the scheme, and m is an integer ≥ 2 such that the Nyquist criterion for detection of a signal at the reference frequency is satisfied. At illustrative timing diagram for a scheme of 10 FBG sensors and a maximum magnetic field frequency of 1 kHz is shown in Figure 7.2. With reference to Figure 7.2 and Equations 7.7 and 7.8, switches $S2$ and $S1$ should be driven at 2 kHz and 40 kHz respectively.

With reference to Figure 7.2, the Processor's sample clock should be driven at $f_s = f_{S1}$ (90° out of phase) such that interleaved signals from each sensor are acquired continuously. These may then be continuously de-interleaved at the Processor unit in a fashion similar to that employed in Sections 5.6.2 and 5.7. After de-interleaving and phase demodulation, the Processor may perform phase-sensitive detection on all signals separately to extract the component at f_{ref}. The amplitude of this component is then the measured quantity, which may be related to the magnetic field strength by Equation 7.6. Thus seen, the LIA technique will allow for absolute measurement of static magnetic fields with a resolution of better than 1 mT—set primarily by acoustic noise in the interferometer. Limitations in the measurement rate and sensor count will be set by the maximum switching rate of commercial optical path switches and by the Processor's capability to perform lock-in amplifications in a parallel architecture.

7.4 Transducer Packaging Considerations

The multiplexed transducer modules in *Subsystem 2* of Figure 7.1 will require appropriate packaging to isolate the FBG and fibre waveplates from bend and strain. Without sufficient isolation, longitudinal straining of the FBG will produce an error in temperature measurements which will affect magnetic field measurement accuracy to a lesser extent via the temperature-derived Verdet constant. Additionally, transverse strain, bend, or twist will introduce or vary the birefringence of the waveplate and the grating regions. Changes in the waveplate birefringence in this manner will alter the beat length of the section, resulting in a corruption of the circular polarisations that are required in the grating. Similarly, the introduction of birefringence in the grating itself will corrupt the circular polarisations, affecting the sensitivity to magnetic circular birefringence.

Such grating packaging requirements are mirrored in the commercial DFB fibre laser industry, where fibre in the grating region must be protected from acoustic interference that will modulate the laser frequency. A common solution is the use of acoustic-dampening gels within which the fibre grating may be potted. For this application however, the non-standard requirements, such as operation at 300 °C and minimal distortion of the magnetic flux density, necessitate the use of dielectric packaging materials whose structural integrity is maintained under combined heating and radioactive dosing. As such, materials research will be required in order to identify appropriate materials for the packaging and acoustic/mechanical isolation of waveplate and grating fibres.

7.5 Chapter Summary

In this chapter, an optical fibre system for quasi-distributed measurement of the tokamak poloidal magnetic field has been proposed. The system is based on a combination of the switched-polarisation sensitisation technique demonstrated in Chapter 5 and the wavelength-switched WDM interferometric interrogation system demonstrated in Chapter 6. Using a multiplexing lock-in amplifier architecture, the proposed technique enables static magnetic field measurement using

the switched-polarisation concept, which may be preferable to the resonant polarimetric approach of Chapter 4 due to the simpler transducer architecture.

The resulting system is capable of measuring bi-directional magnetic field strength at a number of discrete points along an optical fibre. The spatial resolution of the technique is governed by the dimensions of the FBG-based transducers, yielding measurement dimensions of $10 \times 0.01 \times 0.01$ mm. A true dc field resolution of 0.5 mT may be achieved by the method, based on a noise floor of 20 $\mathrm{mT}/\sqrt{Hz}$, bringing the resolution of the switch-based approach in line with the simulated resolution of the resonant polarimetric approach. This measurement resolution allows the switched-polarisation method to compete with the resolution achieved by present inductive techniques for poloidal magnetic field, while surpassing inductive techniques in all other aspects, including spatial resolution, measurement rate, measurement range, and performance under sustained static field strengths.

Chapter 8

Conclusions and Further Work

8.1 Conclusions

Condition monitoring of tokamak fusion reactors via the circulating magnetic fields requires measurement systems that can survive and operate in this harshest of environments for the duration of the machine's lifetime. Present rugged electrical sensors are able to operate in this environment; however, their inability to measure static magnetic fields has been identified as a key problem for the diagnostic set of ITER and future commercial fusion reactors. Additionally, as reactors grow in size and the extent of the required instrumentation increases, the wiring and placement of inductive sensors will become prohibitive. As such, alternative non-electronic techniques for point measurement of the magnetic field will be required to supplement, and ultimately replace, the core inductive diagnostic schemes.

The objective of this thesis has been to demonstrate that passive optical fibre sensors—which have an excellent record of high performance in adverse conditions—can meet both the operational and environmental criteria for in-vessel tokamak magnetic diagnostics. It was firstly shown that the state of the art in optical fibre magnetic sensors will not perform sufficiently well at the levels of temperature, magnetic field strength, and radioactive fluxes expected in next-generation reactors. The relatively undeveloped field of intrinsic magnetophotonic point sensors was identified as the only sensing mechanism that will be suitable

for this application, and on this basis two approaches for point measurement of magnetic field were proposed: measurement of magnetic circular birefringence, and polarimetric measurement of the Faraday rotation.

Both these novel approaches were developed, resulting in the demonstration of two viable techniques for multiplexable point measurement of magnetic field and temperature using fibre optic systems. The first of these approaches—in-grating resonant polarimetry—demonstrated the capability of FBG group delay tailoring to facilitate the enhancement and localisation of magneto-optical Faraday rotation within an optical point sensor, thus circumventing the need for extended optical paths to achieve measurable rotations. This enhancement of group delay was confirmed experimentally using a bespoke procedure for grating fabrication. Through simulation, the structures were shown to be capable of producing sufficiently large Faraday rotations within the grating region to enable their use as novel polarimetric magnetic field sensors.

The second approach—direct measurement of magnetic circular birefringence—was realised in an FBG-based spectrally-encoding embodiment. In order to extract magnetic field strength information from the Bragg grating reflection, a polarisation mode switching scheme was developed that allowed for the separate interrogation of orthogonal linear or circular optical polarisations within the grating. Using this technique, the system was able to detect the Bragg shift due only to magnetic circular birefringence, differentiating this from the far larger common-mode shifts resulting from temperature and strain. Thus, the minimal sensitivity allowed by the small Verdet constant in diamagnetic silica fibres was overcome by the ratiometric processing of orthogonal polarisations having opposing sensitivities to magnetic field.

In the laboratory implementation, measurement resolutions of 20 $\mathrm{mT}/\sqrt{Hz}$ and 0.05 °C were demonstrated for magnetic field and temperature respectively using the polarisation switching technique. For the resonant polarimetric approach, a noise floor of 0.05 $\mathrm{mT}/\sqrt{Hz}$ was predicted through simulation. In both cases, passive interferometric techniques were proposed for phase difference measurement and Bragg wavelength shift detection.

A key requirement exists in both cases for high-resolution interferometric interrogation. Due to the large potential bandwidth of magnetophotonic sensors, measurement rate limitations are imposed primarily by the chosen sensor interrogation technique. Thus, in order to maximise the performance of the proposed sensors, designs and the laboratory demonstration of a novel high-performance FBG interrogation system were disclosed. The proposed system breaks the long-standing trade-off between measurement resolution and rate in a manner which simultaneously delivers interferometric accuracy and unprecedented measurement rates for high numbers of sensors. An alternative scheme was also proposed that allows for vast FBG sensor arrays to be interrogated based on a pulsed TDM approach that retains interferometric accuracy.

Blending the proposed FBG interrogation scheme with the switched-polarisation magnetic field sensor, the design of a switch-based system for measurement of quasi-static static magnetic field was described. In order to illustrate how such a scheme may be deployed in practice as a component of a tokamak diagnostic set, a distributed measurement scheme for a segment of the tokamak poloidal magnetic field was outlined. Importantly, it was shown that by employing a disclosed scheme for multiplexed lock-in amplification, the magnetic field information encoded at a grating polarisation modulation frequency may be extracted. In this way, static field measurement may be enabled for multiplexed intrinsic fibre sensors down to a resolution of 0.5 mT, such that both the resonant polarimetric approach (which is inherently capable of static field measurement at this level) and the switched polarisation approach may be used for dynamic and static field measurement.

In practice, selection between the two techniques will be dependent on the relative difficulties in transducer fabrication and component availability. In terms of static magnetic field measurement, the resonant polarimetric transducers will require a simpler supporting system, while the fabrication of the transducers is an involved process that will not be straightforward to automate. Conversely, the polarisation switching technique employs simple transducers that may be batch-produced, but will require complex signal processing to deliver quasi-distributed

measurement of static fields.

Ultimately, both developed approaches provide spectrally-encoded quasi-distributed reflection-mode measurement of parallel magnetic field strength using only intrinsic magneto-optical interactions. Measurement of temperature at the transducer locations is achieved simultaneously with the magnetic field measurement in both cases. A new class of intrinsic fibre-optic magnetic point sensors has thus been successfully demonstrated that retains the inherent flexibility, small size, and robustness to harsh environmental conditions that are oft-cited benefits of optical fibre transducers, but which were undermined by the transduction mechanisms used by prior-art fibre magnetic sensors.

In terms of the environmental demands placed on the sensors, it was predicted—based on studies on the effects of combined gamma-neutron fluxes on fibres and fibre sensors—that the proposed approaches will be suitable for use in the ITER machine. However, of the three desirable in-vessel measurement locations, only two will be appropriate for the lifetime deployment of sensors. The harshest measurement region—situated in the gaps of the vessel's neutron blanket—was deemed unsuitable for a fibre installation due to the extremely high neutron flux in this area.

Both proposed sensors have been shown to meet and, in most cases, far surpass the operational demands of the ITER magnetic diagnostics. In particular, the measurement rate, spatial resolution, maximum operating temperature, and measurement range of present inductive sensors are exceeded by the fibre systems proposed in this thesis. Of the performance criteria, only the measurement resolution—limited by the ability of the interferometric Bragg-shift detection scheme to overcome the low magneto-optical sensitivity—remains problematic. The desired static field resolution of 0.1 mT may be achieved by the resonant polarimetric approach through further noise reduction at the interferometer platform—however, the switching polarisation technique does not yet meet this criterion. Since the resolution of the polarisation mode switching system may be improved through the use of lock-in methods described herein, it is reasonable to suggest that the required measurement resolution may be achieved in future by

both proposed techniques after further development.

8.2 Further Work

Due to the relative under-development of intrinsic fibre magnetophotonic point sensors prior to the work described in this thesis, a number of avenues of further work may be recommended. In particular, the further development of certain techniques and concepts described here will be required before the proposed technologies may be considered ready for industrial deployment.

8.2.1 Compound Phase-Shifted FBG Sensors

8.2.1.1 Automated and Repeatable Transducer Fabrication

For practical deployment of the resonant polarimetric approach proposed by Chapter 4, automation of the fabrication technique for fibre Bragg gratings incorporating multiple phase-shifts will be required. The technique should utilise a characteristic feature of these structures, as discussed in Section 4.4, which states that the structures may be designed for any core index modulation depth and grating length. Importantly, if the substructure lengths ratio is kept constant, differences in the modulation depth at the design phase and as achieved in practice may be compensated for by adjustments in length.

During writing, the modulation depth is proportional to the total laser fluence, UV wavelength, and chemical composition (photosensitivity) of the fibre. An active grating writing system may thus be developed that uses feedback of the reflected intensity and reflective group delay spectra to monitor the overlapping of peaks in group delay, which will proceed in a manner similar to that illustrated by Figure 4.6. From the growth curves of the peak group delays, it will be possible to view in real-time the growth in group delay, and combination of individual peaks, as substructures are added and extended.

A suitable automatable fabrication technique for compound phase-shifted gratings possessing large reflective group delays will be of use not only to the

proposed measurement application, but also for manufacturing of the tunable delay components discussed in Section 4.7. The key objective of this project should be to enable the determinate, repeatable fabrication of structures incorporating a desired peak in group delay.

8.2.1.2 High Static Field Testing

The proposed Faraday rotation enhancement of resonant polarimetric sensors was demonstrated by implication through the experimentally-confirmed enhancement of group delay at the Bragg wavelength due to resonance superposition. It remains to demonstrate explicitly the expected enhancement of Faraday rotation in such structures, and thus to provide laboratory confirmation of the potential of these structures to be used as magnetic field sensors.

To enable this demonstration, multi-shifted gratings of the type fabricated for Chapter 4 will be required that incorporate superimposed resonances and high reflectivity over the resonant region. A partial implementation of the system illustrated by Figure 4.15 may then be used to detect the differential phase at the Bragg wavelength that is developed by strong magnetisation. The simplest approach may involve a strong permanent magnet, and a laser that is tuned, or preferably locked, to the Bragg wavelength.

By constructing the reciprocal path architecture described in Section 4.6, a differential phase at the interferometer should appear, with magnitude proportional to applied field. As the laser is tuned away from the superimposed resonances, a magnetically-induced phase difference should no longer be detectable, confirming the localisation of the field measurement.

8.2.2 Switched Quasistatic Field Measurement

It remains to demonstrate the lock-in technique proposed in Chapter 7 for measurement of quasi-static fields using the polarisation switching technique of Chapter 5. Initially, this technique should be demonstrated for a single sensor where no multiplexing—and hence no sample de-interleaving at the receiver—is required. In this case, a software implementation of a lock-in amplifier should be developed

that incorporates compensation for, and stabilisation of, the time delay (hence phase shift) imposed by phase demodulation processing.

When magnetised by a static magnetic field, the grating will produce a switching phase signal at the interferometer output as detailed by Section 7.3.1. The switching component will be at precisely the LIA reference frequency, and will thus be extractable by the software lock-in technique. This project will primarily require the design and optimisation of substantial bespoke software and electronics that perform the de-interleaving, phase-shift compensation, and parallel lock-in amplification for multiplexed sensors.

8.2.3 DFB Fibre Laser Sensor for Magnetic Field

In Chapter 5, the possibility of detecting the splitting of a Bragg reflection directly was discussed briefly. It was considered that, due to the bandwidth of FBGs, this approach would be unfeasible for field strengths less than 3 Tesla. However, if the reflection bandwidth of the sensor structure can be reduced then the splitting effect due to magnetic circular birefringence will become apparent at smaller field strengths.

By writing a single central $\pi/2$ phase-shift into an active fibre Bragg grating (one doped with rare earth elements such as erbium), it is possible to achieve lasing within the grating. The FWHM bandwidth of DFB fibre lasers (DFB-FLs) can be extremely small compared to FBGs: usually less than 1 fm. Due to the structural similarity between FBGs and DFB-FLs, their spectrum will shift in an identical manner with changes in grating strain and temperature, and thus fibre lasers may be used as reflection-mode sensors in the same manner as FBGs.

Initially, two lasing modes will appear in the DFB-FL spectrum corresponding to the two axes of linear birefringence. As discussed in Chapter 3, this linear birefringence may be compensated for by introducing twist-induced circular birefringence. It is therefore common practice when packaging commercial DFB-FLs to apply a permanent twist such that only a single lasing mode remains.

Since a parallel magnetic field will vary the level of circular birefringence in the grating, the magnetic field may be used to tune the differential between

lasing modes. This differential may be detected and used to directly calculate the magnetic field strength. In particular, a beating of these two modes—which are circularly polarised in this instance—will occur, giving rise to a beat signal in the radio frequency range. Using a photodetector with appropriately-high bandwidth, this beat frequency f_{beat} may be monitored and related to the magnetic field B by the equation

$$B = \frac{\pi c n_{eff}}{V \lambda_B^2 f_{beat}} \tag{8.1}$$

where n_{eff} is the grating refractive index, V is the Verdet constant, and λ_B is the Bragg (lasing) wavelength. This expression is obtained based on Equation 5.2 by considering that $f_{beat} = c/\Delta\lambda$ at the photodetector. In this instance, the linear birefringence has been assumed to be compensated for prior to magnetisation.

Thus, an appropriately packaged DFB fibre laser may provide a means for directly measuring magnetic circular birefringence without the requirement for active polarisation control or modulation. The measured beat frequency would be proportional only to magnetic field, allowing the measurement to incorporate immunity to common-mode interference from heating or strain.

8.2.4 Rigorous Irradiation Testing of Fibre Sensors

It is clear from Section 3.5's review of fibre irradiation effects that present knowledge of the mechanisms governing the influence of radiation on the performance and failure of optical fibre devices is still immature. This sentiment has been expressed previously by the ITER Physics Basis[PP99].

An exhaustive, comparable round-robin trial of all fibres (including photonic bandgap fibres) and fibre sensors proposed for use in radioactive conditions will be required. These experiments should be constructed so as to take into consideration irradiation conditions such as dose rate, total dose, recovery times, pre-irradiation, and cycled irradiation. The differing chemical composition of fibres must always be noted.

Ideally, a standardised test set should be adopted that may be applied to

candidate fibres and sensors in order to facilitate the comparison of different fibre compositions, sensor architectures, and protective coatings. In contrast, present literature makes no attempt to replicate the irradiation conditions employed by others—likely due to the range of different facilities and sources available. As a result, currently-published studies are often difficult to consolidate.

8.2.5 In-Vessel Trial Installation

A key milestone in the future development of the technology described in this thesis will be an in-vessel industrial trial. Experimental fusion reactors such as MAST (Mega-Ampere Spherical Tokamak) and JET will be the most appropriate test beds for this new technology in the interim period before ITER is operational. During this period it will be desirable to trial the magnetic measurement technique for extended periods of time on either MAST or JET in order to prove the concept and test the durability of selected materials under fusion-relevant radioactive conditions and pulsed or cycling operational regimes. Although materials may be tested separately and in isolation, only a full trial installation will be sufficient proof that the operational and structural integrity of the proposed systems will be maintained over extended periods under fusion reactor conditions.

8.2.6 Implementation of Interferometric TDM Interrogator

Of the two core interrogation schemes proposed by Chapter 6, only the wavelength-switching approach has been demonstrated experimentally. It remains to implement the design in Section 6.3.3, which described a pulsed TDM scheme for FBG interrogation that retains the accuracy provided by interferometric wavelength-shift detection. The development of this scheme will require a technique for capturing the transient, staggered FBG reflections as they are incident at the interferometer. An electronic sample-and-hold approach similar to that employed in [TJA01] may be sufficient for this. Electronic and software development of the control system will be required to synchronise the broadband source pulsing with

the retrieval of the three photodetector voltages. The system may thereafter be trialled for the interrogation of vast sensor arrays, demonstrating its applicability not only to fusion diagnostics but to other large scale operations such as wind farm condition monitoring or sub-sea hydrophone arrays.

8.2.7 Other High Magnetic Field Measurement Applications

Although the tokamak magnetic diagnostics system for nuclear fusion reactors is the most appropriate long-term application for the technology described in this thesis, the techniques will be applicable to all high field strength applications. In particular, Magnetic Resonance Imaging (MRI) scanners and large particle accelerators such as the newly-constructed Large Hadron Collider (LHC) at CERN would benefit from the proposed robust, passive, and dielectric approach.

The vacuum flux density in both MRI machines and the LHC—the relevant areas of which are essentially superconducting solenoids with an air or vacuum core—is usually far above 1 Tesla. Flux densities of over 3 Tesla are common in hospital MRI facilities, while the LHC pushes superconducting magnets to their limit to produce fields of between 8–10 Tesla—very similar to the fields that will be produced in ITER. As such, both these applications will experience the problems with inductive techniques that were described in Chapter 3, such as saturation of the ferromagnetic response and the inability to measure static fields.

In the case of MRI machines, the environment is medicinal and hence entirely benign. A superconducting solenoid is set up to produce a constant large magnetic field, which is retained thereafter by maintaining the superconductivity through cooling. In this case, it may be relatively straightforward to measure the flux density by electronic techniques, such as the Hall effect, or to derive the field from the solenoid current. However, this application may still benefit from the passive, flexible, multiplexing nature of optical fibre sensors—which, based on the work in this thesis, will be capable of measuring the large flux densities.

While MRI machines require field measurement under benign conditions, the LHC solenoids—which are used to divert, capture, and detect particles created by the collider—will require measurement of giant magnetic fields and fluxes within an environment that may be vacuous and possess sources of ionizing radiation. These conditions are thus similar to, though less harsh than, than those in fusion reactors—in general, high temperatures will not be as common, and the radiation fields will be milder. There have recently been trial installations of optical fibre sensors for strain and temperature at the LHC due to their suitability under such conditions[CBI+10]. As such, the trialling of optical fibre magnetic sensors will be an appropriate next step.

Appendix A

Magnetophotonic Simulation of Stratified Periodic Structures

A.1 Theory of Simulation

A succinct approach to the simulation of magnetised stratified periodic media was described and demonstrated by Kato *et al* in [KMT$^+$03]. This procedure—originally used to simulate multilayer stacks with ferromagnetic layers—may be adapted for simulating magnetised dielectric media—such as fibre Bragg gratings—as follows.

The fundamental equations for electromagnetic waves are given by Maxwell's equations

$$\nabla \times \vec{E}(\vec{r},t) = i\omega\mu_0\vec{H}(\vec{r},t) \tag{A.1}$$

and

$$\nabla \times \vec{H}(\vec{r},t) = -i\omega\epsilon_0\tilde{\epsilon}\vec{E}(\vec{r},t) \tag{A.2}$$

where $\vec{E}$ and $\vec{H}$ are the electric and magnetic field vectors. The specific dielectric tensor $\tilde{\epsilon}$ in Equation A.2 is given by

$$\tilde{\epsilon} = \begin{pmatrix} \epsilon_D & 0 & 0 \\ 0 & \epsilon_D & 0 \\ 0 & 0 & \epsilon_D \end{pmatrix} \tag{A.3}$$

when the medium is dielectric, and by

$$\tilde{\epsilon} = \begin{pmatrix} \epsilon_1 & i\epsilon_2 & 0 \\ -i\epsilon_2 & \epsilon_1 & 0 \\ 0 & 0 & \epsilon_3 \end{pmatrix} \tag{A.4}$$

when the medium is either inherently magnetic (a net magnetic moment is provided through doping) or is magnetised by an external field, where off-diagonal components appear in the tensor.

These transverse components are generally given in their complex form, as

$$\epsilon_1 = \epsilon_1' + i\epsilon_1'' \tag{A.5}$$

and

$$\epsilon_2 = \epsilon_2' - i\epsilon_2''. \tag{A.6}$$

The elements are related to the refractive index $n = (n_+ + n_-)/2$, the extinction coefficient $\kappa = (\kappa_+ + \kappa_-)/2$, and their differences $\Delta n = n_+ - n_-$ and $\Delta\kappa = \kappa_+ - \kappa_-$ for right $(+)$ and left $(-)$ circularly polarised light, where

$$\begin{aligned} \epsilon_1' &= n^2 - \kappa^2, \\ \epsilon_1'' &= 2n\kappa, \\ \epsilon_2' &= n\Delta\kappa + \kappa\Delta n, \\ \text{and} \quad \epsilon_2'' &= -n\Delta n + \kappa\Delta\kappa. \end{aligned} \tag{A.7}$$

The above expressions can be simplified for simulation of silica fibre FBGs, where the absorption is negligible and hence the extinction coefficient κ can be treated as zero for short propagation lengths. In this case it follows that

$$\begin{aligned} \epsilon_1'' &= \epsilon_2' = 0, \\ \epsilon_1' &= n^2, \\ \text{and} \quad \epsilon_2'' &= -n\Delta n. \end{aligned} \tag{A.8}$$

From these, we have the simplified expressions

$$\epsilon_1 = n^2 \tag{A.9}$$

and

$$\epsilon_2 = in\Delta n. \tag{A.10}$$

The difference Δn between refractive indices due to magnetic circular birefringence was shown in Chapter 3 to be

$$\Delta n = n_+ - n_- = \frac{VB\lambda}{\pi} \tag{A.11}$$

where B is the strength of the magnetic field ($\mu_0 H$) in Tesla, λ is the optical wavelength in metres, and V is the Verdet constant with units rad/(Tm). As discussed in Chapter 3, the Verdet constant is dependent on wavelength and the dispersion curve $dn/d\omega$ which changes with temperature. The temperature dependence of V is more pronounced in paramagnetic materials and almost negligible in diamagnetic ones. For the purposes of these simulations, V is assumed constant with wavelength since its value changes only a negligible amount over the spectral width of the model.

In [KMT+03], a suitable technique for simulating magnetophotonic effects in thin film magnetic multilayers is described. In this technique, the state of light at any point in one-dimensional space (sufficient for modelling propagation in fibre) is represented as a state vector $\tau(Z)$, comprising the sum of the forward and backward travelling orthogonal circular polarisations by

$$\tau(Z) = \begin{bmatrix} e_X \\ e_Y \\ h_X \\ h_Y \end{bmatrix} = A \cdot \begin{bmatrix} 1 \\ -i \\ i\sqrt{\epsilon_p} \\ \sqrt{\epsilon_p} \end{bmatrix} \cdot e^{ik_p Z} + B \cdot \begin{bmatrix} 1 \\ -i \\ -i\sqrt{\epsilon_p} \\ -\sqrt{\epsilon_p} \end{bmatrix} \cdot e^{-ik_p Z}$$
$$+C \cdot \begin{bmatrix} 1 \\ i \\ -i\sqrt{\epsilon_n} \\ \sqrt{\epsilon_n} \end{bmatrix} \cdot e^{ik_n Z} + D \cdot \begin{bmatrix} 1 \\ i \\ i\sqrt{\epsilon_n} \\ -\sqrt{\epsilon_n} \end{bmatrix} \cdot e^{-ik_n Z} \tag{A.12}$$

where $k_p = (\omega/c)\sqrt{\epsilon_p}$ and $k_n = (\omega/c)\sqrt{\epsilon_n}$ are the wave numbers, $\epsilon_p = \epsilon_1 + \epsilon_2$ and $\epsilon_n = \epsilon_1 - \epsilon_2$ are the permittivities for right and left circular polarisations, and A, B, C, and D are the coupling coefficients. At this stage in the model, these values for wave numbers and permittivities are readily calculated using the input wavelength, parallel magnetic field strength, and initial refractive index.

When a single layer or thin film occupies the spatial region $Z_1 < Z < Z_2$, the state vector can be written from Maxwell's equations as

$$\tau(Z_2) = \Phi(Z_2 - Z_1)\tau(Z_1) \tag{A.13}$$

where Φ is a 4×4 state matrix.

The sixteen elements of the matrix Φ, using phase factors $\delta_p = k_p d$ and $\delta_n = k_n d$, where d is the film thickness, are given by

$$
\begin{aligned}
\phi_{00} &= \tfrac{1}{2}\left(\cos\delta_p + \cos\delta_n\right), & \phi_{10} &= -\tfrac{i}{2}\left(\cos\delta_p - \cos\delta_n\right),\\
\phi_{01} &= \tfrac{i}{2}\left(\cos\delta_p - \cos\delta_n\right), & \phi_{11} &= -\tfrac{1}{2}\left(\cos\delta_p + \cos\delta_n\right),\\
\phi_{02} &= \tfrac{1}{2}\left(\tfrac{1}{\sqrt{\epsilon_p}}\sin\delta_p - \tfrac{1}{\sqrt{\epsilon_n}}\sin\delta_n\right), & \phi_{12} &= -\tfrac{i}{2}\left(\tfrac{1}{\sqrt{\epsilon_p}}\sin\delta_p + \tfrac{1}{\sqrt{\epsilon_n}}\sin\delta_n\right),\\
\phi_{03} &= \tfrac{i}{2}\left(\tfrac{1}{\sqrt{\epsilon_p}}\sin\delta_p + \tfrac{1}{\sqrt{\epsilon_n}}\sin\delta_n\right), & \phi_{13} &= \tfrac{1}{2}\left(\tfrac{1}{\sqrt{\epsilon_p}}\sin\delta_p - \tfrac{1}{\sqrt{\epsilon_n}}\sin\delta_n\right),\\
\phi_{20} &= -\tfrac{1}{2}\left(\sqrt{\epsilon_p}\sin\delta_p - \sqrt{\epsilon_n}\sin\delta_n\right), & \phi_{30} &= \tfrac{i}{2}\left(\sqrt{\epsilon_p}\sin\delta_p + \sqrt{\epsilon_n}\sin\delta_n\right),\\
\phi_{21} &= -\tfrac{i}{2}\left(\sqrt{\epsilon_p}\sin\delta_p + \sqrt{\epsilon_n}\sin\delta_n\right), & \phi_{31} &= -\tfrac{1}{2}\left(\sqrt{\epsilon_p}\sin\delta_p - \sqrt{\epsilon_n}\sin\delta_n\right),\\
\phi_{22} &= \tfrac{1}{2}\left(\cos\delta_p + \cos\delta_n\right), & \phi_{32} &= -\tfrac{i}{2}\left(\cos\delta_p - \cos\delta_n\right),\\
\phi_{23} &= \tfrac{i}{2}\left(\cos\delta_p - \cos\delta_n\right), & \phi_{33} &= \tfrac{1}{2}\left(\cos\delta_p + \cos\delta_n\right).
\end{aligned}
\tag{A.14}
$$

In the special case where there is no incident magnetic field, using the phase factor $\delta = (\omega/c)\sqrt{\epsilon_D}d$, the state matrix simplifies to

$$
\Phi = \begin{pmatrix}
\cos\delta & 0 & 0 & \frac{i}{\sqrt{\epsilon_D}}\sin\delta\\
0 & \cos\delta & -\frac{i}{\sqrt{\epsilon_D}}\sin\delta & 0\\
0 & -i\sqrt{\epsilon_D}\sin\delta & \cos\delta & 0\\
i\sqrt{\epsilon_D}\sin\delta & 0 & 0 & \cos\delta
\end{pmatrix}
\tag{A.15}
$$

but in general the complete description of Φ is used to construct the state matrix for any film of arbitrary thickness, initial refractive index, incident magnetic field, and Verdet constant.

A.2 Solution for Reflectance, Transmittance, and Rotation Angles

Since tangential components of the electromagnetic field are continuous at all boundary surfaces, so too is the state vector $\tau(Z)$. Thus, the state vectors at the front (where $Z = Z_0$) and the back (where $Z = Z_0 + D$) of the structure of thin films can be related by

$$
\tau(Z_0 + D) = \Phi_T \tau(Z_0) \tag{A.16}
$$

where Φ_T is the product—taken in the order of *exit film to entrance film*—of each film's state matrix. In the simulation software developed for this thesis, a subsection of 250 such films is calculated and used as a building block to evaluate without approximation the larger structure, reducing processing time but limiting the spatial step size of the model.

In order to find the optical transmission, reflection, and azimuthal rotation through the structure, we may define the input light to be linearly polarised. Either TE or TM modes may be used for the input vector—here the TM mode has been used. Therefore in the region before the light enters the structure, the state vector is given by the sum of the ingoing TM light and the reflected TM and TE light as

$$\tau(Z) = \begin{bmatrix} 1 \\ 0 \\ 0 \\ n \end{bmatrix} e^{ik(Z-Z_0)} + C_1 \begin{bmatrix} 1 \\ 0 \\ 0 \\ -n \end{bmatrix} e^{-ik(Z-Z_0)} + C_2 \begin{bmatrix} 0 \\ 1 \\ n \\ 0 \end{bmatrix} e^{-ik(Z-Z_0)} \quad (Z \leq Z_0) \tag{A.17}$$

where C_1 and C_2 are arbitrary amplitudes of the reflected TM and TE modes respectively, and the refractive index n has been added to describe the non-unity index of refraction of the external regions—in this case, the regions of fibre core immediately prior to and following the grating structure.

The state vector in the exterior space on the exit side of the structure is given by the sum of the outgoing TM and TE light as

$$\tau(Z) = C_3 \begin{bmatrix} 1 \\ 0 \\ 0 \\ n \end{bmatrix} e^{ik(Z-Z_0-D)} + C_4 \begin{bmatrix} 0 \\ 1 \\ -n \\ 0 \end{bmatrix} e^{-ik(Z-Z_0-D)} \quad (Z \geq Z_0 + D) \tag{A.18}$$

where C_3 and C_4 are arbitrary amplitudes of the outgoing TM and outgoing TE

modes respectively.

A set of simultaneous equations can then be constructed, since we now have the system

$$\begin{pmatrix} C_3 & 0 & 0 & 0 \\ 0 & 0 & C_4 & 0 \\ 0 & 0 & -nC_4 & 0 \\ C_3 & 0 & 0 & 0 \end{pmatrix} = \Phi \begin{pmatrix} 1 & C_1 & 0 & 0 \\ 0 & 0 & 0 & C_2 \\ 0 & 0 & 0 & nC_2 \\ n & -nC_1 & 0 & 0 \end{pmatrix} \tag{A.19}$$

where Φ is defined in its complete form. By performing standard matrix operations on Equation A.19, the system can be restated in the form

$$\begin{pmatrix} \phi_{00} - n\phi_{03} & \phi_{01} + n\phi_{02} & -1 & 0 \\ \phi_{10} - n\phi_{13} & \phi_{11} + n\phi_{12} & 0 & -1 \\ \phi_{20} - n\phi_{23} & \phi_{21} + n\phi_{22} & 0 & n \\ \phi_{30} - n\phi_{33} & \phi_{31} + n\phi_{32} & -n & 0 \end{pmatrix} \begin{pmatrix} C_1 \\ C_2 \\ C_3 \\ C_4 \end{pmatrix} = - \begin{pmatrix} \phi_{00} + n\phi_{03} \\ \phi_{10} + n\phi_{13} \\ \phi_{20} + n\phi_{23} \\ \phi_{30} + n\phi_{33} \end{pmatrix} \tag{A.20}$$

and solved for the coefficients C_1–C_4. These amplitude coefficients are the reflectance R and T transmittance waves as follows:

$$\begin{aligned} R^{TM} &= |C_1|^2, & R^{TE} &= |C_2|^2, \\ T^{TM} &= |C_3|^2, & T^{TE} &= |C_4|^2, \end{aligned} \tag{A.21}$$

$$R = R^{TM} + R^{TE}, \quad T = T^{TM} + T^{TE}.$$

Also, based on the amplitude coefficients, the azimuthal rotation angles θ_T and θ_R via the structure are given, using the ratios $\chi_T = C_4/C_3$ and $\chi_R = C_2/C_1$, by

$$\theta_{T,R} = \frac{1}{2} \tan^{-1} \frac{2\mathrm{Re}\left\{\chi_{T,R}\right\}}{1 - |\chi_{T,R}|^2} \tag{A.22}$$

where $\mathrm{Re}\{\}$ denotes the real part and the subscripts T and R denote rotation incurred upon transmission (Faraday rotation) and upon reflection (Kerr rotation) respectively.

The phase delay of light may then be back-calculated from the azimuthal

rotation by considering the duration required for light to undergo a rotation of $\theta_{T,R}$:

$$t_{delay} = \frac{n\theta_{T,R}}{VBc} \tag{A.23}$$

where c/n is the velocity of light within the structure in m/s and VB is the specific rotary power in rad/m.

A.3 Software Implementation

The programming language C++ was chosen to implement the simulator code, while LabVIEW was used to provide plotting functions and a graphical user interface for parameter input and simulation control, as shown in Figure 4.2 of Chapter 4. The user may specify all grating and material parameters, and the magnitude and location of up to 5 phase shifts along the grating. Apodisation may also be specified.

The user specifies the wavelength step and range for the simulation, and LabVIEW then calls the main C function which performs the analysis described in the above sections, returning a four-element solution vector containing the reflection, transmission, and Faraday and Kerr rotations for each wavelength. These are then used by LabVIEW to construct the four spectra to display.

The sinusoidal index modulation in fibre produced by scanned UV inscription via a phase mask is modelled by selecting the number of step films used to approximate the perturbation. The resultant state matrix for a single perturbation is then used as a building block to construct a true representation of the UV-inscribed FBG. Similarly for each wavelength, prior to calling the main function, the programme calculates the state matrix of a region of unperturbed fibre of specified length to represent each phase shift.

Unwrapping of the azimuthal rotations—calculated via the $\tan^{-1}$ function—is achieved post-calculation by automatically scanning the rotation spectrum arrays to locate step changes $> \pi/2$ between consecutive elements. If a step up is found, it is corrected and a counter is incremented to record the current unwrapping

state. Upon locating a step down, the counter is decremented. Each time a step is found, the counter value is consulted to determine the current unwrapping state.

To implement a scanning Fabry-Perót filter, the user may select the FWHM of the filter, which is modelled by a Gaussian curve of identical bandwidth. This array is then convolved with an input array such as FBG reflectance to produce the filtered spectrum.

A.3.1 Numerical Optimisation of Substructure Ratio

As established in Chapter 3, common resonant structures do not reflect the resonant light. Therefore, an objective of the multi-shift structures is to guarantee high reflectivity over the bandwidth of the resonant region. The second objective of these structures is to ensure that the resonant region is spectrally wide—overcoming the trade-off between FSR and resonance FWHM in basic Fabry-Peroót structures. Finally, the peak of the resonance, expressed either in terms of peak group delay or peak azimuthal rotation, should be as large as possible to amplify the sensitivity of these structures to magnetic field, without compromising the first two objectives.

An algorithm was constructed in order to establish the rules for substructure lengths that yield the optimal reflection mode response for polarimetric sensing. To facilitate this, the algorithm multiplies the reflectivity spectrum by the cosine of the Kerr rotation angle spectrum for each structure to provide a third spectrum. This output spectrum is then convolved with a scanning filter function. The output spectrum then contains the notch that would be developed in the reflection spectrum (nominally totally reflective) if light reflected by the Bragg structure were re-polarising on the original input polarisation axis. By expressing the notch depth as a percentage of the nominal reflectivity at that wavelength, a convenient metric is produced that takes into consideration all three objectives of these structures: high reflectivity, wide resonance, and large peak rotation.

A maximum of three phase-shifts was simulated by the algorithm in order to reduce the processing time. The algorithm calculates the above metric for

every combination of substructure lengths, given some user-defined minimum and maximum substructure lengths and step size. From the results of this analysis, the optimum (logarithmic) structures could be identified and verified.

Bibliography

[AFM02] J. Albert, M. Fokine, and W. Margulis. Grating Formation in Pure Silica-Core Fibers. *Optics Letters*, 27(10):809–811, May 2002. (cited on page 95)

[Agi11] Agiltron. Nanospeed optical switch series, 2011. Available from `http://www.agiltron.com/`. (cited on page 142)

[ASK+95] A. Asseh, H. Storoy, J. T. Kringlebotn, W. Margulis, B. Sahlgren, S. Sandgren, R. Stubbe, and G. Edwall. 10cm Yb3+ DFB Fiber Laser with Permanent Phase Shifted Grating. *Electronics Letters*, 31(12):969–970, 1995. (cited on page 101)

[BBF+01] B. Brichard, P. Borgermans, A. F. Fernandez, K. Lammens, and M. Decréton. Radiation Effect in Silica Optical Fiber Exposed to Intense Mixed Neutron–Gamma Radiation Field. *IEEE Transactions on Nuclear Science*, 48(6):2069–2073, December 2001. (cited on pages 82, 83, 86, 89)

[BBF+08] F. Berghmans, B. Brichard, A. F. Fernandez, A. Gusarov, M. V. Uffelen, and S. Girard. An Introduction to Radiation Effects on Optical Components and Fiber Optic Sensors. In W. J. Bock, I. Gannot, and S. Tanev, editors, *Optical Waveguide Sensing and Imaging*, NATO Science for Peace and Security Series B: Physics and Biophysics, pages 127–165. Springer Netherlands, 2008. (cited on page 93)

[BCB+11] S. Bandyopadhyay, J. Canning, P. Biswas, M. Stevenson, and K. Dasgupta. A Study of Regenerated Gratings Produced in Germanosilicate

Fibers by High Temperature Annealing. *Optics Express*, 19(2):1198–1206, January 2011. (cited on pages 31, 94)

[BCD+95] F. Barone, E. Calloni, L. DiFiore, A. Grado, L. Milano, and G. Russo. High-Performance Modular Digital Lock-In Amplifier. *Review of Scientific Instruments*, 66, 1995. (cited on page 158)

[BCSC08] S. Bandyopadhyay, J. Canning, M. Stevenson, and K. Cook. Ultrahigh-Temperature Regenerated Gratings in Boron-Codoped Germanosilicate Optical Fiber Using 193 nm. *Optics Letters*, 33:1917–1919, 2008. (cited on page 58)

[BGKB04] K. Bohnert, P. Gabus, J. Kostovic, and H. Brandle. Optical Fiber Sensors for the Electric Power Industry. *Optics and Lasers in Engineering*, 43:511–526, July 2004. (cited on pages 46, 122, 150, 151)

[BGNB02] K. Bohnert, P. Gabus, J. Nehring, and H. Brandle. Temperature and Vibration Insensitive Fiber-Optic Current Sensor. *Journal of Lightwave Technology*, 20(2):267–276, February 2002. (cited on page 46)

[Boo04] A. H. Boozer. Physics of Magnetically Confined Plasmas. *Reviews of Modern Physics*, 76(4):1071–1141, October 2004. (cited on page 14)

[Bri09a] B. Brichard. Initial Assessment of Optical Fibres as Current Sensors: Gamma Radiation Effects. Technical Report TW5-IRRCER Deliverable 9, European Fusion Development Agreement, 2009. EFDA Restricted Contract Report. (cited on page 95)

[Bri09b] B. Brichard. Irradiation Testing of a Fibre-Optic Sensor Suitable for Plasma-Current Measurement. Technical Report TW6-TPDS-DIASUP13 Deliverable 1.2, European Fusion Development Agreement, 2009. EFDA Restricted Contract Report. (cited on page 95)

[BS95] J. Ballato and E. Snitzer. Fabrication of Fibers with High Rare-Earth Concentrations for Faraday Isolator Applications. *Applied Optics*, 34(30):6848–6854, October 1995. (cited on page 46)

[BTd96] J. Blake, P. Tantaswadi, and R. T. de Carvalho. In-Line Sagnac Interferometer Current Sensor. *IEEE Transactions on Power Delivery*, 11(1):116–121, January 1996. (cited on page 46)

[BTO+07] B. Brichard, A. L. Tomashuk, H. Ooms, V. A. Bogatyrjov, S. N. Klyamkin, A. F. Fernandez, F. Berghmans, and M. Decréton. Radiation Assessment of Hydrogen-Loaded Aluminium-Coated Pure Silica Core Fibres for ITER Plasma Diagnostic Applications. *Fusion Engineering and Design*, 82:2451–2455, June 2007. (cited on page 89)

[BUF+01] B. Brichard, M. Van Uffelen, A. F. Fernandez, F. Berghmans, M. Decréton, E. Hodgson, T. Shimaka, T. Kakuta, A. Tomashuk, K. Golant, and A. Krasilnikov. Round-Robin Evaluation of Optical Fibres for Plasma Diagnostics. *Fusion Engineering and Design*, 56:917–921, 2001. (cited on page 91)

[BW99] M. Born and E. Wolf. *Principles of Optics*, chapter 1, pages 54–74. Cambridge University Press, seventh edition, 1999. (cited on page 61)

[BWDN01] C. Boulet, D. J. Webb, M. Douay, and P. Niay. Simultaneous Interrogation of Fiber Bragg Grating Sensors Using an Acoustooptic Tunable Filter. *Photonics Technology Letters*, 13(10):1215–1217, November 2001. (cited on page 74)

[Can08] J. Canning. Fiber Gratings and Devices for Sensors and Lasers. *Lasers and Photonics Reviews*, 2(4):275–289, 2008. (cited on page 56)

[CBI+10] A. Cusano, G. Breglio, A. Irace, M. Consales, A. Buosciolo, M. Giordano, A. Cutolo, S. Buontempo, and P. Petagna. Fiber Optic Sensors for CMS-CERN. In *4th European Workshop on Optical Fiber Sensors*, September 2010. (cited on page 204)

[CCK+01] A. E. Costley, D. J. Campbell, S. Kasai, K. E. Young, and V. Zavariaev. ITER R&D: Auxiliary Systems: Plasma Diagnostics. *Fusion Engineering and Design*, 55:331–346, 2001. (cited on pages 21, 26, 79)

[CDSK05] J. Canning, H. J. Deyerl, H. R. Sorensen, and M. Kristensen. Ultraviolet-Induced Birefringence in Hydrogen-Loaded Optical Fiber. *Journal of Applied Physics*, 97, 2005. (cited on pages 58, 101, 115, 147)

[CFK08] G. A. Cranch, G. M. Flockhart, and C. K. Kirkendall. Distributed Feedback Fiber Laser Strain Sensors. *IEEE Sensors Journal*, 8(7):1161–1172, July 2008. (cited on page 33)

[CFK09] G. A. Cranch, G. M. H. Flockhart, and C. K. Kirkendall. Fiber-Optic Magnetic Sensor Utilizing the Lorentzian Force. *Measurement Science and Technology*, 20(3), February 2009. (cited on page 39)

[CKMP10] A. Candiani, M. Konstantaki, W. Margulis, and S. Pissadakis. A Spectrally Tunable Microstructured Optical Fibre Bragg Grating Utilizing an Infiltrated Ferrofluid. *Optics Express*, 18(24), November 2010. (cited on page 40)

[Cla80] A. E. Clark. *Ferromagnetic Materials*. North-Holland Publishing Company, 1980. (cited on page 36)

[CLVB07] G. Cheymol, H. Long, J.F. Villard, and B. Brichard. High Level Gamma and Neutron Irradiation of Silica Optical Fibers in CEA OSIRIS Nuclear Reactor. In *9th European Conference on Radiation and Its Effects on Components and Systems (RADECS 2007)*, pages 1–5, September 2007. (cited on page 92)

[CMM+99] A. Cruden, W.C. Michie, J.R. McDonald, W.I. Madden, P. Niewczas, and I. Andonovic. Advanced Optical Sensors for Transmission and Distribution Applications. *Proceedings of IEEE Transmission and Distribution Conference*, pages 259–265, 1999. (cited on page 46)

[Com03] European Commission. ITER, The Road To Fusion Energy, 2003. Available from `http://ec.europa.eu/research/energy/pdf/fusiontheroadn2.pdf`. (cited on page 3)

[Cor11] Corning. Corning SMF-28e+ Optical Fiber, 2011. Available from `http://www.corning.com/docs/opticalfiber/pi1463.pdf`. (cited on page 80)

[Cou07] World Energy Council. Deciding The Future: Energy Policy Scenarios to 2050 (Executive Summary), 2007. Available from `http://worldenergy.org/documents/scenarios_study_es_online.pdf`. (cited on page 1)

[CS94] J. Canning and M. G. Sceats. π Phase-Shifted Periodic Distributed Structures in Germanosilicate Fiber by UV Post-Processing. *Electronics Letters*, 30(16):1344–1345, 1994. (cited on page 101)

[CSBC08] J. Canning, M. Stevenson, S. Bandyopadhyay, and K. Cook. Extreme Silica Optical Fibre Gratings. *Sensors*, 8:6448–6452, October 2008. (cited on page 58)

[DE05] D. Dahan and G. Eisenstein. Tunable All Optical Delay via Slow and Fast Light Propagation in a Raman Assisted Fiber Optical Parametric Amplifier: A Route to All Optical Buffering. *Optics Express*, 13(16):6234–6249, 2005. (cited on page 126)

[Dia05] JET Magnetic Diagnostics. Errors of the Magnetic Field and Flux Measurements, 2005. Available from `http://users.jet.efda.org/pages/mags/equilibrium/error/error.htm` (restricted access). (cited on page 25)

[Dia10] JET Magnetic Diagnostics. Preliminary Target Parameter Requirements for the ITER Magnetics Diagnostic, 2010. Available from `http://users.jet.efda.org/pages/mags/iter/ITERmags/RefDocIterMags/[3].doc` (restricted access). (cited on page 25)

[Div08] United Nations Population Division. World Population Prospects: 2008 Revision, 2008. Available from `http://esa.un.org/unpd/wpp2008/peps_documents.htm`. (cited on page 1)

[DPBRH82] G. W. Day, D. N. Payne, A. J. Barlow, and J. J. Ramskov-Hansen. Faraday Rotation in Coiled, Monomode Optical Fibers: Isolators, Filters, and Magnetic Sensors. *Optics Letters*, 7(5):238–240, May 1982. (cited on page 46)

[DXT+97] M. Douay, W. X. Xie, T. Taunay, P. Bernage, P. Niay, P. Cordier, B. Poumellec, L. Dong, J. F. Bayon, H. Poignant, and E. Delevaque. Densification Involved in the UV-Based Photosensitivity of Silica Glasses and Optical Fibers. *Journal of Lightwave Technology*, 15(8):1329–1342, August 1997. (cited on page 56)

[EM94] T. Erdogan and V. Mizrahi. Characterization of UV-Induced Birefringence in Photosensitive Ge-Doped Silica Optical Fibers. *Journal of the Optical Society of America B.*, 11(10):2100–2105, 1994. (cited on page 59)

[Erd97] T. Erdogan. Fiber Grating Spectra. *Journal of Lightwave Technology*, 15(8):1277–1294, 1997. (cited on page 61)

[FBB+02] A.F. Fernandez, B. Brichard, P. Borgermans, F. Berghmans, M. Decreton, P. Megret, M. Blondel, and A. Delchambre. Fibre Bragg Grating Temperature Sensors for Harsh Nuclear Environments. In *15th Optical Fiber Sensors Conference Technical Digest (OFS 2002)*, pages 63–66, 2002. (cited on pages 32, 94)

[FKNT00] K. Fujita, A. Kimura, M. Nakazawa, and H. Takahashi. Bragg Peak Shifts of Fibre Bragg Gratings in Radiation Environment. In *SPIE Conference on Fiber Optic Sensor Technology II*, pages 184–191, 2000. (cited on page 94)

[FKSB04] R. S. Fielder, D. Klemer, and K. L. Stinson-Bagby. High Neutron Fluence Survivability Testing of Advanced Fiber Bragg Grating Sensors. In *AIP Conference, Proc. 699: Space Technology and Applications*, page 650657, 2004. (cited on page 94)

[FNM05] G. Fusiek, P. Niewczas, and J. R. McDonald. Extended Step-Out Length Fiber Bragg Grating Interrogation System for Condition Monitoring of Electrical Submersible Pumps. *Optical Engineering*, 44(3), March 2005. (cited on pages 32, 123)

[Fok02] M. Fokine. Thermal Stability of Chemical Composition Gratings in Fluorine-Germanium-Doped Silica Fibres. *Optics Letters*, 27(12):1016–1018, June 2002. (cited on pages 58, 94)

[GBF+00] A. I. Gusarov, F. Berghmans, A. F. Fernandez, O. Deparis, Y. Defosse, D. Starodubov, M. Decreton, P. Megret, and M. Blondel. Behaviour of Fibre Bragg Gratings Under High Total Dose Gamma Radiation. *IEEE Transactions on Nuclear Science*, 47:688–692, 2000. (cited on page 93)

[GBL05] S. Girard, J. Baggio, and J. L. Leray. Radiation-Induced Effects in a New Class of Optical Waveguides: The Air-Guiding Photonic Crystal Fibres. *IEEE Transactions on Nuclear Science*, 52(6):2683–2688, December 2005. (cited on page 92)

[GD00] A. I. Gusarov and D. B. Doyle. Contribution of Photoinduced Densification to Refractive-Index Modulation in Bragg Gratings Written in Ge-Doped Silica Fibers. *Optics Letters*, 25(2):872–874, June 2000. (cited on page 93)

[Ger11] S. Gerasimov, January 2011. Personal communication. (cited on page 25)

[GFVM09] S. J. Goodman, S. Foster, J. Van Velzen, and H. Mendis. Field Demonstration of a DFB Fibre Laser Hydrophone Seabed Array in Jervis Bay, Australia. In *20th International Conference on Optical Fibre Sensors*, Edinburgh, UK, October 2009. (cited on pages 33, 78, 171)

[GGP+94] K. Gill, R. Grabit, M. Persello, G. Stefanini, and F. Vasey. Gamma and Neutron Radiation Damage Studies of Optical Fibres. *Journal of Non-Crystalline Solids*, 216:129–134, 1994. (cited on page 84)

[GR97] R. C. Gauthier and C. Ross. Theoretical and Experimental Considerations for a Single-mode Fiber-optic Bend-type Sensor. *Applied Optics*, 38(25):6264–6273, September 1997. (cited on page 158)

[Gus10] A. Gusarov. Long-Term Exposure of Fiber Bragg Gratings in the BR1 Low-Flux Nuclear Reactor. *IEEE Transactions on Nuclear Science*, 57(4):2044–2048, August 2010. (cited on pages 32, 93)

[GW09] B. O. Guan and S. N. Wang. Fiber Grating Laser Current Sensor Based on Magnetic Force. In *20th International Conference on Optical Fibre Sensors*, Edinburgh, UK, October 2009. (cited on page 40)

[HFJK78] K. O. Hill, Y. Fujii, D. C. Johnson, and B. S. Kawasaki. Photosensitivity in Optical Fiber Waveguides: Application to Reflection Filter Fabrication. *Applied Physics Letters*, 32:647649, 1978. (cited on page 55)

[HHK+08] H. Henschel, S. K. Höffgen, K. Krebber, J. Kuhnhenn, and U. Weinand. Influence of Fiber Composition and Grating Fabrication on the Radiation Sensitivity of Fiber Bragg Gratings. *IEEE Transactions on Nuclear Science*, 55:2235–2242, August 2008. (cited on page 81)

[HKN+99] S. Hara, S. Kasai, T. Nishitani, A. Nagashima, and T. Nakayama. Development of Steady-State Magnetic Sensor. *Review of Scientific Instruments*, 70(1):435–438, January 1999. (cited on pages 3, 27)

[HM97] K. O. Hill and G. Meltz. Fiber Bragg Grating Technology Fundamentals and Overview. *Journal of Lightwave Technology*, 15(8):1263–1276, August 1997. (cited on page 57)

[HWC+07] W. Huang, B. Wang, S. Cao, Y. Sun, L. Weng, and H. Chen. Dynamic Strain Model With Eddy Current Effects for Giant Magnetostrictive Transducer. *IEEE Transactions on Magnetics*, 43(4):1381–1384, April 2007. (cited on page 37)

[IF97] M. Inoue and T. Fujii. A Theoretical Analysis of Magneto-optical Faraday Effect of YIG Films with Random Multilayer Structures. *Journal of Applied Physics*, 81(8):5659–5661, April 1997. (cited on page 103)

[JTAC00] G. A. Johnson, M. D. Todd, B. L. Althouse, and C. C. Chang. Fiber Bragg Grating Interrogation and Multiplexing with a 3×3 Coupler and

a Scanning Filter. *Journal of Lightwave Technology*, 18(8):1101–1105, August 2000. (cited on pages 74, 75, 76, 169)

[KB92] A. D. Kersey and T. A. Berkoff. Fiber-Optic Bragg-Grating Differential-Temperature Sensor. *Photonics Technology Letters*, 4(10):1183–1185, 1992. (cited on page 71)

[KB96] A. D. Kersey and T. A. Berkoff. Fiber Bragg Grating Array Sensor System Using a Bandpass Wavelength Division Multiplexer and Interferometric Detection. *Photonics Technology Letters*, 8(11):1183–1185, 1996. (cited on pages 71, 169)

[KBM92] A. D. Kersey, T. A. Berkoff, and W. M. Morey. High Resolution Fiber Bragg Grating Based Strain Sensor with Interferometric Wavelength Detection. *Electronics Letters*, 28:236–237, 1992. (cited on page 68)

[KBM93] A. D. Kersey, T. A. Berkoff, and W. M. Morey. Multiplexed Fiber Bragg Grating Strain-Sensor System with a Fiber Fabry-Perot Wavelength Filter. *Optics Letters*, 18:1370–1372, 1993. (cited on pages 68, 74)

[KCS02] K. S. C. Kuang, W. J. Cantwell, and P. J. Scully. An Evaluation of a Novel Plastic Optical Fiber Bend Sensor for Axial Strain and Bend Measurements. *Measurement Science and Technology*, 13:1523–1534, 2002. (cited on page 158)

[KDP+97] A. D. Kersey, M. A. Davis, H. J. Patrick, M. LeBlanc, K. P. Koo, C. G. Askins, M. A. Putnam, and E. J. Friebele. Fiber Grating Sensors. *Journal of Lightwave Technology*, 15(8):14421463, August 1997. (cited on page 32)

[KK97] K. Kurihara and Y. Kawamata. Development of a Precise Long-Time Digital Integrator for Magnetic Measurements in a Tokamak. In *17th IEEE/NPSS Symposium in Fusion Engineering*, San Diego, CA, USA, October 1997. (cited on page 27)

[KM94] A. D. Kersey and M. J. Marrone. Fiber Bragg Grating High-Magnetic-Field Probe. *Proceedings of SPIE (10th International Conference on Optical Fiber Sensors)*, 2360:53–56, 1994. (cited on pages 47, 71)

[KMT+03] H. Kato, T. Matsushita, A. Takayama, M. Egawa, K. Nishimura, and M. Inoue. Theoretical Analysis of Optical and Magneto-optical Properties of One-Dimensional Magnetophotonic Crystals. *Journal of Applied Physics*, 93(7):3906–3911, April 2003. (cited on pages 205, 207)

[Kra95] K. S. Krane. *Introductory Nuclear Physics*, chapter 14, pages 538–550. John Wiley & Sons, Inc., first edition, 1995. (cited on page 14)

[Kur56] I. V. Kurchatov. The Possibility of Producing Thermonuclear Reactions in a Gaseous Discharge. *Atomic Energy*, 1(3):359–366, 1956. Lecture given April 26, 1956 at the British Atomic Energy Research Establishment in Harwell, England. (cited on page 13)

[LCC+11] E. Lindner, J. Canning, C. Chojetzki, S. Brückner, M. Becker, M. Rothhardt, and H. Bartelt. Thermal Regenerated Type IIa Fiber Bragg Gratings for Ultra-High Temperature Operation. *Optics Communications*, 284(1):183–185, 2011. (cited on page 94)

[Lee03] B. Lee. Review of the Present Status of Optical Fiber Sensors. *Optical Fiber Technology*, 9:57–79, 2003. (cited on pages 31, 68, 73)

[LHRCQIC11] J.M. Lopez-Higuera, L. Rodriguez Cobo, A. Quintela Incera, and A. Cobo. Fiber Optic Sensors in Structural Health Monitoring. *Journal of Lightwave Technology*, 29(4):587–608, February 2011. (cited on page 32)

[Lim] Relay Engineering Services Limited. ATPS3 Protection Relay Test Set. Available from `http://www.relayeng.com/apts/apts.htm`. (cited on page 155)

[LYSF01] M. Levy, H. C. Yang, M. J. Steel, and J. Fujita. Flat-Top Response in One-Dimensional Magnetic Photonic Bandgap Structures with Faraday Rotation Enhancement. *Journal of Lightwave Technology*, 19(12):1964–1969, December 2001. (cited on page 102)

[MBB+09] P. Moreau, I. Bolshakova, B. Brichard, G. Chitarin, R. Delogu, I. Duran, A. Encheva, Y. Fournier, A. Galo, A. Le-Luyer, J.B. Lister, P. Malard, J.M. Moret, P. Pastor, S. Peruzzo, J. Romero, D. Testa, M. Toussaint, G. Vayakis, and R. Vila. Development of a Magnetic Diagnostic Suitable for the ITER Radiation Environment. In *Advancements in Nuclear Instrumentation Measurement Methods and their Applications (ANIMMA)*, Marseille, France, June 2009. (cited on page 17)

[MC01] G. P. McKnight and G. P. Carman. Large Magnetostriction in Terfenol-D Particulate Composites with Preferred [112] Orientation. *Proceedings of SPIE*, 4333:178–183, 2001. (cited on page 38)

[MGM+01] W. N. MacPherson, M. J. Gander, R. McBride, J. D. C. Jones, P. M. Blanchard, J. G. Burnett, A. H. Greenaway, B. Mangan, T. A. Birks, J. C. Knight, and P. S. Russell. Remotely Addressed Optical Fibre Curvature Sensor Using Multicore Photonic Crystal Fibre. *Optics Communications*, 193(1-6):97–104, 2001. (cited on page 158)

[MMG89] G. Meltz, W. W. Morey, and W. H. Glenn. Formation of Bragg Gratings in Optical Fibers by a Transverse Holographic Method. *Optics Letters*, 14:823825, August 1989. (cited on page 55)

[MRFL84] M. J. Marrone, S. C. Rashleigh, E. J. Friebele, and K. J. Long. Radiation-Induced Effects in a Highly Birefringent Fibre. *Electronics Letters*, 20(5):193–194, March 1984. (cited on page 88)

[NH05] P. Nash and D. Hill. Fibre-Optic Hydrophone Array for Acoustic Surveillance in The Littoral. *Proceedings of SPIE*, 5780:1–10, 2005. (cited on page 171)

[NM07] P. Niewczas and J. R. McDonald. Advanced Optical Sensors for Power and Energy Systems. *IEEE Instrumentation and Measurement Magazine*, 10(1):18–28, February 2007. (cited on page 32)

[NMM+00] P. Niewczas, W.C. Michie, W.I. Madden, A. Cruden, and J.R. McDonald. Field Evaluation of FR5 Glass Optical Current Transducer.

Proceedings of SPIE (Applications of Optical Fiber Sensors), 4074:146–154, 2000. (cited on page 46)

[Nuf11] Nufern. Nupanda: Nufern polarization-maintaining fibers, 2011. Available from `http://www.nufern.com/pdf/marketing_pdf/marketing_pdf11.pdf`. (cited on page 88)

[OBS+05] Y. Okawachi, M. S. Bigelow, J. E. Sharping, Z. M. A. Schweinsberg, D. J. Gauthier, R. W. Boyd, and A. L. Gaeta. Tunable All-Optical Delays via Brillouin Slow Light in an Optical Fiber. *Physics Review Letters*, 94, 2005. (cited on page 126)

[Oka90] H. Okamura. Fiber-Optic Magnetic Sensor Utilizing the Lorentzian Force. *Journal of Lightwave Technology*, 8(10):1558–1564, October 1990. (cited on page 39)

[oLPT11] Encyclopedia of Laser Physics and Technology. Kramers-Kronig Relations, 2011. Available from `http://www.rp-photonics.com/kramers_kronig_relations.html`. (cited on pages 42, 86)

[ON10] P. Orr and P. Niewczas. An Optical Fibre System Design Enabling Simultaneous Point Measurement of Magnetic Field Strength and Temperature Using Low-Birefringence FBGs. *Sensors and Actuators A: Physical*, 163:68–74, September 2010. (cited on page 155)

[PDD06] V. M. N. Passaro, F. Dell'Olio, and F. De Leonardis. Electromagnetic Field Photonic Sensors. *Progress in Quantum Electronics*, 30(2-3):45–73, 2006. (cited on page 34)

[Per11] M. Perry. The Effects of Neutron-Gamma Radiation on Fiber Optical Sensors. Technical report, Institute for Energy and Environment, University of Strathclyde, April 2011. (cited on page 86)

[PH76] A. Papp and H. Harms. Polarization Optics of Liquid-Core Optical Fibers. *Applied Optics*, 16(5):1315–1319, October 1976. (cited on page 59)

[Pho11] EPI Photonics. High speed optical switches, 2011. Available from `http://epiphotonics.com/`. (cited on pages 142, 166, 185)

[POH00] F. Piao, W. G. Oldham, and E. E. Haller. The Mechanism of Radiation-Induced Compaction in Vitreous Silica. *Journal of Non-Crystalline Solids*, 276:61–71, 2000. (cited on page 85)

[PP99] ITER Physics Expert Group on Diagnostics and ITER Physics Basis Editors. Chapter 7: Measurement of Plasma Parameters. *Nuclear Fusion*, 39(12):2541–2575, 1999. (cited on pages 3, 15, 16, 23, 24, 26, 27, 201)

[Pri58] W. Primak. Fast-Neutron-Induced Changes in Quartz and Vitreous Silica. *Physics Review*, 110:1240–1254, June 1958. (cited on pages 85, 86)

[Rao97] Y. J. Rao. In-Fibre Bragg Grating Sensors. *Measurement Science and Technology*, 8:355–375, 1997. (cited on pages 31, 61, 65, 78, 136)

[REW97] A. H. Rose, S. M. Etzel, and C. M. Wang. Verdet Constant Dispersion in Annealed Optical Fiber Current Sensors. *Journal of Lightwave Technology*, 15(5):803–807, May 1997. (cited on pages 46, 137)

[Rog88] A. J. Rogers. Optical Fibre Current Measurement. *International Journal of Optoelectronics*, 3(5):407–591, 1988. (cited on page 59)

[RRH64] R. Rosenberg, C. B. Rubinstein, and D. R. Herriott. Resonant Optical Faraday Rotator. *Applied Optics*, 3(9):1079–1083, September 1964. (cited on page 54)

[RU79] S. C. Rashleigh and R. Ulrich. Magneto-optic Current Sensing with Birefringent Fibers. *Applied Optics*, 34(11):768–770, June 1979. (cited on page 60)

[RWF+04] D. Reilly, A.J. Willshire, G. Fusiek, P. Niewczas, and J.R. McDonald. A Fibre Bragg Grating Based Sensor for Simultaneous AC Current and Temperature Measurement. In *IEEE Sensors Journal*, volume 3, pages 1426–1429, October 2004. (cited on page 35)

[SCT+07] J. Sun, C. C. Chan, K. M. Tan, X. Y. Dong, and P. Shum. Application of an Artificial Neural Network for Simultaneous Measurement of Bending Curvature and Temperature with Long-Period Fiber Gratings. *Sensors and Actuators A: Physical*, 137(2):262–267, 2007. (cited on page 158)

[SD79] A. Sugimura and K. Daikoku. Wavelength Dispersion of Optical Fibres Directly Measured by Difference Method in the 0.8–1.6μm range. *Review of Scientific Instruments*, 50(3), 1979. (cited on page 116)

[SFC+94] L. Sandlund, M. Fahlander, T. Cedell, A. E. Clark, J. B. Restorff, and M. Wun-andFogle. Magnetostriction, Elastic Moduli, and Coupling Factors of Composite Terfenol-D. *Journal of Applied Physics*, 75(10):5656–5658, May 1994. (cited on page 36)

[SH97] B. R. L. Siebert and H. Henschel. Calculation of Fast Neutron Dose in Plastic-Coated Optical Fibres. In *4th European Conference on Radiation and its Effects on Components and Systems (RADECS 97)*, Cannes, France, September 1997. (cited on page 82)

[She81] S. K. Sheem. Optical Fiber Interferometers with 3×3 Directional Couplers: Analysis. *Journal of Applied Physics*, 52(6):3865–3872, 1981. (cited on page 72)

[SHHK05] L. Skuja, M. Hirano, H. Hosono, and K. Kajihara. Defects in Oxide Glasses. *Physica Status Solidi (C)*, 2(1):15–24, 2005. (cited on pages 80, 84)

[SHS93] F. Schliep, R. Hereth, and G. Schiffner. Phase Sensitive Investigations of 3×3 Singlemode Fibre Directional Couplers. *Electronics Letters*, 29(1):68–70, January 1993. (cited on pages 72, 178)

[SLO00] M. J. Steel, M. Levy, and R. M. Osgood. Large Magnetooptical Kerr Rotation From Photonic Bandgap Structures With Defects. *Journal of Lightwave Technology*, 18(9):1289–1296, September 2000. (cited on page 100)

[Smi80] A. M. Smith. Birefringence Induced by Bends and Twists in Single-mode Optical Fiber. *Applied Optics*, 19(15):2606–2611, August 1980. (cited on page 59)

[SMP00] M. Sedlar, V. Matejec, and I. Paulicka. Optical Fibre Magnetic Field Sensors Using Ceramic Magnetostrictive Jackets. *Sensors and Actuators A: Physical*, 84(3):297–302, 2000. (cited on pages 35, 36)

[Sys11] Stanford Research Systems. About Lock-In Amplifiers, 2011. Available from `http://www.thinksrs.com/downloads/PDFs/ApplicationNotes/AboutLIAs.pdf`. (cited on page 188)

[TaFBNT06] M. D. Todd, M. Seaver ad F. Bucholtz, J. M. Nichols, and S. T. Trickey. Modeling and Measurement of Accuracy/Distortion in an Operationally Passive FBG Demodulation Technique. *Proceedings of SPIE*, 6371, November 2006. (cited on page 92)

[TBF97] G. J. Tearney, B. E. Bouma, and J. G. Fujimoto. High Speed Phase and Group-Delay Scanning with a Grating-Based Phase-Control Delay Line. *Optics Letters*, 22:1811–1813, 1997. (cited on page 126)

[TJA01] M. D. Todd, G. A. Johnson, and B. L. Althouse. A Novel Bragg Grating Sensor Interrogation System Utilizing a Scanning Filter, a Mach-Zehnder Interferometer and a 3×3 Coupler. *Measurement Science and Technology*, 12:771–777, 2001. (cited on pages 74, 166, 202)

[TJC99] M. D. Todd, G. A. Johnson, and C. C. Chang. Passive, Light Intensity-Independent Interferometric Method for Fibre Bragg Grating Interrogation. *Electronics Letters*, 35(22):1970–1971, October 1999. (cited on page 72)

[TSB02] M. D. Todd, M. Seaver, and F. Bucholtz. Improved, Operationally-Passive Interferometric Demodulation Method Using 3×3 Coupler. *Electronics Letters*, 38(15):784–786, July 2002. (cited on pages 72, 123, 166)

[TTC+10] D. Testa, M. Toussaint, R. Chavan, J. Guterl, J. B. Lister, J.M. Moret, A. Perez, F. Sanchez, B. Schaller, G. Tonetti, A. Encheva,

G. Vayakis, C. Walker, Y. Fournier, T. Maeder, A. Le-Luyer, Ph. Moreau, G. Chitarin, E. Alessi, R. S. Delogu, A. Gallo, N. Marconato, S. Peruzzo, M. Preindl, H. Carfantan, E. Hodgson, J. Romero, R. Vila, B. Brichard, and L. Vermeeren. The Magnetic Diagnostics Set for ITER. *IEEE Transactions on Plasma Science*, 38(3):284–294, March 2010. (cited on pages 16, 26)

[VAB+06] M. Vasiliev, K. E. Alameh, V. I. Belotelov, V. A. Kotov, and A. K. Zvezdin. Magnetic Photonic Crystals: 1-D Optimization and Applications for the Integrated Optics Devices. *Journal of Lightwave Technology*, 24(5):2156–2162, May 2006. (cited on page 100)

[VBL+99] M. Vallet, F. Bretenaker, A. Le Floch, R. Le Naour, and M. Oger. The Malus Fabry-Perot Interferometer. *Optics Communications*, 168:423–443, September 1999. (cited on page 54)

[VKA+08] M. Vasiliev, V. A. Kotov, K. E. Alameh, V. I. Belotelov, and A. K. Zvezdin. Novel Magnetic Photonic Crystal Structures for Magnetic Field Sensors and Visualizers. *IEEE Transaction on Magnetics*, 44(3):323–328, March 2008. (cited on page 102)

[VUBN+99] M. Van Uffelen, F. Berghmans, A. Nowodzinski, P. Jucker, B. Brichard, F. Vos, and M. Decreton. Fiber-Optic Link Components for Maintenance Tasks in Thermonuclear Fusion Environments. In *5th European Conference on Radiation and its Effects on Components and Systems (RADECS 99)*, pages 491–496, 1999. (cited on pages 85, 86, 89, 90, 91)

[VVI+09] V. V. Voloshin, I. L. Vorob'ev, G. A. Ivanov, A. O. Kolosovskii, Y. K. Chamorovskii, O. V. Butov, and K. M. Golant. Radiation Resistant Optical Fiber with a High Birefringence. *Journal of Communications Technology and Electronics*, 54(7):847–851, 2009. (cited on page 88)

[WEL+06] T. R. Wolinski, S. Ertman, P. Lesiak, A. W. Domanski, A. Czapla, R. Dabrowski, E. Nowinowski-Kruszelnicki, and J. Wojcik. Photonic Liquid Crystal Fibers: A New Challenge for Fiber Optics and Liq-

uid Crystals Photonics. *Opto-electronics Review*, 14(4):329–334, 2006. (cited on page 40)

[WKB94] R.S. Weis, A.D. Kersey, and T.A. Berkoff. A Four-Element Fiber Grating Sensor Array with Phase-Sensitive Detection. *Photonics Technology Letters, IEEE*, 6(12):1469–1472, December 1994. (cited on page 170)

[WL97] L. Wei and J. W. Y. Lit. Phase-Shifted Bragg Grating Filters with Symmetrical Structures. *Journal of Lightwave Technology*, 15(8):1405–1410, August 1997. (cited on page 101)

[WLZ07] Z. P. Wang, X. Y. Liu, and Y. M. Zhang. Theoretical Analysis of the Effects of Linear Birefringence upon Optical Glass Current Transformers with Different Optical Designs. *Measurement*, 40:811–815, August 2007. (cited on page 54)

[Woo95] R.D. Woolley. Tokamak Poloidal Magnetic Field Measurements Accurate for Unlimited Time Durations. In *16th IEEE/NPSS Symposium on Fusion Engineering*, volume 2, pages 1530–1533, September 1995. (cited on pages 3, 27)

[WRD+91] P. A. Williams, A. H. Rose, G. W. Day, T. E. Milner, and M. N. Deeter. Temperature Dependence of the Verdet Constant in Several Diamagnetic Glasses. *Applied Optics*, 30(10), April 1991. (cited on pages 47, 134)

[WSE+06] T. R. Wolinski, K. Szaniawska, S. Ertman, P. Lesiak, and A. W. Domanski. Photonic Liquid Crystal Fibers: New Merging Opportunities. In *Proceedings of the Symposium on Photonics Technologies for 7th Framework Program*, pages 95–99, Wroclaw, October 2006. (cited on page 40)

[YKIO82] T. Yoshino, K. Kurosawa, K. Itoh, and T. Ose. Fiber-Optic Fabry-Perot Interferometer and its Sensor Applications. *IEEE Journal of Quantum Electronics*, 18(10):1624–1633, October 1982. (cited on page 53)

[YZZ+04] Y. S. Yu, Z. Y. Zhao, Z. C. Zhuo, W. Zheng, Y. Qian, and Y. S. Zhang. Bend Sensor Using an Embedded Etched Fiber Bragg Grating. *Microwave and Optical Technology Letters*, 43(5):414–417, December 2004. (cited on page 158)

[ZCW+02] M. Zhang, C. C. Chan, D. N. Wang, J. M. Gong, W. Jin, and M. S. Demokan. Time Division Multiplexed Strain Sensing System by the use of Dual-Wavelength Fiber Bragg Gratings. *Sensors and Actuators A: Physical*, 100(2):175–179, 2002. (cited on pages 78, 170)

[ZK97] A. K. Zvezdin and V. A. Kotov. *Modern Magnetooptics and Magnetooptical Materials*, chapter 2. Institute of Physics Publishing, first edition, 1997. ISBN 0 7503 0362 X. (cited on page 42)

[ZL93] F. Zhang and J. W. Y. Lit. Temperature and Strain Sensitivity Measurements of High-Birefringent Polarization-Maintaining Fibers. *Applied Optics*, 32(13):2213–2218, May 1993. (cited on page 150)

[ZL95] R. Zengerle and O. Leminger. Phase-Shifted Bragg Grating Filters with Improved Transmission Characteristics. *Journal of Lightwave Technology*, 13(12):2354–2358, December 1995. (cited on page 101)

[ZZZ+09] Y. Zhao, H. W. Zhao, X. Y. Zhang, B. Yuan, and S. Zhang. New Mechanisms of Slow Light and Their Applications. *Optics and Laser Technology*, 41(5):517–525, 2009. (cited on page 111)